Electronic Control of Protein Interactions

Mark Anthony Sellick

Submitted in accordance with the requirements for the degree of
Doctor of Philosophy

The University of Leeds
Centre for Doctoral Training in Molecular-Scale Engineering
School of Electronic and Electrical Engineering
September 2016

The candidate confirms that the work submitted is his own and that appropriate credit has been given where reference has been made to the work of others.

Acknowledgements

I would first like to acknowledge my supervisor Professor Christoph Wälti for his invaluable guidance and support during my studies. Doctor Steven Johnson and Doctor Simon White, the other members of the coiled coil team, have also been integral to this project and I thank them for their assistance and friendship.

I would also like to thank Doctor Franziska Thomas and Professor Dek Woolfson for their insights and assistance designing and synthesising the peptides used in this work.

I must also thank all the members of the Bioelectronics Group, past and present, for their expertise and friendship over the years. Thanks also to the members of the various biology and chemistry groups in Leeds and Bristol for helping the confused physicist who could occasionally be found in their labs asking odd questions and trying not to break anything.

Thanks also go to my friends in the original cohort of the Centre for Doctoral Training in Molecular Scale Engineering: Will, Billa, Andy, Scott and Olly. I could not have asked for a better group of friends to go through the CDT experience with.

Finally and most importantly, thank you to my family, and particularly my wife Laura, for their unwavering love and support.

Abstract

This thesis details work carried out with the aim of demonstrating electronic control of protein interactions. A pair of coiled coil peptides including an acidic peptide and an alkaline peptide were designed and synthesised. Characterisation studies were carried out in solution using CD and FRET, which showed that heterodimers were preferentially formed at neutral and weakly alkaline pH and that homodimers of the alkaline peptide were preferentially formed at strongly alkaline pH. This demonstrated that the peptides had pH dependent binding behaviour, as intended. Characterisation was then performed using FRET, SPR, and CD with the alkaline peptide immobilised on surfaces. It was shown that the pH dependent binding behaviour was retained, with the acidic peptides dissociating from the alkaline peptide monolayer only above a certain alkaline binding pH. This binding pH was typically lower than the pH at which homodimer preferentially formed in solution and could be changed by varying the concentration and pH at which the monolayers were formed. This led to the conclusion that the binding pH depended on the density of the monolayer. Experiments were performed to demonstrate that the pH of a solution in the vicinity of an electrode could be changed electrochemically and measured using optical techniques. It was shown that the pH changes immediately at the electrode surface were significantly larger than those observed further into the solution. Monolayers of heterodimers were then immobilised on electrodes via the alkaline peptide and it was demonstrated that the acidic peptide could be removed from the monolayer by application of a current to the electrode. Control experiments demonstrated that the removal of the acidic peptide was caused by the pH change at the electrode surface that was induced by the current application. Electronic control of protein interactions was therefore demonstrated.

Table of contents

List of tables and illustrative material

List of abbreviations

°C: Degree Celsius

A: Ampere

AFM: Atomic force microscope/microscopy

APTES: (3-aminopropyl)triethoxysilane

BCECF: (2′,7′ –*bis*-(Carboxyethyl)-5-(and-6)-carboxyfluorescein)

CIIPHH: Copper (II) perchlorate hexahydrate

CD: Circular dichroism (spectroscopy)

CLSM: Confocal laser scanning microscope/microscopy

deg: Degree

DCM: Dichloromethane

DIC: Diisopropylcarbodiimide

DMF: Dimethylformamide

DNA: Deoxyribonucleic acid

DTT: Dithiothreitol

EDC: 1-ethyl-3-(3-dimethylaminopropyl)carbodiimide

Fmoc: Fluorenylmethyloxycarbonyl chloride

FRET: Förster resonance energy transfer

h: Hour

HEPES: (4-(2-hydroxyethyl)-1-piperazineethanesulfonic acid)

HPLC: High performance liquid chromatography

ITO: Indium tin oxide

K_d: Dissociation constant

L: Litre

LD: Linear dichroism

m: Metre

M: Molar

MALDI-TOF: Matrix assisted laser desorption time-of flight

MES: 2-(N-morpholino)ethanesulfonic acid

min: Minute

MPTMS: (3-mercaptopropyl)trimethoxysilane

MRME: Mean residue molar ellipticity

NHS: N-hydroxysuccinimide

PBS: Phosphate buffered saline

PTFE: Polytetrafluoroethylene

QCM-D: Quartz crystal microbalance with dissipation monitoring

s: Second

SAM: Self-assembled monolayer

SCE: Saturated calomel electrode

SHE: Standard hydrogen electrode

SNARF: Seminaphtharhodafluor

SPR: Surface plasmon resonance (spectroscopy)

t-Boc: *tert*-butyloxycarbonyl

TFA: Trifluoroacetic acid

T_m: Melting temperature

UV: Ultra violet

V: Volt

1. Introduction

1.1. Aim of this work

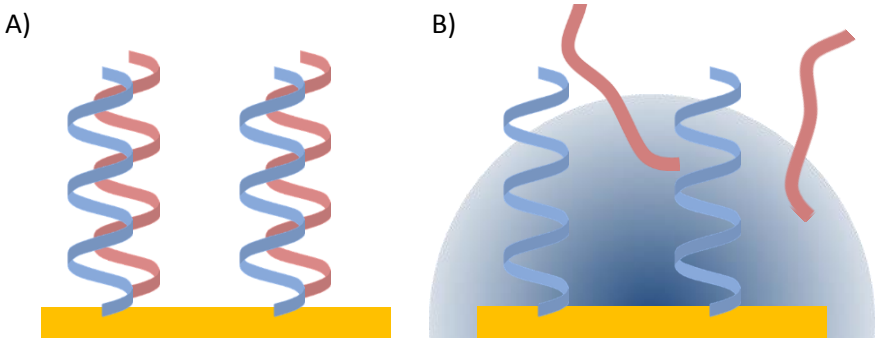

Figure 1.1: Diagram illustrating the aim of the present work. Peptide B (shown in blue) of a pH sensitive coiled coil pair A (shown in red) and B is immobilised on an electrode. A) At neutral solution pH the peptide A binds to the peptide B. B) The electrode can be used to locally change the solution pH. The change in pH prevents the binding and the peptide A is therefore released into the solution.

This report details work carried out with the aim of developing a technique for the electronic control of protein interactions via localised electrochemically induced pH changes. A specific type of protein, known as a coiled coil peptide, is used in this work as a system to demonstrate electronic control of protein interactions. Electrochemical control of pH near electrodes is used to control the pH-sensitive interactions of two coiled coil peptides when one of the pair is immobilised on the electrode surface, see Figure 1.1.

1.2. Motivation

The word 'protein' was coined by the Swedish chemist Jöns Jacob Berzelius in 1838.[1,2] In a letter to Gerardus Johannes Mulder, discussing Mulder's discovery that fibrin (a protein involved in blood clotting) and albumin (the main protein found in human blood plasma) had almost identical elemental compositions, Berzelius wrote:

"The name protein that I propose for the organic oxide of fibrin and albumin, I wanted to derive from πρωτειοζ [Greek 'proteios' meaning 'standing in front' or 'in the lead'], *because it seems to be the primitive or principal substance of animal nutrition, which plants prepare for the herbivores, and the latter then furnish for carnivores."*[3]

At that time, only a handful of proteins were known, and their functions were a mystery. Nowadays, over 50,000 protein families are known,[4] and though the precise function of a particular protein may remain unknown, a huge range of processes for which they are responsible has been identified. A handful of examples demonstrates the wide-ranging roles of proteins in the human body, see Figure 1.2. Haemoglobin, present in red blood cells, is responsible for the binding and transport of oxygen. Insulin is produced in the pancreas and regulates the absorption

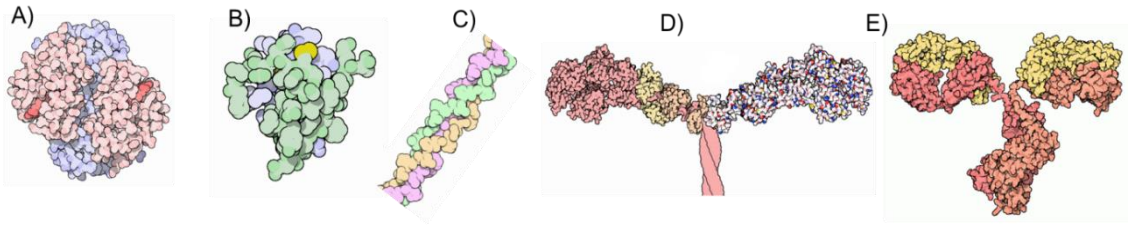

Figure 1.2: Drawings of A) haemoglobin (Protein Data Bank ID: 2HHB), B) insulin (PDB ID: 1TRZ), C) collagen (PDB ID: 1BKV), D) myosin (PDB ID: 1B7T), and E) immunoglobulin (PDB ID: 1IGT). Adapted from Protein Data Bank.[22]

of glucose from the blood, among other functions. Other proteins, such as keratin and collagen, are structural. Keratin is the main component of nails and hair, whereas collagen is found in most fibrous tissue. Immunoglobulins, or antibodies, are part of the immune system. They recognise foreign objects such as bacteria and viruses and either neutralise them directly or mark them for destruction by other parts of the immune system. Motor proteins such as the myosin family are involved in muscle contraction. Finally, enzymes are a major class of proteins that function as biological catalysts to lower the activation energy of chemical reactions. The ability to control proteins and their interactions is therefore of great interest for biological research and medical and industrial applications, and some examples are given below.

Most proteins measure a few nanometres across, and so their diverse structures and functions make them molecules of great interest in the field of nanotechnology. However, to harness the power of proteins it will be necessary to develop techniques for controlling their structures, functions and interactions. Electronics is the most developed area of nanotechnology, driven by the necessity for ever greater computing power. Computing devices including transistors using 14 nm processes are currently available to consumers, 14 nm being similar to the length of a myosin molecule. Research into electronic control of proteins, interfacing the best of human nanotechnology with the incredible nanotechnology that nature has evolved over millions of years, is therefore extremely worthwhile.

An obvious application is as a tool for interactomics research, which is the study of protein interactions. The mapping of the human genome was completed in 2003, but true understanding of the genome requires not only mapping the human proteome (i.e. the set of proteins encoded by the genome),[5,6] but also, ultimately, an understanding of the human interactome, i.e. the interactions between all the proteins encoded by the genome.[7,8] Techniques for electronic control of protein interactions have the potential to greatly facilitate interactomics research, just as the development of automated DNA sequencing made possible the mapping of the human genome.

There is significant potential for industrial applications of electronic control of protein interactions. Enzymes have been used for centuries to make products such as wine, cheese and leather and today many industries exploit the catalytic properties of enzymes to enable or enhance

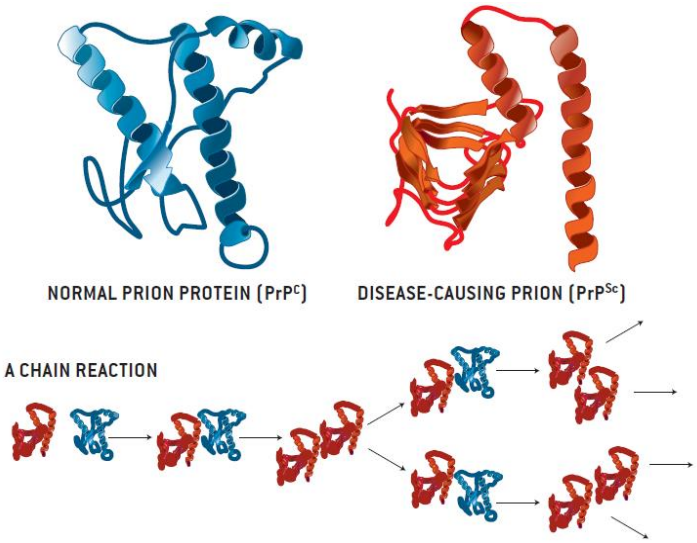

Figure 1.3: Prions are misfolded versions of native proteins that induce misfolding via protein-protein interactions, thereby leading to more misfolded proteins, which then go on to misfold further native proteins and/or aggregate into amyloids. Adapted from Prusiner.[23] Copyright Lucy Reading-Ikkanda/Scientific American Magazine. Used with permission.

desirable chemical reactions.[9] A technique enabling electronic activation and deactivation of enzymes might therefore be extremely valuable.

Other similar hybrid bioelectronic devices can be envisaged, and may find uses in next generation computers, for example. It will soon become impossible to continue reducing the size of transistors using the current top-down semiconductor fabrication approach.[10] One potential solution to allow continued progress in computing power is to utilise a bottom-up approach to fabrication, in which the properties of biomolecules such as proteins are harnessed.[11] Techniques for electronic control of protein interactions may very well be required for this approach to succeed.

Medical applications are also possible. Undesirable protein-protein interactions are implicated in a number of diseases. Amyloidosis is caused when aggregates of misfolded proteins (called amyloids) deposit in organs, causing damage and/or impairing organ function. Amyloid deposits in the brain are probable factors in the brain damage caused by neurological conditions such as Alzheimer's and Huntington's diseases. Prions are misfolded versions of native proteins that induce misfolding via protein-protein interactions, thereby leading to more misfolded proteins, which then go on to misfold further native proteins and/or aggregate into amyloids, see Figure 1.3. Examples of prion diseases are scrapie (in sheep), bovine spongiform encephalopathy (BSE, in cows) and Creutzfeldt-Jakob disease (CJD), fatal familial insomnia (FFI) and kuru (in humans). These prion diseases are infectious, untreatable and fatal, and as many as 1 in 2,000 people in the UK may be infected with vCJD prions, as a result of the BSE epidemic in the late 1980s.[12] Devices for electronic control of protein interactions could therefore be very valuable for research into these diseases, or even as implants for therapeutic applications.

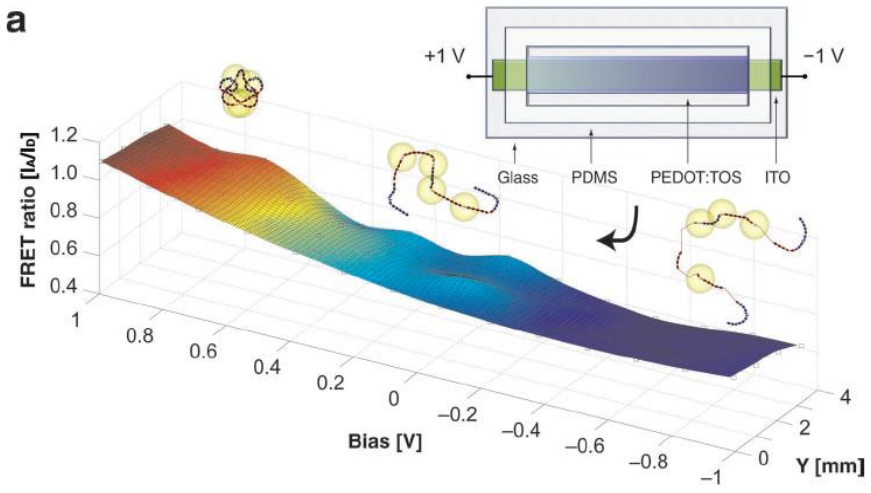

Figure 1.4: Electrical control of protein conformation. A potential gradient was applied across an indium tin oxide (ITO) electrode on which a conducting polymer film (PEDOT:TOS) had been formed. The conformation of adsorbed fibronectin, as measured by FRET, varied across the gradient, from completely folded at the positive end to unfolded at the negative end. Adapted from Wan *et al*.[21]

1.3. Previous work in the field

A number of studies have been performed on the effect of electric fields on proteins and peptides.[13] The use of electric fields to orient proteins and peptides is reasonably well established and not particularly pertinent to the current work, but there are also reports of electric fields used to control protein and peptide conformation. In a study of bacteriorhodopsin, Porschke appears to have been the first to convincingly demonstrate an electric field induced conformational change.[14] Rochu *et al* also found evidence for field induced unfolding in their work on acetylcholinesterase (an enzyme for breaking down choline esters).[15] In a more decisive report, Washizu *et al* used electric fields to control the conformation of flagellin filaments (the main component of bacterial flagellum), and demonstrated the ability to dynamically switch between conformational states by varying the field strength.[16] Kitagawa *et al* reported the ability to change the structure of an electrode-immobilised peptide containing the non-proteinogenic amino acid α-aminoisobutyric acid from alpha helical to 3_{10}-helical by changing the bias of an applied potential.[17] Simulations by Baumketner of the effect of electric fields on alanine peptides showed that the increasing field strengths could induce coil-helix transitions[1] and thereby dissociate preformed beta sheets.[18]

Jeuken and coworkers have demonstrated electronic control of a ubiquinol oxidase (an enzyme that plays a role in bacterial electron transport) contained within lipid bilayers on electrode surfaces. The bilayers contained ubiquinone, allowing the control of the ubiquinol oxidase activity through electrochemical reduction of the ubiquinone. In later work the lipid bilayers were formed into vesicles and the enzyme activity was monitored via a pH sensitive

[1] Coil in this context refers to a random coil structure, i.e. an unfolded protein/peptide, not a coiled coil as used in this work.

fluorescent dye[2] within the vesicles which detected the proton gradient induced by the action of the ubiquinol oxidase.[19,20]

Wan *et al* used a conducting polymer on indium tin oxide (ITO) electrodes to electrically control fibronectin (a large protein found in the extracellular matrix) conformation.[21] The steady-state application of a potential gradient across the electrode led to a matching gradient in adsorbed fibronectin conformations, from folded at the positive end to unfolded at the negative end, as measured by Förster resonance energy transfer (FRET), see Figure 1.4. The authors suggest that local pH changes caused by redox reactions of the polymer may be the cause of the conformation changes. No attempts to dynamically control the adsorbed fibronectin conformation by varying the potential were reported.

Despite these studies into electronic control of protein conformation and activity, there appears to have been little or no work on electronic control of protein interactions. This work therefore aims to show that such control is possible and worthy of further research.

1.4. Overview

This work comprises eight chapters and two appendices. This first chapter gives an introduction with the motivation for researching electronic control of protein interactions and an overview of the thesis. Chapter 2 contains background information and literature reviews on the topic of electrochemical control of pH, and the topics of proteins and peptides in general, and coiled coils and their applications. Chapter 3 contains explanations of the experimental techniques used in the research. Chapters 4-7 are experimental results chapters. Each contains specific details of the materials and methods used to obtain the data in that chapter. Chapter 4 details the design, synthesis and solution characterisation of the peptides and the data show that a system of coiled coil peptides with pH dependent interactions was successfully designed and synthesised. Chapter 5 details the characterisation of the interactions of the peptides when one of the pair is immobilised on a surface. The data show that pH dependent interactions were retained after immobilisation, and that the pH range in which interactions occurred was different to when the peptides were in solution. Chapter 6 details the characterisation of electrochemical control of pH and the data show that large changes in pH were obtained at the electrode surface. Chapter 7 details experiments performed to demonstrate electronic control of the peptide interactions, and the data show that electronic control of peptide interactions was indeed demonstrated. Chapter 8 contains conclusions and suggestions for further work. Appendix A1 contains details of electrochemical pH change experiments performed with competing electrodes, Appendix A2

[2] It is interesting to note that in this form the work of Jeuken and coworkers is, in a way, the exact opposite of the work presented here. They electronically controlled a protein in order to produce a pH change whereas here the idea is to electronically produce a pH change to control a protein.

contains details of electrochemical pH measurement experiments, and Appendix A3 contains additional experimental material omitted from the results chapters.

1.5. References

1. Hartley, H. Origin of the Word ‘Protein’. *Nature* **168,** 244–244 (1951).
2. Vickery, H. B. The origin of the word protein. *Yale J. Biol. Med.* **22,** 387–93 (1950).
3. Tanford, C. & Reynolds, J. *Nature’s Robots: A History of Proteins*. (Oxford University Press, 2004).
4. Kunin, V., Cases, I., Enright, A. J., de Lorenzo, V. & Ouzounis, C. A. Myriads of protein families, and still counting. *Genome Biol.* **4,** 401 (2003).
5. Uhlen, M. *et al.* Tissue-based map of the human proteome. *Science* **347,** 1260419–1260419 (2015).
6. Kim, M.-S. *et al.* A draft map of the human proteome. *Nature* **509,** 575–581 (2014).
7. Bonetta, L. Protein–protein interactions: Interactome under construction. *Nature* **468,** 851–854 (2010).
8. Rolland, T. *et al.* A Proteome-Scale Map of the Human Interactome Network. *Cell* **159,** 1212–1226 (2014).
9. Kirk, O., Borchert, T. V. & Fuglsang, C. C. Industrial enzyme applications. *Curr. Opin. Biotechnol.* **13,** 345–351 (2002).
10. Lu, W. & Lieber, C. M. Nanoelectronics from the bottom up. *Nat. Mater.* **6,** 841–850 (2007).
11. Varghese, S., Elemans, J. A. A. W., Rowan, A. E. & Nolte, R. J. M. Molecular computing: paths to chemical Turing machines. *Chem. Sci.* **6,** 6050–6058 (2015).
12. Gill, O. N. *et al.* Prevalent abnormal prion protein in human appendixes after bovine spongiform encephalopathy epizootic: large scale survey. *BMJ* **347,** f5675–f5675 (2013).
13. Porschke, D. Effects of Electric Fields on Biopolymers. *Annu. Rev. Phys. Chem.* **36,** 159–178 (1985).
14. Porschke, D. Electrostatics and electrodynamics of bacteriorhodopsin. *Biophys. J.* **71,** 3381–3391 (1996).
15. Rochu, D., Pernet, T., Renault, F., Bon, C. & Masson, P. Dual effect of high electric field in capillary electrophoresis study of the conformational stability of Bungarus fasciatus acetylcholinesterase. *J. Chromatogr. A* **910,** 347–357 (2001).
16. Washizu, M., Shikida, M., Aizawa, S. -i. & Hotani, H. Orientation and transformation of flagella in electrostatic field. *IEEE Trans. Ind. Appl.* **28,** 1194–1202 (1992).
17. Kitagawa, K., Morita, T. & Kimura, S. A helical molecule that exhibits two lengths in

response to an applied potential. *Angew. Chem. Int. Ed. Engl.* **44,** 6330–3 (2005).

18. Baumketner, A. Electric Field as a Disaggregating Agent for Amyloid Fibrils. (2014).

*19. Daskalakis, N. N., Evans, S. D. & Jeuken, L. J. C. Vesicle-modified electrodes to study proton-pumping by membrane proteins. *Electrochim. Acta* **56,** 10398–10405 (2011).

*20. Daskalakis, N. N., Müller, A., Evans, S. D. & Jeuken, L. J. C. Driving bioenergetic processes with electrodes. *Soft Matter* **7,** 49 (2011).

21. Wan, A. M. D. *et al.* Electrical control of protein conformation. *Adv. Mater.* **24,** 2501–2505 (2012).

22. Protein Data Bank. *Research Collaboratory for Structural Bioinformatics* Available at: http://www.rcsb.org/pdb/home/home.do. (Accessed: 30th August 2012)

23. Prusiner, S. B. Detecting mad cow disease. *Sci. Am.* **291,** 86–93 (2004).

2. Background and literature review

2.1. Introduction

This chapter contains background information and a review of the literature relevant to this work. Section 2.2 introduces the concept of electrochemical pH control and how it may be measured, then reviews applications of the technique in the literature. Section 2.3 is a brief introduction to proteins and peptides. Section 2.4 focuses on coiled coil peptides, which are the peptides used in this work. The basic principles and features of coiled coils are presented, followed by a review of coiled coil monolayers and applications of coiled coils in the literature.

2.2. Electrochemical pH control

This section introduces the concept of electrochemical control of pH, which will be used to control peptide interactions in this work. The basic phenomenon of pH changes near electrode surfaces is simple to understand by considering electrodes in water. Near an anode (i.e. an electrode from which electrons flow into the solution), H^+ ions will be depleted, thereby increasing the pH. Near a cathode (i.e. an electrode into which electrons flow from the solution) OH^- ions will be depleted, decreasing the pH.[1] However, even in deionised water there are multiple reactions capable of causing pH change. Considering only the anode, the following reactions are possible, all of which will increase the local pH:

Water reduction:

$$2H_2O + 2e^- \rightarrow H_2 + 2OH^-$$

Proton reduction:

$$2H^+ + 2e^- \rightarrow H_2$$

(or, equivalently: $2H_3O^+ + 2e^- \rightarrow H_2 + 2H_2O$)

Dissolved oxygen reduction:

$$O_2 + 2H_2O + 4e^- \rightarrow 4OH^-$$

$$O_2 + 2H_2O + 2e^- \rightarrow H_2O_2 + 2OH^-$$

$$O_2 + 4H^+ + 4e^- \rightarrow 2H_2O$$

$$O_2 + 2H^+ + 2e^- \rightarrow H_2O_2$$

Similarly, reactions are possible that will decrease the local pH at the cathode:

Water oxidation:

$$2H_2O \rightarrow O_2 + 4H^+ + 4e^-$$

Hydroxyl oxidation:

$$4OH^- \rightarrow O_2 + 2H_2O + 4e^-$$

Dissolved hydrogen oxidation:

$$H_2 \rightarrow 2H^+ + 2e^-$$

$$H_2 + 2OH^- \rightarrow 2H_2O + 2e^-$$

Naturally, when other chemical species are present, such as those in buffers, the situation becomes increasingly complex.[2]

Though they are often overlooked, near-electrode pH changes are of interest in many branches of electrochemistry.[1] The pH changes can have a deleterious effect, for example an increase in acidity at an electrode surface may cause unexpectedly rapid corrosion of the electrode,[1] and an increase in alkalinity may affect the composition of deposited metals and alloys.[3,4] The effect may even have medical implications: Ballestrasse *et al* conducted a theoretical study of pH changes around stimulation microelectrodes used in the body for various medical purposes, predicting that large pH changes might occur on micrometre length scales at current densities lower than those presently used for neural stimulation.[5] It has been shown that positive and negative electrode potentials lead to increased or decreased blood clotting respectively,[6] and Simona *et al* have shown that decreased clotting at the cathode may partially be caused by alkali peptide hydrolysis caused by the local electrochemical increase in pH.[7]

2.2.1. Measurement of electrochemical pH changes

A variety of techniques have been used to study near-electrode pH change. In their 1983 review of near-electrode pH changes Kuhn and Chan divide measurement techniques into three sections: electrical, optical and sampling methods.[1] The sampling methods involved removal of near-electrode solution for outside measurement, either by direct removal through outlets near the electrode,[8,9] or by flash-freezing and slicing off thin layers of solution.[10] As well as being difficult to perform, these *ex situ* methods necessarily involved significant disturbances to the systems and hence have fallen out of use.

Electrical techniques typically involve the use of one or more pH sensitive electrodes in the vicinity of the working electrode. Kuhn and Chan note that the effects of ohmic drop (i.e. solution resistance) and shielding will present problems if one attempts to measure near-electrode

pH while current flows. Shielding is where the presence of the pH electrode very near the working electrode may block or distort the current densities. The dependence of the ohmic drop on distance is greatest in the immediate vicinity of the electrode, meaning that very precise positioning of the pH electrode is necessary to avoid large errors.[11] The resistivity of the solution will also be affected by changes in pH, thereby causing changes to the ohmic drop.[12] Slow response times and disturbances caused by gas evolution were also noted as problems by Kuhn and Chan, and while a recent study using a rotating ring disc electrode setup with iridium oxide as the pH probe was able to correct for the effects of ohmic drop, slow response times and gas evolution still proved problematic.[13]

Despite the limitations of optical approaches at the time, Kuhn and Chan ended their section on measurement with the conclusion that optical methods seemed most promising, and the subsequent development of confocal scanning laser microscopy (CLSM) has borne this out. CSLM builds three-dimensional fluorescence images from thin image 'slices' (see Section 3.2.3) and so is ideally suited to *in situ* and minimally disruptive spatial mapping of near electrode pH changes when used in combination with pH sensitive fluorescent dyes such as fluorescein, (2′,7′ –*bis*-(Carboxyethyl)-5-(and-6)-carboxyfluorescein) (BCECF), and seminaphtharhodafluor (SNARF) dyes. Some examples of work using this approach are presented below.

Boldt *et al* used SNARF-1 to detect pH changes caused by oxidation of nitrite or reduction of benzoquinone at platinum microelectrodes.[14] The equations for these processes are:

Nitrite oxidation to nitrate:

$$NO_2^- + H_2O \rightarrow NO_3^- + 2H^+ + 2e^-$$

Benzoquinone reduction to hydroquinone:

$$C_6H_4O_2 + 2H_2O + 2e^- \rightarrow C_6H_4(OH)_2 + 2OH^-$$

At a distance 30 μm from the electrode 2 s pulses of 1.4 V (vs. Ag pseudo-reference, leading to 150 nA peak current, which corresponded to 1900 A m^{-2} current density) applied to a 5 μm radius electrode in 5 mM bicine buffer with 10 mM nitrite caused oxidation of the nitrite, leading to generation of protons and a change from pH 9 to pH 6. Similarly, 2 s pulses of -0.5 V (-30 nA peak current, -380 A m^{-2} current density) in 5 mM 2-(N-morpholino)ethanesulfonic acid (MES) buffer with 10 mM benzoquinone led to reduction of the benzoquinone and a change from pH 6 to pH 8.5 30 μm from the electrode. By varying the buffer concentration they were able to modulate the pH change. 50 μm from the electrode they recorded a pH change of 1 unit (10 mM buffer), 3 units (5 mM) and 4 units (2.5 mM and 1.25 mM). Between 30 μm and 40 μm they recorded a pH change of 4 units for all buffer concentrations. At 70 μm from the electrode, they

recorded pH changes of 0 units (10 mM and 5 mM buffer), 1 unit (2.5 mM), and 2 units (1.25 mM).

Cannan *et al* used fluorescein to detect pH changes caused by reduction of benzoquinone.[15] Voltages of -0.1 V to -0.25 V (vs. Ag pseudo-reference, no current values given) were applied to 25 μm radius platinum electrodes in 0.2 M potassium chloride at pH 5.5 with 1 mM benzoquinone. The spatial extent of the pH gradient depended strongly on the applied voltage until it became diffusion limited at -0.25 V, where the pH gradient extended approximately 200 μm into solution in all directions. Finite element modelling of the pH gradient suggested that the pH reached a value of pH 10.5 in the vicinity (~ 50 μm) of the electrode. A second publication by the same group used a similar approach to study pH changes caused by reduction of water and oxygen.[16] Constant currents of 5 nA and 10 nA (no voltage values given) were applied to 25 μm diameter gold electrodes (giving current densities of 10 A m^{-2} and 20 A m^{-2} respectively) in 0.1 M potassium nitrate at pH 4.36, creating hemispherical pH gradients with radii of 24 and 49 μm respectively. In addition, constant currents of 4 nA, 7 nA, and 10 nA (no voltage values given) were applied to 80 μm diameter platinum electrodes (giving current densities of 0.8 A m^{-2}, 1.4 A m^{-2}, and 2 A m^{-2} respectively) in 0.1 M potassium nitrate at pH 5.04, creating hemispherical pH gradients with radii of 63 μm, 114 μm and 149 μm respectively. In all cases, the experimental data were a good match to predictions obtained from finite element modelling.

Klauke *et al* used SNARF-1 modified microbeads to probe pH changes near a gold microelectrode in 0.1 mM (4-(2-hydroxyethyl)-1-piperazineethanesulfonic acid) (HEPES) buffer containing 50 mM perchlorate. The beads were held in place by optical tweezers to enable spatial mapping of the changes.[17] The application of 2 V (vs. Au pseudo-reference, current values not given) or – 2 V caused a change in pH from pH 7.4 to < pH 6.8 or > pH 9 respectively, at a distance of 5 μm from the electrode. Using a series of beads spaced throughout the solution they measured a pH gradient extending approximately 30 μm into the solution, with pH > 10.5 at 3 μm from the electrode. This method of holding the beads (and therefore the dye) in place had an advantage over measurement with free dye in that it prevented potential changes in fluorescence caused by movement of the dye molecules. On the other hand, the presence of the relatively large (6 μm diameter) beads may have affected the diffusion and distribution of pH changes.

Gabi *et al* used fluorescein and carboxyeosin to measure pH changes in 150 mM NaCl near transparent indium tin oxide (ITO) microelectrodes.[18] Application of 4 A m^{-2} current density (1 μA current, voltage values not given) for 6 s resulted in a pH gradient extending 150 μm into the solution and a change from pH 6.5 to pH < 4.5 in the immediate vicinity of the electrode.

Suzurikawa *et al* used a photoconductive planar electrode where conductivity was induced by illumination. They used BCECF as the pH sensitive dye to measure pH gradients in the pH 7.2 phosphate buffered saline (PBS) near the electrodes.[19] Application of 5 V or – 4V (current values not given) for 400 ms led to pH changes in the immediate vicinity of the electrode

of -0.5 units and 0.6 units respectively, with the gradient in both cases extending 100 μm into the solution

Leenheer *et al* used BCECF to measure pH change near patterned gold catalytic areas on fluorine doped tin oxide electrodes in 66 mM sodium sulphate at pH 5.3.[20] Application of -4 μA current resulted in a change of pH to > 7.5 in the vicinity of the gold areas.

2.2.2. Applications of electrochemical pH changes

Electrochemical pH change has been taken advantage of by many research groups. One advantageous use is to control the deposition, swelling, or dissolution of various types of thin films. For example, Boulmedais *et al* controlled the build-up and dissolution of polyelectrolyte multilayers on an indium tin oxide (ITO) substrate by varying the voltage between 0 V and 1.8 V (vs. Ag). They concluded that the electrochemically induced pH change near the electrode played some part in the process.[21] Schmidt *et al* used gold coated silicon substrates and a voltage range of 0 V to -1 V (vs. SCE) to increase local pH and thereby dissolve hydrogen bonded thin (~150 nm) films.[22] The same group also used gold coated (5 nm Ti, 100 nm Au) silicon substrates and a voltage range of -1 V to 1 V (vs. Ag/AgCl) to alter the near-electrode pH and reversibly swell polyelectrolyte multilayer thin films.[23] Shacham *et al* used ITO on glass and gold (5 nm Cr, 200 nm Au) on glass and a voltage range of -1.6 V to 2.5 V (vs. Ag/AgCl) to control the sol-gel deposition of ZrO_2 thin films, allowing them to create films that were extremely smooth.[24] Diguéz *et al* used glass coated with ITO as a substrate on which the dissolution and stability tuning of PLL/DNA multilayers was performed. pH was reduced from 7.4 to 4 at the electrode by application of 1 Am^{-2} (~ 1.9 V vs. Ag/AgCl) and reduced from 7.4 to 6 by 0.01 A m^{-2} (~1.2 V). Decay of the pH gradient depended on buffer concentration, and for their conditions (10mM HEPES) the decay length was around 1 μm.[25]

There are other reported uses for electronic pH control. Graf *et al* demonstrated the release of a fluorescent dye from vesicles embedded in a polyelectrolyte multilayer deposited on an indium tin oxide (ITO) electrode. They used a galvanostatic (i.e. constant) current of 20 mA m^{-2} for 25 minutes. They suggest the system could be used for externally controlled drug release.[26] Tam *et al* used a mixed polymer brush modified ITO coated glass electrode which was reversibly switched between on/off states by the application of 0.85 V (vs. Ag/AgCl), mimicking the switching capabilities of transistors.[27,28] Kwon *et al* attached a polymer matrix containing insulin to a platinum electrode. 5 mA applied current caused controllable release of the insulin as the hydrogen bonding between the polymers was disrupted.[29] Guillaume-Gentil *et al* created polyelectrolyte films on which stem cell sheets could be formed and controllably released by pH changes caused by underlying electrodes.[30] Maurer *et al* used a silicon chip with individually addressable platinum electrodes to remove *t*-Boc protecting groups from peptide chains using a voltage of 3 V for 60 seconds. This allowed them to build up five different peptide chains by

repeated cycles of selective deprotection and immersion in desired peptide solution.[31] They also used a similar deprotection technique for production of DNA microarrays, but used an organic base to spatially confine the pH changes.[32]

Gabi *et al* observed the effect of pH change on a fluorescently labelled polyelectrolyte and living cells.[18] The polyelectrolyte was absorbed onto a glass surface with an ITO electrode and desorbed by pH changes. Application of 4 A m^{-2} current density for 30 s in H_2O led to desorption at distances up to 20 μm from the electrode. The use of 10x diluted McIlvaine buffer solutions limited the extent of desorption to 5-10 μm from the electrode and no desorption was observed for undiluted buffer. They also tested the effect of currents applied to living cells on the electrodes. Application of current densities higher than 0.57 A m^{-2} caused a significant increase in propidium iodide staining of the cells, indicating either cell death or increased opening of membrane pores. However, the authors note that it was not possible to discern between electrochemical changes in pH and electrochemical generation of reactive species as the reason for the effect on the cells.

2.3. Proteins and peptides

The basic building blocks of proteins and peptides are small molecules called amino acids, each with the generic structure NH_2-CHR-COOH, where R denotes a side chain, see Figure 2.1. Each type of amino acid has a different side chain and has different properties as a result, see Figure 2.2. There are 22 proteinogenic amino acids, i.e. amino acids found in natural peptides and proteins. The amino group of one amino acid can covalently bind to the carboxyl group of another. This is known as a peptide bond and the amino acids are known as amino acid residues when bonded in this manner. Multiple amino acids can bond in this manner in a non-branching linear chain to form a peptide or protein, with the side chains extending outwards from the peptide-bonded backbone. The difference between proteins and peptides is chiefly one of size, peptides being shorter and proteins longer chains. The boundary between the two is ill-defined; the International Union of Pure and Applied Chemistry (IUPAC) suggests that a protein should have a sequence of greater than 50 amino acids but acknowledges the lack of agreement.[33] The linear sequence of amino acids that comprise a protein is known as the primary structure of the protein. Each amino acid has a three letter and a one letter code, see Table 2.1. The primary structure is conventionally written as a string of the one letter codes from the N-terminal (i.e. the free amine group) on the left to the C-terminal (i.e. the free carboxyl group) on the right. For example, the primary structure of beefy meaty peptide (also known as delicious peptide) is KGDEESLA.[34] The

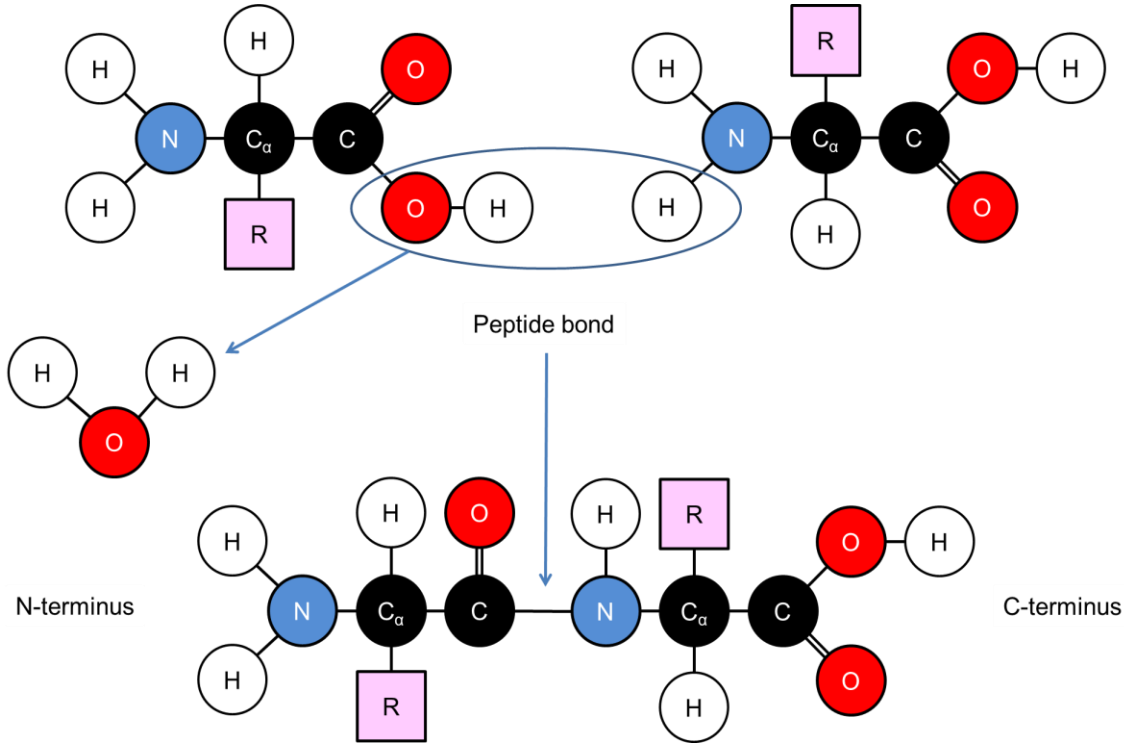

Figure 2.1: Illustration of the formation of a peptide bond between two generic amino acids. R denotes a side chain, which is different for each type of amino acid, and is attached to the alpha carbon. The carboxyl group of one amino acid bonds with the amino group of another to form a peptide, with water as a byproduct. Additional amino acids can bind via peptide bonds at the N- or C-terminal to increase the length of the peptide.

side chains that differentiate the amino acids have various properties: some are hydrophobic while others are polar or charged. The structural details and function of a protein are

determined by the side chains, because of their interactions with solvents and each other. This leads to secondary, tertiary and (sometimes) quaternary structure, which are described below.

Hydrogen bonding between residues leads to the formation of local structures (as opposed to the global structure of the protein, see below) such as alpha helices, beta sheets and turns. Alpha helices are right-handed spirals in the protein structure, where every N-H group is hydrogen bonded to the C=O group of the amino acid residue four places earlier in the sequence, creating a helical structure with 3.6 residues per turn, see Figure 2.3. Beta sheets are made up of beta strands, which are sections of the peptide in extended conformations, typically 3-10 amino acid residues long, see Figure 2.4. Two or more adjacent beta strands can hydrogen bond via the N-H and C=O groups of the amino acid residues to form parallel or antiparallel beta sheets, depending on which direction adjacent beta strands are oriented in. Turns are defined as structures where the C_α atoms (i.e. the carbon atom to which the side chains are bonded) of two residues around one to five places apart in sequence are less than 7 Å apart and the separating residues do not form any other secondary structure element.[35] Other less common secondary structure elements exist, such as 3_{10}- and π-helices, beta hairpins, and alpha strands.[36] Certain residues favour the formation

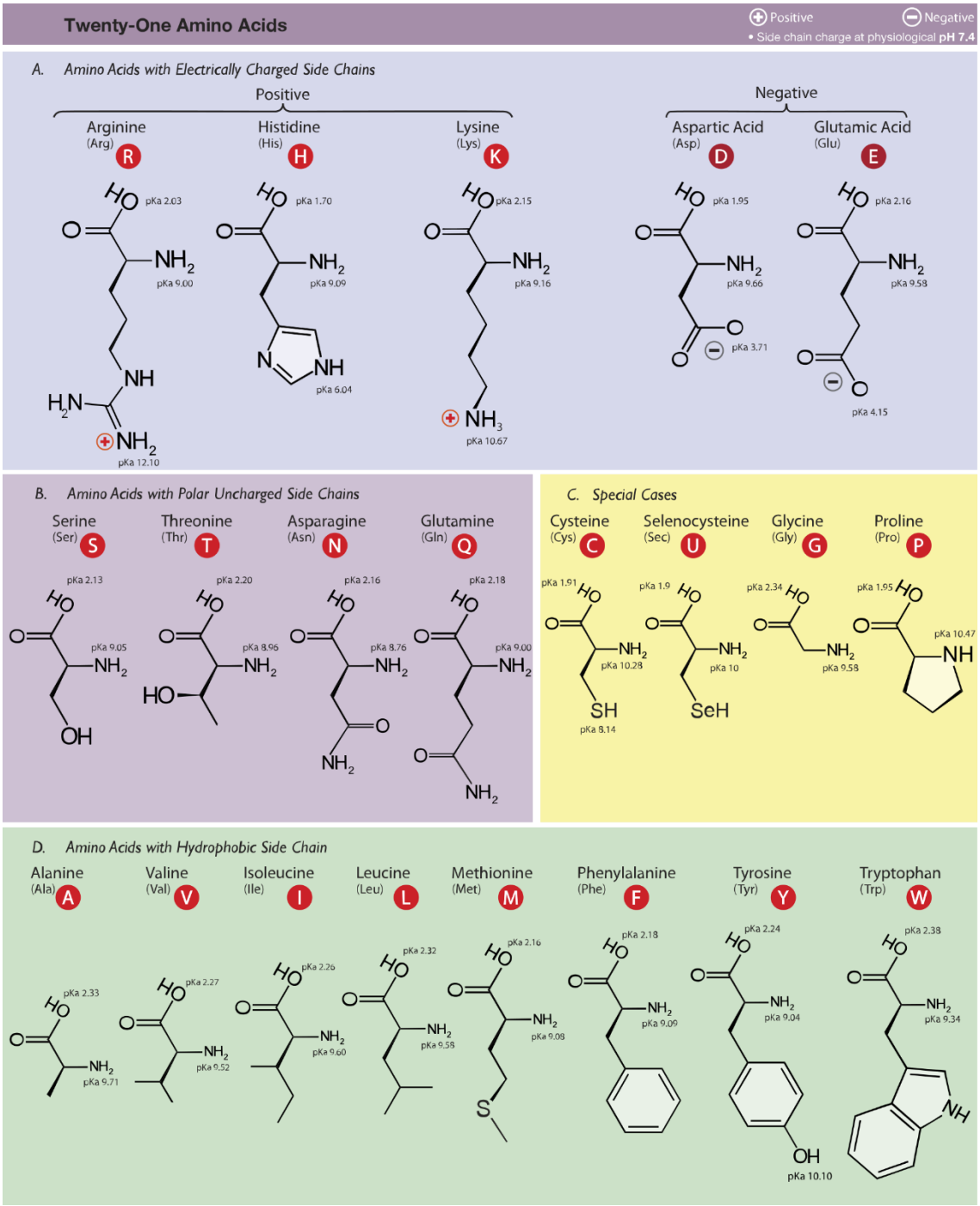

Figure 2.2: Chemical structures of 21 amino acids found in natural peptides and proteins (pyrrolysine not shown since it is not known to be found in human proteins). Adapted from Cojocari.[170]

of different secondary structure elements: for example alanine, leucine and glutamic acid are known to favour alpha helix formation.[37]

The tertiary structure of a protein is the overall structure, or fold, of the protein. It determines the protein's function, and is itself determined by the primary and secondary structure and environment of the protein. It is very difficult to predict the tertiary structure of a protein, even when the primary structure and environment are fully known. This is largely because of the computational time necessary to simulate the vast number of possible conformations a protein

Amino acid	Three letter code	One letter code	Side chain properties
Alanine	Ala	A	Hydrophobic
Arginine	Arg	R	Positive charge
Asparagine	Asn	N	Polar
Aspartic acid	Asp	D	Negative charge
Cysteine	Cys	C	Hydrophobic
Glutamic acid	Glu	E	Negative charge
Glutamine	Gln	Q	Polar
Glycine	Gly	G	No side chain
Histidine	His	H	Positive charge, aromatic
Isoleucine	Ile	I	Hydrophobic
Leucine	Leu	L	Hydrophobic
Lysine	Lys	K	Positive charge
Methionine	Met	M	Hydrophobic
Phenylalanine	Phe	F	Hydrophobic
Proline	Pro	P	Hydrophobic
Pyrrolysine	Pyl	O	Polar, aromatic
Selenocysteine	Sec	U	Negative charge
Serine	Ser	S	Polar
Threonine	Thr	T	Polar
Tryptophan	Trp	W	Hydrophobic, aromatic
Tyrosine	Tyr	Y	Hydrophobic, aromatic
Valine	Val	V	Hydrophobic

Table 2.1: The 22 amino acids found in natural peptides and proteins.

could adapt. Further complexity is added by the fact that very different primary sequences can lead to similar conformations.[36]

The quaternary structure is the structure formed by two or more proteins if they combine into a single protein complex. One example of quaternary structure is the coiled coil, formed when two or more alpha helical peptides associate and wind around each other, see Figure 2.5.[3] While coiled coils of up to five individual peptides have been identified,[38] the coiled coils used in this work are exclusively dimers, and these will be the focus of the following section.

2.4. Coiled coils

In a letter to *Nature* in 1952, Crick suggested that difficulties in fitting the alpha helix structure to the X-ray diffraction pattern of alpha keratin (a structural protein that is the main component of nails and hair) might be resolved by a model in which alpha helices coiled round each other, calling this postulated structure a coiled coil.[39] This letter introduced the idea of 'knobs-into-holes packing', though this phrase did not appear until a more detailed paper in 1953.[40] Crick asks the reader to imagine wrapping a piece of paper round an alpha helix and

[3] Note that alpha helical sections within a single protein can associate into a coiled coil, in which case the coil would be part of the tertiary structure rather than the quaternary. Some texts instead define coiled coils and other structures made of secondary structure elements as 'supersecondary' structure.

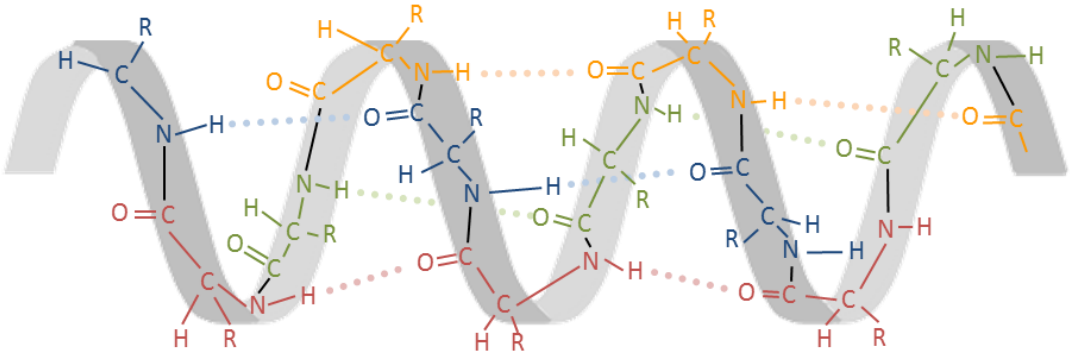

Figure 2.3: Diagram of an alpha helix, with the general shape of the helix shown in grey and peptide bonds between individual amino acid residues shown in black. Every N-H group is hydrogen bonded (pale dotted line) to the C=O group of the amino acid four places along in the sequence. Adapted from Griffiths *et al.*[171] Copyright 2002 by W.H. Freeman and Company. Used with permission of the publisher.

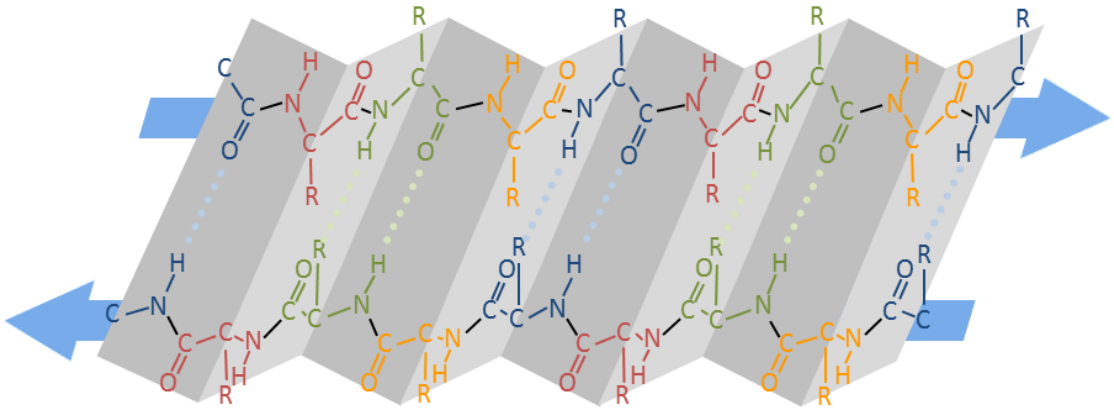

Figure 2.4: Diagram of an antiparallel beta sheet formed from two beta strands. Adapted from Griffiths *et al.*[171] Copyright 2002 by W.H. Freeman and Company. Used with permission of the publisher.

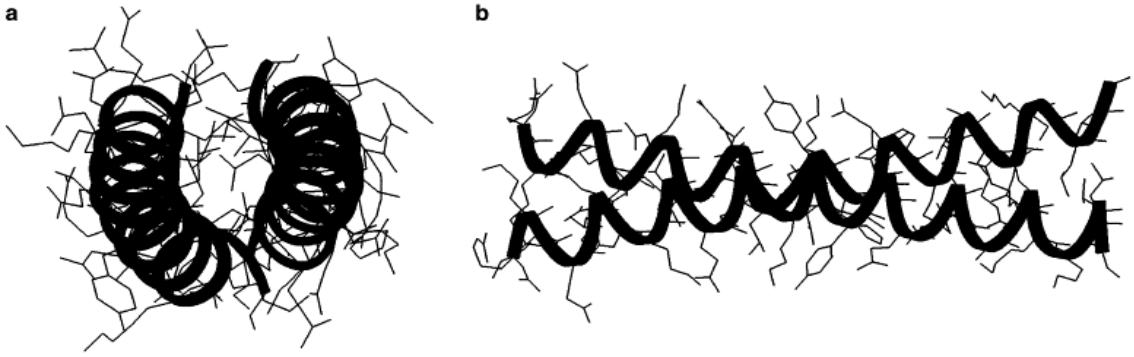

Figure 2.5: Top down (a) and side (b) views of the parallel homodimeric coiled coil in the GCN4 leucine zipper (PDB ID: 2ZTA). Two right handed alpha helices (bold lines) coil around each other to form a left handed supercoil. The interaction is driven by the side chains (thin lines), with hydrophobic side chains shielded from solution in the interior of the coiled coil and hydrophilic side chains extending out into the solution on the exterior. Adapted from Kohn *et al.*[56]

marking the positions of the side chains, then repeating this for a second alpha helix. Overlaying the two pieces of paper, as in Figure 2.6, demonstrates that in order for the side chains to pack efficiently (i.e. in a ‘knobs-into-holes’ manner), the helices cannot simply pack in parallel, but

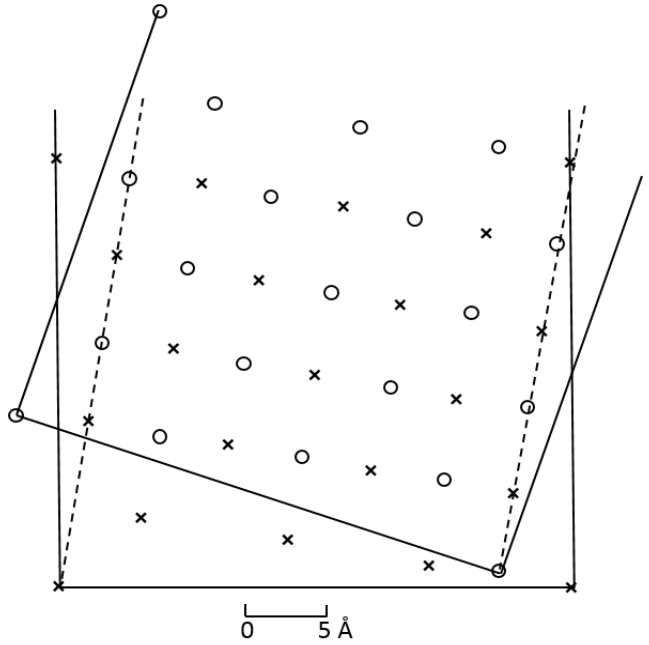

Figure 2.6: Crick's diagram of 'Knobs-into holes packing'. The reader is asked to visualise wrapping paper around alpha helices, marking the positions of side chains (here using crosses on the vertical piece of paper and circles on the tilted piece), then overlaying the unfolded pieces of paper. Optimal spacing of the side chains requires the tilting of one piece, showing that the alpha helices must coil round each other for efficient packing. Adapted from Crick.[40]

must coil around each other.[4] Although they did not use the term coiled coil, Pauling and Corey simultaneously and independently discovered the structure and published it at almost exactly the same time.[41]

By 1972, Hodges *et al* were proposing a repeating 7 amino acid pattern to the tropomyosin (a protein found in muscle cells and cell cytoskeletons) coiled coil of the form (H-P-P-H-P-P-P) where P represents polar residues and H represents hydrophobic residues forming the interface which the coiled coil shields from solution.[42] With the completion of the tropomyosin primary sequence, McLachlan and Stewart confirmed this and proposed the model, nomenclature, and helical wheel diagram, see Figure 2.8, that remain in use today: a repeating heptad labelled (*a-b-c-d-e-f-g*) (or (*a'-b'-c'-d'-e'-f'-g'*) for the other peptide in the coil), where residues in the *a* and *d* positions have hydrophobic side chains that form the core of the coil, residues in the *e* and *g* positions have charged side chains that add specificity to the structures, and residues in the *b*, *c*, and *f* positions form the solvent exposed exterior of the coil and hence are generally polar.[43] The right handed alpha helices in the left handed coiled coil are slightly distorted so that they have 3.5 residues per turn rather than the 3.6 of traditional alpha helices.

[4] For readers unsatisfied by this model, Crick recommends "*using (say) the handle of a broomstick (to represent the polypeptide backbone) and knobs of plasticine (to represent side-chains) placed over nails carefully inserted in the correct positions on the broomstick.*" It is unclear whether the requested care is for reasons of safety or merely scientific accuracy.

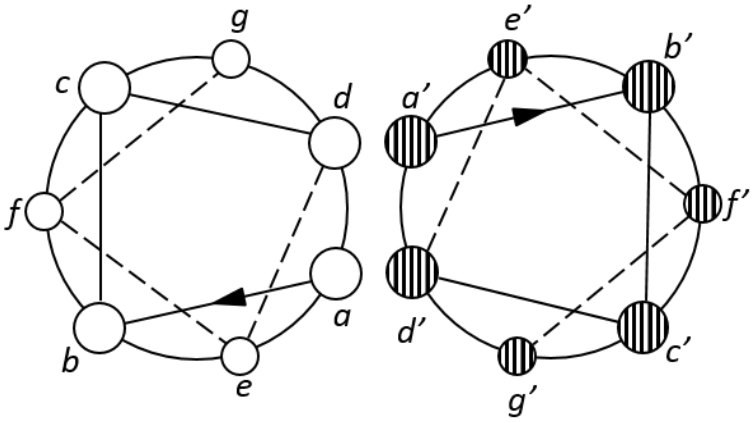

Figure 2.7: McLachlan and Stewart's original helical wheel representation of a pair of interacting helices in a parallel coiled coil, showing the positions, labelled *a-f*, of the residues. The hydrophobic side chains of *a* and *d* residues form the core that the coil shields from solution. The *e* and *g* residues have charged side chains which add specificity. The *b*, *c*, and *f* residues are exposed to solution and so generally have polar side chains. Adapted from McLachlan and Stewart.[43]

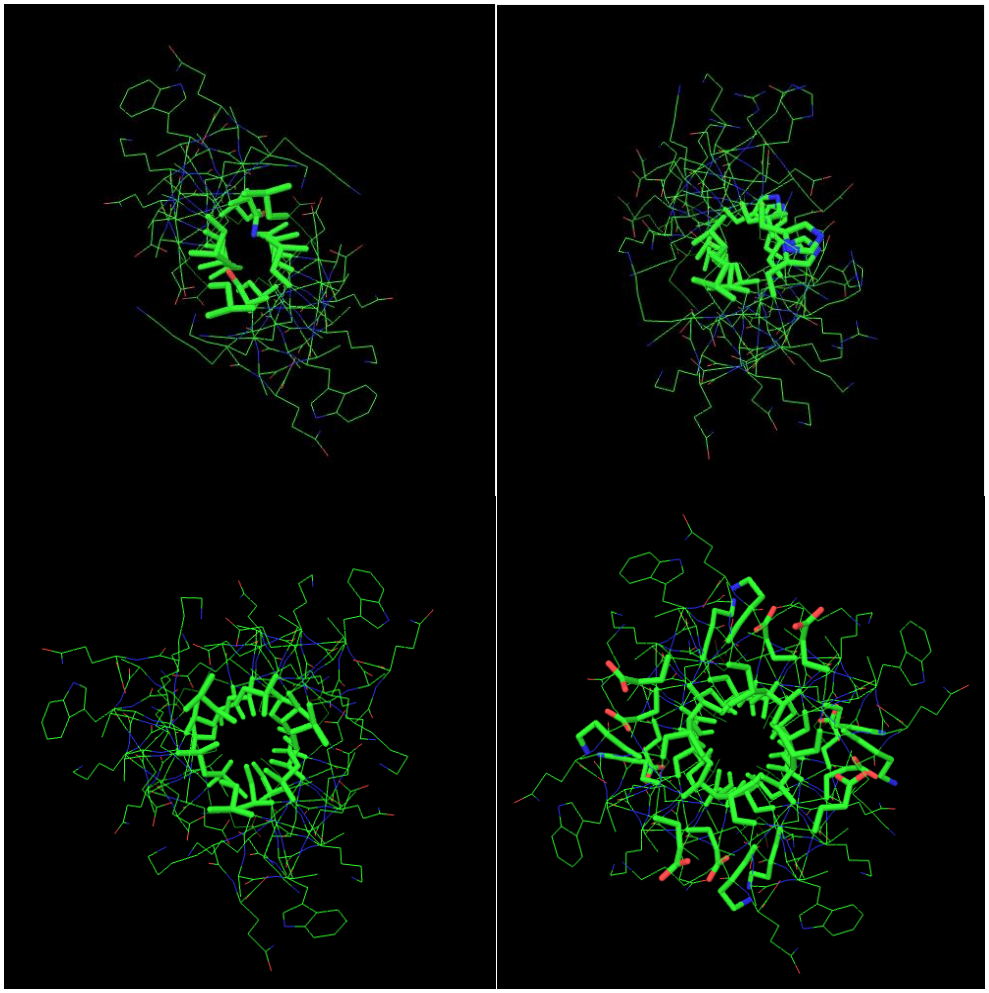

Figure 2.8: Top-down representations of homodimeric coiled coil structures, produced using the built-in examples in CCBuilder.[172]
A) CC-Di: A parallel dimer (sequence EIAALKQEIAALKKENAALKWEIAALKQ)
B) Anti-Parallel Dimer (sequence KENEISHHAKEIERLQKEIERHKQSIKKLKQSE)
C) CC-Tri: A trimer (sequence EIAAIKQEIAAIKKEIAAIKWEIAAIKQ)
D) CC-Tet: A tetramer (sequence ELAAIKQELAAIKKELAAIKWELAAIKQ).

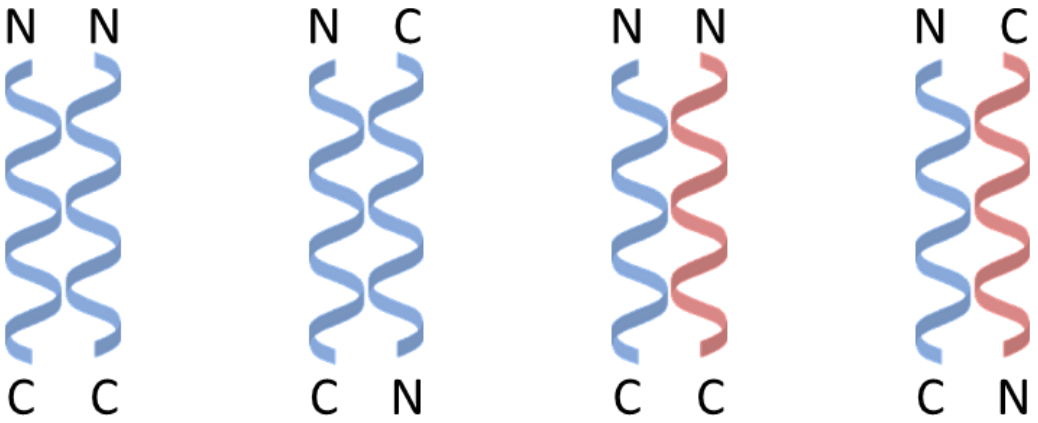

Figure 2.9: Schematic representations of different types of coiled coil, with the N and C terminals of each peptide marked. From left to right: Parallel homodimer, antiparallel homodimer, parallel heterodimer, antiparallel heterodimer.

Since these early discoveries, coiled coil sequences have been found in a wide variety of proteins and it is now predicted that up to 10% of proteins may contain the coiled coil motif.[38] Starting with Hodges *et al* in 1981, the creation of synthetic designed coiled coils has allowed researchers to probe the all-important relationship between amino acid sequence and protein folding in a relatively simple and controllable context.[44]

2.4.1. Coiled coil design principles

From the large body of work studying naturally occurring, synthetic, and simulated coiled coils a number of design rules have been elucidated that in principle allow one to use the primary structure of the peptides to predict or engineer properties of the coil such as helix orientation (i.e. parallel or antiparallel), oligomerisation state (i.e. dimer, trimer, etc.) and the preference for homomers or heteromers in mixed systems, see Figures 2.7, 2.8 and 2.9. The main design principles are examined below. The focus of this work is dimeric coiled coils and so all discussion below should be taken to refer to dimers unless otherwise noted.

Length of the peptides

In general, adding additional heptad pairs to a coiled coil will increase its stability by increasing the number of favourable interactions between the two peptides.[45] More strictly, adding additional heptad pairs of the same or greater stability as the existing pairs will increase the overall stability of the coil; Kwok and Hodges have shown that the insertion of an additional but less stable heptad pair can result in an overall destabilisation of a coiled coil by decreasing what can be thought of as the stability density of the coil.[46]

*Hydrophobic core (*a *and* d *positions):*

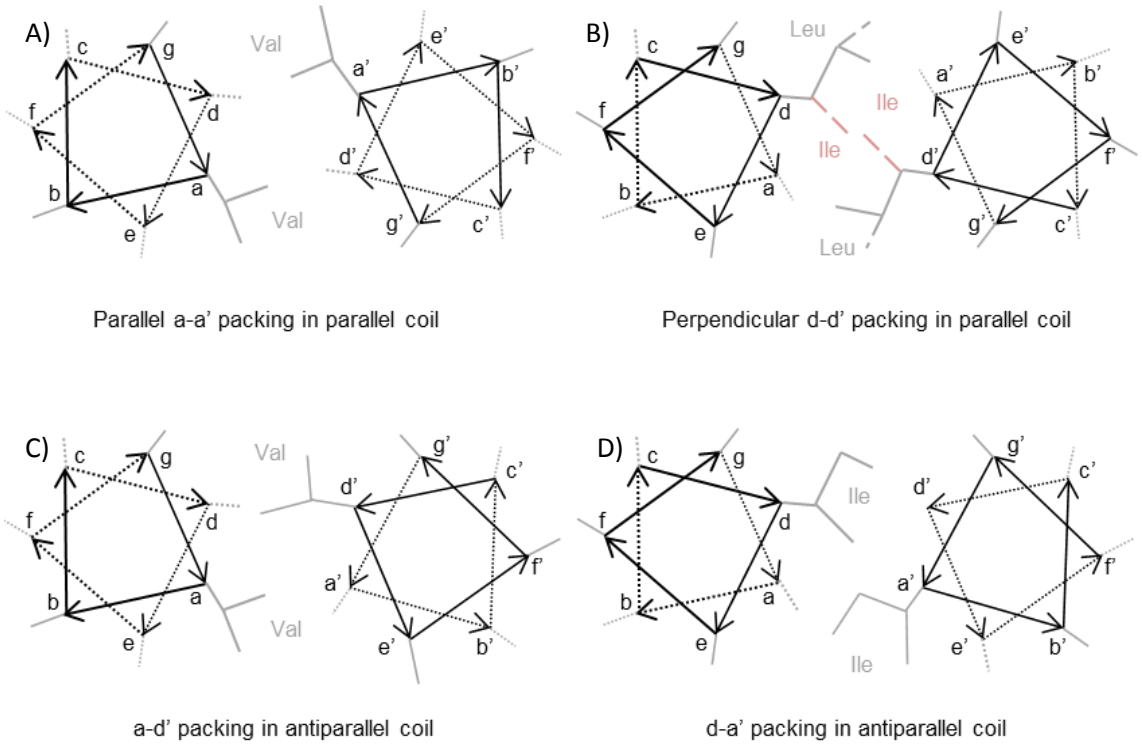

Figure 2.10: Packing of side chains in the hydrophobic core *a* and *d* positions for parallel (A and B) and antiparallel (C and D) coils. α-β bond angles shown in grey, with relevant side chains for each case drawn fully. There is a steric clash (red) in the case of parallel coils with isoleucines in the *d* positions (both leucine and isoleucine are shown in B, with differences denoted by dashed lines). This explains the lack of the β-branching residues (i.e. isoleucine and valine) in *d* positions in natural parallel coils and hence their use to specify orientation in synthetic coils.

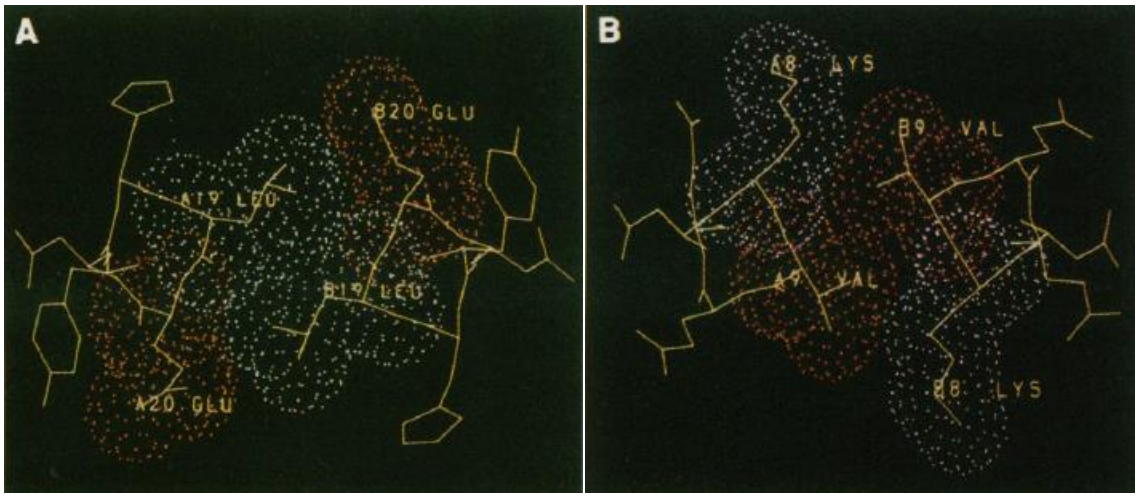

Figure 2.11: Representations of side chain packing in the GCN4-p1 parallel homodimer (PDB ID: 2ZTA). A) Perpendicular *d-d'* packing of leucine residues, with the van der Waals surfaces of leucine residues shown in blue and glutamic acid residues shown in red. B) Parallel *a-a'* packing of valine residues, with van der Waals surfaces of valine residues shown in red and lysine residues shown in purple. Adapted from O'Shea *et al*.[49]

The hydrophobic residues in the *a* and *d* positions are the main driving force for coiled coil assembly and consequently the properties of the coil may be tuned by changes to the residues in these positions. Among the amino acids with hydrophobic side chains, those with bulkier aromatic structures (phenylalanine, tryptophan and tyrosine) are rarely found in the *a* or *d* positions of natural or designed coiled coil dimers because of steric constraints.[47,48] In fact, steric

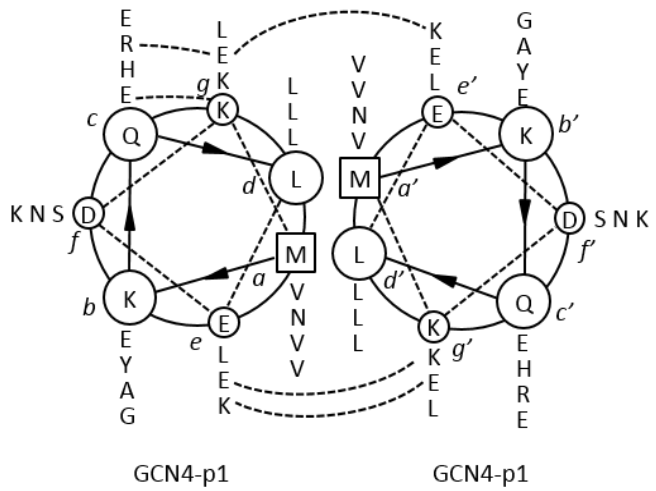

Figure 2.12: Helical wheel diagram of the GCN4-p1 parallel homodimer (PDB ID: 2ZTA), showing electrostatic interactions with dotted lines. Residues at each position are shown radiating outwards from the centre in order of primary sequence. Adapted from O'Shea *et al*.[49]

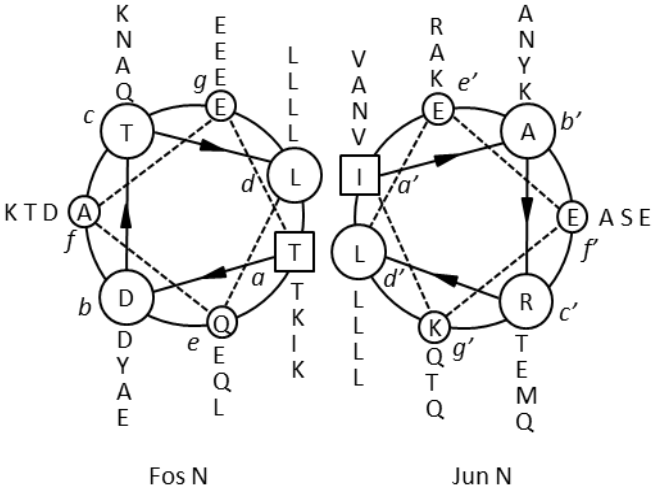

Figure 2.13: Helical wheel diagram of the parallel Fos N/Jun N heterodimer from the transcription factors FOS and JUN (PDB ID: 1A02). Residues at each position are shown radiating outwards from the centre in order of primary sequence. Adapted from O'Shea *et al*.[57]

constraints play a large role in determining the choices from the suitable hydrophobic non-aromatic amino acids (which are alanine, isoleucine, leucine, methionine and valine, since proline and cysteine are unsuitable for reasons given below) for the *a* and *d* positions in parallel coils. Importantly, the constraints on the two positions are different, because of the different angles at which the side chains of residues in these positions orient into the core. In parallel coils the α-β bond vectors (i.e. the vector between the alpha carbon and the first carbon of the side chain, called the beta carbon) of residues in opposite *d* positions point directly into the core at each other (this is known as parallel packing), whereas the vectors of residues in opposite *a* positions point slightly outwards and in opposite directions (perpendicular packing).[49] This means that residues with branching structures at the β-carbon (isoleucine and valine) cannot pack well at opposite *d*

positions since there is no room for both branches of the side chain, see Figures 2.10 and 2.11, hence the preference for leucine at *d* positions of natural and designed parallel coiled coils (leucine is presumably favoured over the other non-branching residues because its side chain is more hydrophobic).[48] The packing of *a* residues not only allows the possibility of β-branched side chains, but favours them since they pack additional hydrophobic hydrocarbon into the core.[48] Therefore the 'typical' parallel coiled coil has leucines in *d* positions with isoleucines and valines in the *a* positions. Deviation from this rule allows control over oligomerisation state, i.e. the number of peptides in the coil. In fact, trimers (three peptide coils) appear to be the default state for coiled coils, with the above pattern necessary to specify for dimers unless other design rules are used to influence the oligomerisation state.[48] Higher oligomerisation states may even allow the use of the hydrophobic residues with aromatic side chains: Liu *et al* designed a peptide with all tryptophans in the *a* and *d* position that formed a stable coiled coil pentamer.[50]

Less work has been done on the packing of *a* and *d* residues in antiparallel coils. In this case the side chain from an *a* position on one peptide must pack with the side chain of the *d'* position on the other peptide, and vice versa. Figure 2.11 shows that this avoids the tight side chain packing of the parallel *d-d'* case, meaning that β-branching residues such as isoleucine are not necessarily disfavoured at the *d* positions in antiparallel coils. This means that the pattern of hydrophobic residues in the coil core can in principle be used to control helix orientation. Indeed, Gurnon *et al* showed that a peptide with *d* position isoleucines and *a* position alanines had a strong preference for forming antiparallel over parallel coils.[51] Modelling results from Ramos *et al* led them to conclude that while *d* position isoleucines favour antiparallel dimers, β-branched side chains in the matching *a'* positions lead to a preference for parallel orientation.[52] Overall, as might be expected from the lack of tight *d-d'* packing in antiparallel coils, the available evidence seems to suggest that packing constraints are more restrictive in parallel coils.[53,54]

*Interhelical salt bridges (*e *and* g *positions):*

Control may also be exerted over coiled coil assembly by the choice of amino acids for the *e* and *g* positions on either side of the hydrophobic core. It is well established that residues with charged side chains such as lysine (positive) and glutamic acid (negative) in these positions can interact electrostatically with the matching residues in the opposite peptide, acting to stabilise the coil through electrostatic attraction, or discouraging coil formation through electrostatic repulsion.[43,55] When the interaction is attractive, the residues are said to form a salt bridge. In parallel coils, the interactions are between the *g* position residue in one peptide and the *e'* position residue in the next heptad of the other peptide, i.e. an g_n:e'_{n+1} interaction.[56] In antiparallel coils the interactions are simply *e*:*e'* and *g*:*g'*.[48] By including appropriate patterns of charged residues in the *e* and *g* positions, preferences for desired coiled coil assemblies can be engineered into the peptides. For example, a preference for homo- or heterodimerisation can be dictated by the *e* and

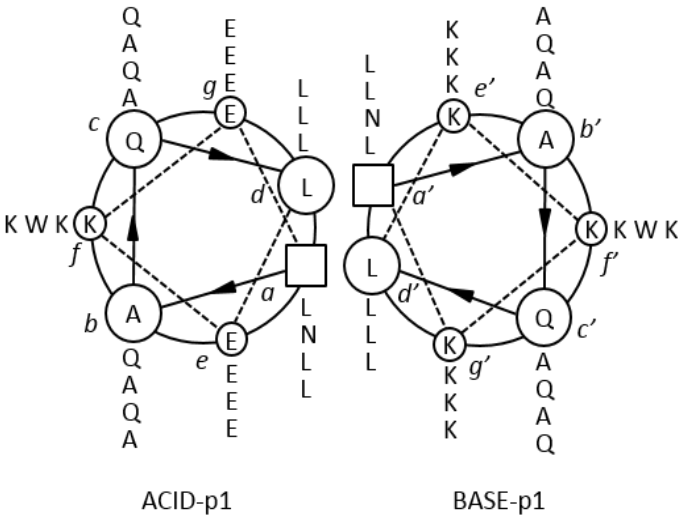

Figure 2.14: Helical wheel diagram of the parallel ACID-p1/BASE-p1 heterodimer, also known as the peptide velcro system. Residues at each position are shown radiating outwards from the centre in order of primary sequence. The boxes at the *a* and *a'* positions are blank because the N-terminals of the peptides are at the *b* and *b'* positions. Adapted from O'Shea *et al*.[58]

g residues. The natural GCN4 leucine zipper sequence (from a transcription factor protein that control transcription of genetic information) contains both lysine and glutamic acid residues in the *e* and *g* positions, which are arranged such that the parallel homodimer has three stabilising salt bridges, see Figure 2.12.[49] The Hodges *et al* synthetic coiled coil homodimer (based on tropomyosin, and the first example of a *de novo* designed coiled coil) features exclusively glutamic acid at the *e* positions and lysine at the *g* positions, giving two homodimer stabilising salt bridges per heptad.[44]

In contrast, the sequence segments corresponding to the coiled coil part of the natural oncoproteins Fos and Jun (which are transcription factors) contain a pattern of lysines and glutamic acids that stabilises heterodimers and destabilises homodimers, see Figure 2.13.[57] This inspired the peptide velcro system, developed by O'Shea *et al*, which is an early example of a synthetic parallel coiled coil that uses charged *e* and *g* residues to favour heterodimer formation, see Figure 2.14.[58] One of the peptides, called ACID-p1, contains glutamic acid at all *e* and *g* positions, whereas its counterpart, BASE-p1, contains lysine at all *e* and *g* positions. The electrostatics leave heterodimers free to form while discouraging homodimers because of the mutual repulsion.

In addition to control over homo/heterodimerisation, a number of studies have shown the possibility of using charged residues at the *e* and *g* positions to influence helix orientation [51,59–62] and oligomerisation state.[63,64] For example, Monera *et al* designed peptides such that four coiled coils were possible: parallel with attractive electrostatic interactions, parallel with repulsive electrostatic interactions, antiparallel with attractive electrostatic interactions and antiparallel with repulsive electrostatic interactions.[59] The only difference between the peptides with

attractive and repulsive electrostatic interactions was the positions of lysine and glutamic acid residues in the *e* and *g* positions, while the only difference between parallel and antiparallel peptides was the position of N- or C-terminal cysteines intended to form disulphide bridges. All four possibilities were found to form as coiled coils, suggesting a single disulphide bridge located at the ends of the peptides was enough to overcome ten repulsive electrostatic interactions. However, when exposed to increasing concentrations of the denaturant urea, the coils with repulsive electrostatic interactions were found to be significantly less stable. Evidence that the electrostatic interactions were responsible for the difference in stability was provided by repeating the urea denaturation with the addition of salts that masked the charges and significantly reduced the difference in stability between coils with attractive and repulsive interactions. Denaturation with the charged molecule guanidinium chloride showed similar results to urea with salt, providing further evidence for the role of the electrostatic interactions in determining orientation preference in these coils.

The above experiment demonstrates that when electrostatic interactions are used to determine coiled coil properties, those properties can be modified by changes in solution which negate the charge effects, such as increased salt concentration leading to charge screening.[62] A change in solution pH can have a similar effect by leading to protonation or deprotonation of the charged residues.[65,66] For example, Zhou *et al* used the 5-heptad Hodges homodimer mentioned above,[44] denoted EK since it contains only glutamic acid residues at *e* positions and only lysine residues at *g* positions, with two variants: EE, containing glutamic acid residues in all *e* and *g* positions; and KK, containing lysine residues in all *e* and *g* positions.[67] At neutral pH and low salt concentrations EK formed homodimers and EE and KK were unstructured. At acidic pH where the glutamic acid residues became protonated, thereby removing the electrostatic repulsion that prevented coil formation, EE homodimers formed. Similarly, at basic pH where the lysine residues became deprotonated, KK homodimers formed. In addition, increasing the salt concentration at neutral pH led to the formation of EE and KK homodimers through screening of the charged residues. O'Shea *et al*'s peptide velcro system of ACID-p1 and BASE-p1, based on the same principles as EE and KK, showed similar pH and salt dependent behaviour.[58] Note that it is possible that increased salt concentrations could lead to increased homodimer stability through increasing the strength of hydrophobic interactions rather than charge screening, but the evidence suggests that charge screening is the dominant effect in peptides.[68,69,5] Similarly, metal ions have been used to control coiled coil formation in combination with charged residues in the

[5] This is fortunate, because the effect of ions on hydrophobicity, known as Hofmeister effects, are extremely complex and poorly understood. A handful of despairing quotes from the conclusion of a recent review are illustrative: "*Hofmeister effects have escaped explanation for almost 130 years now*," "*it takes a certain amount of chutzpah or naivete to tackle the problem*," and "*the necessity for rebuilding theoretical foundations… is obvious*".[169]

e and *g* positions. Kohn *et al* designed a 35 residue parallel homodimer with negatively charged γ-carboxyglutamic acid (Gla) side chains in the *e* and *g* positions in one heptad.[22] In benign pH 7 buffer the peptides did not form coiled coils, whereas the equivalent peptides with uncharged glutamine residues in place of the Gla residues did form coiled coils. The conclusion was that the negatively charged Gla residues in opposing *e* and *g* positions destabilised the coil due to electrostatic repulsion. This was tested by introducing La^{3+} ions to solutions of the peptide. In the presence of the metal ions, coiled coils formed because the Gla side chains bound to the ions. Similar results were seen with Yb^{3+}, Ca^{2+} and Zn^{2+} ions. The coil formation was also shown to be pH dependent. As the pH was decreased from neutral, coiled coil formation increased because the Gla side chains in the *e* and *g* positions became protonated, removing the unfavourable electrostatic interaction between the peptides.

*Solvent exposed exterior (*b, c*, and* f *positions):*

In comparison to the core (*a* and *d*) and core flanking (*e* and *g*) positions, the solvent exposed exterior (*b*, *c* and *f*) positions have received little attention. They are typically filled by polar amino acids such as alanine, glutamic acid, lysine and glutamine which are known to encourage the formation of alpha helices.[37,48] It has been shown that incorporation of the beta sheet favouring residue threonine into the *f* positions of a coiled coil can lead to a switch to beta sheet conformation upon heating.[70] The relative lack of interest in these positions reflects the assumption that they exert little control over coil properties other than general stability,[71] particularly in the case of dimers. Nevertheless, the effect of residues in these positions on coiled coil stability can be quite dramatic. Dahiyat *et al* synthesised and tested the melting temperatures of coiled coil dimers based on the GCN4-p1 peptide with altered residues at the *b*, *c*, and *f* positions.[72] The native GCN4 peptide had a melting temperature of 57 ºC, and by altering the surface exposed residues to alternative polar amino acids they were able to create dimers with melting temperatures as high as 72 ºC, and as low as 15 ºC for a random sequence of polar residues. Additionally, Zitzewitz *et al* showed that just changing the *f* position residues of the GCN4-p1 peptide led to significant changes in stability.[73] Kaplan *et al* were able to increase the affinity of synthetic coiled coil peptides for natural coiled coil peptide targets by up to 80 times by introducing residues that were more favourable to alpha helix formation at the solvent exposed positions.[74]

As the oligomerisation state of coils increases, the opportunity for *b* and *c* residue side chains to interact with side chains on adjacent peptides increases, thereby presenting opportunities to use these positions to control the coil properties.[75–77] For example, Fairman *et al* showed that replacing the native *b* and *c* position residues of Lac21, which forms a homotetramer, with glutamic acid or lysine strongly discourages homotetramer formation and leads to stable heterotetramers.[78] The solvent exposed positions can also be used to control oligomerisation state;

Dahiyat *et al* converted GCN4-p1 from a dimer to a tetramer by replacing all *b*, *c*, and *f* position residues with alanines.[72]

Buried polar residues:

The natural GCN4 leucine zipper contains an asparagine residue at the *a* position of the third heptad, see Figure 2.9,[49] and a number of other natural coiled coils similarly contain polar residues in the hydrophobic core.[48,79] In the parallel GCN4 coil, the asparagine residues are in opposite heptads and are close enough to form a hydrogen bond, but the overall effect is to destabilise the coil since the hydrogen bond is not as strong as the hydrophobic interaction that could exist were the asparagines replaced with hydrophobic residues. The reason for their presence became more clear after Harbury *et al* replaced the asparagine with valine and discovered that the mutated peptide formed a mixture of dimers and trimers.[80] In a trimer the asparagine residues of the native peptide would be unable to hydrogen bond and so would be purely destabilising, whereas in the dimer the hydrogen bond is able to form and adds back some stability, leading to a preference for dimers at the cost of overall reduced stability. Kim and coworkers replicated this behaviour in the synthetic peptide velcro system[81] and then exploited it to create the antiparallel heterodimer system ACID-a1 and BASE-a1.[82] Whereas ACID-p1 and BASE-p1 both contained an asparagine in the second heptad *a* position, ACID-a1's asparagine is in the third heptad *a* position and BASE-a1's asparagine is in the first heptad *d* position, so that a hydrogen bond only forms when the peptides form an antiparallel coil. Other researchers have investigated the use of different polar residues and have shown that they can also be used to control coiled coil properties.[83–86] For example, Akey *et al* showed that GCN4-p1 formed trimers instead of dimers when its *a* position asparagine was replaced with a *d* position threonine.[87]

Special residues:

Glycine and proline are well known as helix breakers from studies of alpha helices, and so are rarely used in the heptads of designed coiled coils, except as deliberate helix breakers for the purpose of control experiments (as in this work, see Chapters 4-7 below). Proline's inability to donate hydrogen bonds and its structural rigidity make it a particularly good disruptor of alpha helices, and hence coiled coils, though there is evidence that a proline residue at the start of an alpha helix may act as a helix initiator.[88]

Cysteine residues can be included in coiled coils to form stabilising disulphide bonds between the peptides. This is commonly used to determine orientation preference in coiled coils: by adding cysteine residues to the ends of the peptides a mixture of disulphide bonded parallel and antiparallel coils is forced, and the ratio of the two products indicates the natural preference of the coil.[59,60,82] End-terminal cysteine residues are also used to selectively immobilise peptides on surfaces via thiol chemistry.[89–92] In both uses, a linker comprised of 2-3 glycine residues is

commonly included to add flexibility for bond formation. Section 2.3.2 reviews the properties of surface-immobilised coiled coils.

Finally, designed coiled coils often include tryptophan and/or tyrosine since they are fluorophores and their absorption can be used for purification and concentration determination, see Sections 3.3.5. These residues typically occupy the *f* positions to minimise interference with coil formation.

2.4.2. Coiled coil monolayers

A number of groups have immobilised coiled coil peptides on surfaces in self assembled monolayers (SAMs). This is typically achieved through use of a cysteine residue at the N- or C-terminal, allowing the thiol group to covalently bond to the surface (see above). This section will focus on the properties of the monolayers, whereas the applications of surface immobilised coiled coils will be covered in Section 2.3.3 below.

Atanassov *et al* formed monolayers of parallel coiled coil heterodimers on gold substrates at a concentration of 500 μM in pH 7.2 phosphate buffer.[93] Each monomer contained 21 amino acids (3 heptads) with an additional CGG linker at the N-terminal. Using ellipsometry, AFM and XPS they calculated a monolayer thickness of ~ 4 nm with a 30 º tilt angle and a density of 10^{14} peptide cm^{-2}, corresponding to an area per peptide of 0.9 nm^2. X-ray photoelectron spectroscopy (XPS) analysis also revealed that each coiled coil was bound to the gold via two cysteine residues (i.e. each monomer was individually bound to the surface). A previous work by the same group included antiparallel heterodimers and reported similar monolayer properties.[94] They showed using circular dichroism spectroscopy (CD) that the peptides had alpha helical structure when immobilised on gold colloids and this was taken as evidence that the peptides retained a coiled coil structure on immobilisation.

Minelli *et al* formed monolayers of parallel homodimers on gold substrates at a concentration of 11 μM in 100 mM phosphate buffer of varying pH.[95] Each monomer contained 34 amino acids (5 heptads) with an additional CGGGE linker at the N-terminal. Using surface plasmon resonance spectroscopy (SPR) they calculated a density of 1.27 x 10^{14} peptide cm^{-2} for monolayers formed at pH 4 (where the peptides formed coiled coils in solution) and 0.14 x 10^{14} peptide cm^{-2} for monolayers formed at pH 7 (where the peptides did not form coiled coils in solution). Using quartz crystal microbalance with dissipation monitoring (QCM-D) they showed that the surface immobilised peptides transitioned from coiled coil to uncoiled over the same pH range as in solution, and using SPR they showed that gold nanoparticles functionalised with the peptides bound to the monolayer at pH 4 and were released at high pH, and that the nanoparticles did not bind at pH 7. They therefore concluded that surface immobilisation did not have a significant effect on the coiled coil properties.

White *et al* have performed a number of studies of monolayers of BASE-C peptide, which is the 30 amino acid (4 heptad) BASE-a1 peptide with an additional GGGSC linker at the C-terminal. Monolayers of BASE-C formed on gold substrates at 2.6 μM concentration in 100 mM pH 7 phosphate buffer were calculated to have a density of 8 x 10^{12} peptide cm^{-2} from SPR data.[89] The complementary ACID peptide was found to bind to the monolayer with a dissociation constant (K_d) of 30 μM, which is significantly lower than the 30 nM K_d of parallel ACID:BASE heterodimers in solution. A separate publication used BASE-C monolayers formed at 260 μM concentration in 100 mM pH 7 phosphate buffer.[90] Ellipsometry measurements measured a monolayer thickness of 2.9 nm. The density of the monolayer was not calculated. Using electrochemical impedance spectroscopy (EIS), no binding of ACID to the BASE-C monolayer was detected. However, by diluting the BASE-C immobilisation solutions with a 19 amino acid peptide BLK-C which does not form coiled coils, monolayers were formed to which ACID peptides could bind. A ratio of 50:50 BASE-C:BLK-C formed the monolayer with the best binding, and solutions of < 20 % BASE-C or > 70 % BASE-C formed monolayers incapable of binding ACID peptides. They concluded that the binding of ACID peptides was strongly dependent on the monolayer density, and that high density monolayers were not conducive to binding. A subsequent publication formed monolayers on glass slides through the use of a mercaptosilane and copper ion immobilisation scheme.[92] BASE-C was immobilised at 26 μM concentration in 100 mM pH 7 phosphate buffer via covalent bonding of the thiol group of the C-terminal cysteine to the surface bound copper ions. A monolayer density of 3.3 x 10^{13} peptide cm^{-2} was estimated on the basis of CD measurements of the monolayer. Molecular dynamics simulations returned a comparable density of 4.4 x 10^{13} peptide cm^{-2}. CD measurements of the monolayers showed alpha helical structure indicative of coiled coils at pH 5 and above, whereas CD measurements taken in solution showed alpha helical structure only above pH 9. This indicates a significant change in conformational behaviour with pH between solution and surface peptides, in contrast to the findings of Minelli *et al* where no change was observed.[63]

2.4.3. Applications of coiled coils

Coiled coils have proven to be valuable tools for research into protein folding, but they are also attractive for more practical uses. In particular, their strong, specific, and often switchable binding properties make them useful for solving a variety of molecular-scale engineering challenges. Examples of a number of the areas in which coiled coils have been used are now given.

Protein interactions and structure:

Many of the applications of coiled coils involve their incorporation into existing proteins to modify interactions or structure. A system originally developed by Chang *et al* for improving

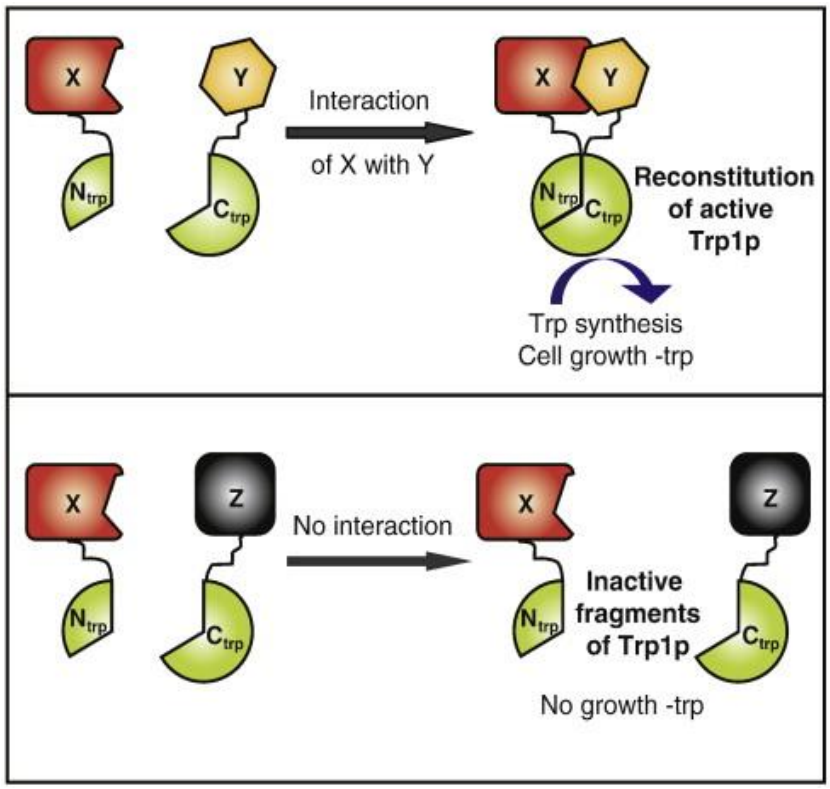

Figure 2.15: Diagram of O'Hare *et al*'s split enzyme sensor for protein-protein interactions. The tryptophan synthesising enzyme Trp1p (shown in green) was split into two fragments. The enzyme only reassembled when fragment labelled proteins (shown as X and Y) interacted. This led to tryptophan synthesis which allowed growth of a tryptophan deficient cell strain. When the labelled proteins did not interact (X and Z) no cell growth occurred. In order for the enzyme to reassemble a coiled coil linker was necessary. Adapted from O'Hare *et al*.[127]

the efficiency of binding between subunits in recombinant T-cell receptor complexes by adding ACID-p1 to one subunit and BASE-p1 to the other has led to a large number of publications where the peptides have been used to strengthen, induce or control for protein interactions, particularly in soluble recombinant versions of membrane proteins.[96–114] For example, Takagi *et al* used this technique to show that the binding activity of a certain membrane protein's extracellular region is dependent on spatial separation of subunits in the cytoplasmic domain by demonstrating increased target binding upon specific cleavage of a coiled coil clasp in the cytoplasmic region.[115]

Wranik *et al* used the peptide velcro heterodimer to assemble bispecific antibodies.[116] By attaching ACID-p1 to one heavy chain and BASE-p1 to another they demonstrated the production of bispecific (i.e. heterodimeric) antibodies with structures highly similar to the native antibody (the coiled coil being proteolytically removed after assembly).

Yuzawa *et al* used a coiled coil heterotrimer to control the activity of mutant RNaseT1 (an enzyme that catalyses the degradation of RNA).[117] Two of the coiled coil peptides were introduced into the enzyme in such a way that it could not fold correctly unless the third peptide was added to form the coiled coil. Hence the enzymatic activity could be controlled by addition of the third peptide.

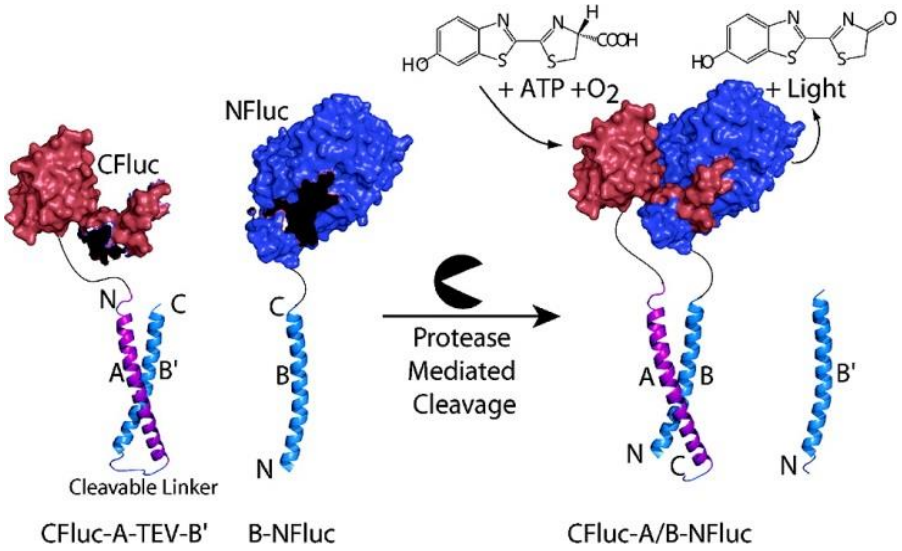

Figure 2.16: Diagram of Shekhawat *et al*'s split enzyme protease sensor. One fragment of the firefly luciferase (NFluc, in blue) had an attached BASE-a1 peptide (labelled B) whereas the other fragment had a complete ACID-a1 BASE-a1 coiled coil with the two peptides (labelled A and B') joined by a cleavable linker. When combined, the protein fragments only combined if a protease was present to cleave the linker, allowing B' to be replaced by B. Therefore the presence of the protease could be detected by the luminescence of the recombined luciferase. Adapted from Shekhawat *et al*.[121]

Coiled coils have also been used to control or enhance the recombination of split protein fragments.[118,119] Common examples are the recombination of firefly luciferase[120–122] (an enzyme responsible for the bioluminescence of fireflies) and green fluorescent protein[123–125] (a fluorescent protein originally found in jellyfish). These split proteins can act as sensors; for example O'Hare *et al* split an enzyme that catalyses tryptophan biosynthesis and used it to sense protein-protein interactions in *Mycobacterium smegmatis*, a model for *Mycobacterium tuberculosis*.[126,127] They created a strain of *M. smegmatis* that could not synthesise its own tryptophan and hence would only grow when the proteins labelled with the split enzyme fragments interacted, allowing the reconstitution of the protein, see Figure 2.15. A coiled coil linker proved necessary to reassemble the split enzyme; fragments without the coiled coil peptides were unable reassemble even when attached to interacting proteins. Shekhawat *et al* went further and used coiled coils to create autoinhibited split protein sensors using both firefly luciferase and beta-lactamase (a bacterial antibiotic enzyme).[121] BASE-a1 was added to one of the protein fragments while the other had a complete ACID-a1 BASE-a1 coiled coil with the two peptides joined by flexible linkers. Thus the protein recombination could only occur when the linker was cleaved, see Figure 2.16. The design was improved by the use of complete coils on both fragments and this system was used as a specific biosensor for the clinically relevant protein caspase-3 (an enzyme involved in cell apoptosis) by use of a caspase-3 cleavable linker. Finally, the authors demonstrated that the system can behave as an AND logic gate, using a caspase-3 cleavable linker on one of the fragments and a tobacco etch virus protease cleavable linker on the other so that the enzyme activity (i.e the output) was only evident when both proteases (i.e. the inputs) were present.

One interesting and seemingly unique application of coiled coils for protein research was demonstrated by Böttcher *et al*.[128] To investigate the plasticity of the hepatitis B capsid (i.e. the protein shell that forms the exterior of the virus) they inserted the ACID-p1 sequence into the capsid sequence. The resulting capsid-like particles were very similar in structure to those without the ACID-p1 sequence. However, the application of conformational stress by the addition of BASE-p1 peptide to form a coiled coil with the inserted ACID-p1 induced dramatic but ordered change in the structure, thereby showing its high plasticity and adaptability.

In an application that shows promise for the use of coiled coils in tissue engineering, Kobatake *et al* used a coiled coil to bind growth factor proteins to surface-bound extracellular matrix proteins and showed that the growth factor proteins retained their activity.[129] A number of other groups have also investigated the applications of coiled coils to growth factor binding.[130–133]

Ghadiri and coworkers have developed a system of 'self-replicating' coiled coil peptides on which they have based a number of proof-of-concept applications.[134–137] The basis of the system is a homodimeric coiled coil peptide and a pair of fragments (of the same peptide) whose thioester promoted amide bonding into the full peptide is catalysed by existing complete peptides. By creating fragments made entirely or partially of D-amino acids they were able to demonstrate the emergence of homochirality in the system, suggesting an insight into the origin of homochirality on Earth.[138] An expanded version of the system has also been used to perform OR, NOR and NOTIF logic functions.[139]

Labelling:

Hori *et al* used ACID-a1 and BASE-a1 in combination with an intein to label maltose binding protein with fluorescein, a fluorescent dye.[140] Yano *et al* used coiled coils to rapidly and specifically label cell membrane proteins with fluorescent dyes.[141] Tsutsumi *et al* developed a coiled coil fluorescent labelling system based on an antiparallel GCN4 mutant trimer, consisting of a probe peptide with fluorescent dye and two tag peptides.[142,143] The wavelength of the dye emission shifts upon a transition from a hydrophilic to hydrophobic environment, and when the coil forms the dye moves from being solvent exposed into the hydrophobic core and thus the coil formation can be detected by the change in fluorescence. Sakamoto *et al* incorporated a heme with one peptide from a coiled coil heterodimer into apomyoglobin (i.e. a myoglobin lacking a heme unit; myoglobin being an iron and oxygen binding protein like haemoglobin) and were then able to bind a flavin group with the complementary peptide through coiled coil formation.[144] By altering the position at which the flavin group was attached to its peptide the electron transport from the flavin to the heme was modified. Boucher *et al* used coiled coils to label epidermal growth factor with alkaline phosphatase (an enzyme that removes phosphate groups from molecules) and biotin in order to demonstrate an alternative strategy for western blot analysis.[145]

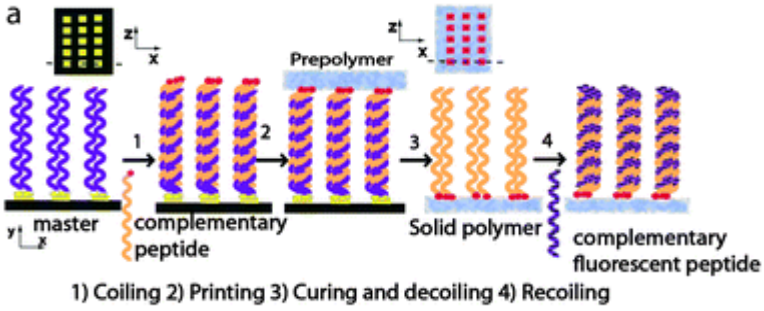

Figure 2.17: Coiled coil microcontact printing. One of the coiled coil par was immobilised on a master surface in a defined pattern. 1) The complementary peptide was introduced to form coiled coils. 2) An elastomeric prepolymer bound to the second peptide. 3) The polymer-peptide hybrid was transferred to a new surface, replicating the original pattern. 4) The fluorescently labelled complementary peptide was added to make the pattern fluorescent. Adapted from Laromaine *et al*.[150]

Surface immobilisation:

Hodges and co-workers have developed a protein purification system taking advantage of the strong and specific binding of coiled coils.[146] By expressing the protein of interest with a coiled coil sequence at one end, the solution containing the protein can be purified by running it over a surface on which the complementary coiled coil peptide has been immobilised. The captured protein can then be eluted by unbinding the coil (by, for example, changing the pH). They used the same system to develop reusable surfaces for SPR experiments.[147] One peptide is immobilised on the gold surface of the SPR chips and the other is attached to a binder of interest. The binder can be immobilised on the surface via the coiled coil interaction, then removed after the experiment by coil dissociation. They claim that the expensive chips have been reused up to 150 times by this method and each experiment could in principle use a different binder. Similarly, Liberelle *et al* used coiled coils to improve their enzyme-linked immunosorbent assays (ELISA).[148]

Minelli *et al* used the pH dependent binding of a coiled coil to control the binding and release of gold nanoparticles from a gold surface with a peptide monolayer.[95]

Yu *et al* used a coiled coil to aid their investigation of the effect of nanocrystallisation on the adherence of biofilms to stainless steel using atomic force microscopy (AFM).[149] A short peptide representing a biofilm was expressed with one of the coiled coil peptides and the other coiled coil peptide was immobilised on gold-coated AFM tips, allowing the binding of the 'biofilm' to the tips via the coiled coil interaction.

Laromaine *et al* developed a coiled coil based microcontact printing system.[150] A master template with of a pattern of one of the coiled coil peptides was introduced to a solution of the complementary peptides which were then bound to an elastomeric prepolymer. This could stick to another surface, thereby breaking the coils and replicating the original pattern on the new surface, see Figure 2.17.

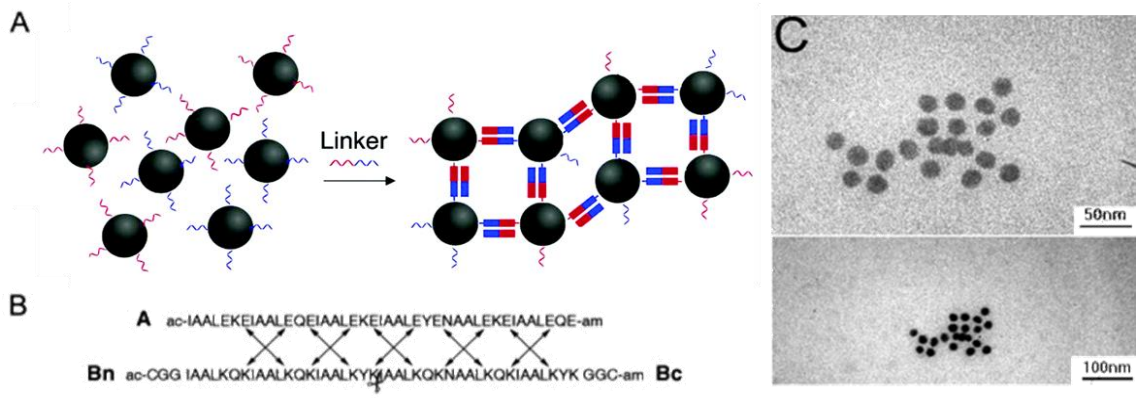

Figure 2.18: A) Diagram of Ryadnov *et al*'s belt and braces peptide linker system. Gold nanoparticles were functionalised with three-heptad brace peptides which could be linked together into coiled coils by a six-heptad brace peptide. B) Primary sequences of the peptides with electrostatic interactions shown by arrows. The scissor symbol separates the two brace sequences. C) Transmission electron micrograph of a resulting nanoparticle network. Adapted from Ryadnov *et al*.[160]

Hybrid materials:

A number of authors have investigated hybrid peptide-polymer conjugates using coiled coils and polymer chains, often noting the increased control that the environmental (eg. pH, temperature, concentration) dependence of coiled coil formation adds to the polymers.[151–155] Shu *et al* used a novel approach by attaching poly(ethylene glycol) (PEG) to an *f* position side chain in a central heptad rather than the usual N-terminal, reasoning that terminal PEGylation may cause steric hindrance and destabilisation of the coils.[156,157] They showed that side PEGylation increased the helicity and stability of the coils and did not significantly affect oligomerisation state or cofactor binding.

Fortier *et al* used coiled coils to bind DNA/polyethylenimine complexes to epidermal growth factor receptors, resulting in increased uptake into cells and thereby demonstrating potential for improved gene delivery techniques.[158]

Coiled coils have also been used for directed construction or immobilization of nanomaterials. By functionalizing regions of a gold surface with thiolated BASE-C petides and adding ACID peptides to bacteriophage particles, White *et al* demonstrated the specific immobilization of the particles to desired regions of a chip.[89] Similarly, Sweeney *et al* used the peptides to direct bacteriophages to assemble into wire-like structures and demonstrated that the assembled structures depended on the peptides used.[159] When the peptide velcro system was used (i.e. ACID-a1 at one end of the bacteriophage particles and BASE-a1 at the other) filaments were observed with an average length of 4.5 μm (corresponding to eight phage particles), whereas using Fos and Jun resulted in shorter filaments with an average length of 3.1 μm (six phages). They also created three-branched structures by use of a trimeric coiled coil. Minelli *et al* exploited the pH dependence of surface immobilised coiled coils with charged *e* and *g* position residues to demonstrate reversible binding, including pH dependent reversible binding of peptide

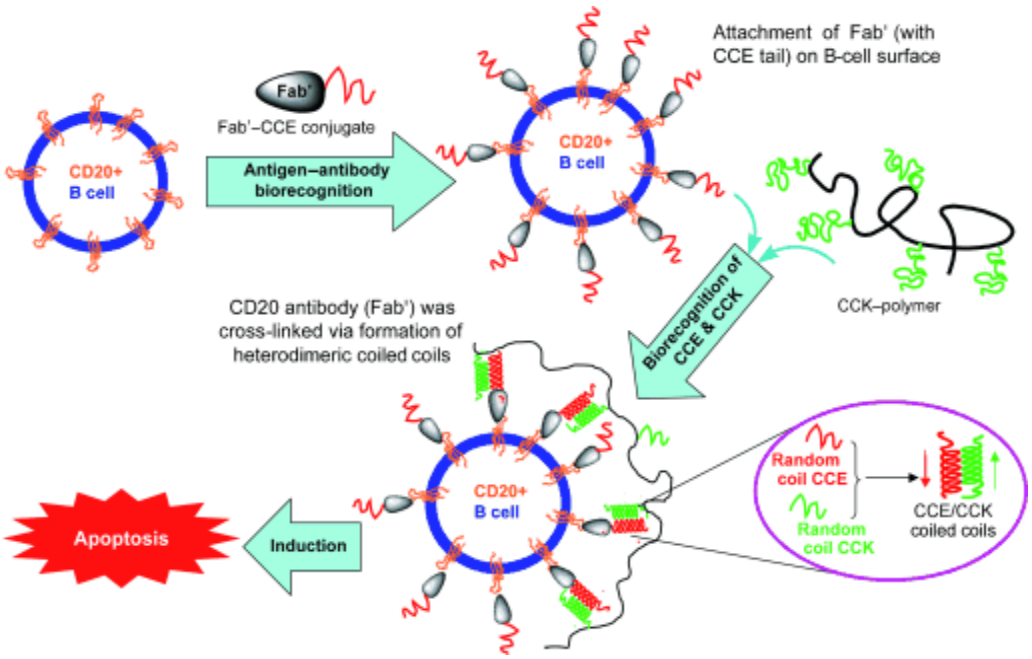

Figure 2.19: Diagram of coiled coil mediated cell apoptosis. A B-cell with surface displayed biomarkers (CD20) for non-Hodgkin's lymphoma was introduced to antibody (Fab') fragments with attached coiled coil peptides (CCE) and the antibodies bound the biomarkers. A polymer with the complementary peptide (CCK) was introduced and the coiled coil formed, resulting in cross-linking of the antibody fragments via the polymer, which triggered apoptosis of the cell. Adapted from Wu *et al*.[161]

functionalised gold nanoparticles.[95] Ryadnov *et al* designed a coiled coil 'belt and braces' system in which two three heptad 'brace' peptides could be linked by a six heptad 'belt' peptide, see Figure 2.18.[160] By functionalising gold nanoparticles with the brace peptides, then adding the linking belt peptide, they were able to assemble nanoparticle networks.

Medical applications:

Coiled coils have also been demonstrated as having potential for medical applications. Indeed, drug delivery is often cited as the inspiration for creating the hybrid coiled coil-polymer systems mentioned above, since polymers such as polyethylene glycol (PEG) and N-(2-hydroxypropyl)methacrylamide (HPMA) are non-toxic and non-immunogenic and so can be used to protect drugs from the immune system. Kopeček and coworkers have developed a peptide-polymer conjugate hydrogel that induces apoptosis in non-Hodgkin's lymphoma (NHL) B-cells and has been shown to be effective both in vitro and in vivo (in mice).[155,161–163] A coiled coil peptide was attached to an antibody fragment that could recognise and bind to a reliable biomarker for NHL on cell surfaces. The complementary peptide was bound to the N-(2-hydroxypropyl)methacrylamide (HPMA) polymer and when the peptide-polymer was introduced, the coiled coil formed and the polymer cross-linked the antibody fragment, triggering apoptosis of the cell, see Figure 2.19. Pechar and coworkers have developed a similar system involving coiled coil binding of antibody fragments to HPMA.[164,165] In one study they attached the drug doxorubicin to the HPMA and by use of a specific antibody fragment demonstrated

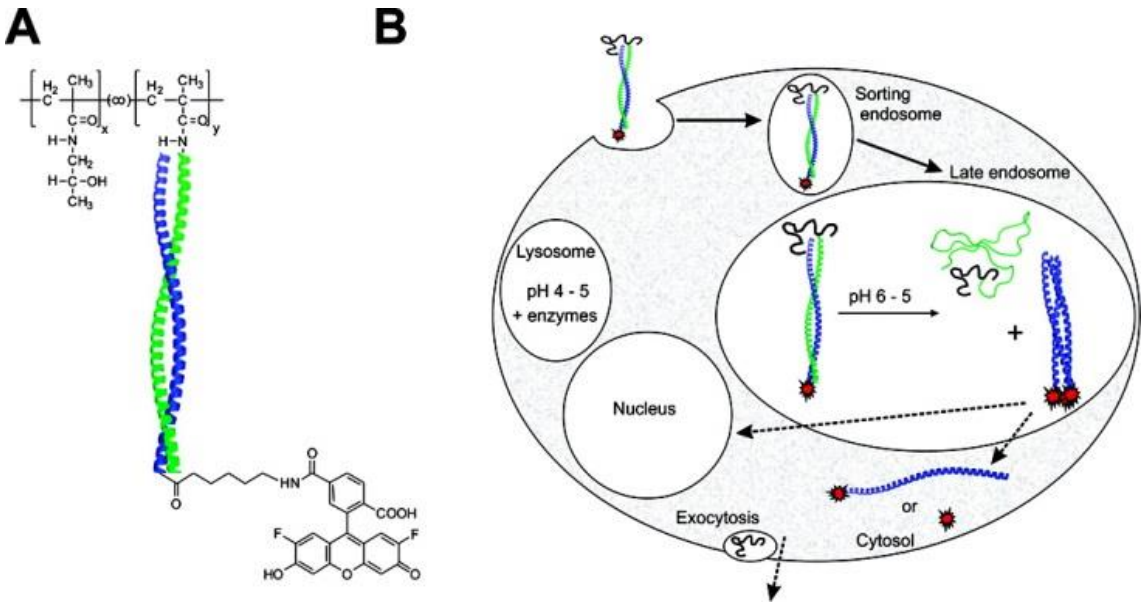

Figure 2.20: Diagram of drug delivery via a hybrid coiled coil-polymer system. One peptide (blue) of a coiled coil pair was attached to a cargo molecule while the other (green) was attached to a biocompatible polymer. In the neutral pH of the extracellular environment the peptides formed a coiled coil. Once the complex was taken into the cell, the lower pH environment caused the peptides to dissociate, releasing the cargo. Adapted from Apostolovic *et al*.[167]

highly targeted delivery of the drug to cancerous mouse cells.[166] Apostolovic *et al* developed a proof of concept system in which one coiled coil peptide was attached to a 'drug' (actually a fluorescent dye) and the complementary peptide to HPMA.[167] The peptides formed a coiled coil in the extracellular pH 7.4 environment and the complexes were taken up into the cell by endocytosis. Once in the cell, the low pH environment caused the coil to dissociate, thereby releasing the drug, see Figure 2.20. Instead of increasing therapeutic effectiveness by using coiled coils to attach non-immunogenic polymers, Craig *et al* have proposed using coiled coils to attach highly immunogenic proteins in order to stimulate immune response against a target molecule (to improve vaccines, for example).[168]

Electronic components:

Ashkenasy and coworkers have investigated the electronic properties of coiled coils with a view towards using them as components in molecular electronic devices.[93,94] They found that the transport of charge through coiled coils and their effect on the work function of gold surfaces when immobilised depended on orientation, with differences between parallel and antiparallel coils.[94]

2.5. References

*1. Kuhn, A. T. & Chan, C. Y. pH changes at near-electrode surfaces. *J. Appl. Electrochem.*

13, 189–207 (1983).

2. Auinger, M. *et al.* Near-surface ion distribution and buffer effects during electrochemical reactions. *Phys. Chem. Chem. Phys.* **13,** 16384–94 (2011).
3. Dahms, H. & Croll, I. M. The Anomalous Codeposition of Iron-Nickel Alloys. *J. Electrochem. Soc.* **112,** 771 (1965).
4. Ji, J., Cooper, W. C., Dreisinger, D. B. & Peters, E. Surface pH measurements during nickel electrodeposition. *J. Appl. Electrochem.* **25,** 642–650 (1995).
5. Ballestrasse, C. L., Ruggeri, R. T. & Beck, T. R. Calculations of the pH changes produced in body tissue by a spherical stimulation electrode. *Ann. Biomed. Eng.* **13,** 405–24 (1985).
6. Chopra, P. S., Srinivasan, S., Lucas, T. & Sawyer, P. N. Relation between thrombosis on metal electrodes and the position of metal in the electromotive series. *Nature* **215,** 1494 (1967).
7. Simona, B. R., Brunisholz, R. A., Morhard, R., Hunziker, P. & Vörös, J. Coagulation at the blood-electrode interface: the role of electrochemical desorption and degradation of fibrinogen. *Langmuir* **30,** 7227–34 (2014).
8. Yannakopoulos, T. & Brenner, A. lsolation of the Diffusion Layer at an Electrode and the Determination of Concentration Polarization. *J. Electrochem. Soc.* **105,** 521 (1958).
9. Brenner, A. & Wranglen, E. G. Cathode film studies by the drainage method. *Sartrych ur Sven. Kem. Tidskr.* **67,** 81 (1955).
10. Flatt, R. K., Wood, R. W. & Brook, P. A. The concentration profiles in solution at dissolving anode surfaces (1) zinc, copper and brasses by the freezing techniques. *J. Appl. Electrochem.* **1,** 35–39 (1971).
11. Metrohm. Ohmic Drop Part 1 – Basic Principles. *Autolab Appl. Note EC03* 1–2 (2011).
12. Hayes, M., Kuhn, A. T. & Patefield, W. Techniques for the determination of ohmic drop in half-cells and full cells: A review. *J. Power Sources* **2,** 121–136 (1977).
13. Steegstra, P. & Ahlberg, E. In situ pH measurements with hydrous iridium oxide in a rotating ring disc configuration. *J. Electroanal. Chem.* **685,** 1–7 (2012).
14. Boldt, F.-M. *et al.* Real-Time pH Microscopy down to the Molecular Level by Combined Scanning Electrochemical Microscopy / Single-Molecule Fluorescence Spectroscopy microscopy (SECM) and single-molecule fluorescence. *Anal. Chem.* **76,** 3473–3481 (2011).

*15. Cannan, S., Douglas Macklam, I. & Unwin, P. R. Three-dimensional imaging of proton gradients at microelectrode surfaces using confocal laser scanning microscopy. *Electrochem. commun.* **4,** 886–892 (2002).

16. Rudd, N. C. *et al.* Fluorescence Confocal Laser Scanning Microscopy as a Probe of pH Gradients in Electrode Reactions and Surface Activity. *Anal. Chem.* **77,** 6205–6217

(2005).

17. Klauke, N., Monaghan, P., Sinclair, G., Padgett, M. & Cooper, J. Characterisation of spatial and temporal changes in pH gradients in microfluidic channels using optically trapped fluorescent sensors. *Lab Chip* **6,** 788–93 (2006).
18. Gabi, M., Sannomiya, T., Larmagnac, A., Puttaswamy, M. & Vörös, J. Influence of applied currents on the viability of cells close to microelectrodes. *Integr. Biol.* **1,** 108–15 (2009).
19. Suzurikawa, J., Nakao, M., Kanzaki, R. & Takahashi, H. Microscale pH gradient generation by electrolysis on a light-addressable planar electrode. *Sensors Actuators B Chem.* **149,** 205–211 (2010).
*20. Leenheer, A. J. & Atwater, H. A. Imaging Water-Splitting Electrocatalysts with pH-Sensing Confocal Fluorescence Microscopy. *J. Electrochem. Soc.* **159,** H752–H757 (2012).
21. Boulmedais, F., Tang, C. S., Keller, B. & Vörös, J. Controlled Electrodissolution of Polyelectrolyte Multilayers: A Platform Technology Towards the Surface-Initiated Delivery of Drugs. *Adv. Funct. Mater.* **16,** 63–70 (2006).
22. Schmidt, D. J. & Hammond, P. T. Electrochemically erasable hydrogen-bonded thin films. *Chem. Commun.* **46,** 7358–60 (2010).
23. Schmidt, D. J., Min, Y. & Hammond, P. T. Mechanomutable and reversibly swellable polyelectrolyte multilayer thin films controlled by electrochemically induced pH gradients. *Soft Matter* **7,** 6637 (2011).
24. Shacham, R., Mandler, D. & Avnir, D. Electrochemically induced sol-gel deposition of zirconia thin films. *Chemistry* **10,** 1936–43 (2004).
25. Diéguez, L., Darwish, N., Graf, N., Vörös, J. & Zambelli, T. Electrochemical tuning of the stability of PLL/DNA multilayers. *Soft Matter* **5,** 2415 (2009).
26. Graf, N. *et al.* Electrochemically Stimulated Release from Liposomes Embedded in a Polyelectrolyte Multilayer. *Adv. Funct. Mater.* **21,** 1666–1672 (2011).
27. Tam, T. K. *et al.* Electrochemical nanotransistor from mixed-polymer brushes. *Adv. Mater.* **22,** 1863–6 (2010).
28. Tam, T. K. *et al.* Reversible 'closing' of an electrode interface functionalized with a polymer brush by an electrochemical signal. *Langmuir* **26,** 4506–13 (2010).
29. Kwon, I. C., Bae, Y. H. & Kim, S. W. Electrically erodible polymer gel for controlled release of drugs. *Nature* **354,** 291–3 (1991).
30. Guillaume-Gentil, O. *et al.* pH-controlled recovery of placenta-derived mesenchymal stem cell sheets. *Biomaterials* **32,** 4376–84 (2011).
31. Maurer, K., McShea, A., Strathmann, M. & Dill, K. The removal of the t-BOC group by electrochemically generated acid and use of an addressable electrode array for peptide

synthesis. *J. Comb. Chem.* **7,** 637–40 (2005).

32. Maurer, K. *et al.* Electrochemically generated acid and its containment to 100 micron reaction areas for the production of DNA microarrays. *PLoS One* **1,** e34 (2006).
33. Dixon, H. B. F. & Moss, G. P. Glossary of Nomenclature and Symbolism for Amino Acids and Peptides. *Int. Union Pure Appl. Chem.* **56,** 595–624 (1984).
34. Yamasaki, Y. & Maekawa, K. A Peptide with Delicious Taste. *Agric. Biol. Chem.* **42,** 1761–5 (1978).
35. Rose, G. D., Glerasch, L. M. & Smith, J. A. Turns in Peptides and Proteins. *Adv. Protein Chem.* **37,** 1–109 (1985).
36. Branden, C. & Tooze, J. *Introduction to Protein Structure*. (Garland Publishing, 1999).
37. Pace, C. N. & Scholtz, J. M. A helix propensity scale based on experimental studies of peptides and proteins. *Biophys. J.* **75,** 422–427 (1998).
38. Moutevelis, E. & Woolfson, D. N. A Periodic Table of Coiled-Coil Protein Structures. *J. Mol. Biol.* **385,** 726–732 (2009).

*39. Crick, F. H. C. Is α-Keratin a Coiled Coil? *Nat. Publ. Gr.* **170,** 882–883 (1952).

*40. Crick, F. H. C. The packing of α-helices: simple coiled-coils. *Acta Crystallogr.* **6,** 689–697 (1953).

41. Pauling, L. & Corey, R. B. Compound helical configurations of polypeptide chains: structure of proteins of the alpha-keratin type. *Nature* **171,** 59–61 (1953).

*42. Hodges, R. S., Sodek, J., Smillie, L. B. & Jurasek, L. Tropomyosin: Amino Acid Sequence and Coiled-Coil Structure. *Cold Spring Harb. Symp. Quant. Biol.* **37,** 299–310 (1973).

*43. McLachlan, A. D. & Stewart, M. Tropomyosin coiled-coil interactions: evidence for an unstaggered structure. *J. Mol. Biol.* **98,** 293–304 (1975).

44. Hodges, R. S., Saund, A. K., Chong, P. C. S., St, S. a & Reid, R. E. Synthetic Model for Two-stranded α-Helical Coiled-coils. *Biol. Chem.* **256,** 1214–1224 (1981).
45. Apostolovic, B., Danial, M. & Klok, H.-A. Coiled coils: attractive protein folding motifs for the fabrication of self-assembled, responsive and bioactive materials. *Chem. Soc. Rev.* **39,** 3541–75 (2010).

*46. Kwok, S. C. & Hodges, R. S. Effect of chain length on coiled-coil stability: decreasing stability with increasing chain length. *Biopolymers* **76,** 378–90 (2004).

47. Parry, D. A. Coiled-coils in alpha-helix-containing proteins: analysis of the residue types within the heptad repeat and the use of these data in the prediction of coiled-coils in other proteins. *Biosci. Rep.* **2,** 1017–1024 (1982).

*48. Woolfson, D. N. The Design of Coiled-Coil Structures and Assemblies. *Adv. Protein Chem.* **70,** 79–112 (2005).

*49. O'Shea, E., Klemm, J., Kim, P. & Alber, T. X-ray structure of the GCN4 leucine zipper,

a two-stranded, parallel coiled coil. *Science (80-.).* **254,** 539–544 (1991).

50. Liu, J., Yong, W., Deng, Y., Kallenbach, N. R. & Lu, M. Atomic structure of a tryptophan-zipper pentamer. *Proc. Natl. Acad. Sci. U. S. A.* **101,** 16156–16161 (2004).
51. Gurnon, D. G., Whitaker, J. A. & Oakley, M. G. Design and characterization of a homodimeric antiparallel coiled coil. *J. Am. Chem. Soc.* **125,** 7518–7519 (2003).
52. Ramos, J. & Lazaridis, T. Computational analysis of residue contributions to coiled-coil topology. *Protein Sci.* **20,** 1845–1855 (2011).
53. Apgar, J. R., Gutwin, K. N. & Keating, A. E. Predicting helix orientation for coiled-coil dimers. *Proteins Struct. Funct. Genet.* **72,** 1048–1065 (2008).
54. Walshaw, J. & Woolfson, D. N. Socket: a program for identifying and analysing coiled-coil motifs within protein structures. *J. Mol. Biol.* **307,** 1427–1450 (2001).
55. Woods, E. F. Studies on the denaturation of tropomyosin and light meromyosin. *Int. J. Protein Res.* **1,** 29–43 (1969).
56. Kohn, W. D. & Hodges, R. S. De novo design of α-helical coiled coils and bundles: Models for the development of protein-design principles. *Trends Biotechnol.* **16,** 379–389 (1998).
57. O'Shea, E. K., Rutkowski, R. & Kim, P. S. Mechanism of specificity in the Fos-Jun oncoprotein heterodimer. *Cell* **68,** 699–708 (1992).
*58. O'Shea, E. K., Lumb, K. J. & Kim, P. S. Peptide 'Velcro': design of a heterodimeric coiled coil. *Curr. Biol.* **3,** 658–67 (1993).
59. Monera, O. D., Kay, C. M. & Hodges, R. S. Electrostatic interactions control the parallel and antiparallel orientation of alpha-helical chains in two-stranded alpha-helical coiled-coils. *Biochemistry* **33,** 3862–3871 (1994).
60. McClain, D. L., Woods, H. L. & Oakley, M. G. Design and Characterization of a Heterodimeric Coiled Coil that Forms Exclusively with an Antiparallel Relative Helix Orientation. *J. Am. Chem. Soc.* **123,** 3151–3152 (2001).
61. Monera, O. D., Zhou, N. E., Kay, C. M. & Hodges, R. S. Comparison of antiparallel and parallel two-stranded alpha-helical coiled-coils. Design, synthesis, and characterization. *J. Biol. Chem.* **268,** 19218–19227 (1993).
62. McClain, D. L., Binfet, J. P. & Oakley, M. G. Evaluation of the energetic contribution of interhelical Coulombic interactions for coiled coil helix orientation specificity. *J. Mol. Biol.* **313,** 371–83 (2001).
63. Lombardi, A, Bryson, J. W. & DeGrado, W. F. De novo design of heterotrimeric coiled coils. *Biopolymers* **40,** 495–504 (1996).
64. Beck, K., Gambee, J. E., Kamawal, A. & Bächinger, H. P. A single amino acid can switch the oligomerization state of the alpha-helical coiled-coil domain of cartilage matrix protein. *EMBO J.* **16,** 3767–3777 (1997).

65. Dutta, K., Alexandrov, A., Huang, H. E. & Pascal, S. M. pH-induced folding of an apoptotic coiled coil. *Protein Sci.* **10,** 2531–2540 (2001).

66. Apostolovic, B. & Klok, H.-A. pH-sensitivity of the E3/K3 heterodimeric coiled coil. *Biomacromolecules* **9,** 3173–80 (2008).

67. Zhou, N. E., Kay, C. M. & Hodges, R. S. The role of interhelical ionic interactions in controlling protein folding and stability. De novo designed synthetic two-stranded alpha-helical coiled-coils. *J. Mol. Biol.* **237,** 500–12 (1994).

68. Goto, Y., Takahashi, N. & Fink, A. L. Mechanism of acid-induced folding of proteins. *Biochemistry* **29,** 3480–3488 (1990).

69. Goto, Y. & Aimoto, S. Anion and pH-dependent conformational transition of an amphiphilic polypeptide. *J. Mol. Biol.* **218,** 387–396 (1991).

70. Ciani, B., Gail Hutchinson, E., Sessions, R. B. & Woolfson, D. N. A designed system for assessing how sequence affects α to β conformational transitions in proteins. *J. Biol. Chem.* **277,** 10150–10155 (2002).

71. Litowski, J. R. & Hodges, R. S. Designing Heterodimeric Two-stranded α-Helical Coiled-coils. *J. Biol. Chem.* **277,** 37272–9 (2002).

72. Dahiyat, B. I., Gordon, D. B. & Mayo, S. L. Automated design of the surface positions of protein helices. *Protein Sci.* **6,** 1333–7 (1997).

73. Zitzewitz, J. A., Ibarra-Molero, B., Fishel, D. R., Terry, K. L. & Matthews, C. R. Preformed secondary structure drives the association reaction of GCN4-p1, a model coiled-coil system. *J. Mol. Biol.* **296,** 1105–1116 (2000).

74. Kaplan, J. B., Reinke, A. W. & Keating, A. E. Increasing the affinity of selective bZIP-binding peptides through surface residue redesign. *Protein Sci.* **23,** 940–53 (2014).

75. Betz, S. F. & DeGrado, W. F. Controlling topology and native-like behavior of de novo designed peptides. Design and Characterization of antiparallel four stranded coiled coils. *Biochemistry* **35,** 6955–6962 (1996).

76. Vu, C., Robblee, J., Werner, K. M. & Fairman, R. Effects of charged amino acids at b and c heptad positions on specificity and stability of four-chain coiled coils. *Protein Sci.* **10,** 631–637 (2001).

77. Root, B. C., Pellegrino, L. D., Crawford, E. D., Kokona, B. & Fairman, R. Design of a heterotetrameric coiled coil. *Protein Sci.* **18,** 329–336 (2009).

78. Fairman, R. *et al.* Design of heterotetrameric coiled coil: Evidence for increased stabilization by Glu-Lys ion pair interactions. *Biochemistry* **35,** 2824–2829 (1996).

79. Conway, J. F. & Parry, D. A. Structural features in the heptad substructure and longer range repeats of two-stranded alpha-fibrous proteins. *Int. J. Biol. Macromol.* **12,** 328–334 (1990).

80. Harbury, P. B., Zhang, T., Kim, P. S. & Alber, T. A switch between two-, three-, and

four-stranded coiled coils in GCN4 leucine zipper mutants. *Science* **262,** 1401–1407 (1993).

*81. Lumb, K. & Kim, P. A buried polar interaction imparts structural uniqueness in a designed heterodimeric coiled coil. *Biochemistry* **37,** 13042 (1998).

82. Oakley, M. G. & Kim, P. S. A buried polar interaction can direct the relative orientation of helices in a coiled coil. *Biochemistry* **37,** 12603–10 (1998).

83. Campbell, K. M. & Lumb, K. J. Complementation of buried lysine and surface polar residues in a designed heterodimeric coiled coil. *Biochemistry* **41,** 7169–75 (2002).

84. Campbell, K. M., Sholders, A. J. & Lumb, K. J. Contribution of Buried Lysine Residues to the Oligomerization Specificity and Stability of the Fos Coiled Coil †. *Biochemistry* **41,** 4866–4871 (2002).

85. Eckert, D. M., Malashkevich, V. N. & Kim, P. S. Crystal structure of GCN4-pIQI, a trimeric coiled coil with buried polar residues. *J. Mol. Biol.* **284,** 859–865 (1998).

86. Gonzalez, L., Woolfson, D. N. & Alber, T. Buried polar residues and structural specificity in the GCN4 leucine zipper. *Nat. Struct. Biol.* **3,** 1011–1018 (1996).

87. Akey, D. L., Malashkevich, V. N. & Kim, P. S. Buried polar residues in coiled-coil interfaces. *Biochemistry* **40,** 6352–6360 (2001).

88. Kim, M. K. & Kang, Y. K. Positional preference of proline in alpha-helices. *Protein Sci.* **8,** 1492–1499 (1999).

89. White, S. J. *et al.* Directed surface attachment of nanomaterials via coiled-coil-driven self-assembly. *Nanotechnology* **23,** 495304 (2012).

*90. White, S. J. *et al.* On-surface assembly of coiled-coil heterodimers. *Langmuir* **28,** 13877–82 (2012).

91. Stevens, M. M. *et al.* pH-dependent behavior of surface-immobilized artificial leucine zipper proteins. *Langmuir* **20,** 7747–52 (2004).

*92. White, S. J. *et al.* The Influence of Two-Dimensional Organization on Peptide Conformation. *Angew. Chemie Int. Ed.* **54,** 974–978 (2015).

93. Atanassov, A., Hendler, Z., Berkovich, I., Ashkenasy, G. & Ashkenasy, N. Force modulated conductance of artificial coiled-coil protein monolayers. *Biopolymers* **100,** 93–9 (2013).

94. Shlizerman, C., Atanassov, A., Berkovich, I., Ashkenasy, G. & Ashkenasy, N. De novo designed coiled-coil proteins with variable conformations as components of molecular electronic devices. *J. Am. Chem. Soc.* **132,** 5070–6 (2010).

95. Minelli, C., Liew, J. X., Muthu, M. & Andresen, H. Coiled coil peptide-functionalized surfaces for reversible molecular binding. *Soft Matter* **9,** 5119 (2013).

96. Chang, H.-C. *et al.* A General Method for Facilitating Heterodimeric Pairing Between Two Proteins- Application to Expression of α and β T-Cell Receptor Extracellular

Segments. *Proc. Natl. Acad. Sci. U. S. A.* **91,** 11408–11412 (1994).

97. Liu, J. *et al.* Crystallization of a deglycosylated T cell receptor (TCR) complexed with an anti-TCR Fab fragment. *J. Biol. Chem.* **271,** 33639–46 (1996).
98. Khandekar, S. S. *et al.* Affinity and kinetics of the interactions between an αβ T-cell receptor and its superantigen and class II-MHC/peptide ligands. *Mol. Immunol.* **34,** 493–503 (1997).
99. Golden, A. *et al.* High-level production of a secreted, heterodimeric αβ murine T-cell receptor in Escherichia coli. *J. Immunol. Methods* **206,** 163–169 (1997).
100. Kern, P., Hussey, R., Spoerl, R., Reinherz, E. L. & Chang, H.-C. Expression, purification, and functional analysis of murine ectodomain fragments of CD8αα and CD8αβ dimers. *J. Biol. Chem.* **274,** 27237–27243 (1999).
101. Schepers, K. *et al.* Differential kinetics of antigen-specific CD4+ and CD8+ T cell responses in the regression of retrovirus-induced sarcomas. *J. Immunol.* **169,** 3191–9 (2002).
102. Bronke, C. *et al.* Direct ex vivo detection of HLA-DR3-restricted cytomegalovirus- and Mycobacterium tuberculosis-specific CD4+ T cells. *Hum. Immunol.* **66,** 950–61 (2005).
103. Crawford, F., Huseby, E., White, J., Marrack, P. & Kappler, J. W. Mimotopes for alloreactive and conventional T cells in a peptide-MHC display library. *PLoS Biol.* **2,** E90 (2004).
104. Crawford, F. *et al.* Use of baculovirus MHC/peptide display libraries to characterize T-cell receptor ligands. *Immunol. Rev.* **210,** 156–70 (2006).
105. Crawford, F. *et al.* Specificity and detection of insulin-reactive CD4+ T cells in type 1 diabetes in the nonobese diabetic (NOD) mouse. *Proc. Natl. Acad. Sci. U. S. A.* **108,** 16729–34 (2011).
106. Ding, Y. H., Baker, B. M., Garboczi, D. N., Biddison, W. E. & Wiley, D. C. Four A6-TCR/peptide/HLA-A2 structures that generate very different T cell signals are nearly identical. *Immunity* **11,** 45–56 (1999).
107. Baker, B. M., Gagnon, S. J., Biddison, W. E. & Wiley, D. C. Conversion of a T cell antagonist into an agonist by repairing a defect in the TCR/peptide/MHC interface: implications for TCR signaling. *Immunity* **13,** 475–84 (2000).
108. Baker, B. M., Turner, R. V, Gagnon, S. J., Wiley, D. C. & Biddison, W. E. Identification of a Crucial Energetic Footprint on the α1 Helix of Human Histocompatibility Leukocyte Antigen (Hla)-A2 That Provides Functional Interactions for Recognition by Tax Peptide-HLA/A2–Specific T Cell Receptors. *J. Exp. Med.* **193,** 551–562 (2001).
109. Davis-Harrison, R. L., Armstrong, K. M. & Baker, B. M. Two different T cell receptors use different thermodynamic strategies to recognize the same peptide/MHC ligand. *J. Mol. Biol.* **346,** 533–50 (2005).

110. Busch, R., Pashine, A., Garcia, K. C. & Mellins, E. D. Stabilization of soluble, low-affinity HLA-DM/HLA-DR1 complexes by leucine zippers. *J. Immunol. Methods* **263,** 111–21 (2002).

111. Jun, C. D., Shimaoka, M., Carman, C. V, Takagi, J. & Springer, T. A. Dimerization and the effectiveness of ICAM-1 in mediating LFA-1-dependent adhesion. *Proc. Natl. Acad. Sci. U. S. A.* **98,** 6830–5 (2001).

112. Takagi, J., DeBottis, D. P., Erickson, H. P. & Springer, T. a. The Role of the Specificity-Determining Loop of the Integrin β Subunit I-like Domain in Autonomous Expression, Association with the α Subunit, and Ligand Binding. *Biochemistry* **41,** 4339–47 (2002).

113. Kohli, R. M., Takagi, J. & Walsh, C. T. The thioesterase domain from a nonribosomal peptide synthetase as a cyclization catalyst for integrin binding peptides. *Proc. Natl. Acad. Sci. U. S. A.* **99,** 1247–52 (2002).

114. Jiang, P., Ko, L., Jansen, K. R., Golde, T. E. & Yen, S.-H. Using leucine zipper to facilitate alpha-synuclein assembly. *FASEB J.* **22,** 3165–74 (2008).

115. Takagi, J., Erickson, H. P. & Springer, T. A. C-terminal opening mimics 'inside-out' activation of integrin α5β1. *Nat. Struct. Biol.* **8,** 531–533 (2001).

116. Wranik, B. J. *et al.* LUZ-Y: A novel platform for the mammalian cell production of full-length IgG bispecific antibodies. *J. Biol. Chem.* **287,** 43331–43339 (2012).

117. Yuzawa, S., Mizuno, T. & Tanaka, T. Activating an enzyme by an engineered coiled coil switch. *Chem. - A Eur. J.* **12,** 7345–7352 (2006).

118. Sugimoto, K., Mori, Y., Makino, K., Ohkubo, K. & Morii, T. Functional reassembly of a split PH domain. *J. Am. Chem. Soc.* **125,** 5000–4 (2003).

119. Park, S.-Y., Zheng, X. & Kim, Y.-G. Characterization of functional, noncovalently assembled zinc finger nucleases. *Biochem. Biophys. Res. Commun.* **453,** 289–95 (2014).

120. Selgrade, D. F., Lohmueller, J. J., Lienert, F. & Silver, P. A. Protein scaffold-activated protein trans-splicing in mammalian cells. *J. Am. Chem. Soc.* **135,** 7713–9 (2013).

121. Shekhawat, S. S., Porter, J. R., Sriprasad, A. & Ghosh, I. An autoinhibited coiled-coil design strategy for split-protein protease sensors. *J. Am. Chem. Soc.* **131,** 15284–90 (2009).

122. Kondo, N., Miyauchi, K., Meng, F., Iwamoto, A. & Matsuda, Z. Conformational changes of the HIV-1 envelope protein during membrane fusion are inhibited by the replacement of its membrane-spanning domain. *J. Biol. Chem.* **285,** 14681–8 (2010).

123. Ghosh, I., Hamilton, A. & Regan, L. Antiparallel leucine zipper-directed protein reassembly: application to the green fluorescent protein. *J. Am. Chem. Soc.* **122,** 5658–5659 (2000).

124. Magliery, T. J. *et al.* Detecting protein-protein interactions with a green fluorescent protein fragment reassembly trap: scope and mechanism. *J. Am. Chem. Soc.* **127,** 146–57

(2005).

125. Kojima, T., Karasawa, S., Miyawaki, A., Tsumuraya, T. & Fujii, I. Novel screening system for protein-protein interactions by bimolecular fluorescence complementation in Saccharomyces cerevisiae. *J. Biosci. Bioeng.* **111,** 397–401 (2011).
126. Tafelmeyer, P., Johnsson, N. & Johnsson, K. Transforming a (β/α)8--barrel enzyme into a split-protein sensor through directed evolution. *Chem. Biol.* **11,** 681–9 (2004).
127. O'Hare, H., Juillerat, A., Dianisková, P. & Johnsson, K. A split-protein sensor for studying protein-protein interaction in mycobacteria. *J. Microbiol. Methods* **73,** 79–84 (2008).
128. Böttcher, B., Vogel, M., Ploss, M. & Nassal, M. High plasticity of the hepatitis B virus capsid revealed by conformational stress. *J. Mol. Biol.* **356,** 812–22 (2006).
129. Kobatake, E., Takahashi, R. & Mie, M. Construction of a bFGF-tethered extracellular matrix using a coiled-coil helical interaction. *Bioconjug. Chem.* **22,** 2038–42 (2011).
130. Le, P. U. *et al.* Escherichia coli expression and refolding of E/K-coil-tagged EGF generates fully bioactive EGF for diverse applications. *Protein Expr. Purif.* **64,** 108–117 (2009).
131. Murschel, F. *et al.* Coiled-coil-mediated grafting of bioactive vascular endothelial growth factor. *Acta Biomater.* **9,** 6806–6813 (2013).
132. Boucher, C., Liberelle, B., Jolicoeur, M., Durocher, Y. & De Crescenzo, G. Epidermal growth factor tethered through coiled-coil interactions induces cell surface receptor phosphorylation. *Bioconjug. Chem.* **20,** 1569–1577 (2009).
133. Boucher, C. *et al.* Human corneal epithelial cell response to epidermal growth factor tethered via coiled-coil interactions. *Biomaterials* **31,** 7021–7031 (2010).
134. Lee, D. H., Granja, J. R., Martinez, J. a, Severin, K. & Ghadiri, M. R. A self-replicating peptide. *Nature* **382,** 525–528 (1996).
135. Severin, K., Lee, D. H., Martinez, J. A. & Ghadiri, M. R. Peptide Self-Replication via Template-Directed Ligation. *Chem. Eur. J.* **3,** 1017–1024 (1997).
136. Lee, D. H., Severin, K., Yokobayashi, Y. & Ghadiri, M. R. Emergence of symbiosis in peptide self-replication through a hypercyclic network. *Nature* **390,** 591–594 (1997).
137. Severin, K., Lee, D. H., Martinez, J. A., Vieth, M. & Ghadiri, M. R. Dynamic Error Correction in Autocatalytic Peptide Networks. *Angew. Chem. Int. Ed.* **37,** 126–128 (1998).
138. Saghatelian, A., Yokobayashi, Y., Soltani, K. & Ghadiri, M. R. A chiroselective peptide replicator. *Nature* **409,** 797–801 (2001).
139. Ashkenasy, G. & Ghadiri, M. R. Boolean logic functions of a synthetic peptide network. *J. Am. Chem. Soc.* **126,** 11140–11141 (2004).
140. Hori, Y., Egashira, Y., Kamiura, R. & Kikuchi, K. Noncovalent-interaction-promoted

ligation for protein labeling. *Chembiochem A Eur. J. Chem. Biol.* **11,** 646–8 (2010).

141. Yano, Y. *et al.* Coiled-coil tag-probe system for quick labeling of membrane receptors in living cells. *ACS Chem. Biol.* **3,** 341–345 (2008).
142. Nomura, W. *et al.* Development of crosslink-type tag-probe pairs for fluorescent imaging of proteins. *Biopolymers* **94,** 843–852 (2010).
143. Tsutsumi, H. *et al.* Fluorogenically active leucine zipper peptides as tag-probe pairs for protein imaging in living cells. *Angew. Chemie - Int. Ed.* **48,** 9164–9166 (2009).
144. Sakamoto, S., Ito, A., Kudo, K. & Yoshikawa, S. De novo design, synthesis, and function of semiartificial myoglobin conjugated with coiled-coil two-α-helix peptides. *Chem. - A Eur. J.* **10,** 3717–3726 (2004).
145. Boucher, C., St-Laurent, G., Jolicoeur, M., Crescenzo, G. De & Durocher, Y. Protein detection by Western blot via coiled-coil interactions. *Anal. Biochem.* **399,** 138–140 (2010).
146. Tripet, B. *et al.* Engineering a de novo-designed coiled-coil heterodimerization domain off the rapid detection, purification and characterization of recombinantly expressed peptides and proteins. *Protein Eng.* **9,** 1029–1042 (1996).
147. Cachia, P. J., Kao, D. J. & Hodges, R. S. Synthetic peptide vaccine development: measurement of polyclonal antibody affinity and cross-reactivity using a new peptide capture and release system for surface plasmon resonance spectroscopy. *J. Mol. Recognit.* **17,** 540–557 (2004).
148. Liberelle, B. *et al.* New ELISA approach based on coiled-coil interactions. *J. Immunol. Methods* **362,** 161–167 (2010).
149. Yu, B., Davis, E. M., Hodges, R. S., Irvin, R. T. & Li, D. Y. Surface nanocrystallization of stainless steel for reduced biofilm adherence. *Nanotechnology* **19,** 335101 (2008).
150. Laromaine, A., Akbulut, O., Stellacci, F. & Stevens, M. M. Supramolecular replication of peptide and DNA patterned arrays. *J. Mater. Chem.* **20,** 68 (2010).
151. Petka, W. A., Harden, J. L., McGrath, K. P., Wirtz, D. & Tirrell, D. A. Reversible hydrogels from self-assembling artificial proteins. *Science (80-.).* **281,** 389–392 (1998).
152. Pechar, M., Kopečková, P., Joss, L. & Kopeček, J. Associative diblock copolymers of poly(ethylene glycol) and coiled-coil peptides. *Macromol. Biosci.* **2,** 199–206 (2002).
153. Vandermeulen, G. W. M., Tziatzios, C. & Klok, H. A. Reversible self-organization of poly(ethylene glycol)-based hybrid block copolymers mediated by a de novo four-stranded α-helical coiled coil motif. *Macromolecules* **36,** 4107–4114 (2003).
154. Vandermeulen, G. W. M., Tziatzios, C., Duncan, R. & Klok, H. A. PEG-based hybrid block copolymers containing α-helical coiled coil peptide sequences: Control of self-assembly and preliminary biological evaluation. *Macromolecules* **38,** 761–769 (2005).
155. Yang, J., Xu, C., Wang, C. & Kopecek, J. Refolding hydrogels self-assembled from N-

(2-hydroxypropyl)methacrylamide graft copolymers by antiparallel coiled-coil formation. *Biomacromolecules* **7,** 1187–95 (2006).

156. Shu, J. Y., Tan, C., DeGrado, W. F. & Xu, T. New Design of Helix Bundle Peptide-Polymer Conjugates. *Biomacromolecules* **9,** 2111–2117 (2008).
157. Shu, J. Y., Lund, R. & Xu, T. Solution Structural Characterization of Coiled-Coil Peptide−Polymer side-conjugates. *Biomacromolecules* **13,** 1945–1955 (2012).
158. Fortier, C., De Crescenzo, G. & Durocher, Y. A versatile coiled-coil tethering system for the oriented display of ligands on nanocarriers for targeted gene delivery. *Biomaterials* **34,** 1344–1353 (2013).
159. Sweeney, R. Y., Park, E. Y., Iverson, B. L. & Georgiou, G. Assembly of Multimeric Phage Nanostructures Through Leucine Zipper Interactions. *Biotechnol. Bioeng.* **95,** 539–545 (2006).
160. Ryadnov, M. G., Ceyhan, B., Niemeyer, C. M. & Woolfson, D. N. 'Belt and braces': a peptide-based linker system of de novo design. *Journal of the American Chemical Society* **125,** 9388–94 (2003).
161. Wu, K., Liu, J., Johnson, R. N., Yang, J. & Kopeček, J. Drug-free macromolecular therapeutics: Induction of apoptosis by coiled-coil-mediated cross-linking of antigens on the cell surface. *Angew. Chemie - Int. Ed.* **49,** 1451–1455 (2010).
162. Wu, K., Yang, J., Liu, J. & Kopeček, J. Coiled-coil based drug-free macromolecular therapeutics: In vivo efficacy. *J. Control. Release* **157,** 126–131 (2012).
163. Kverka, M. *et al.* Immunogenicity of coiled-coil based drug-free macromolecular therapeutics. *Biomaterials* **35,** 5886–5896 (2014).
164. Pechar, M. *et al.* Coiled coil peptides as universal linkers for the attachment of recombinant proteins to polymer therapeutics. *Biomacromolecules* **12,** 3645–3655 (2011).
165. Pechar, M. *et al.* Coiled Coil Peptides and Polymer–Peptide Conjugates: Synthesis, Self-Assembly, Characterization and Potential in Drug Delivery Systems. *Biomacromolecules* **15,** 2590–2599 (2014).
166. Pola, R. *et al.* Polymer therapeutics with a coiled coil motif targeted against murine BCL1 leukemia. *Biomacromolecules* **14,** 881–889 (2013).
167. Apostolovic, B., Deacon, S. P. E., Duncan, R. & Klok, H. A. Hybrid polymer therapeutics incorporating bioresponsive, coiled coil peptide linkers. *Biomacromolecules* **11,** 1187–1195 (2010).
168. Craig, P. O., Alzogaray, V. & Goldbaum, F. a. Polymeric display of proteins through high affinity leucine zipper peptide adaptors. *Biomacromolecules* **13,** 1112–1121 (2012).
169. Salis, A. & Ninham, B. W. Models and mechanisms of Hofmeister effects in electrolyte solutions, and colloid and protein systems revisited. *Chem. Soc. Rev.* **43,** 7358–7377

(2014).

170. Cojocari, D. Amino Acids - Wikimedia Commons. (2010). Available at: https://commons.wikimedia.org/wiki/File:Amino_Acids.svg. (Accessed: 14th April 2017)

171. Griffiths, A. J. F., Miller, J. H. & Gelbart, W. M. *Modern Genetic Analysis*. (W. H. Freeman, 2002).

172. Wood, C. W. *et al.* CCBuilder: an interactive web-based tool for building, designing and assessing coiled-coil protein assemblies. *Bioinformatics* **30,** 3029–35 (2014).

3. Experimental techniques

3.1. Introduction

In this section, the basics of the experimental techniques used in this work will be described. Specific details of the techniques such as the makes and models of equipment, and the conditions and chemicals used are described in the methods and materials section of the relevant experimental chapter.

3.2. Peptide synthesis

In this work, a number of peptides were designed and synthesised. This section describes the techniques used for the synthesis, purification and initial characterisation of the peptides. The design of the peptides and the outcomes of the synthesis process are described in Chapter 4.

3.2.1. Solid phase peptide synthesis

Most laboratory-scale peptide synthesis is performed in the so-called solid phase.[1] Solid phase peptide synthesis involves the covalent bonding of the first amino acid in the peptide sequence to a solid polymer resin, followed by the sequential addition of the following amino acids. The immobilisation of the growing peptide chains on the resin greatly simplifies the process of washing away reagents and byproducts at each step of the synthesis.[2]

The amino acids used in the synthesis are protected, meaning that their N-terminal amines are blocked by a covalently bound molecule, typically fluorenylmethyloxycarbonyl chloride (Fmoc) or *tert*-butyloxycarbonyl (*t*-Boc). These groups prevent peptide bonds forming between the blocked amine group of the protected amino acid and the free carboxyl groups of another amino acid, see Figure 3.1. In order for the peptide bond to form, the protecting group must be removed. The protecting groups therefore allow the synthesis to proceed in a controlled manner, with one amino acid added at a time. Reactive side chain groups are also protected to prevent unwanted reactions, such as branching of the peptide chain. The groups used to protect the side chains vary, depending on the synthesis scheme.

The synthesis thus proceeds from the C-terminal to the N-terminal one residue at a time with each residue addition requiring a four step deprotection-wash-coupling-wash cycle, see Figure 3.1.

In order to add an additional residue to the peptide, the N-terminal amine of the previously added residue must therefore be deprotected. This is accomplished by mild bases such as piperidine for Fmoc protection or strong acids such as trifluoroacetic acid (TFA) for *t*-Boc protection. Once the N-terminal amine of the peptide chains have been freed of the protecting groups, the deprotection agent and removed protecting groups must be washed away. The immobilisation of the peptide chains on the resin makes this step straightforward.

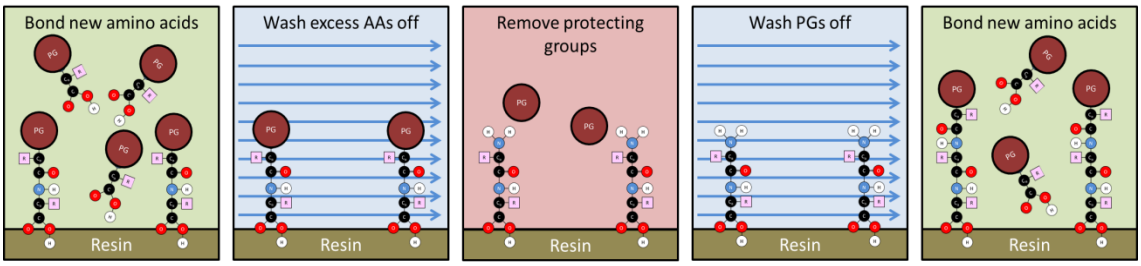

Figure 3.1: Illustration of the solid phase peptide synthesis cycle. 1) Amino acids (AAs) with protecting groups (PGs) at the N-terminals peptide bond via their C-terminals to the unprotected N-terminals of the immobilised peptide chain. 2) Unbound excess amino acids are washed away while the growing peptide chains remain bound to the resin. 3) Deprotection agent is introduced to remove protecting groups. 4) Deprotecting agent and removed protecting groups are washed away. 5) The cycle starts again with the introduction of the next amino acid.

The next amino acid in the sequence is then introduced in excess and the carboxyl group of the new amino acid forms a peptide bond with the deprotected free amine at the N-terminal of the growing peptide chains. Activating groups, such as diisopropylcarbodiimide (DIC), are used to activate the C-terminal carboxyl group to speed up the coupling reaction, often assisted by rapid heating of the solution via microwaves. Of course, the new residue's N-terminal amine group is protected so that only one residue is added to each peptide chain. Finally, the excess amino acid must be washed away to complete the cycle, again made simple by the immobilisation of the peptide on the resin.

After all residues have been added, the peptide must be removed from the resin and any side chain protecting groups removed. In *t*-Boc schemes, both processes are achieved at once using anhydrous hydrogen fluoride, whereas Fmoc schemes use TFA. In both cases, scavenging species are necessary to prevent the removed protecting molecules causing unwanted reactions. Since the use of hydrogen fluoride in *t*-Boc schemes requires specialised equipment and is potentially more dangerous, both to the newly synthesised peptide and the user, Fmoc schemes are often preferred. However, *t*-Boc schemes can be cheaper and faster, and tend to have fewer problems with solubility and aggregation of the peptide products.

In this work, peptides were synthesised in a microwave-assisted Fmoc scheme using piperidine for deprotection and DIC as an activator. See Section 4.2.1 for details.

3.2.2. High performance liquid chromatography (HPLC)

High performance liquid chromatography (HPLC, sometimes referred to instead as high pressure liquid chromatography) is commonly used for the purification of peptides and other chemicals.[3] A sample of impure peptides is dissolved in solvent which is then forced through a column of solid absorbent material at high pressure. Different peptides are slowed by the column to different extents depending on their size, charge, hydrophobicity etc., resulting in the separation of the desired peptides from any undesired molecules, for example shorter peptides created by incomplete reactions in the synthesis. The time it takes a peptide to pass through the column is called its retention time. UV light is used to detect the absorption of the solution as it leaves the

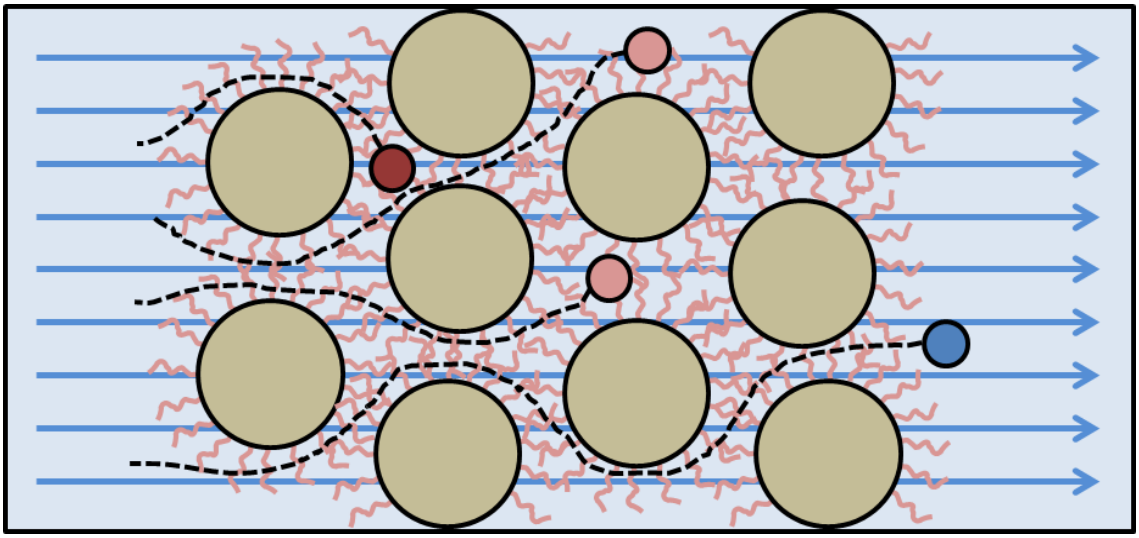

Figure 3.2: Illustration of the interior of a reverse-phase HPLC column. The column is packed with a silica scaffold (shown in brown) covered in hydrophobic molecules (pink lines). As polar solvent passes through the column, hydrophilic molecules (shown in blue) pass through more quickly than hydrophobic molecules (shown in pink and red), leading to separation by hydrophobicity.

column, giving an indication of how concentrated the peptide is at that time. Assuming the desired peptide is the dominant product, the absorption spectrum will therefore indicate when it came off the column. Some machines also divert a portion of the solution to a mass spectrometer (see below) to enable identification and more precise collection of the desired peptide. In all cases, the solvent coming off in the column is separated into multiple 'fractions' with the aim that at least one of the fractions will be pure and only contain the desired peptide.

Size-exclusion HPLC (where molecules are separated by size) and ion-exchange HPLC (where molecules are separated by charge) are sometimes used for peptide purification but due to its general advantage in both speed and efficiency, the most common technique is reverse-phase HPLC, where molecules are separated by hydrophobicity.[3] In this technique, the solid material in the column is non-polar (i.e. hydrophobic, typically a silica scaffold covered with covalently-bound hydrocarbons) and the solvent is polar. The peptide solution is injected into the column and solvent flowed through at high pressure. More polar peptides are more likely to remain in the solvent and pass through the column quickly, and less polar peptides are more likely to be attracted to the non-polar solid and pass through the column more slowly, see Figure 3.2. The peptides therefore come out of the column in order of hydrophobicity. Retention times (i.e. the time the peptide is retained in the column) can be altered by changing the composition of the solvent, and so it is common to use a gradient elution in which the composition of the solvent is gradually changed over the course of the purification. For example, once the peptide solution has been injected into the column, the purification may start with a 10% solution of acetonitrile in water and finish with 90% acetonitrile. As the amount of acetonitrile increases, the solvent becomes increasingly non-polar, thereby decreasing the attraction between non-polar peptides and column and decreasing retention time. This means that later-eluting peptides come off the

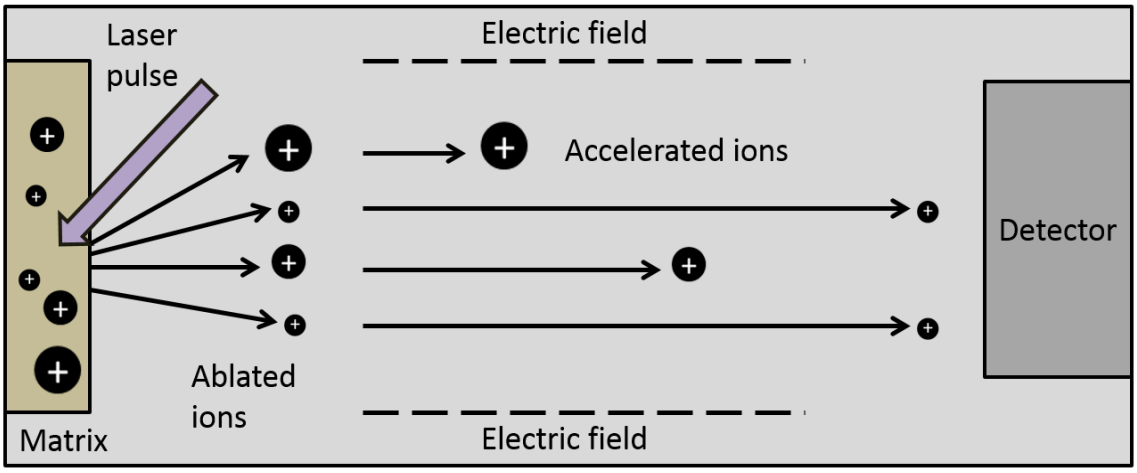

Figure 3.3: Illustration of MALDI-TOF mass spectrometry. The molecules to be analysed are embedded in a crystallised matrix (shown in brown). A laser pulse vaporises the matrix, leading to a gaseous phase of ions, which are accelerated through an electric field. Ions of lesser mass travel to the detector more quickly, and the mass-to-charge ratio of the ions can be calculated from the known electric field strength.

column more quickly, and have sharper peaks in the absorption graph than they would otherwise, allowing them to be distinguished and collected more accurately, as well as reducing the overall purification time.

Peptide detection is usually performed at 220 nm and/or 280 nm due to absorption of light by the peptide bonds and tryptophan, tyrosine and phenylalanine side chains at these respective wavelengths. An HPLC graph plots absorption against time, and a single sharp peak indicates pure peptide.

In this work, reverse-phase HPLC was used for peptide purification with various solvents, depending on the peptide being purified. See Section 4.2.2 for details.

3.2.3. Mass spectrometry

Mass spectrometry is a technique used to analyse the composition of chemical samples. In the case of peptide synthesis it can be used to confirm the presence of the intended product and its purity in the fractions produced by HPLC. As mentioned above, it is also possible to use a mass spectrometer to automatically direct the collection of fractions during HPLC. In this work, matrix assisted laser desorption time-of flight (MALDI-TOF) mass spectrometry was used. See Section 4.2.3 for details of the materials and methods.

In the MALDI process, a peptide sample is mixed with a matrix material and deposited on a metal plate. The solvents are evaporated to leave a crystallised matrix in which the peptides are embedded. The purpose of the matrix material is to absorb energy from laser pulses and cause the peptide-matrix mixture to vaporize, producing a hot gaseous plume of peptide and matrix material in which the peptides are ionised by protonation and deprotonation (although the precise mechanism of ionisation is not fully understood).[4]

Once ionised, the peptides are accelerated by an electric field. All ions of the same charge will receive the same amount of kinetic energy from the field, but their velocities will differ due to their different masses, see Figure 3.3. Since the electric field strength is known, the mass-to-charge ratio of the ions can be determined by measuring the time taken by the ion to travel a known distance through a field-free portion of the detector. This is known as time-of-flight (TOF) separation. The potential energy, E_p, of a particle of charge q in an electric field with a voltage V is given by:

$$E_p = qV$$

As the particles are accelerated by the voltage, the potential energy is converted to kinetic energy:

$$E_K = \frac{1}{2}mv^2$$

where m is the mass of the particle and v the velocity. Thus:

$$E_p = E_k \Rightarrow qV = \frac{1}{2}mv^2$$

Once the particle leaves the field and enters the field-free region of the detector, the velocity will be constant and is given by:

$$v = \frac{x}{t}$$

where x is the distance the particle travels in the time period t. Substituting for v gives:

$$qV = \frac{1}{2}m\left(\frac{x}{t}\right)^2$$

and rearranging for t:

$$t = \sqrt{\frac{mx^2}{2qV}} = \frac{x}{\sqrt{2V}}\sqrt{\frac{m}{q}}$$

Since the distance x is the known length of the field-free region of the detector, and the voltage V is also known, the mass-to-charge ratio $\frac{m}{q}$ can then be calculated from the time-of-flight t. In addition, since the time-of-flight depends on the mass-to-charge ratio, the peptides will arrive at the detector at different times depending on their mass and charge. By measuring the amount of peptide reaching the detector at each time, a plot of signal intensity against mass-to-charge ratio can be produced. This will indicate the purity of the peptide sample, with a single sharp peak indicating a pure sample. The results can be distorted if the vaporization process causes the peptides to become fragmented. So-called 'soft' ionisation techniques such as MALDI and electrospray ionization (ESI) are therefore preferred for large biomolecules such as peptides, since they impart less energy to the molecules and are therefore less likely to cause fragmentation than 'hard' ionisation techniques such as electron ionisation (EI).[5]

3.3. Peptide characterisation

The properties of peptides, and in particular the dependence of their dimerisation behavior on solution pH, were characterised using a number of techniques, which are described in this section. The results of the characterisation are presented in Chapters 4 and 5.

3.3.1. Circular dichroism spectroscopy (CD)

Circular dichroism (CD) spectroscopy is an optical technique widely used for the study of protein and peptide secondary structures.[6] Left circularly polarised light and right circularly polarised light are sequentially passed through a sample of the peptide in solution. Peptide secondary structure elements have characteristic differences in their absorption of the two polarisations and these differences (called the circular dichroism) are detected over a range of UV wavelengths. The obtained CD spectra can then be compared to spectra for known structures in order to identify the secondary structure of the peptide in question. Figure 3.4 shows examples of typical spectra for a number of secondary structure elements. Quantitative estimates of the percentage of elements such as alpha helices and beta sheets present can in principle be obtained since the spectrum should be the sum of the percentages of the component spectra.[7]

The CD signal for alpha helices is the largest and has the most easily recognisable spectral characteristics. It consists of two overlapping negative peaks at 222 nm and 208 nm, and a positive peak at 192 nm. The peaks arise from electron transitions in the peptide bond; the 222 nm peak comes from the $n \rightarrow \pi^*$ transition, i.e. the transition of electrons from the non-bonding molecular orbital to the antibonding π^* molecular orbital formed from the p orbitals of the carbon, nitrogen and oxygen atoms, see Figure 3.5. The 192 nm and 208 nm peaks come from the $\pi \rightarrow \pi^*$ transition, i.e. the transition from the bonding π molecular orbital to antibonding π^* molecular orbital. The $\pi \rightarrow \pi^*$ transition results in both positive and negative peaks because the alpha helical structure

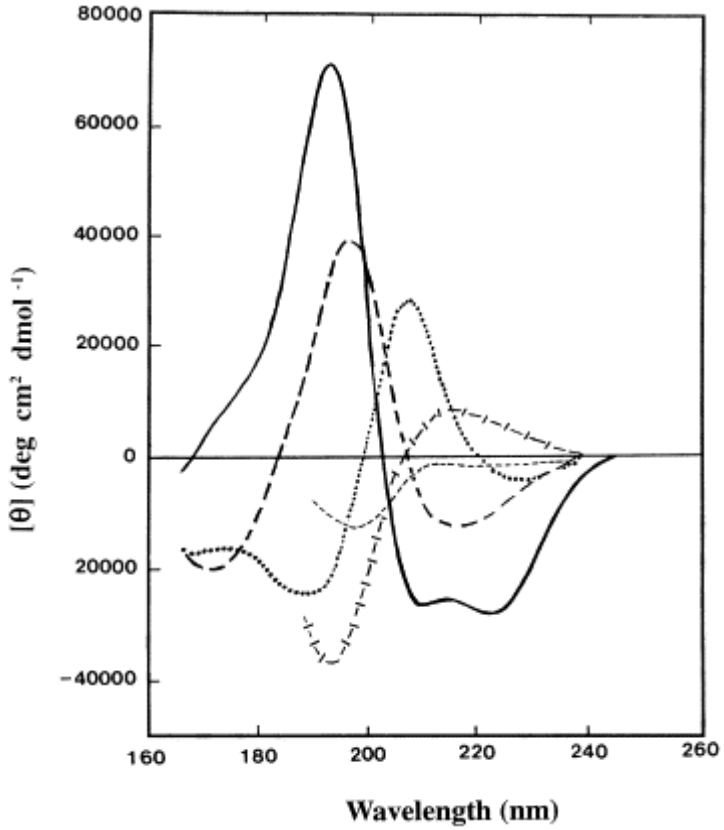

Figure 3.4: Typical CD spectra for alpha helix (solid line), antiparallel beta sheet (long dashed line), type I beta turn (dotted line), extended 31-helix (cross dashed line), irregular structure (short dashed line). Reproduced from Kelly *et al*.[6]

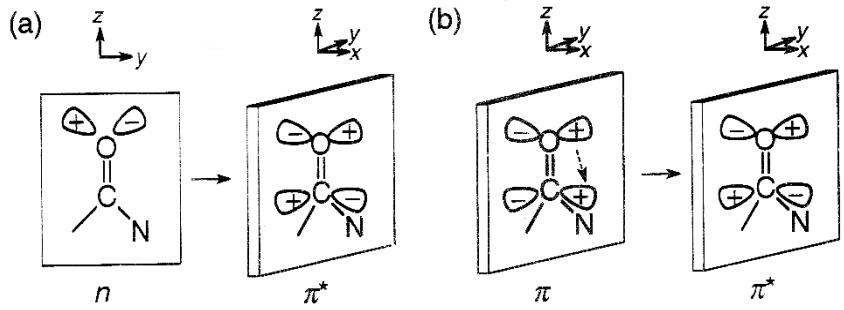

Figure 3.5: Schematic illustrations of (a) n → π* and (b) π → π* transitions in peptides. Reproduced from Rodger and Nordén.[7]

leads to two possible couplings of transition moments in neighbouring peptide bonds (in fact, n residues leads to n possible couplings, but only the single highest and lowest energy couplings are not cancelled out by others).[7] So-called head-to-head coupled moments give the higher energy transition (the 192 nm peak) which is polarised perpendicular to the helix axis, whereas head-to-tail coupled moments give the lower energy transition (the 208 nm peak) polarised parallel to the helix axis.

CD signal is the difference between absorption of left and right circularly polarised light, i.e. $\Delta A = (A_L - A_R)$ where A_L and A_R are, respectively, the left and right absorbances.[8,9] Early

CD spectrometers worked by measuring the polarisation of linearly polarised light into elliptically polarized light by the sample.[7] For this reason, CD is often still given in degrees, the unit of ellipticity. Conversion is via the formula:

$$\Delta A = \frac{4\pi\theta(degrees)}{180\ln(10)} = \frac{\theta(millidegrees)}{32982}$$

To facilitate comparisons between different samples and measurement conditions, CD spectra in the literature are often given in terms of units such as molar ellipticity and mean residue molar ellipticity (MRME). Molar ellipticity, $[\theta]$, corrects for concentration using Beer's Law, and is defined as:

$$[\theta] = 3298.2\frac{\Delta A}{Cl}$$

where C is the molar concentration of peptide bonds and l the path length (in cm), i.e. the distance the light travels through the solution. To correct for the size of the peptide or protein being studied, molar ellipticity can then be converted to MRME by dividing by the number of amino acid residues in the peptide or protein.

In this work, CD is used to characterise coiled coil formation in peptides. The peptides show an alpha helical structure when formed into coiled coils, and so an increase in ellipticity of the 192 nm, 208 nm and 222 nm peaks indicates an increase in the number of coiled coils in the system. It was proposed by Cooper and Woody that the stronger reliance of the $\pi\rightarrow\pi^*$ transition peaks on the alpha helical structure means that a slight shift in conformation of an alpha helix upon forming a coiled coil may potentially be detected by a slight decrease in the intensity of the 208 nm peak.[10] Since the 222 nm peak should remain unaffected by the formation of the coiled coil, it is common to use the ratio of the two peak intensities to distinguish between 'pure' alpha helices ($\theta_{222}/\theta_{208} \approx 0.8\text{-}0.9$) and coiled coils ($\theta_{222}/\theta_{208} \geq 1.0$).[11–19]

Determination of melting temperatures with CD

As the temperature of a solution of peptides increases, the peptides gain thermal (i.e. vibrational) energy. With enough thermal energy, the hydrogen bonds that form the secondary structure of the peptides may be broken. In the case of coiled coils, loss of alpha helical structure indicates the dissociation of the coil and can be monitored easily with CD. The temperature at which half of the coiled coils have dissociated is called the melting temperature, T_m. It can be calculated by measuring CD spectra at a range of temperatures and plotting the change in signal at one of the characteristic alpha helical wavelengths (eg. 192 nm) against temperature. A sigmoidal dose response curve can then be fitted to the data:

$$y = A_1 + \frac{A_2 - A_1}{1 + 10^{\mathrm{p}\log(x_0 - x)}}$$

where A_1 and A_2 are the bottom and top asymptotes, respectively, $\log x_0$ is the centre, and p is the Hill slope.[20] The curve can then be differentiated to find the melting temperature, which will be the point at which the second derivative of the ellipticity, θ_{192} vs. temperature, T, equals zero, i.e.:

$$T_m = T \;\Leftrightarrow\; \frac{d^2\theta_{192}}{dT^2} = 0$$

Surface CD

While CD is usually used to analyse molecules in solution, efforts have been made since 1970 to use CD for studying thin films or monolayers of molecules.[21] A key consideration with these types of sample is that the molecules may be anisotropic, i.e. they might not be randomly oriented as they would be in solution. Since the polarised light used in CD will always contain linear components, there is also a linear dichroism (LD) signal. LD is a technique used to analyse the orientation of molecules. When a sample is isotropic the LD signal is too small to be of consequence, but in an oriented sample the LD signal (as well as linear birefringence) could be one or two orders of magnitude larger than the CD signal and may therefore obscure it.[7]

In 1970 Tunis-Schneider and Maestre claimed that the LD signal from an oriented DNA film could be eliminated by averaging the CD spectra taken from different rotations of a sample about the optical axis.[21] This rotation method was subsequently used to study polypeptide monolayers,[22] and oriented peptides embedded in lipid bilayers.[23] However, the method was criticised by multiple authors,[24,25] and it was shown by Shindo *et al* that Tunis-Schneider's original analysis was only valid for an ideal CD spectrometer and even then only if the LD signal was small, i.e. if the sample did not have macroscopic anisotropy.[26,27]

Noting that the signal from just a single monolayer of protein would likely be too small to give useful CD spectra, McMillin and Walton increased their CD signal by passing light through multiple quartz slides onto which proteins had adsorbed.[28] A small difference between the solution and surface spectra was noted, and ascribed to orientation effects, but was within the range of experimental error. This multi-plate method has since been used in many surface CD papers,[29–32] though the number of plates considered necessary has varied from 16 to as few as 3.[33,34] Presumably the use of multiple plates reduces the anisotropy, since the molecules are likely to be oriented differently on each plate. It does not appear to have been rigorously shown anywhere that this is the case; however since LD signals are typically much larger than CD signals

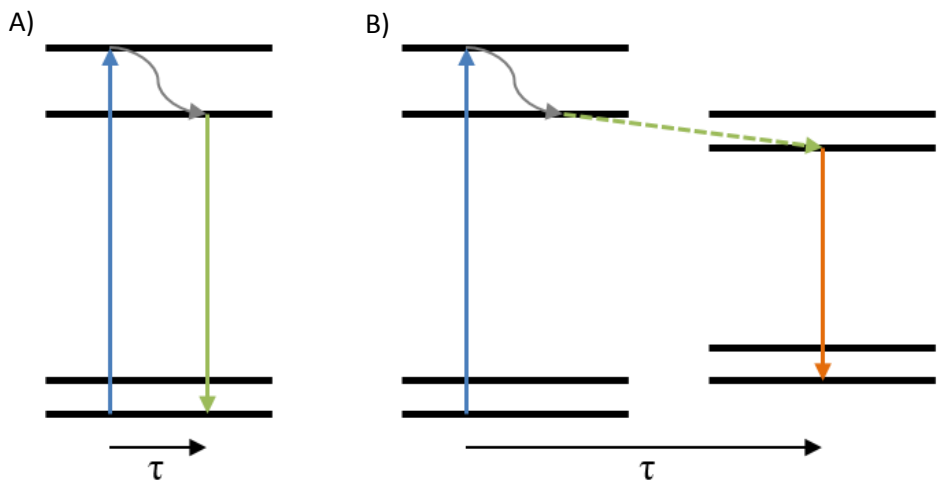

Figure 3.6: Illustration of FRET, showing electronic states of the fluorophores. Multiple energy levels are shown for each of the ground (bottom) and excited (top) states to indicate the existence of multiple vibrational energy levels. A) When no acceptor fluorophore is present, excitation (blue arrow) of the donor fluorophore excites electrons from the ground state to a higher vibrational energy level in the excited state. The electrons rapidly relax (grey arrow) to the lowest vibrational energy level of the excited state and then decay (green arrow) to the ground state by emission of light at the donor wavelength. B) When an acceptor fluorophore is within a few nanometres of a donor fluorophore, excitation energy is non-radiatively transferred to the acceptor, causing acceptor emission (orange arrow) and supressing the donor emission. τ is the fluorescence lifetime, i.e. the time between absorption and emission.

it may be valid to assume that the influence of LD is negligible if, for example, one obtains something that clearly resembles an alpha helical CD spectrum for a known alpha helical peptide.[35] In this work, surface CD is used primarily to detect binding of coiled coil peptides. Care is taken to avoid any changes in rotation of the samples, meaning that any changes in the spectra can be ascribed to changes caused by binding, regardless of whether the changes are caused by changes in the circular dichroism signal or the linear dichroism signal. See Sections 5.2.6 and 5.3.3 for more detail.

3.3.2. Förster resonance energy transfer (FRET)

Förster resonance energy transfer (FRET, also known as fluorescence resonance energy transfer) is a phenomenon in which energy from an excited fluorophore (the donor) is non-radiatively transferred to a different fluorophore (the acceptor) nearby, causing excitation and emission from the acceptor, see Figure 3.6.[36] For FRET to occur there must be some overlap between the donor emission spectrum and the acceptor excitation spectrum and the fluorophores must be within a few nanometres of each other. The efficiency with which energy is transferred, *E*, is inversely proportional to the sixth power of the distance, *r*, between the two fluorophores:

$$E = \frac{1}{1 + \left(\frac{r}{R_0}\right)^6}$$

where R_0 is the Förster distance, defined as the distance at which the non-radiative transfer efficiency is 50%, which can be calculated for any two dyes from their excitation and emission spectra. This strong dependence on distance means that FRET can be used for extremely precise measurements of the distance between the two fluorophores if the changes in acceptor and donor emission can be measured accurately. By labelling molecules of interest, such as peptides, with a FRET pair (i.e. two dyes which show FRET) it is possible to study interactions and binding by monitoring changes in FRET efficiency.

FRET can be monitored by optical spectrometry. In this work it is used to assess the binding of peptides, see Sections 4.2.6 and 5.2.4. One peptide of a coiled coil pair is labelled with a donor dye and the other is labelled with a corresponding acceptor dye. When the peptides are mixed in solution and excited at the donor excitation wavelength, emission at the acceptor emission wavelength indicates the formation of heterodimers since the dyes will only be close enough to each other for FRET to occur if the peptides are bound as a coiled coil. Importantly, the formation of homodimers will not lead to any emission at the acceptor wavelength, so FRET is a direct test of heterodimer formation.

Determination of dissociation constants using FRET

FRET can be used to calculate the dissociation constant (K_d) of a peptide dimer. K_d is defined as:

$$K_d = \frac{[A]_{free}[D]_{free}}{[AD]}$$

where $[A]_{free}$ is the concentration of unbound acceptor-labelled peptide, $[D]_{free}$ the concentration of the unbound donor-labelled peptide and $[AD]$ the concentration of acceptor-donor heterodimers. If the emission of an acceptor dye attached to one of the peptides is measured as a function of concentration of the acceptor-labelled peptide against a constant concentration of the donor-labelled peptide, a binding curve is produced, from which the K_d may be calculated by fitting the curve with the equation:[37]

$$y = L + (Y - L)\left(1 - \frac{2K_d}{x - [A] + K_d + \sqrt{(K_d + [A] - x)^2 + 4K_d x}}\right)$$

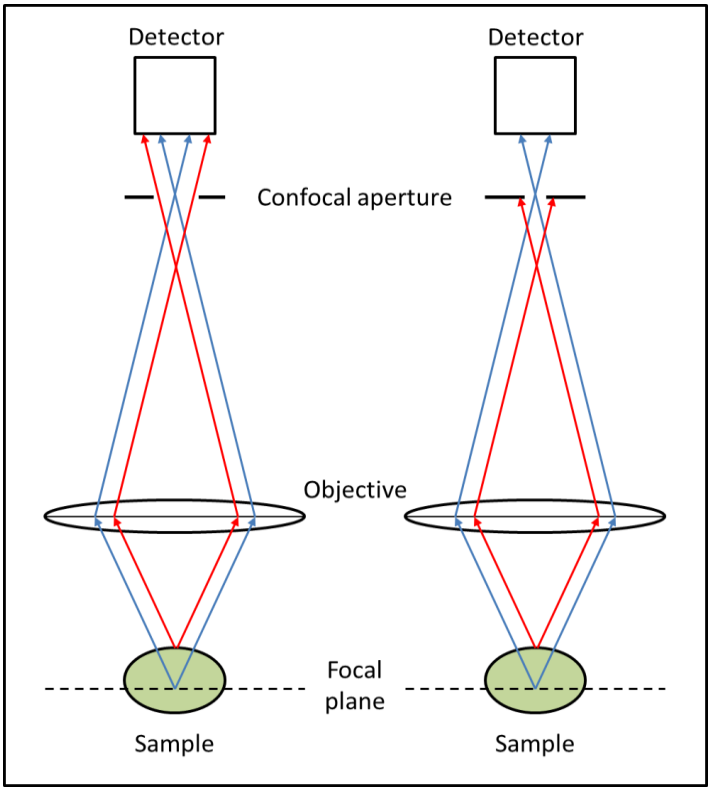

Figure 3.7: Illustration of confocal microscopy. Light from the focal plane (shown in blue) reaches the detector, while out-of-focus light (shown in red) can be blocked by reducing the size of the confocal aperture.

where y is the measured FRET emission, L the minimum FRET emission, Y the maximum FRET emission, $x = [D]$ the (constant) total concentration of donor-labelled peptide, and $[A]$ the (variable) total concentration of acceptor-labelled peptide. For a derivation of this equation, see Appendix Section A3.2.

3.3.3. Confocal laser scanning microscopy (CLSM)

In standard wide-field optical microscopy the entire sample is illuminated by a light source and all reflected or emitted light is collected. This has the advantage of speed but the disadvantage that out of focus light is collected, giving a large and usually unwanted background signal. In confocal laser scanning microscopy (CLSM), out-of-focus light is eliminated by use of a pinhole known as the confocal aperture at the confocal plane of the lens, see Figure 3.7, which greatly improves the depth resolution of the images.[38,39] However, only a small area of the sample is illuminated at any one time, so to acquire a 2D image, laser light is scanned across the sample to image the entire desired area. A stack of these 2D images at different depths can be combined to build a 3D image which is in focus over the entire depth of the sample.

In this work, CLSM is used in combination with FRET (see Section 3.2.2) to monitor the binding of peptides to an immobilised peptide monolayer (see Section 5.2.4 for more details).

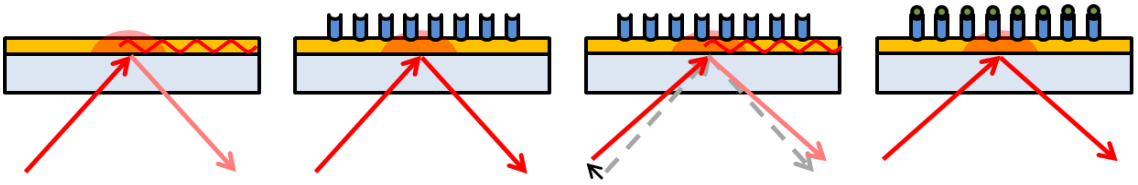

Figure 3.8: Illustration of SPR as used to detect molecular binding. 1) Light is totally internally reflected from the boundary between glass and a thin layer of gold. At a certain angle, the energy leaks into the gold layer and excites surface plasmons (red wave), leading to a reduction in reflected light intensity. 2) Binding of molecules to the gold changes the refractive index of the gold layer leading to a loss of surface plasmon resonance, and an increase in reflected light intensity. 3) The angle of the incident light is changed to restore the surface plasmon resonance. The change in angle acts as the detection method for the binding event. 4) A target molecule binds to the initial molecular layer, leading to a loss of surface plasmon resonance. The angle of incidence can again be changed to restore the resonance and thereby record the binding.

Measuring pH changes with CLSM

CLSM can be used in combination with pH sensitive fluorescent dyes to image spatial and temporal electrochemical pH changes. A number of fluorescent dyes have pH-sensitive emission but the most suitable for pH change imaging are dyes with two emission peaks, both of which are sensitive to pH change but in opposite directions. For example, the dye SNARF-4F used in this work (see Section 6.2 for details) has an emission peak at 590 nm which decreases in intensity as pH increases and a second peak at 650 nm which increases in intensity as pH increases. By measuring the intensity of each peak at known pH values and taking the ratio of the two intensities, a calibration curve of ratio vs. pH can be plotted. This allows unknown pH values to be determined by measuring the peak intensities. Taking the ratio of the two intensities is necessary to remove dependence on absolute intensity, which may vary due to changes in imaging conditions or errors in the dye concentration in solution, for example.

3.3.4. Surface plasmon resonance spectroscopy (SPR)

Surface plasmon resonance spectroscopy (SPR) is an optical technique for measuring changes at a surface, for example the binding of molecules to that surface.[40,41] At the boundary between a medium of higher refractive index and a medium of lower refractive index, light passing through the medium of higher refractive index may undergo total internal reflection. Despite the name, in total internal reflection some electric field from the light leaks into the medium of lower refractive index in the form of an evanescent wave with an amplitude that decays exponentially with distance from the boundary. If a thin film of metal (usually gold) is present at the boundary, the evanescent wave may excite electrons in the gold in way that leads to surface plasmons, see Figure 3.8. These are electromagnetic surface waves at the interface between the metal and a dielectric (the medium of lower refractive index). Resonance occurs at the maximum conversion of incident light energy to surface plasmons, which will be when the momentum of the incoming photons matches the momentum of surface plasmons. This in turn depends on the refractive index of the media in contact with the metal. If the refractive index of the media in the vicinity of the metal were to change, for example due to the binding of biomolecules on the metal

surface, then the momentum of the plasmons would change. In order to retain resonance conditions it would then be necessary to change the momentum of the incoming photons, which can be done by changing the wavelength of the light or by changing the angle of incidence (since momentum is a vector). Most SPR instruments take the latter approach, detecting the change in conditions at the metal surface by the adjustment in angle needed to retain maximum absorption of the incident light.

SPR is widely used for detecting the interactions of biomolecules such as proteins and peptides. A target is immobilised on the metal surface (this process can itself be measured by SPR if desired) and then the binding of other biomolecules to the target is monitored in real time by the instrument. While SPR has the advantage of being a label-free technique, the immobilisation of the target molecule may well affect the binding behaviour. Therefore one should exercise caution when forming conclusions about solution binding behavior on the basis of SPR data, but this means SPR is ideally suited to the study of binding to monolayers, as in this work. See Section 5.2.5 for details.

3.3.5. Concentration determination by UV spectroscopy

The concentration of peptides in solution can be determined using UV spectroscopy. Beer's Law states:

$$C = \frac{A}{\varepsilon L}$$

where C is concentration, A is absorbance, ε is molar extinction coefficient and L is path length. For peptides, it is usual to use the absorption and extinction coefficient at 280 nm, where tryptophan and tyrosine side chains absorb, along with disulphide bonds formed by pairs of cysteine residues. The extinction coefficient of a peptide at 280 nm, ε_{280}, may be estimated from the following formula:[42]

$$\varepsilon_{280} = N_Y \varepsilon_Y + N_W \varepsilon_W + N_{CC} \varepsilon_{CC}$$

where N_a is the number of amino acid residues of species a, and ε_a is the extinction coefficient of amino acid a at 280 nm. CC refers to a pair of cysteines assumed to form a disulphide bond. For peptides measured in water at 280 nm, the extinction coefficients are $\varepsilon_Y = 1490$, $\varepsilon_W = 5500$, and $\varepsilon_{CC} = 250$.

When peptides are labelled with fluorescent dyes, it is important to correct the absorbance to remove any influence from the dye absorption at 280 nm.

3.4. Electrochemistry

The electrochemical techniques described in this section were used to change the solution pH in the vicinity of electrodes. The results are presented in Chapters 7 and 8. Electrochemical pH change in this work was achieved by the application of constant currents by a potentiostat in a three electrode electrochemical cell, as described below. Changes in pH were monitored by use of a pH sensitive fluorescent dye, as described in Section 3.2.3.

3.4.1. The electrochemical cell

A standard electrochemical cell uses three electrodes immersed in solution.[43] The working electrode is defined as the electrode where the reaction of interest take place. Current flows between between the working electrode and a second electrode, known as the counter or auxiliary electrode. In order to gauge the potential of the working electrode, a third electrode of known potential is used, called the reference electrode. No current passes through the reference electrode, it simply provides a known and stable reference potential against which the working electrode potential can be measured and controlled. The working and counter electrodes tend to be made from inert conductors such as gold or platinum while the reference electrode is more complex. A common reference electrode is the silver chloride electrode in which the reaction between silver and silver chloride provides the stable reference potential:

$$AgCl \rightleftharpoons Ag^{+} + Cl^{-}$$

Since a variety of reference electrodes are in use, all are measured against the standard hydrogen electrode (SHE) for purposes of comparison. The silver chloride reference electrode used in this work used a 3 M KCl solution as an electrolyte and had a potential of 0.21 V vs. SHE.

3.5. References

*****1. Amblard, M., Fehrentz, J.-A., Martinez, J. & Subra, G. Methods and protocols of modern solid phase peptide synthesis. *Mol. Biotechnol.* **33,** 239–54 (2006).

2. Merrifield, R. B. Solid Phase Peptide Synthesis. I. The Synthesis of a Tetrapeptide. *J. Am. Chem. Soc.* **85,** 2149 (1963).

3. Mant, C. T. *et al.* in *Methods in Molecular Biology, vol. 386: Peptide Characterization and Application Protocols* (ed. Fields, G.) 3–55 (Human Press, 2007). doi:10.1007/978-1-59745-430-8

4. Knochenmuss, R. Ion formation mechanisms in UV-MALDI. *Analyst* **131,** 966 (2006).

5. Hillenkamp, F., Karas, M., Beavis, R. C. & Chait, B. T. Matrix-assisted laser desorption/ionization mass spectrometry of biopolymers. *Anal. Chem.* **63,** 1193A–

1203A (1991).

*6. Kelly, S. M., Jess, T. J. & Price, N. C. How to study proteins by circular dichroism. *Biochim. Biophys. Acta* **1751,** 119–139 (2005).

7. Rodger, A. & Nordén, B. *Circular Dichroism & Linear Dichroism*. (Oxford University Press, 1997).

8. Velluz, L., Legrand, M. & Grosjean, M. *Optical Circular Dichroism: Principles, Measurements, and Applications*. (Academic Press, 1965).

9. Drake, A. F. Circular Dichroism. *Methods Mol. Biol.* **22,** 219 (1994).

10. Cooper, T. M. & Woody, R. W. The effect of conformation on the CD of interacting helices: a theoretical study of tropomyosin. *Biopolymers* **30,** 657–76 (1990).

11. Dutta, K., Alexandrov, A., Huang, H. E. & Pascal, S. M. pH-induced folding of an apoptotic coiled coil. *Protein Sci.* **10,** 2531–2540 (2001).

12. Zhou, N. E., Kay, C. M. & Hodges, R. S. The role of interhelical ionic interactions in controlling protein folding and stability. De novo designed synthetic two-stranded alpha-helical coiled-coils. *J. Mol. Biol.* **237,** 500–12 (1994).

13. Quistgaard, E. M. *et al.* Structural and biophysical characterization of the cytoplasmic domains of human BAP29 and BAP31. *PLoS One* **8,** e71111 (2013).

14. Arnold, G. E., Day, L. a & Dunker, a K. Tryptophan contributions to the unusual circular dichroism of fd bacteriophage. *Biochemistry* **31,** 7948–56 (1992).

15. Taira, J., Jelokhani-Niaraki, M., Osada, S., Kato, F. & Kodama, H. Ion-channel formation assisted by electrostatic interhelical interactions in covalently dimerized amphiphilic helical peptides. *Biochemistry* **47,** 3705–14 (2008).

16. Gaspar, D. *et al.* A biophysical approach to phospholipase A2 activity and inhibition by anti-inflammatory drugs. *Biophys. Chem.* **152,** 109–17 (2010).

17. Marshall, C. B., Chakrabartty, A. & Davies, P. L. Hyperactive antifreeze protein from winter flounder is a very long rod-like dimer of alpha-helices. *J. Biol. Chem.* **280,** 17920–9 (2005).

18. Muhle-Goll, C. *et al.* The dimerization stability of the HLH-LZ transcription protein family is modulated by the leucine zippers: a CD and NMR study of TFEB and c-Myc. *Biochemistry* **33,** 11296–11306 (1994).

19. Lavigne, P. *et al.* Preferential heterodimeric parallel coiled-coil formation by synthetic Max and c-Myc leucine zippers: a description of putative electrostatic interactions responsible for the specificity of heterodimerization. *J. Mol. Biol.* 505–520 (1995). doi:10.1006/jmbi.1995.0634

20. Help Online - Origin Help - Fit Sigmoidal. Available at: http://www.originlab.com/doc/Origin-Help/Fitting-Sigmoidal. (Accessed: 20th February 2017)

21. Tunis-Schneider, M. J. B. & Maestre, M. F. Circular Dichroism Spectra of Oriented and Unoriented Deoriyribonucleic Acid Films- A Preliminary Study. *J. Mol. Biol.* **52,** 521–541 (1970).
22. Cornell, D. G. Circular Dichroism of Polypeptide Monolayers. *J. Colloid Interface Sci.* **70,** 167–180 (1979).
23. Olah, G. A. & Huang, H. W. Circular dichroism of oriented α helices . I . Proof of the exciton theory. *J. Chem. Phys.* **89,** 2531–2538 (1988).
24. Norden, B. Linear and Circular Dichroism of Polymeric Pseudoisocyanine. *J. Phys. Chem.* **81,** 151–159 (1977).
25. Jensen, H. P., Schellman, J. A. & Troxell, T. Modulation Techniques in Polarization Spectroscopy. *Appl. Spectrosc.* **32,** 192–200 (1978).
26. Shindo, Y. & Nishio, M. The Effect of linear Anisotropies on the CD Spectrum : Is It True That the Oriented Polyvinyalcohol Film Has a Magic Chiral Domain Inducing Optical Activity in Achiral Molecules ? *Biopolymers* **30,** 25–31 (1990).
27. Shindo, Y. & Ohmi, Y. Problems of CD Spectrometers. 3. Critical Comments on Liquid Crystal Induced Circular Dichroism. *J. Am. Chem. Soc.* **107,** 91–97 (1985).
*28. McMillin, C. R. & Walton, A. G. A Circular Dichroism Technique for the Study of Adsorbed Protein Structure. *J. Colloid Interface Sci.* **48,** 345–9 (1974).
29. Blondelle, S. E., Ostresh, J. M., Houghten, R. A. & Pérez-Payá, E. Induced conformational states of amphipathic peptides in aqueous/lipid environments. *Biophys. J.* **68,** 351–9 (1995).
30. Vermeer, A. W. P. & Norde, W. CD Spectroscopy of Proteins Adsorbed at Flat Hydrophilic Quartz and Hydrophobic Teflon Surfaces. *J. Colloid Interface Sci.* **397,** 394–397 (2000).
31. Fears, K. P. & Latour, R. A. Assessing the Influence of Adsorbed-State Conformation on the Bioactivity of Adsorbed Enzyme Layers. *Langmuir* **25,** 13926–33 (2009).
32. Hylton, D. M., Shalaby, S. W. & Latour, R. A. Direct correlation between adsorption-induced changes in protein structure and platelet adhesion. *J. Biomed. Mater. Res. A* **73,** 349–58 (2005).
33. Gallardo, I. F. & Webb, L. J. Demonstration of α-Helical Structure of Peptides Tethered to Gold Surfaces Using Surface Infrared and Circular Dichroic Spectroscopies. *Langmuir* **28,** 3510–5 (2012).
34. Smith, L. J. & Clark, D. C. Measurement of the secondary structure of adsorbed protein by circular dichroism. 1. Measurements of the helix content of adsorbed melittin. *Biochim. Biophys. Acta* **1121,** 111–118 (1992).
35. Rodger, A. Personal Communication. (2012).
36. Forster, T. Energiewanderung und Fluoreszenz. *Naturwissenschaften* **33,** 166–175

(1946).

*37. Song, Y., Rodgers, V. G. J., Schultz, J. S. & Liao, J. Protein interaction affinity determination by quantitative FRET technology. *Biotechnol. Bioeng.* **109,** 2875–83 (2012).

38. Minsky, M. Microscopy Apparatus. *US Patent 3013467* (1957).

39. Minsky, M. Memoir on inventing the confocal scanning microscope. *Scanning* **10,** 128–138 (1988).

40. Pockrand, I., Swalen, J. D., Gordon, J. G. & Philpott, M. R. Surface plasmon spectroscopy of organic monolayer assemblies. *Surf. Sci.* **74,** 237–244 (1978).

41. Nguyen, H., Park, J., Kang, S. & Kim, M. Surface Plasmon Resonance: A Versatile Technique for Biosensor Applications. *Sensors* **15,** 10481–10510 (2015).

42. Gill SC, V. H. P. Calculation of protein extinction coefficients from amino acid sequence data. *Anal Biochem.* **1;182(2),** 319–26. (1989).

43. Hamann, C. H., Hamnett, A. & Vielstich, W. *Electrochemistry*. (Wiley-VCH, 2007).

4. Peptide design, synthesis, and solution characterisation

4.1. Introduction

The purpose of the experiments detailed in this section was to design and synthesise a coiled coil heterodimer system with pH dependent binding. The pH dependence was intended to enable the peptide interactions to be electronically controlled by electrochemical pH change (described in Section 2.3). Although the critical information for electronic control of the peptide interactions was the pH dependence of the interactions when the peptides were immobilised on a surface, their pH dependence in solution was studied for comparison, and the results are presented in this chapter. Experiments to determine surface pH dependence are reported in Chapter 5 and the relation of surface pH dependence to the solution pH dependence is discussed there.

This chapter details the design of the synthetic peptides used in this work, as well as their synthesis and characterisation in solution. The materials and methods used are described in detail in Section 4.2. Characterisation of the peptide purity and mass was performed by reverse-phase HPLC (see Section 3.1.2) and MALDI-TOF mass spectrometry (see Section 3.1.3). Characterisation of peptide interactions in solution and their dependence on pH was performed by CD spectroscopy (see Section 3.2.1) and FRET spectroscopy (see Section 3.2.2). The results of these experiments are presented and discussed in Section 4.3. The findings are summarised in Section 4.4 and references are detailed in Section 4.5.

Peptide synthesis, purification and some CD measurements in this chapter were performed in the Woolfson Laboratory at the University of Bristol with the assistance of Dr. Franziska Thomas. Some CD measurements were performed at the Diamond Light Source with the assistance of Dr. Simon White and Dr. Steven Johnson. The peptides K4, K4-L, E4P and E4P-L were synthesised entirely by Dr. Thomas, and purified by the author. The peptides K4C, K4C-L, E4 and E4-L were jointly synthesised and purified. Mass spectrometry was performed by Dr. Thomas with the author's assistance in sample preparation.

4.2. Materials and methods

4.2.1. Peptide synthesis and labelling

Peptides were synthesised from the C to N-terminal on an H-Rink Amide Chemmatrix resin in dimethylformamide (DMF) using a CEM Liberty Blue microwave assisted peptide synthesizer. Fmoc (9-fluorenylmethoxycarbonyl) was used as the transient protecting group for all residues. Glutamic acid side chains were protected with *t*-Bu (*tert*-butyl) groups. Lysine and tryptophan side chains were protected with *t*-Boc (*tert*-butoxycarbonyl) groups. The second heptad f-position lysine side chain, the intended label position, was protected with an Alloc (allyloxycarbonyl) group. Asparagine side chains were protected with triphenylmethyl (Trt) groups. Piperidine was used for Fmoc deprotection and 1 M diisopropylcarbodiimide (DIC) for

carboxyl group activation (see Section 3.2.1), with 0.5 M 1-hydroxy-benzotriazole (HOBt) to prevent racemisation. Acetylation of the N-terminal was performed with a 1:9 ratio of acetic acid anhydride:pyridine.

For fluorescent labelling, Alloc deprotection was performed with 2 mM phenylsilane in degassed dichloromethane (DCM) with 100 μM $Pd(PPh_3)_4$ as a scavenger. 2.5 mg of the fluorescent dye was dissolved in 600 μL 6 μM N,N-Diisopropylethylamine (DIPEA) then added to 40 mg peptide resin and incubated overnight in darkness. The resin was then washed with DMF and DCM before peptide cleavage.

To cleave the peptides from the resin, the resin was incubated for 3 hours in a 90:5:5 ratio of trifluoroacetic acid (TFA):triisopropylsilane:water. TFA was then removed from the filtered peptide extract under nitrogen flow and the remaining extract was suspended in 40 mL chilled diethyl ether then centrifuged to isolate the peptides. Diethyl ether was decanted and the precipitate dissolved in a 5 mL 1:1 ratio of acetonitrile:water and then lyophilised.

4.2.2. Peptide purification

Reverse-phase HPLC purification of synthesised peptides was performed using a Phenomenex Luna column (5 μM, 150 x 10 mm). Table 1 gives the compositions of the buffers used.

Buffer	Composition
A	0.1% TFA in water
B	0.1% TFA in acetonitrile
C	20 mM triethylamine and 20 mM acetic acid in water, pH 9.5
D	1% Buffer C in acetonitrile

Table 4.1: Buffers used for peptide purification.

K4 peptides and variants were purified in Buffer A using a gradient of 10-50% Buffer B over 30 minutes. E4 and E4-L were purified in Buffer C using a gradient of 15-45% Buffer D over 30 minutes. E4P and E4P-L were purified in Buffer A using a gradient of 20-60% Buffer B over 30 minutes. The use of basic buffer system C and D for E4 and E4-L was necessary to ensure the optimal ionisation state of these peptides during the purification and hence optimise the retention time.

Characterisation was performed by analytical HPLC using a Jasco chromatography system with a Phenomenex Kinetex column (5 μM, 100 x 4.6 mm) for Buffer A and Buffer B, and a Grace Vydac 214TP C8 column (5 μM, 250 x 4.6 mm) for Buffer C and Buffer D. K4 peptides and variants were characterised in Buffer A using a gradient of 10-70 % Buffer B over 20 minutes. E4 and E4-L were characterised in Buffer C using a gradient of 10-60 % Buffer D over 20 minutes. E4P and E4P-L were characterised in Buffer A using a gradient of 20-80 % Buffer B over 20 minutes.

4.2.3. Mass spectrometry

Mass spectrometry was performed on an Applied Biosystems 4700 Proteomics Analyzer MALDI-TOF instrument using an α-cyano-4-hydroxycinnamic acid (CHCA) matrix.

4.2.4. Peptide concentration determination

Peptide concentrations were determined by measuring absorbance at 280 nm using a Thermo Scientific NanoDrop 2000 UV-Vis spectrophotometer and calculating the concentration using Beer's Law (see Section 3.2.6). Labelled peptide absorbances were corrected by subtracting a correction factor to remove the contribution of the dye to the 280 nm absorbance. In the case of ATTO 488, which was used for K4-L and K4C-L, the correction factor was 0.1 times the absorbance at 498 nm, and in the case of ATTO 594, used for E4-L and E4P-L, the correction factor was 0.51 times the absorbance at 601 nm. Correction factors were obtained from the manufacturer.[1]

4.2.5. CD measurements

CD measurements in the Woolfson Laboratory were performed on a JASCO J-810 spectropolarimeter fitted with a Peltier temperature controller. 100 μM total peptide concentration was used in 50 mM sodium phosphate buffer at pH 7.5 with 5 mM NaCl. Spectra were taken at 50 nm min^{-1} scanning speed at 20 °C in 1 mm path length quartz cuvettes from Starna Scientific. Melting curves were obtained by heating from 5 °C to 90 °C at a rate of 40 °C h^{-1} with the signal at 222 nm measured at 1 °C intervals. The melting temperatures (T_m) were determined by finding the minima of the second derivatives of the 222 nm CD vs. temperature curves.

CD measurements at the Diamond Light Source B23 Synchrotron Radiation CD Beamline were performed on a nitrogen-flushed Module X end-station spectrophotometer fitted with a Peltier temperature controller. All measurements used 30 μM total peptide concentration in 50 mM sodium phosphate buffer. Spectra were taken from 180-260 nm in 0.5 mm path length quartz cuvettes from Starna Scientific, with bandwidth 1 nm and 1 s scan time per 1 nm step. Melting curves were obtained by heating from 5 °C to 90 °C with spectra taken at 5 °C intervals. Three scans were taken and averaged at each temperature. The 222 nm CD data were plotted against temperature and standard dose-response curves were fitted to the data using OriginPro 8.5.1. Melting temperatures were determined by finding the zero of the second derivatives of the fitted 222 nm CD vs. temperature curves. Melting temperatures were also calculated from the 193 nm CD signals but showed no significant difference to those derived from the 222 nm signals, so they have not been included below.

All other CD measurements were performed on an Applied Photophysics Chirascan CD spectrometer fitted with a Peltier temperature controller, using 30 μM total peptide concentration in 50 mM sodium phosphate buffer. Spectra were taken from 180-300 nm in 1 mm path length quartz cuvettes from Starna Scientific, with bandwidth 2.5 nm and 0.5 s scan time per 1 nm step. Melting curves were obtained by heating from 5 °C to 90 °C with spectra taken at 5 °C intervals. The melting temperatures were determined as above.

4.2.6. FRET measurements

FRET measurements were performed using a Shimadzu RF-5301PC spectrofluorophotometer. For initial experiments, a solution of 2 μM K4C-L in 150 mM NaCl was used with 3 mM dithiothreitol (DTT) as a reducing agent to prevent the formation of disulphide bonds between the peptides, and 0.05% Tween-20 detergent to prevent the peptide sticking to surfaces. For each pH a solution of E4-L in 10 mM phosphate buffer, 150 mM NaCl and 0.05% Tween-20 at the appropriate pH was created and serially diluted to give a range of concentrations. Each concentration of E4-L was then mixed with an equal volume of 150 mM NaCl with 3 mM DTT and 0.05% Tween-20 (giving a final concentration of 5 mM phosphate buffer, 150 mM NaCl and 0.05% Tween-20) and immediately measured with an excitation of 501 nm (which is the excitation wavelength of ATTO 488, the donor dye) to obtain the emission spectra of the acceptor dye at this wavelength. Next, an equal volume of the K4C-L solution was mixed with the E4-L for that concentration value (giving a final concentration of 1 μM K4C-L, 5 mM phosphate buffer, 150 mM NaCl and 0.05% Tween-20) and immediately measured with an excitation of 501 nm.

For later experiments with reduced salt and higher buffer strength the K4C-L solution instead contained 10 mM NaCl and the E4-L solutions were in 50 mM phosphate buffer, giving a final concentration of 1 μM K4C-L, 50 mM phosphate buffer, 5 mM NaCl and 0.05% Tween-20. The reasons for the change in conditions are given below.

To give the peptides time to form dimers and equilibrate, measurement was continuously performed for 15 minutes, resulting in 20 spectra for each concentration value. In all cases, equilibrium was reached after 10 spectra, so the final 10 spectra were averaged and used for K_d determination (see below).

To determine a K_d for each pH, the 627 nm emission intensity for the E4-L solution was subtracted from the 627 nm emission intensity for the mixed E4-L+K4C-L solution for each E4-L concentration value and then the corrected intensities were plotted against E4-L concentration to give a binding curve. To determine the K_d, these curves were then fitted in OriginPro 8.5.1 using Equation 1 from Section 3.3.2.

4.3. Results and discussion

4.3.1. Peptide design

Using the CC-A_N^4 and CC-B_N^4 peptides designed by Thomas *et al*[2] as a starting point, a new set of peptides was designed with a number of variants of two core peptides, called E4 and K4. The primary objective was to produce a pair of coiled coil forming peptides where heterodimer formation was dependent on pH. The primary sequences of the peptides described in this section are given in Table 4.2.

E4 was based on CC-A_N^4. Preliminary experiments with CC-A_N^4 showed that it was insoluble in phosphate buffer below pH 5. Consequently, the *f* position glutamines (Q) in the first, second and fourth heptads were replaced with lysines (K). Adding charged lysine side chains in the exterior *f* positions was intended to increase solubility. Unfortunately, the solubility was not significantly improved by these changes, see below.

E4P was designed to be used as a control peptide which would not form a coiled coil despite having an almost identical primary sequence to E4. The sequence was identical to E4 with the exception of the *d* position in the second heptad, where a leucine (L) was replaced by a proline (P). Proline residues are known to prevent coiled coil formation, see Section 2.3.1, and the placement of the proline residue in this central core position was intended to maximise coil disruption with minimal change to the charge and hydrophobicity of the peptide. In order to be able to carry out FRET experiments, see Section 3.3.2, labelled variants of E4 and E4P were also designed and designated E4-L and E4P-L respectively. In both cases, the second heptad *f* position lysine was labelled with the fluorescent dye ATTO 594. FRET relies on the proximity of dye molecules so the second heptad was chosen as the location for the dye since central heptads should be more tightly bound in a coiled coil and thus less susceptible to random thermally-induced dissociation that would lead to fluctuations in FRET signal. The solvent exposed *f* position was chosen as the dye location since this is the furthest position from the tightly packed hydrophobic core, thereby minimising any dye-induced disruption to coil formation.

K4 was based on CC-B_N^4. To facilitate the formation of self-assembled monolayers a short flexible sequence of glycine and serine residues terminating in a cysteine residue (GGSC) was added at the C terminal to create the variant K4C. For consistency, the sequence GGS was therefore added to K4.

In order for the labelled variants K4-L and K4C-L to have dye molecules as close as possible to the dye on E4-L peptides when heterodimers were formed, the second heptad *f* position tyrosine (Y) was moved to the third heptad *f* position and replaced by a lysine (K) in the second heptad, to which the dye was attached. This was important to preserve the optical activity of the tyrosine (see Section 3.2.6) and this change was therefore made to the unlabelled K4 and K4C as

			Heptad 1							Heptad 2							Heptad 3							Heptad 4										
			a	*b*	*c*	*d*	*e*	*f*	*g*	*a*	*b*	*c*	*d*	*e*	*f*	*g*	*a*	*b*	*c*	*d*	*e*	*f*	*g*	*a*	*b*	*c*	*d*	*e*	*f*	*g*				
CC-A_N^4	G	E	I	A	A	L	E	Q	E	I	A	A	L	E	K	E	N	A	A	L	E	W	E	I	A	A	L	E	Q	G	G			
E4	G	E	I	A	A	L	E	K	E	I	A	A	L	E	K*	E	N	A	A	L	E	W	E	I	A	A	L	E	Q	G	G			
E4P	G	E	I	A	A	L	E	K	E	I	A	A	P	E	K*	E	N	A	A	L	E	W	E	I	A	A	L	E	Q	G	G			
CC-B_N^4	G	K	I	A	A	L	K	Q	K	I	A	A	L	K	Y	K	N	A	A	L	K	K	K	I	A	A	L	E	K	G	G			
K4	G	K	I	A	A	L	K	Q	K	I	A	A	L	K	K*	K	N	A	A	L	K	Y	K	I	A	A	L	E	K	G	G	G	S	
K4C	G	K	I	A	A	L	K	Q	K	I	A	A	L	K	K*	K	N	A	A	L	K	Y	K	I	A	A	L	E	K	G	G	G	S	C

Table 4.2: Primary sequences of peptides used in this work. Asterisks indicate the positions at which fluorescent dyes were added to create labelled variants.

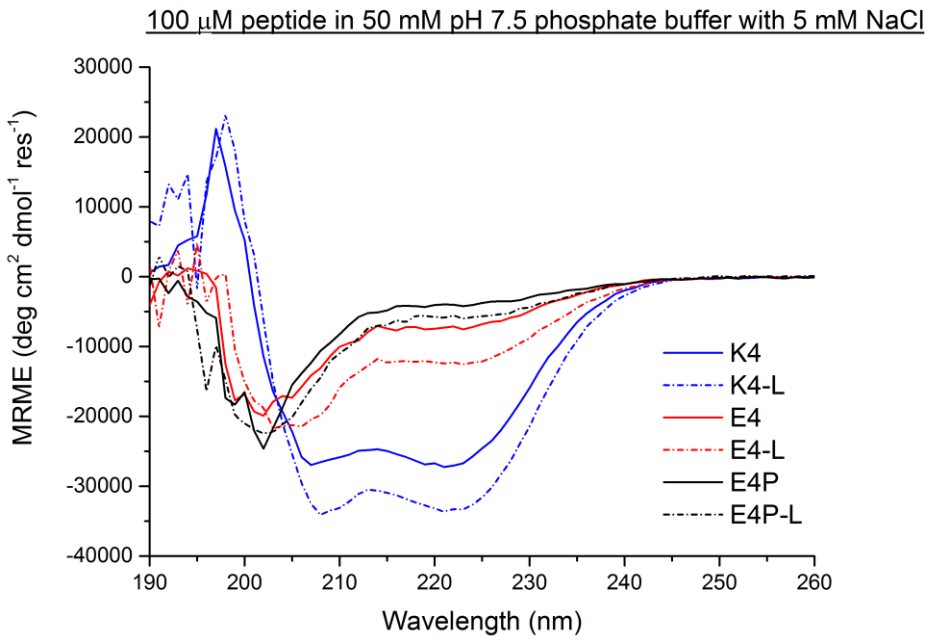

Figure 4.1: CD spectra for individual unlabelled (solid lines) and labelled (dashed lines) peptides at 100 μM concentration in 50 mM pH 7.5 phosphate buffer with 5 mM NaCl. K4 appeared to form coiled coil homodimers under these conditions whereas E4 and E4P showed little evidence of coil formation. In all cases the signal was higher for the labelled peptides.

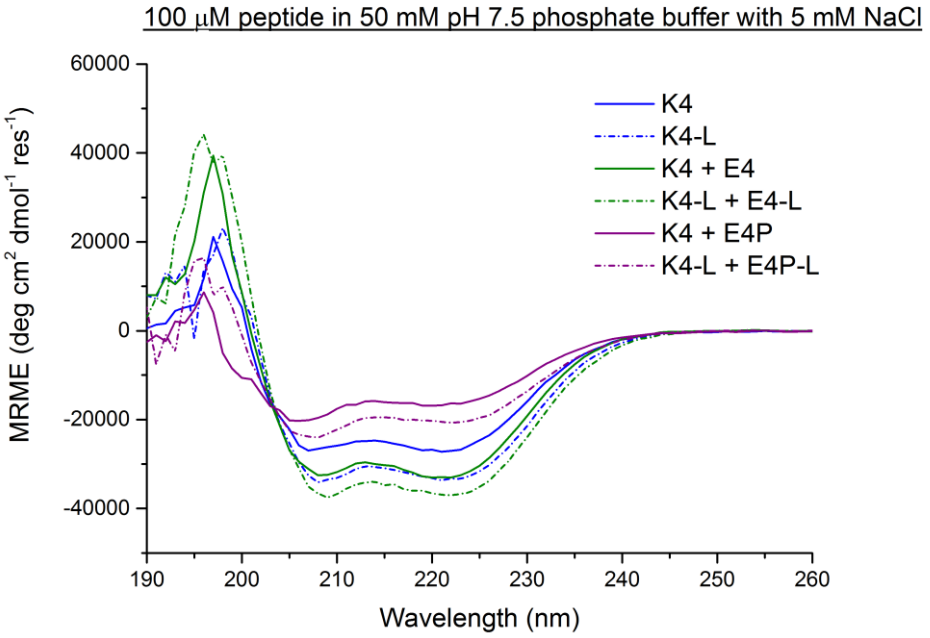

Figure 4.2: CD spectra for unlabelled (solid lines) and labelled (dashed lines) peptides at 100 μM concentration in 50 mM pH 7.5 phosphate buffer with 5 mM NaCl. K4 spectra are identical to those from Figure 4.1 and are included for comparison. The mix of K4+E4P was less helical than K4, which was less helical than the mix of K4+E4. In all cases the signal was higher for the labelled peptides.

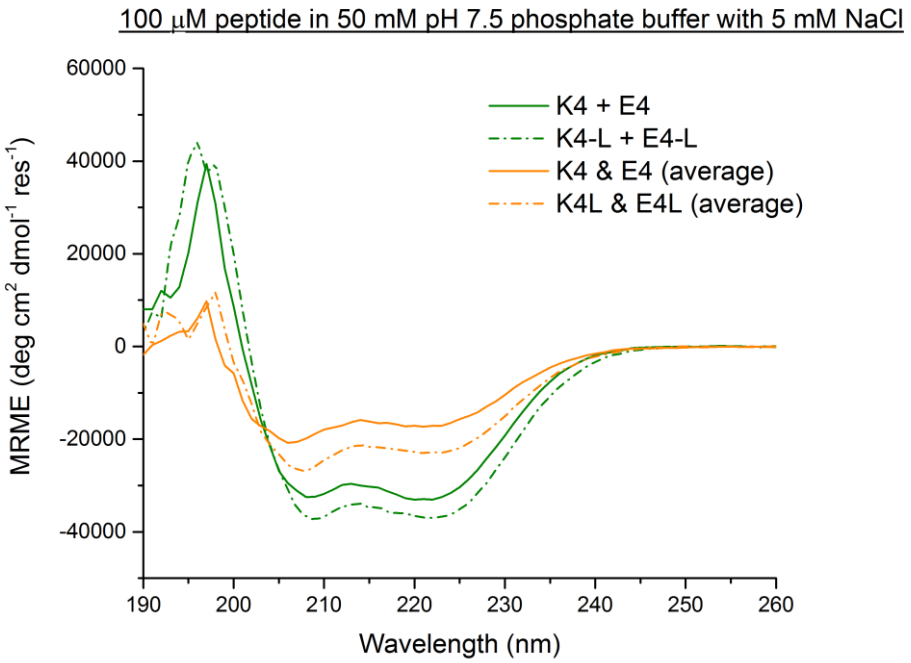

Figure 4.3: CD spectra for unlabelled (solid lines) and labelled (dashed lines) peptides at 100 μM concentration in 50 mM pH 7.5 phosphate buffer with 5 mM NaCl. K4 + E4 and K4-L + E4-L spectra are identical to those from Figure 4.2. The K4 & E4 and K4-L & E4-L spectra are mathematical averages of the K4 and E4 spectra and K4-L and E4-L spectra from Figure 4.1 respectively. The difference between the averaged spectra of the individual and the observed spectra for the mixed peptides indicated that the mixed peptides interacted with each other.

well for consistency. The dye used for K4-L and K4C-L was ATTO 488, which is a FRET partner to ATTO 594 with a Förster radius of 5.7 nm.[3]

4.3.2. Peptide synthesis

All peptide variants were synthesised, labelled and purified successfully, as confirmed by HPLC and mass spectrometry, see Figures A3.2 and A3.3 in Appendix A3. Small peaks can be seen at the start and/or end of some of the HPLC traces, but these did not indicate purified peptide product and were not collected. In all cases a pure product was obtained with the correct mass, though fragmentation of the flurophore was observed in the mass spectra for E4-L and E4P-L. Unfortunately the solubility of E4 and variants at low pH was not noticeably greater than that of CC-B_N[4] and so pH 5 is the most acidic pH value used in this work since it is the lowest pH at which E4 could be dissolved.

4.3.3. CD measurements

CD measurements at pH 7.5 and 100 μM concentration were performed for K4, E4, E4P and for the combinations E4+K4 and E4P+K4 with both labelled and unlabelled variants. Measurements of individual variants were performed to determine the propensity of the peptides to form homodimers. Figure 4.1 shows that E4 and E4P had no alpha helical structure, whether labelled or not, and so it was concluded that they did not form homodimers at pH 7.5. In contrast,

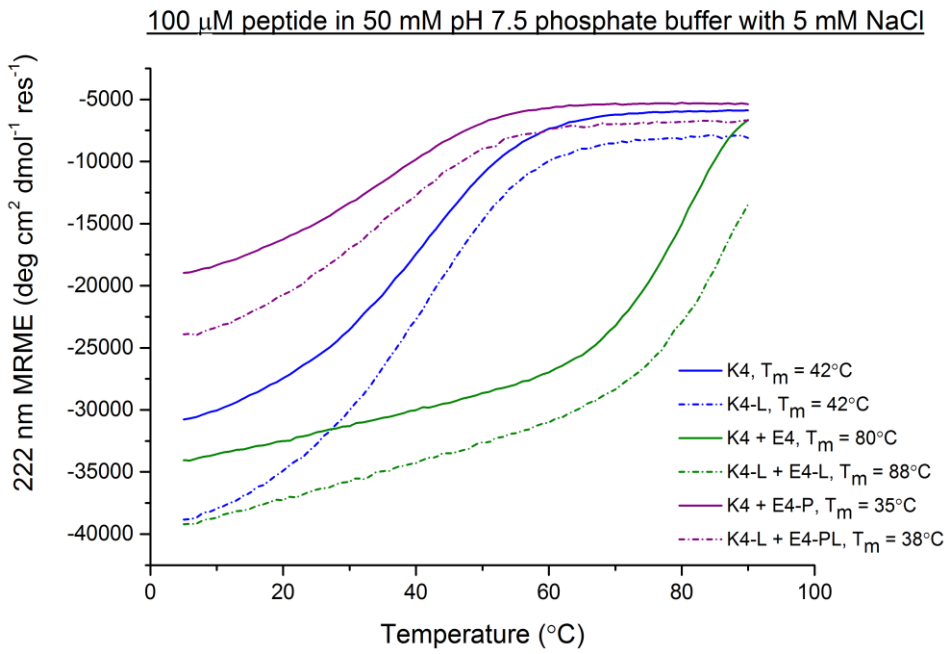

Figure 4.4: CD melting curves for unlabelled (solid lines) and labelled (dashed lines) peptides at 100 μM concentration in 50 mM pH 7.5 phosphate buffer with 5 mM NaCl. Melting temperatures were calculated from the second derivatives of fits to the curves (not shown). The similar melting temperatures for K4 and the mix of K4+E4P implies that the helical content seen in the spectra for K4+E4P came from K4 homodimers. The melting temperature for K4+E4 was significantly higher than for K4, implying that heterodimers were preferentially formed in the mixed case. Melting temperatures for the labelled peptides were the same or slightly higher than for the unlabelled peptides in all cases.

K4 and K4-L did appear to form homodimers at pH 7.5. In all cases, the signal for the labelled peptides was more intense. The reason for this could not be concluded from the CD spectra: it might have been that the dyes themselves exhibited CD at the measured wavelengths, or it might be that the presence of the dyes increased the tendency of the peptides to form alpha helical structures and/or coiled coils. Later results suggested the latter reason, see below.

The existence of K4 homodimers at pH 7.5 made the analysis of the results for mixed peptides more difficult. The spectra are shown in Figure 4.2, along with the spectra for K4 and K4-L for comparison. It can be seen that the mixture of E4P+K4 contained significantly less helical structure than K4 by itself and so it was concluded that E4P did not form heterodimers with K4 and that the helical structure observed was primarily from K4 homodimers. Subtracting the 222 nm CD ($\theta_{222} = -4000$ deg cm^2 dmol res^{-1}) for the E4P solution, where no alpha helical content was seen, from the 222 nm CD for the E4P+K4 and K4 solutions yielded $\theta_{222} = -12340$ deg cm^2 dmol res^{-1} and $\theta_{222} = -23050$ deg cm^2 dmol res^{-1} respectively. Since the K4 solution contained twice as much K4 as the E4P+K4 solution, this doubling in signal is exactly what would have been expected if E4P and K4 did not form heterodimers.

Comparing the K4 and E4+K4 spectra in Figure 4.2 it can be seen that the E4+K4 spectrum had significantly higher alpha helical content and so it was concluded that E4+K4 heterodimers were formed in preference to K4 homodimers. Figure 4.3 shows that the mathematical average of the individual K4 and E4 solutions produced spectra with lower alpha

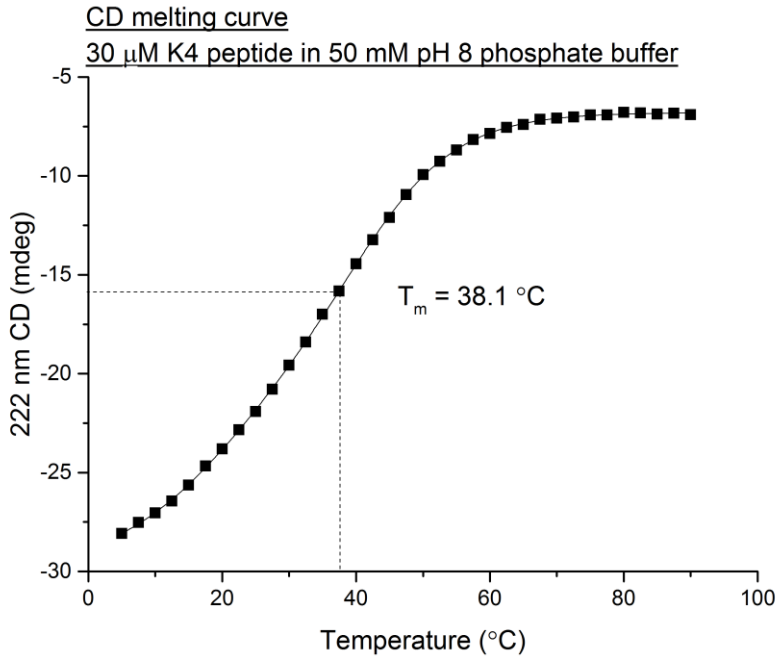

Figure 4.5: Melting curve for 30 μM K4 peptide in 50 mM pH 8 phosphate buffer, with dotted lines indicating the melting temperature.

helical content than the observed spectra for the mixed solution of K4+E4, which indicated that there was an interaction between the two peptides. The same conclusions applied to the labelled peptides, though the alpha helical signal was more intense than for the unlabelled equivalent in each case. The data are noisy below ~ 200 nm because of high buffer absorbance at these wavelengths. High voltage (HV) data for the measurements shown in Figures 4.1 and 4.2, indicating the voltage applied to the photomultiplier tubes, can be found in Appendix Section A3.1.

To assess the strength of coiled coil binding, the peptide solutions were heated until the coils dissociated, and a melting temperature (T_m) was obtained, as described above, by measuring the 222 nm CD as the temperature increased. The results for 100 μM peptide concentration at pH 7.5 are shown in Figure 4.4. It can be seen that the E4P+K4 mixture had the lowest melting temperature at 35 ºC and that the K4 homodimers had a similar melting temperature of 42 ºC. From this it can be concluded that the melting species in the E4P+K4 mixture was likely to have been K4 homodimers and this was further evidence that the helical structure seen in the CD spectrum for E4P+K4 in Figure 4.4 was caused by K4 homodimers. The E4+K4 mixture had a melting temperature of 80 ºC, which was approximately twice the melting temperature of the K4 and E4P+K4 solutions. This suggested that strongly bound heterodimers dominated the E4+K4 mixture at pH 7.5. The melting temperatures of the labelled peptides were higher than their unlabelled versions in the cases of E4-L+K4-L and E4P-L+K4-L, which suggested that the more intense CD spectra seen for the labelled peptides was caused by an increased tendency for coiled coil formation rather than any CD signal from the dye molecules themselves.

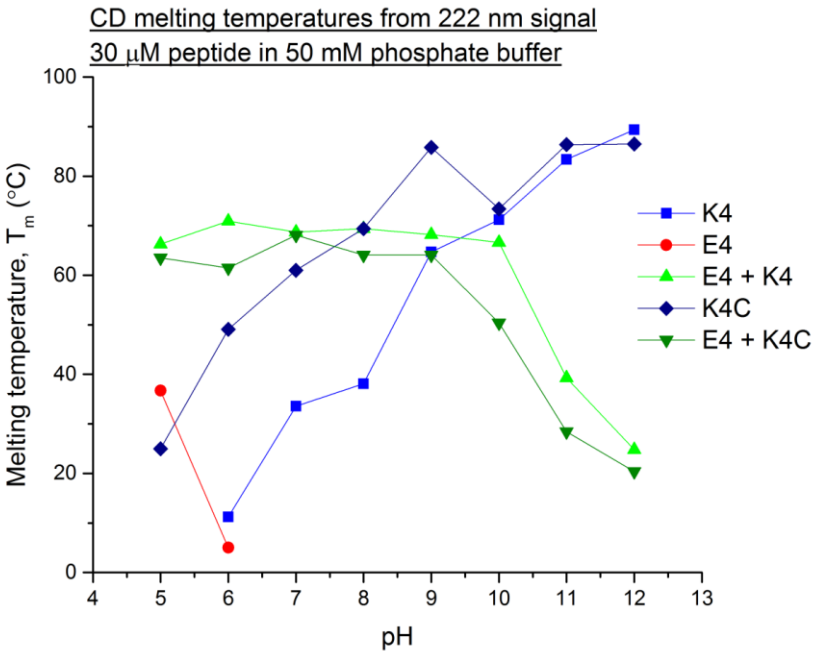

Figure 4.6: Summary of the melting temperatures obtained by CD for 30 μM peptide in 50 mM phosphate buffer over the pH range 5-12. Melting temperatures for E4 above pH 6 and K4 at pH 5 were below 5 ºC and so could not be calculated from this temperature range. K4C homodimers were significantly more stable than K4 homodimers because of the presence of a disulphide bond between the cysteine residues. In contrast, the mixtures of E4+K4 and E4+K4C showed little difference in melting temperature until pH 10.

To assess how homodimer and heterodimer formation varied with pH, melting curves were obtained for E4, K4, K4C, E4+K4 and E4+K4C over the pH range 5-12. In these experiments the peptide concentration was lowered to preserve material and complete CD spectra were taken for each temperature rather than just a measurement at 222 nm as in Figure 4.4. The lowered peptide concentration may explain the slightly lower melting temperatures for K4 and E4+K4 seen in Figure 4.6 at pH 7.5 as compared to Figure 4.4. It has been shown previously that increased peptide concentration can lead to an increase in coiled coil formation.[4] As an example of the experiments performed, the CD spectra taken during the melting experiment for E4+K4 at pH 8 is shown in Figure A3.4 in Appendix A3, and the 222 nm signal plotted as a function of temperature and the fitted curve are shown in Figure 4.5. A summary of the measured melting temperatures for all the peptides and mixtures is shown in Figure 4.6. Some E4 homodimer formation was evident at pH 5, but since the melting temperature had dropped to ~ 5 ºC at pH 6, E4 was not assessed at any higher pH values.

The melting temperature for K4 homodimers was less than 5 ºC at pH 5 and increased steadily to 89 ºC at pH 12. The sharp increase at pH 9 may indicate that the pK_a (i.e. the pH at which half the side chains are protonated) of the *e* and *g* position lysines was between pH 8 and 9, such that at pH 8 the majority of lysines were protonated and electrostatic repulsion hindered the formation of coiled coils whereas at pH 9 the majority of the lysines were deprotonated and the electrostatic repulsion became negligible, leading to significantly stronger coiled coils. Note that the pK_a of an isolated lysine side chain is known to be pH 10.67, but it is well established

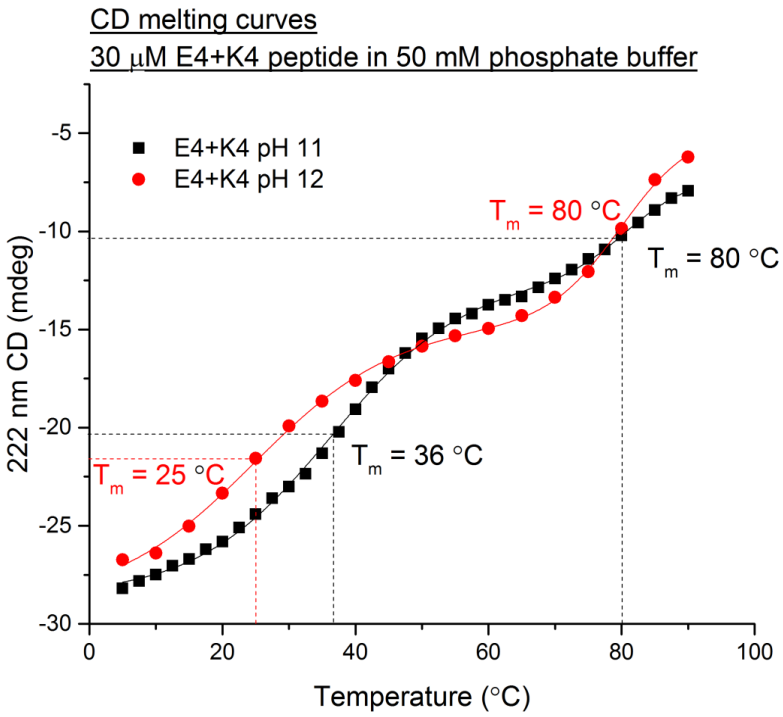

Figure 4.7: CD melting curves for E4+K4 mixtures at pH 11 and pH 12, showing evidence of two melting species per curve. Since the higher melting temperatures compared well to the melting temperatures for K4 homodimers, it was assumed that the higher melting temperature was for K4 homodimers in the mixture while the lower melting temperature was for heterodimers.

that the pK_a can vary in the context of an actual peptide because of the effects of the peptide conformation and neighbouring side chains etc.[5–7]

By comparing the K4 melting temperatures to those for K4C a significant increase in homodimer stability afforded by the disulphide bonded cysteines of the K4C dimers can be seen. It is known that disulphide bonds can significantly increase the stability of coiled coils (see Section 2.3.1). It can be seen from Figure 4.6 that at pH 5 the K4C homodimers had a melting temperature of 25 ºC, meaning that at room temperature K4C formed homodimers an entire pH point before K4 homodimers. The significant increase in melting temperature over K4 homodimers continued until pH 10 and above, at which point the melting temperatures were very similar. This implied that the disulphide bond conferred no additional stability once the lysines had deprotonated and removed the electrostatic barrier to coiled coil formation. Alternatively, it has been shown that strongly alkaline conditions can break disulphide bonds,[8,9] so it may be that there was no difference in melting temperature between K4 and K4C at pH > 10 because the disulphide bonds were broken (and note that this the breaking of the bonds was increasingly likely at the high melting temperatures measured at these pH values). Indeed, this may explain the decrease in melting temperature seen at pH 10, assuming that this melting temperature was not an error. A repeat of the pH 9 K4C melting temperature measurement showed a difference of ~ 0.1 ºC, so this data point appears to be reliable, but the pH 10 K4C melting temperature

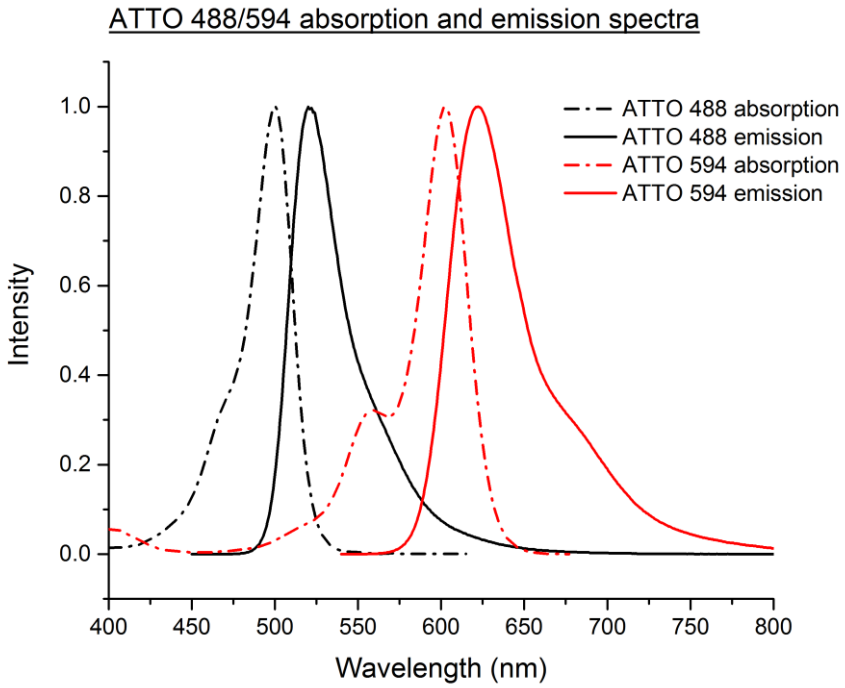

Figure 4.8: Absorption spectra (dashed lines) and emission spectra (solid lines) for ATTO 488 (black) and ATTO 594 (red). Data obtained from manufacturer.[1]

measurement was not repeated, so the decrease in melting temperature from pH 9 to pH 10 for K4C may be an error.

For the mixture of E4+K4 it can be seen that the melting temperature was stable across the pH range 5-10; and remained in the range ~ 60-70 ºC for all pH values in this range. The stability of the melting temperature suggested that heterodimers dominated the mixture until pH 10, where the melting temperature of K4 homodimers exceeded the melting temperature of the E4+K4 mixture. Therefore it is likely that at pH 10 K4 homodimers were the dominant species. At pH 11 and 12 the melting curves showed evidence of two distinct melting temperatures, see Figure 4.7. The higher melting temperature of ~ 80 ºC for both pH 11 and 12 was assumed to correspond to the K4 homodimer melting temperature at these pH values and compared well to the measured K4 melting temperature at pH 11 (83 ºC) and pH 12 (89 ºC). It was therefore assumed that the lower melting temperature corresponded to E4+K4 heterodimers and it is these melting temperatures that were plotted for the E4+K4 mixture in Figure 4.6. For pH 11 the melting temperature of the heterodimers was 39 ºC and for pH 12 the melting temperature was 25 ºC.

For the mixture of E4+K4C the melting temperatures were similar in stability to those of E4+K4 in the pH range 5-9. The similarity of the two sets of melting temperatures was further evidence that the calculated melting temperature was primarily that of the heterodimers, where the cysteine of the K4C had nothing to form a disulphide bond with and therefore should have had no significant effect on stability. The melting temperature of the E4+K4C mixture began to

decrease at pH 10, one pH point earlier than E4+K4. This is because the K4C homodimer melting temperature was higher than the E4+K4C melting temperature at pH 8, rather than at pH 10 as in the case of E4+K4. The disulphide bonded K4C homodimers were more strongly bound than the K4 homodimers and so they began to dominate the mixture at a lower pH. However, at pH 12 there was little difference between the melting temperatures of E4+K4 heterodimers and E4+K4C heterodimers, reflecting the similarity of the K4 and K4C melting temperatures at this pH.

In summary, the CD results indicated that a coiled coil system with pH dependent binding was successfully designed and synthesised. E4 peptides formed homodimers at low pH but not at neutral or alkaline pH. K4 and K4C peptides formed homodimers at neutral and alkaline pH, with the melting temperature of the homodimers increasing as the pH increased. E4+K4 and E4+K4C peptide mixtures were concluded to form heterodimers at acidic and neutral pH but to dissociate in favour of forming K4 or K4C homodimers at high alkaline pH. This suggested that the peptides would be utilisable in the planned electronic pH control experiments. However, since CD spectra do not distinguish between homodimers and heterodimers, direct evidence of heterodimer behaviour was necessary.

4.3.4. FRET measurements

Although it was possible to draw conclusions about the behaviour of heterodimers in the mixed solutions from the CD melting curves, the fact it was not possible to distinguish between homodimers and heterodimers in the CD spectra meant that direct evidence of the behaviour of heterodimers was required. For this, FRET measurements were used. K4C peptides were labelled with the fluorescent dye ATTO 488 and E4 peptides were labelled with ATTO 594. When excited at 501 nm (the excitation maximum of ATTO 488), emission at 627 nm (the emission maximum of ATTO 594) should only be seen if the dyes are within close proximity, i.e. if the labelled peptides have formed a heterodimer. It can be seen in Figure 4.8 that ATTO 488 has negligible emission at 627 nm. Thus, since only heterodimers give a signal, this technique measured heterodimer formation directly. K4C-L peptides were used instead of K4-L peptides due to a lack of material for the K4-L peptides. 3 mM dithiothreitol (DTT) was used to prevent formation of disulphide bonds between K4C peptides so that they would behave equivalently to K4 peptides in these experiments. Note that DTT was not used in the CD experiments because it absorbs strongly at 280 nm.[10]

The effect of pH on E4-L+K4C-L heterodimers was assessed via concentration titrations using FRET. The fluorescence of a concentration range of E4-L was measured against a constant concentration of K4C-L when excited at the donor excitation maximum of 501 nm. Figure 4.9 shows that as the concentration of E4-L in solution was increased, the intensity of the donor emission peak at 523 nm (from the ATTO 488 dye on the K4-L) decreased while the intensity of the acceptor emission peak (from the ATTO 594 dye on the E4-L) increased. Since the solution

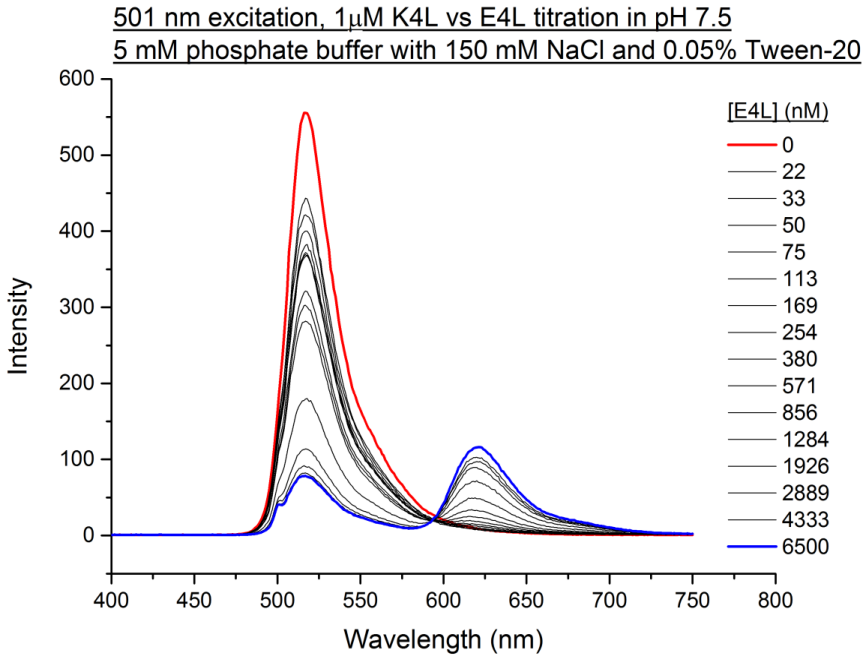

Figure 4.9: Fluorescence emission spectra for 1 μM K4-L mixed with varying concentrations of E4-L in 5 mM pH 7.5 phosphate buffer with 150 mM NaCl. The spectrum for pure K4-L is shown in bold in red and the spectrum for 6.5 μM E4-L is shown in bold in blue. All intermediate spectra shown in black. As the concentration of E4-L increased, the emission at 523 nm (the donor emission wavelength) decreased while the emission at 627 nm (the acceptor emission wavelength) increased. This is characteristic of FRET and implied increased formation of heterodimers as the concentration of E4-L increased.

was excited at the donor excitation wavelength, this was evidence of FRET, which implied that the dyes came into close proximity through the formation of heterodimers. As the concentration of E4-L increased, more heterodimers could be formed, leading to increased FRET. The measured intensities of the donor and acceptor emission peaks were plotted against E4-L concentration to obtain binding curves from which K_d values were calculated by fitting the curves with the equation described in Section 3.3.2. The binding curves and fits for the initial

pH	Acceptor emission (627 nm)		Donor emission (523 nm)	
	K_d (nM)	[K4C-L] (nM)	K_d (nM)	[K4C-L] (nM)
7.5	2±3	471±15	3±5	288±21
9.5	3±4	405±16	21±14	436±64
10.5	19±7	313±15	2±4	322±35
11.0	14±7	711±16	44±13	713±43
11.5	525±89	1036±86	286±218	1261±462
12.0	Not calculable	Not calculable	Not calculable	Not calculable

Table 4.3: K_d values and concentrations of K4-L for each pH. Values calculated from curves fitted to FRET data. Values calculated using both acceptor and donor emission are shown. Since the concentration of K4C-L was measured as 1000 nM, these values are not reliable, but do indicate the significant increase in K_d at pH 11.5. It was not possible to calculate K_d values in the measured concentration range at pH 12.

experimental conditions of 5 mM phosphate buffer and 150 mM NaCl are shown in Figure 4.10. It can be seen that changes in pH did not significantly affect heterodimer formation in the pH range 5.5-11.5. It was thought that the relatively high NaCl concentration might be screening the charged groups and therefore reducing the pH sensitivity of the binding. Additionally, the weak

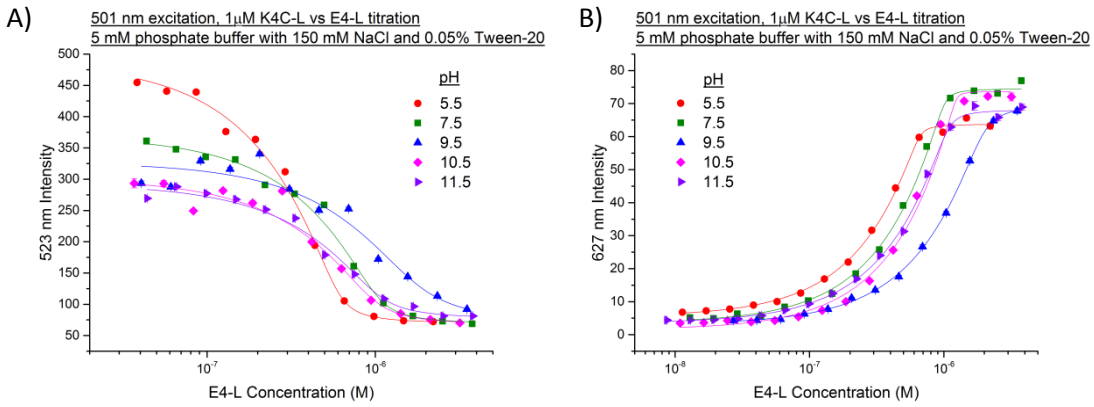

Figure 4.10: FRET binding curves for 1 μM K4-L mixed with varying concentrations of E4-L in 5 mM phosphate buffer with 150 mM NaCl over the pH range 5.5-11.5. The emission intensity of the donor emission peak (A) and acceptor emission peak (B) were plotted as a function of E4-L concentration and the data fitted to obtain K_d values.

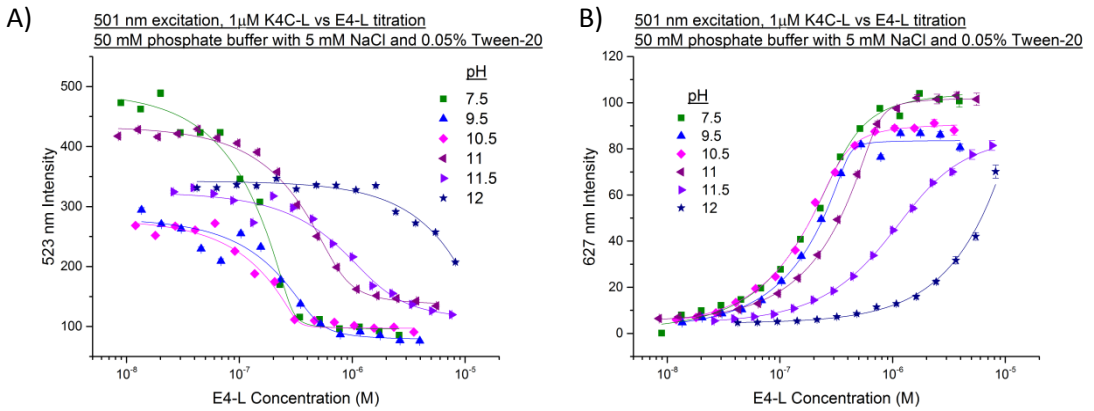

Figure 4.11: FRET binding curves for 1 μM K4-L mixed with varying concentrations of E4-L in 50 mM phosphate buffer with 5 mM NaCl over the pH range 7.5-12. The emission intensity of the donor emission peak (A) and acceptor emission peak (B) are plotted as a function of E4-L concentration and the data fitted to obtain K_d values, see Table 4.3.

buffer strength used in these experiments could have meant that the pH of the solutions was unstable, particularly since the addition of peptides to the solutions may itself have changed the pH, and this effect would have varied with peptide concentration.

To counter these issues, the NaCl concentration was reduced to 5 mM and the buffer concentration increased to 50 mM. pH testing of the solutions before and after the addition of peptide showed that the pH values were stable at this buffer strength. The results of the experiments with these conditions are shown in Figure 4.11. The formation of heterodimers showed little pH sensitivity in the range 7.5-11, with reduced heterodimer formation only apparent at pH 11.5-12. It is possible that asparagine deamidation was responsible for the dramatic loss of heterodimer formation at pH 12 because of the significant passage of time (~18 h) between preparing the K4C-L solutions and measuring them.[11] SPR studies of K4C monolayers showed that the ability of the monolayer to bind E4 was destroyed by 16.5 hour incubation in pH 12 phosphate buffer (see Section 5.3.3). However, the reduced heterodimer formation at pH 11.5 was probably not caused by asparagine deamidation since a repeat (not shown) of the

measurements at this pH with a solution prepared one week (rather than 18 h) before measurement showed no additional reduction in heterodimer formation.

The K_d values obtained from the curve fitting are summarized in Table 4.3. When the value of the donor-labelled peptide (K4C-L) concentration was fixed at the measured value of 1 μM, the fits did not correspond well to the measured data and so this parameter was left free to vary in the fits shown in Figure 4.10 and 4.11. Note that a K_d value for pH 12 was not calculable from the data. The K4C-L concentration returned by the free fits is also given in Table 4.3 and since it deviated from the known value quite significantly, the calculated K_d values are probably of use only as a quantitative comparison between the binding curves rather than absolute values comparable with the literature. As such, they confirmed what was apparent from visual inspection of Figure 4.12: that heterodimer formation remained largely independent of pH up to pH 11.5-12. This conclusion matches that obtained from the CD melting curves, where the E4+K4 mixture showed little variation in stability until pH 11-12. Note that the melting temperatures at pH 11 and 12 for E4+K4 heterodimers were 39 ºC and 25 ºC respectively and the FRET measurements were performed at 20 ºC.

In summary, the FRET results showed that E4+K4C heterodimers formed with similar binding strengths across a pH range of 5.5-11. Only at higher alkaline pH values 11.5-12 did a reduction in binding strength become apparent.

4.4. Conclusions

A new system of coiled coils with pH dependent binding was designed and successfully synthesised. Pure product was obtained for each peptide and mass spectrometry indicated that the mass of each peptide was as expected. ATTO dyes were successfully attached to the peptides to form labelled versions for FRET studies. Unfortunately, the E4 peptides were found to be insoluble below pH 5.

CD studies at neutral pH showed that the E4P peptides functioned as intended and did not form coiled coil heterodimers with K4 peptides. CD melting temperature studies showed that E4 peptides behaved as intended and formed homodimers at acidic pH but not at neutral pH. In contrast, although K4 peptides formed homodimers at alkaline pH as intended, they also formed homodimers at neutral pH. However, the melting temperatures of E4+K4 solutions were higher than K4 solutions at neutral and weakly alkaline pH, leading to the conclusion that strongly bound E4+K4 heterodimers dominated the mixed solutions at neutral pH and that K4 homodimers only dominated at pH 11-12. Similar results were seen with K4C peptides, except that the K4C homodimers were bound more strongly because of the possibility of disulphide bonds between cysteine residues, leading to higher melting temperatures at acidic to weakly alkaline pH than the

K4 homodimers, and the dominance of K4C homodimers in mixed E4+K4C solutions becoming apparent at pH 10 rather than pH 11.

FRET studies were used to lend support to these conclusions by allowing heterodimers to be directly distinguished from homodimers. The results showed that K4C homodimers (behaving as K4 homodimers because of the use of DTT to prevent disulphide bonds) began to affect the binding strengths of E4+K4C heterodimers at pH 11.5-12, which compared well with the CD results.

The aim of this chapter was therefore achieved. A system of peptides with pH dependent binding was synthesised and characterised. In a mixed solution of E4 and K4/K4C peptides, heterodimers preferentially formed at weakly acidic, neutral and weakly alkaline pH values, but at strongly alkaline pH values K4/K4C homodimers preferentially formed. To use the peptides to demonstrate electronic control of peptide interactions using electrochemical pH control it was necessary to demonstrate that the pH dependent behaviour of the peptide would be retained when immobilised on a surface. Chapter 5 details the experiments performed to demonstrate this.

4.5. References

1. ATTO-TEC: ATTO-TEC GmbH at <https://www.atto-tec.com/>

*2. Thomas, F., Boyle, A. L., Burton, A. J. & Woolfson, D. N. A Set of de Novo Designed Parallel Heterodimeric Coiled Coils with Quantified Dissociation Constants in the Micromolar to Sub-nanomolar Regime. *J. Am. Chem. Soc.* **135,** 5161–5166 (2013).

3. ATTO-TEC GmbH. Förster-radius of selected ATTO-Dye Pairs. (2011). Available at: https://www.atto-tec.com/fileadmin/user_upload/Katalog_Flyer_Support/R(0)-Values_2011.pdf. (Accessed: 11th November 2015)

*4. White, S. J. *et al.* The Influence of Two-Dimensional Organization on Peptide Conformation. *Angew. Chemie Int. Ed.* **54,** 974–978 (2015).

5. Dutta, K., Alexandrov, A., Huang, H. E. & Pascal, S. M. pH-induced folding of an apoptotic coiled coil. *Protein Sci.* **10,** 2531–2540 (2001).

*6. O'Shea, E. K., Lumb, K. J. & Kim, P. S. Peptide 'Velcro': design of a heterodimeric coiled coil. *Curr. Biol.* **3,** 658–67 (1993).

7. Anderson, D. E., Becktel, W. J. & Dahlquist, F. W. pH-induced denaturation of proteins: a single salt bridge contributes 3-5 kcal/mol to the free energy of folding of T4 lysozyme. *Biochemistry* **29,** 2403–2408 (1990).

8. Florence, T. M. Degradation of protein disulphide bonds in dilute alkali. *Biochem. J.* **189,** 507–520 (1980).

9. He, H. T. *et al.* Synthesis and chemical stability of a disulfide bond in a model cyclic pentapeptide: Cyclo(1,4)-Cys-Gly-Phe-Cys-Gly-OH. *J. Pharm. Sci.* **95,** 2222–2234

(2006).

10. Greenfield, N. J. Using circular dichroism spectra to estimate protein secondary structure. *Nat Protoc.* **1,** 2876–2890 (2007).
11. Patel, K. & Borchardt, R. T. Chemical pathways of peptide degradation. II. Kinetics of deamidation of an asparaginyl residue in a model hexapeptide. *Pharm. Res.* **7,** 703–711 (1990).

5. Peptide monolayer characterisation

5.1. Introduction

The purpose of the experiments in this chapter was to establish that the pH dependent peptide interactions studied in solution were also pH dependent when the peptides were immobilised on surfaces, in order to confirm that electronic control of peptide interactions through electrochemical pH change would be possible. The effect of immobilisation conditions on the pH dependent behaviour of the peptides was studied to assess the optimal conditions for demonstration of electronic control of peptide interactions.

This chapter details the characterisation of self-assembled monolayers of the peptides whose design and solution characterisation was detailed in Chapter 4. The materials and methods used are described in detail in Section 5.2. The effect of immobilisation conditions on monolayer density was assessed using CLSM (see Section 3.3.3) and surface CD (see Section 3.3.1). Characterisation of interactions between E4 peptides and immobilised K4C peptides, and the effect of pH on the interactions was performed by CLSM and FRET (see Sections 3.3.3 and 3.3.2 respectively), SPR (see Section 3.3.4) and surface CD (see Section 3.3.1). The results of these experiments are presented and discussed in Section 5.3. The findings are summarised in Section 5.4 and references are detailed in Section 5.5.

Surface CD measurements of monolayers formed at various pH values in this chapter, see Figure 5.11, were performed at the Diamond Light Source with the assistance of Dr. Simon White and Dr. Steven Johnson. All other work in this chapter was performed solely by the author.

5.2. Materials and methods

5.2.1. General materials and methods

Unless otherwise indicated, all chemicals were purchased from Sigma-Aldrich. Where the term ‘phosphate buffer’ is used, it refers to sodium phosphate buffer in 18.2 MΩ deionised H_2O made by mixing Na_2HPO_4 and NaH_2PO_4 in a ratio calculated to produce the desired pH. The pH was then adjusted to the correct value using NaOH or HCl and the buffer filtered using syringes with 0.22 μM filters. pH measurements were performed using a Mettler Toledo MP225 pH meter.

5.2.2. Surface cleaning

All surfaces were cleaned by being rinsed with acetone and then ultrasonicated in acetone for 10 min. The rinse and ultrasonication process was then repeated with isopropanol, then ethanol, then water. The surfaces were then immersed in a beaker of piranha solution (7:3 ratio of sulphuric acid:hydrogen peroxide) for 5 minutes, then turned over and immersed for a

further 5 minutes to ensure both faces were cleaned. The surfaces were then rinsed in water and ultrasonicated in water for 10 min. The rinse and ultrasonication process was then repeated with ethanol. The surfaces were then dried with a nitrogen stream.

5.2.3. Monolayer formation

For peptide immobilisation on gold surfaces via the C-terminal cysteine of the peptides, a peptide solution in phosphate buffer was introduced to the freshly cleaned surface and incubated at room temperature for at least 18 hours. In the case of fluorescently labelled peptides, incubation was performed in the dark to prevent photobleaching.

For peptide immobilisation on glass or indium tin oxide (ITO) surfaces via the C-terminal cysteine, the freshly cleaned surfaces were rinsed and ultrasonicated in isopropanol then incubated in a 2% solution of (3-mercaptopropyl)trimethoxysilane in isopropanol for at least 18 hours. After silanisation, the surfaces were immersed 10 times in isopropanol then 10 times in ethanol and then incubated in a 1 mM solution of copper (II) perchlorate hexahydrate in ethanol for 10 minutes. The surfaces were then immersed 10 times in ethanol then 10 times in phosphate buffer, then a peptide solution in the same phosphate buffer was introduced to the surface and incubated for at least 18 hours.

5.2.4. Surface FRET measurements

FRET measurements were performed on an Olympus IX81 Confocal Laser Scanning Microscope with an Olympus UPLSAPO 10x NA:0.40 objective. Fluorescently labelled peptide monolayers were formed as above (at 165 μM concentration in 50 mM pH 7.5 phosphate buffer) on No. 2 thickness glass cover slips on which open-ended hollow glass cylinders had been attached to form a cell enabling the monolayers to be controllably immersed in liquid. All measurements were performed in 50 mM phosphate buffer with 5 mM NaCl and 0.05% Tween-20 detergent to prevent non-specific binding of peptides to surfaces. After initial focusing by eye, z-scans at the donor and acceptor emission wavelengths (508-538 nm and 612-642 nm respectively) were used to find the focal plane to within 0.2 μm. Wavelength scans from 500-700 nm (resolution 2 nm, bandwidth 2 nm) were then performed. E4-L binding was performed by incubation with 1 μM E4-L solution at pH 7.5 for 30 min. Measurement at a new buffer pH was preceded by in situ emptying and refilling of the cell 3 times with water and 3 times with the new buffer.

The dyes were excited by a 488 nm Ar laser and emission was passed through a 405/488 nm dichroic mirror and measured at 523 nm and 627 nm with a bandwidth of 30 nm. Settings used were: 256x256 pixel scan area, corresponding to 1268x1268 μm, 4 μs/pixel scan speed, 50 μm confocal aperture, 800 V PMT voltage.

5.2.5. SPR measurements

SPR measurements were performed on a GE Healthcare Biacore 3000 instrument. Bare Au SPR chips were purchased from GE Healthcare and cleaned via 10 minutes ultrasonication in acetone then ethanol. Peptides were then immobilised as above at varying concentrations and pH values outside of the instrument. In all experiments the buffer used was 50 mM phosphate buffer with 5 mM NaCl and 0.05% Tween-20, and was at pH 6 with a flow rate of 10 μL min^{-1} unless otherwise indicated. An initial 20 minute injection of pH 11.5 buffer at 5 μL min^{-1} was found to be necessary to clear non-specifically bound mass and enable binding of E4 to the K4C monolayer. E4 was then injected at 5 μM concentration in pH 6 buffer for 10 minutes at 5 μL min^{-1} followed by 10 minutes of 5 μL min^{-1} pH 6 buffer for dissociation. For standard experiments, a sequential series of 10 min injections at pH 7.5, 8.5, 9.5, 10.5, 11.5 and 12 were then performed at 10 μL min^{-1}, each followed by 10 min injection of pH 6 buffer at 10 μL min^{-1}. For monolayer stability experiments, the above sequence (or a truncated version) was performed on a monolayer injected with strongly alkaline buffers overnight at 1 μL min^{-1}.

5.2.6. Surface CD

For surface CD, glass slides were cleaned and had peptide monolayers formed as above at 30 μM concentration. The majority of measurements were performed using a custom cuvette and slides from Hellma Analytics, shown in Figure 5.1 and used in White *et al*.[1] Each slide had monolayers formed on each surface such that for each slide used, 2 functionalised surfaces were scanned. All scans were performed at 20 ºC with a bandwidth of 1 nm and 2 s scan time per 1 nm wavelength step. For each experiment a blank spectrum was taken at each pH used using slides on which a silane-copper monolayer had been formed as above, but with no peptide monolayer, and using the same settings and number of slides as the rest of the measurements in that experiment. For each measurement, the acquired spectra were averaged and the average of the blank scans was subtracted. The blanked scans were then normalised to 0 mdeg at their maximum wavelength by subtraction of a constant baseline.

Initial scans to measure the effect of monolayer formation pH were performed at Diamond Light Source using an Applied Photophysics Chirascan-plus CD spectrometer fitted with a Peltier temperature controller. Three slides were used for each pH. Slides were washed by repeated immersion in 50 mM phosphate buffer at the monolayer formation pH before measurement. 10 scans were taken in 50 mM phosphate buffer at the formation pH, for a total of ~ 30 min scan time.

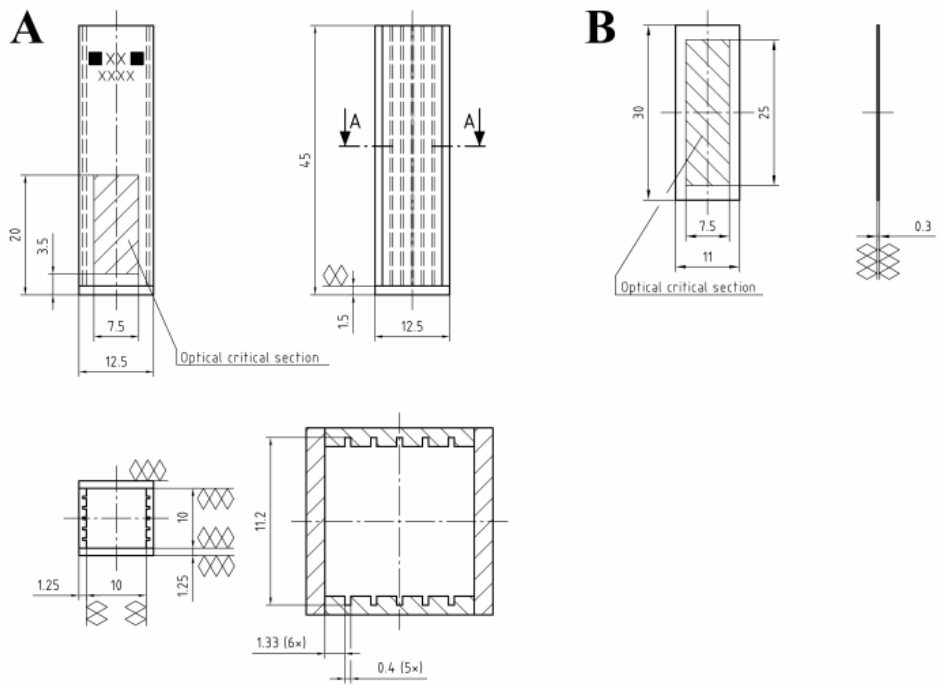

Figure 5.1: Schematics of **A**) the custom CD cuvette, and **B**) the accompanying slides used for surface CD measurements in this work. Reproduced from White *et* al.[1] The optical critical section is the section of the cuvette and slides through which the light passed in the CD spectrometer.

All other scans were performed at the University of Leeds using an Applied Photophysics Chirascan-plus CD spectrometer fitted with a Peltier temperature controller. 5 slides were used and 5 scans were taken and averaged for a total of ~15 min scan time. pH incubations were performed by immersing each slide in the appropriate 50 mM phosphate buffer for 10 minutes, then in 50 mM pH 6 phosphate buffer for 5 minutes to reverse any potential changes in conformation caused by the change in pH. E4 incubations used the same process but were performed in 10 μM E4 in 50 mM pH 6 phosphate buffer for 30 minutes, then 50 mM pH 6 phosphate buffer for 10 minutes. Before each scan, slides were washed by repeated immersion in 50 mM pH 6 phosphate buffer, then repeated immersion in 10 mM pH 6 phosphate buffer. Measurement was performed in 10 mM pH 6 phosphate buffer.

To prevent any changes in the measured signal caused by linear dichroism or changes in orientation (see Section 3.3.1), each slide was inserted into the cuvette in the same location and with the same orientation for each scan.

A new cell design that was intended to reduce the buffer path length to a minimal level is shown in Figure 5.2. Two 1 mm thick glass ‘window’ slides with three of the 0.3 mm peptide slides above were separated by 0.1 mm thick polytetrafluoroethylene (PTFE) spacers with the whole assembly held together by acrylic end pieces screwed at the top and bottom. The cell was assembled while submerged in the measurement buffer to ensure the presence of solution between the slides. Based on the thickness of the spacers, the path length through solution using the cell

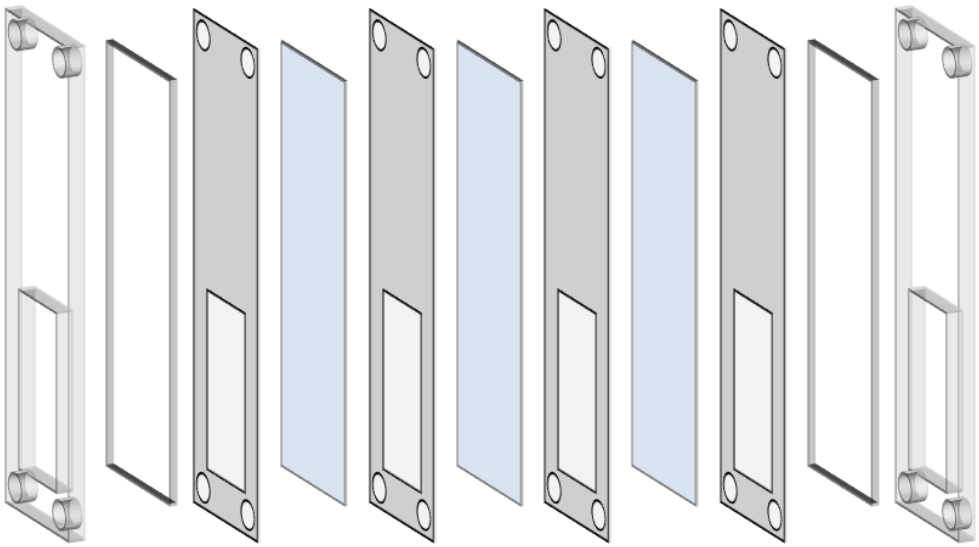

Figure 5.2: Design of the minimal path length cell. Components from left: acrylic end piece, 1 mm thick glass slide, 0.1 mm PTFE spacer (grey), 0.3 mm peptide coated glass slide (shown in blue for clarity only). The cell was assembled by being screwed together while submerged in solution to ensure the presence of liquid between the slides. The total path length through solution was approximately 0.4 mm.

with 3 slides and hence 4 spacers was approximately 0.4 mm, as compared to 9.1 mm path length through solution using the custom cuvette with 3 slides.

5.3. Results and discussion

5.3.1. Surface FRET measurements

CLSM was used to perform FRET measurements of E4-L binding to K4C-L monolayers. Surfaces were imaged using a 488 nm laser to excite the ATTO 488 donor dye on the K4C-L peptides. Increased emission intensity at the acceptor wavelength (627 nm) was therefore evidence that the K4C-L and E4-L peptides came into close enough proximity to enable FRET, as was decreased emission intensity at the donor wavelength (523 nm).

Figure 5.3 shows the results of an initial experiment in which E4-L was added to a K4C-L monolayer and then washed with buffers of increasing pH. It can be seen that the addition of the E4-L solution caused a significant increase in intensity at the acceptor emission wavelength and a significant decrease in intensity at the donor emission wavelength. This implied that E4-L peptides came into close proximity with the K4C-L peptide monolayer. The FRET signal remained after washing and replacing the E4-L solution with pH 7.5 buffer, implying that E4-L peptides were bound to the K4C-L monolayer. A relatively constant linear dissociation rate of approximately 0.6% min^{-1} of bound E4-L was evident from inspection of the 627 nm emission intensity. The dissociation rate of E4-L from the surface did not appear to be affected by the increasing pH of subsequent buffer washes and incubations, i.e. it did not appear that any of the higher pH buffers caused the E4-L to dissociate any faster than it would have done had all

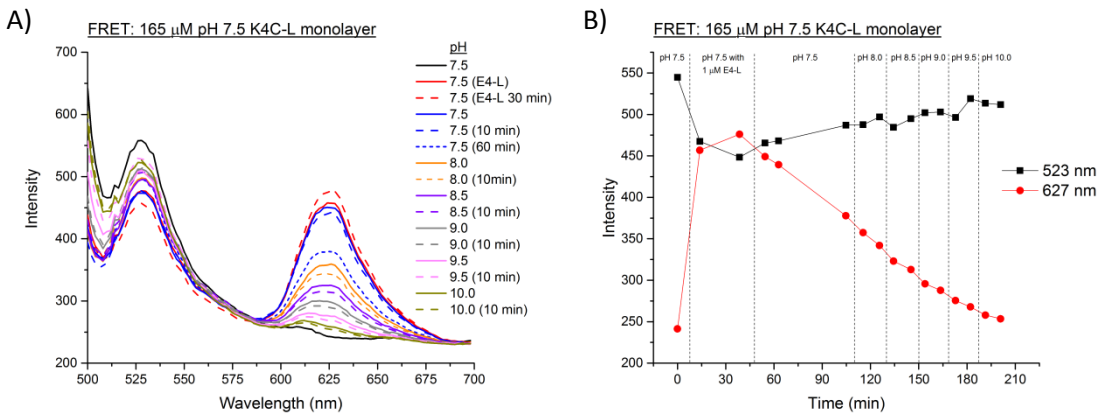

Figure 5.3: Fluorescence emission spectra (A) and emission peak values over time (B) for a surface FRET experiment. The surfaces were excited at 488 nm and the emission from the donor (523 nm) and acceptor (627 nm) dyes monitored. Addition of E4-L caused a decrease in 523 nm emission and an increase in 627 nm emission, characteristic of FRET. This indicated that E4-L was binding to the K4C-L monolayers. Subsequent buffer washes and incubations caused dissociation of the E4-L, but this did not seem to be significantly affected by the pH of the buffers. By pH 10, almost all E4-L had dissociated.

subsequent washes been at pH 7.5. Therefore, the E4-L may have been non-specifically bound to the surface, i.e. it may not have formed coiled coils with the immobilised K4C-L peptides.

To determine if the E4-L peptides were specifically bound to the K4C-L monolayer, the experiment was repeated with an immediate jump from pH 7.5 buffer to pH 10 buffer. The results of this experiment and a

Condition	Δ 523 nm	Δ 627 nm	Condition	Δ 523 nm	Δ 627 nm
E4-L addition at pH 7.5	-40	+168	E4-L addition at pH 7.5	-155	+252
E4-L incubation (10 min)	-55	+35	E4-L incubation (10 min)	-148	+64
E4-L incubation (30 min)	-3	+32	E4-L incubation (30 min)	-38	+39
pH 7.5 wash	+7	-41	pH 7.5 wash	+85	-89
pH 7.5 incubation (10 min)	+15	-25			
pH 10 wash	+52	-136	pH 10 wash	+71	-216
pH 10 incubation (10 min)	+41	-15			
			pH 10.5 wash	+237	-42

Table 5.1: Values from Figure 5.4 for the changes in 523 nm and 627 nm emission intensities for surface FRET experiments upon changes in condition in two experiments. In both experiments, washing with pH 10 buffer caused a significantly larger decrease in 627 nm emission intensity than washing with pH 7.5 buffer, indicating that the E4-L was specifically removed by the high pH of the pH 10 buffer.

subsequent experiment without 10 minute buffer incubations are shown in Figure 5.4. It can be seen that the pH 10 buffer caused a significant increase in the dissociation rate. The decrease in 627 nm intensity and/or increase in 523 nm intensity on going from pH 7.5 buffer to pH 10 buffer was noticeably larger than the change on going from pH 7.5 buffer with E4-L to pH 7.5 or from pH 7.5 buffer to a repeat of pH 7.5 buffer. Values for the emission intensity changes are given in

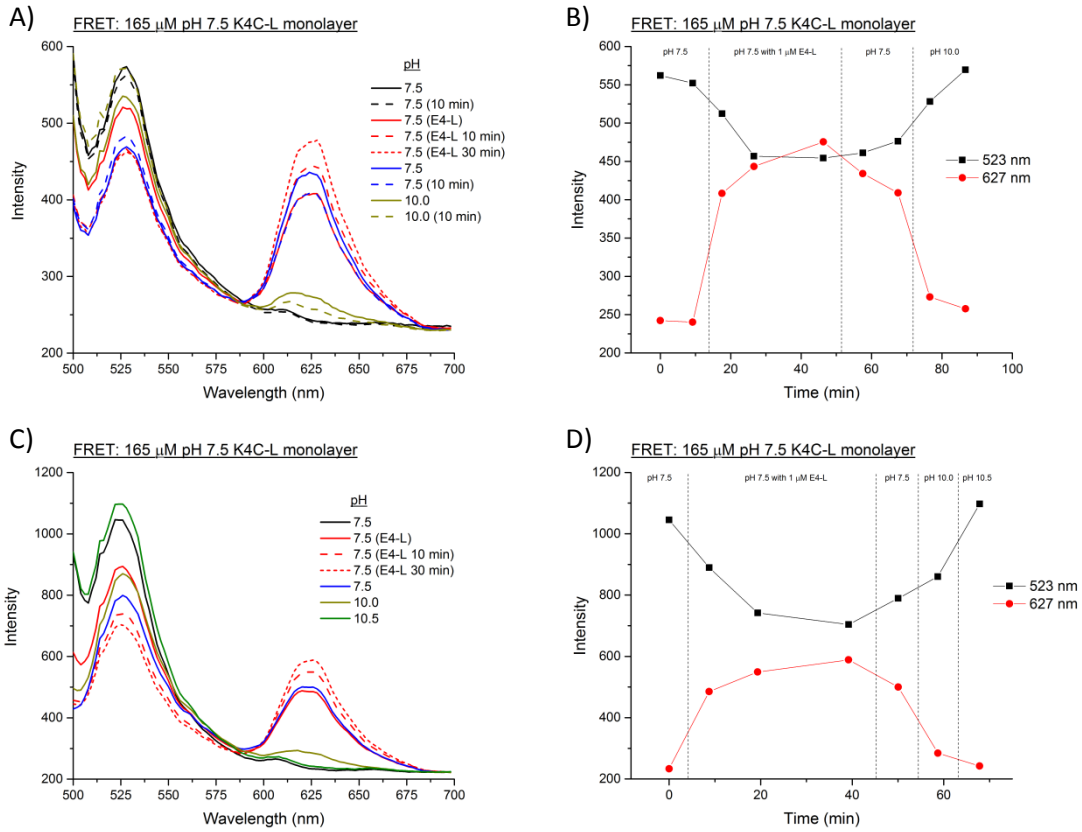

Figure 5.4: Fluorescence emission spectra and emission peak values over time for two surface FRET experiments (A and B, and C and D respectively). The surfaces were excited at 488 nm and the emission from the donor (523 nm) and acceptor (627 nm) dyes monitored. Addition of E4-L caused a decrease in 523 nm emission and an increase in 627 nm emission, characteristic of FRET. This indicated that E4-L was binding to the K4C-L monolayer. pH 10 washes and incubation caused a significant loss of bound E4-L, indicating that the E4-L was specifically bound in pH-dependent coiled coils. The data are summarised in Table 5.1.

Table 5.1. The fact that the decrease in 627 nm emission intensity was significantly larger (by 240-330%) after a pH 10 wash than after a pH 7.5 wash implied that the E4-L peptides were specifically bound to the K4C-L peptides in pH sensitive coiled coils and that release of the bound peptide could be triggered by high pH values. The effect of the pH could also be demonstrated by considering dissociation rates. The linear dissociation rates of E4-L estimated from the difference between the 627 nm emission intensity after 30 min of E4-L and the intensity after the pH 7.5 wash were approximately 1% min^{-1} and 2% min^{-1} for the first and second experiments, respectively (comparable to 0.6% min^{-1}) above, whereas the rates estimated from the 627 nm emission intensity values from before and after the pH 10 wash were approximately 9% min^{-1} for both experiments. The significantly faster dissociation rate caused by the pH 10 wash further confirmed the conclusion that the E4-L was specifically bound to the K4C-L in a pH dependent interaction.

Figure 5.5 shows the results of two control experiments. To determine the amount of 627 nm emission caused by direct excitation of the ATTO 594 dye by 488 nm light, the above experiment was repeated with a K4C (i.e. unlabelled) monolayer, such that there was no possibility of FRET. Some 627 nm emission from E4-L was seen as a result of direct 488 nm

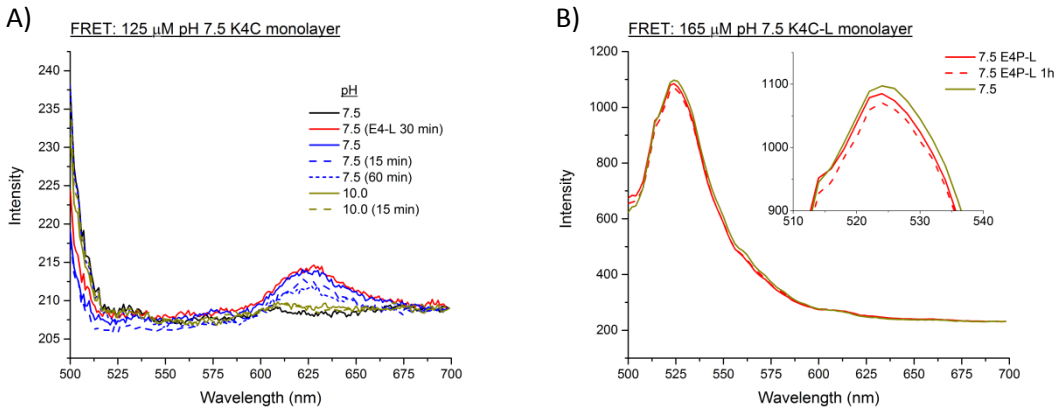

Figure 5.5: Fluorescence emission spectra for two control experiments. A) a K4C (i.e. unlabelled) monolayer was formed and tested with E4-L. As expected, there was no donor emission peak, since the donor dye was not present, and minimal acceptor emission, since no FRET could occur. B) Effect of E4P-L on a K4C-L monolayer. As expected, there was minimal acceptor emission since E4P-L does not form coiled coils, and hence minimal FRET occurred.

excitation, but amounted to only ~ 2% of the 627 nm emission seen from E4-L on labelled K4C-L monolayers shown in Figures 5.3 and 5.4. It was therefore concluded that direct excitation of ATTO 594 at 488 nm was not significant. However, the small amount of emission caused by direct 488 nm excitation that is visible in Figure 5.5 confirmed that E4-L also rapidly dissociated from an unlabelled monolayer at pH 10.

Finally, to further prove that the binding between E4-L and K4C-L monolayers was specifically due to formation of coiled coils, the experiment was repeated with E4P-L, a peptide that does not form coiled coils because of the inclusion of a proline residue (see Section 4.3.3). It can be seen in Figure 5.5B that the FRET signal given by E4P-L was negligible. Since E4P-L should have had almost identical properties (e.g. in terms of charge and size) to E4-L with the exception of its coil forming propensity, it was concluded that the FRET signal given by E4-L binding was indeed due to coiled coil formation.

Note from the results of Chapter 4 that K4+E4 and K4C+E4 heterodimers did not show any significant room temperature dissociation until pH values greater than pH 11 in solution, whereas the results here show that surface dissociation occurred at pH 10. It has previously been shown that BASE-C peptide, which has a similar primary structure to K4C, shows alpha helical structure at significantly lower pH when immobilised on surface than it does in solution.[1] It was shown that this was because the peptides were forced into close proximity within the monolayer and hence the shielding of hydrophobic core residues was energetically favourable despite the presence of electrostatic repulsion from *e* and *g* position lysines. Similarly, the crowded conditions of the K4C monolayer may have led to the lower dissociation pH of E4 when compared to K4 and E4 heterodimers in solution. The reason heterodimers dissociated in solution was because at some pH homodimer formation became preferable over heterodimer formation. From the work on BASE-C, it is known that surface immobilised peptides form homodimers at a lower pH than in solution, so it stands to reason that K4C monolayers formed homodimers and ejected

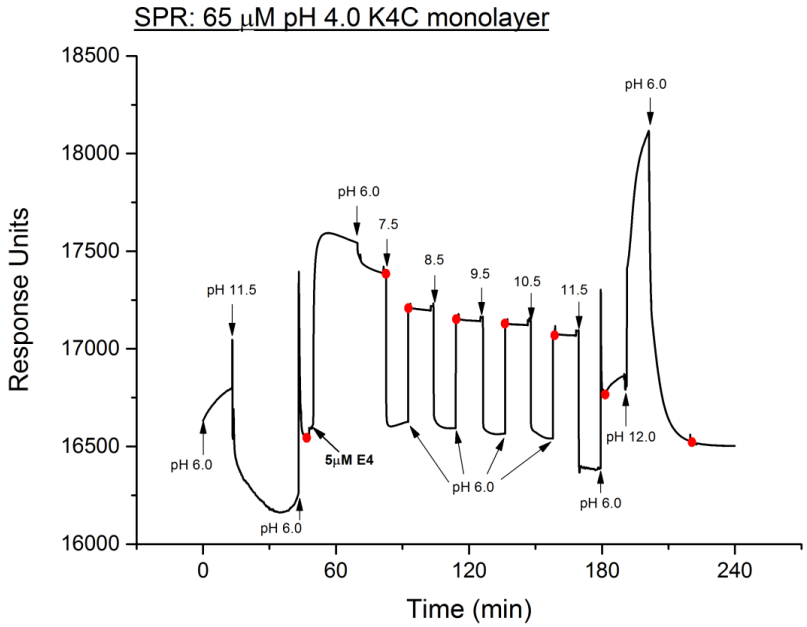

Figure 5.6: SPR experiment for a K4C monolayer formed at 65 μM concentration at pH 4. Arrows point to the times at which the indicated pH injections began. Changes in pH caused changes in refractive index, observed as large vertical shifts in the response curve. Injection of 5 μM pH 6 E4 solution caused a large response that persisted after the injection ended, indicating that E4 bound to the K4C monolayer. The effects of the injections may be easily seen by comparing the red circles at the end of each injection. A significant loss of bound E4 occurred as a result of the pH 11.5 injection.

any bound E4 at a lower pH than the heterodimers dissociated in solution. If this was the case, then the density of the K4C monolayer should have affected the pH at which E4 dissociated. SPR measurements were used to test this theory.

5.3.2. SPR measurements

SPR was used to assess E4 binding to and unbinding from K4C monolayers formed on gold surfaces under varying conditions intended to alter the density of the formed monolayers. The full SPR data from an experiment performed on a K4C monolayer formed from a 65 μM solution at pH 4 is shown in Figure 5.6. The binding of the E4 to the K4C monolayer can clearly be seen, followed by a removal of non-specifically bound peptide by the pH 6 and 7.5 injections. These were followed by gradual dissociation during the following injections until the pH 11.5 injection, which caused a significant loss of bound E4. After the pH 11.5 injection, around half of the E4 had dissociated. A pH 12 injection then caused all the remaining E4 to dissociate. The experiment may be summarized by considering the signal immediately after each injection (marked by red circles on the graph). Figure 5.7 shows these summaries for monolayers formed at various pH values in the range pH 4-7.5. It can be seen that significantly more E4 bound to K4C monolayers formed in the pH range 4-6 than bound to K4C monolayers formed in the pH range 6.5-7.5. It can also be seen that the amount of E4 removed per injection increases sharply for the pH 11.5 injection for monolayers formed at pH 4 and 5, but that this sharp increase in dissociation occurred earlier, after the pH 10.5 wash, for monolayers formed at higher pH.

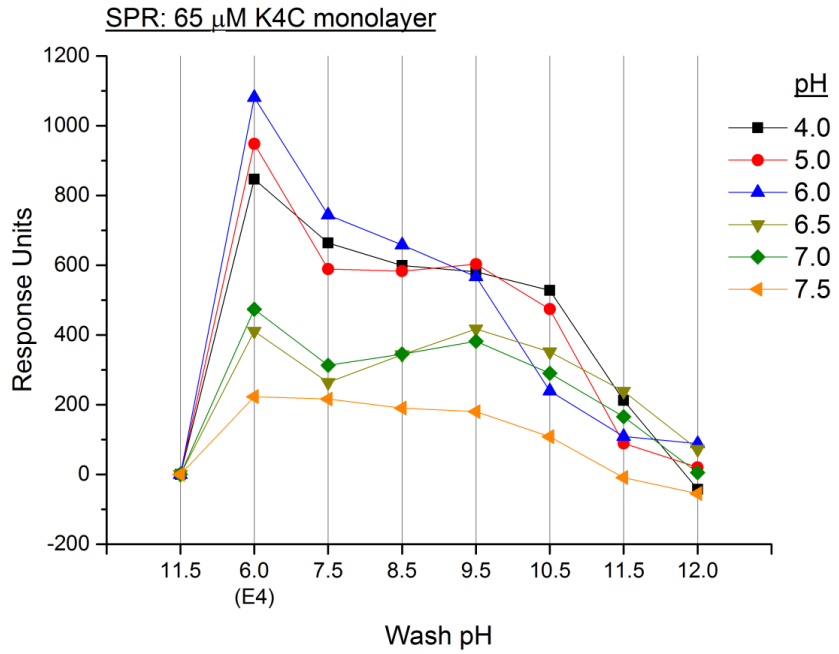

Figure 5.7: Summary of SPR experiments performed on K4C monolayers formed at 65 μM concentration at various pH values. Data points mark the response caused by the indicated injections, corresponding to the points marked on Figure 5.6 by red circles. Monolayers formed at pH 4-6 bound significantly more E4 than those at higher pH. Significant loss of E4 occurred during the pH 11.5 injection for monolayers formed at pH 4 and 5, but during the pH 10.5 injection for higher pH values.

From our work on the BASE-C peptide, and our knowledge of the effects of pH on K4C homodimer formation in solution (see Section 4.3.3), it seems highly likely that the K4C monolayers formed at higher pH values would have been more densely packed. Since a higher proportion of the peptides in the immobilisation solution would have formed homodimers at higher pH values, they were more likely to have immobilised on the surface as coiled coils, forming a more ordered and densely packed monolayer. As explained above, this might have led to the reduction in E4 dissociation pH since the individual K4C peptides in more densely packed monolayers would have found it energetically favourable to form homodimers with neighbouring K4C peptides (thus ejecting any bound E4) at lower pH values. That is, K4C monolayers formed at higher pH formed more dense monolayers and therefore formed surface homodimers at lower pH, which means that E4 was removed at a lower pH Similarly, more densely packed monolayers were probably less likely to have accepted E4 binding in the first place, which could explain the observed reduction of E4 binding with increasing pH.

To further test these theories, the same experiment was performed with K4C monolayers formed at pH 4 at a range of solution concentrations from 11.4 μM – 294 μM. It is well-established that more concentrated immobilisation solutions can lead to more densely packed monolayers, so these experiments were intended to form a range of monolayer densities at a constant pH. The results are summarised in Figure 5.8. It can be seen that, while the monolayers formed at 65 μM, 165 μM and 294 μM bound a similar amount of E4, the injection pH required to dissociate a significant amount of E4 varied from pH 10.5 for the two most concentrated immobilisation

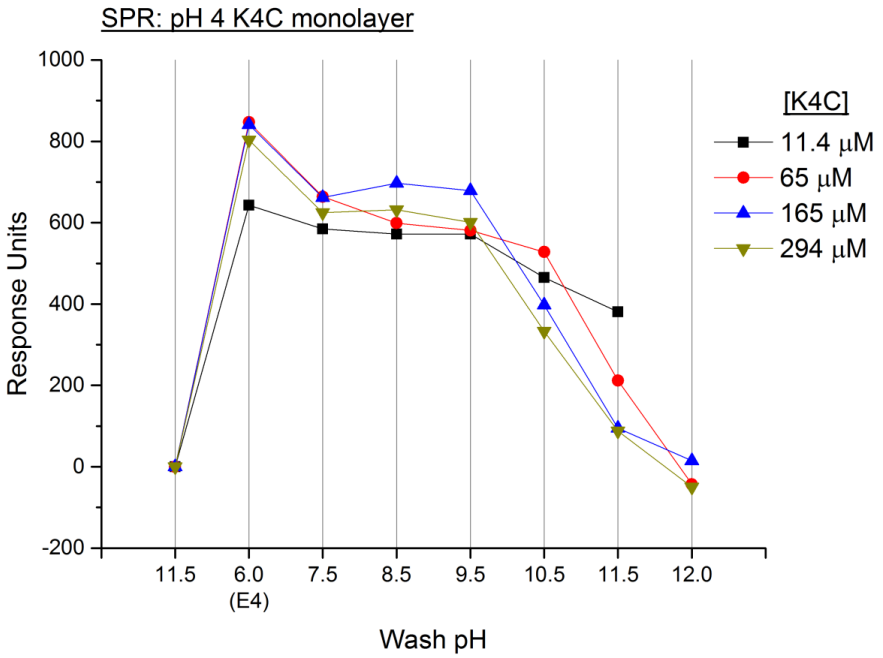

Figure 5.8: Summary of SPR experiments performed on K4C monolayers formed at 65 µM concentration at various pH values. Data points mark the response caused by the indicated injections, corresponding to the points marked on Figure 5.6 by red circles. Significant loss of E4 occurred during the pH 10.5 injection for monolayers formed at higher concentrations, but during the pH 11.5 injection or later for lower concentrations.

solutions to pH 11.5 for the 65 µM solution and a presumed pH 12 or higher for the 11.4 µM monolayer (unfortunately the pH 12 injection data for this concentration could not be obtained due to an instrument fault). These experiments lent support to the theorised reasons for the dependence of E4 dissociation pH on monolayer formation pH.
SPR was also used to test the resilience of the K4C monolayers to extended incubation in pH 11.5 and pH 12 solutions. The results are shown in Figures 5.9 and 5.10. In both experiments the data from two flow channels on the same chip are shown, with one channel having been subjected to a 16.5 hour incubation in pH 6 buffer and the other to a 16.5 hour injection of pH 11.5 or pH 12 buffer. It can be seen that the long injection of pH 11.5 buffer did not noticeably affect the ability of the K4C monolayer to bind E4 but that the long injection of pH 12 left the K4C monolayer unable to bind E4 in any significant quantity. This may be due to deamidation of the asparagine residues in the peptides. Deamidation rates are known to increase at high pH and the process converts asparagine residues into aspartic acid or isoaspartic acid, which would disrupt coil formation.[2]

5.3.3. Surface CD

Surface CD was used to measure the secondary structure of K4C monolayers immobilised on glass surfaces at various pH values in the range pH 2-8 since the SPR data shown in Figure 5.7 demonstrated that acidic formation pH values for the K4C monolayer resulted in increased binding of E4. The results are shown in Figure 5.11. It can be seen that the monolayers

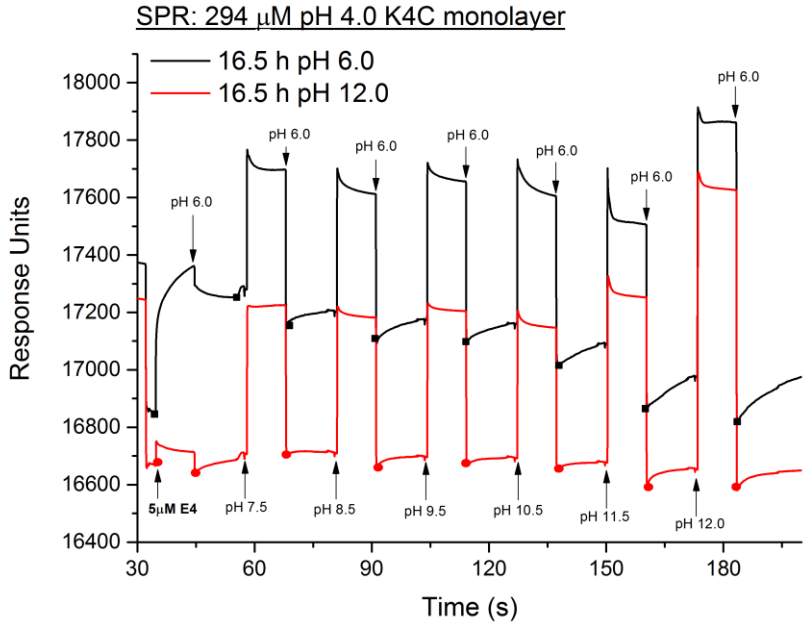

Figure 5.9: SPR experiment for a K4C monolayer formed at 294 μM concentration at pH 4. The black curve is for an area of the chip that had been injected with pH 6 buffer for 16.5 hours whereas the red curve is for an area injected with pH 12 buffer for 16.5 hours. Injection of 5 μM pH 6 E4 solution caused a large response that persisted after the injection ended for the pH 6 area, but not for the pH 12 area, indicating that extended exposure to pH 12 buffer left the monolayer unable to bind to E4.

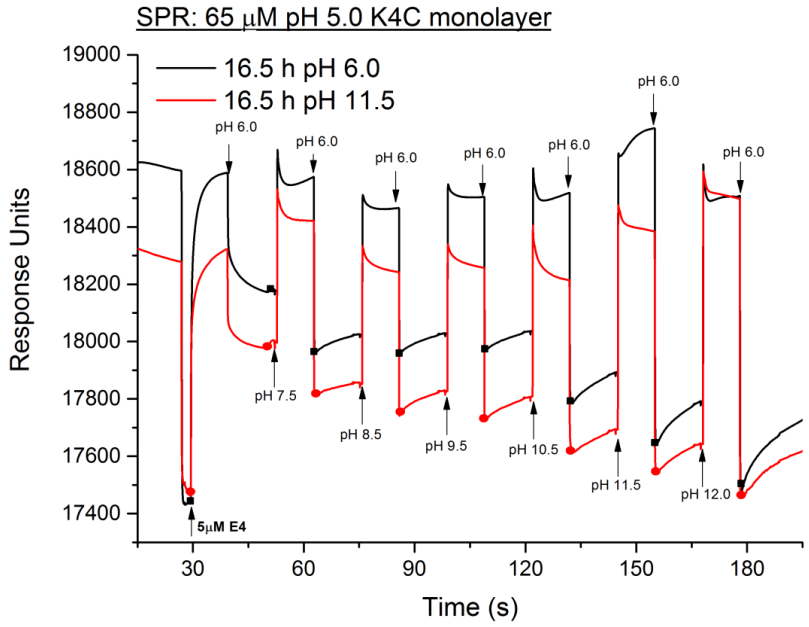

Figure 5.10: SPR experiment for a K4C monolayer formed at 65 μM concentration at pH 5. The black curve is for an area of the chip that had been injected with pH 6 buffer for 16.5 hours whereas the red curve is for an area injected with pH 11.5 buffer for 16.5 hours. Injection of 5 μM pH 6 E4 solution caused a large response that persisted after the injection ended for both areas, indicating that extended exposure to pH 11.5 buffer had no effect on the monolayer binding behaviour.

formed at pH 2-5 showed little evidence of alpha helical structure whereas the monolayers formed at pH 6, 7 and 8 showed an increasing amount of alpha helical structure. This was not unexpected, and supported the conclusions from the SPR experiments that higher formation pH led to denser,

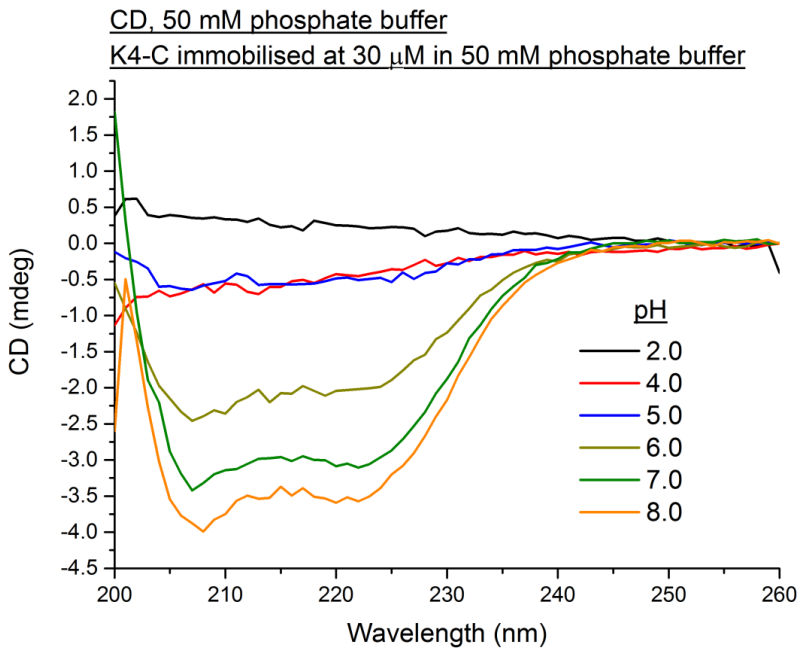

Figure 5.11: Surface CD spectra for monolayers formed at 30 μM concentration at various pH values. Alpha helical spectra were seen for pH 6-8, with the intensity decreasing with pH. At lower pH values no alpha helical content was evident.

more helical monolayers. However, since both a less dense monolayer and a less helical monolayer would have been expected to show a decrease in alpha helical signal, it would not have been meaningful to attempt to quantify the alpha helical content of the monolayer. Note that these spectra were measured using 3 slides (for a total of 6 surfaces) and 50 mM buffer and that these conditions gave rise to a large amount of noise at lower wavelengths, which obscured the 193 nm peak. For subsequent measurements 10 mM buffer and 5 slides (10 surfaces) were used to allow the 193 nm peak to be distinguished.

Since pH 6 was the first monolayer formation pH value at which alpha helical structure could clearly be seen, and also the monolayer formation value with the highest E4 binding from the SPR data in Figure 5.7, it was chosen as the formation pH for monitoring E4 binding using CD. Spectra for a monolayer formed from a 30 μM E4+K4C mixture immobilised at pH 6 are shown in Figure 5.12. A mixed solution was chosen in order to guarantee that the K4C monolayer would be formed with room to accept E4 binding. Figure 5.12 shows the effect on the spectra of a series of 10 minute incubations in buffers of increasing pH compared with spectra repeatedly incubated in pH 6 buffer. After the series of pH washes, the slides were incubated in 10 μM E4 at pH 6 for 30 minutes and then pH 11 buffer for 10 minutes, and this was then repeated. Figure 5.13A plots the signal at 222 nm (indicative of alpha helical formation) against the incubation conditions. In Figure 5.13B each 222 nm intensity for the increasing pH incubations was corrected by subtracting the 222 nm intensity of the corresponding pH 6 wash (i.e. the 222 nm intensity for the pH 8 incubation, which was the third incubation, had the 222 nm intensity for the third pH 6 incubation subtracted). This correction was intended to correct for any signal loss that might have

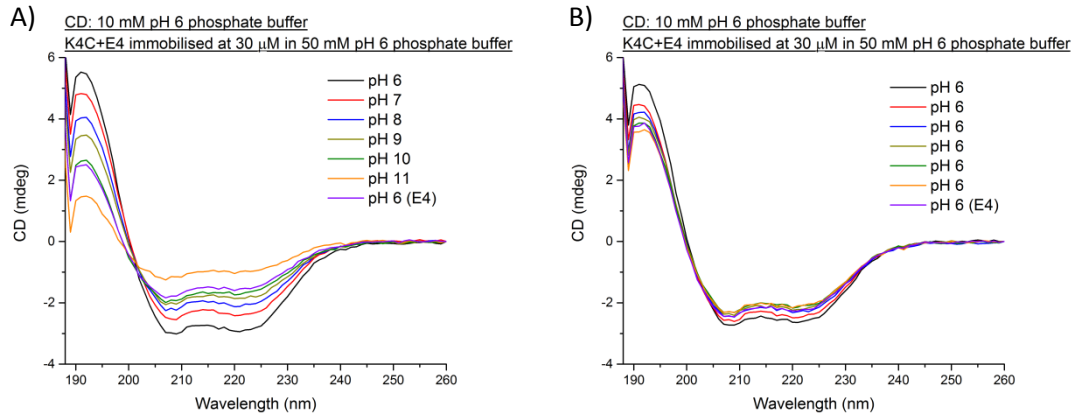

Figure 5.12: Surface CD spectra for K4C+E4 monolayers formed at 30 μM concentration at pH 6, and exposed to washes of increasing pH (left) or repeated pH 6 washes (right). Washes decreased the alpha helical content, but the pH did not have a significant effect until pH 11, where the spectrum indicated the removal of specifically bound E4 from the monolayer. Incubation in 10 μM pH 6 E4 solution caused a large increase in alpha helical content for the monolayer washed with pH 11 but not the monolayer washed with pH 6, confirming that the pH 11 wash removed bound E4 that could then be replaced.

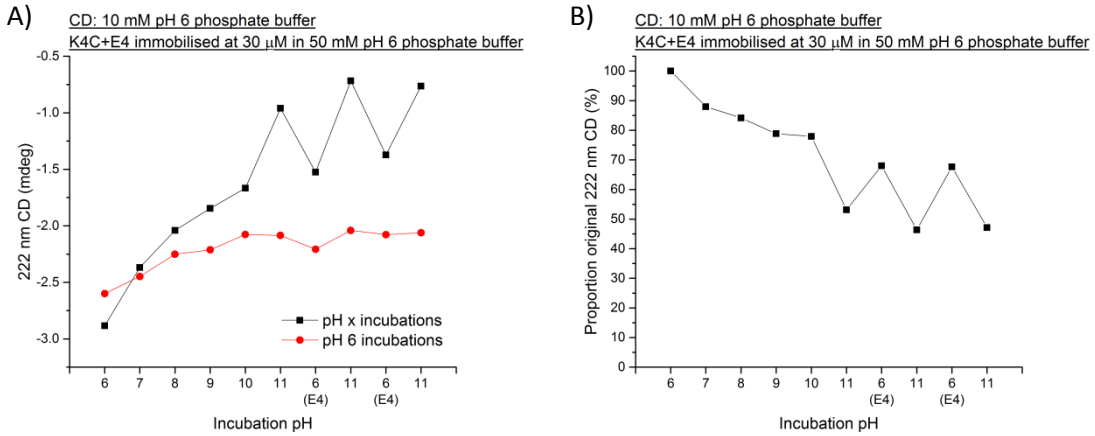

Figure 5.13: A) 222 nm CD signals from Fig 5.12 for K4C+E4 monolayers formed at 30 μM concentration at pH 6, and exposed to washes of increasing pH (black curve) or repeated pH 6 washes (red curve). Washes decreased the alpha helical content, but the pH did not have a significant effect until pH 11, where the spectrum indicated the removal of specifically bound E4 from the monolayer. Incubation in 10 μM pH 6 E4 solution caused a large increase in alpha helical content for the monolayer washed with pH 11 but not the monolayer washed with pH 6, confirming that the pH 11 wash removed bound E4 that could then be replaced. Removal and binding of E4 was performed multiple times. B) The data from Fig 5.12 A for increasing pH washes corrected by subtraction of the pH 6 wash data from Fig 5.12 B and plotted as a proportion of the original 222 nm CD signal.

occurred because of damage to the monolayer or loss of immobilised peptide over time. The corrected intensities were then plotted as a percentage of the original signal (i.e. the signal at the first measurement in pH 6 buffer). Figure 5.13B therefore shows the percentage decrease in 222 nm intensity caused by each change in pH.

Fig 5.13A shows that the total result of the incubations at pH 6-10 was a decrease in 222 nm signal of around 1.2 mdeg. This can be interpreted as the dissociation of non-specifically bound peptide since a similar trend was seen for repeated pH 6 incubations, with a decrease in signal of around 0.5 mdeg. A similar effect was seen in the FRET and SPR data, where washes at neutral to weakly basic pH values caused a decrease in signal intensity. Figure 13B shows that

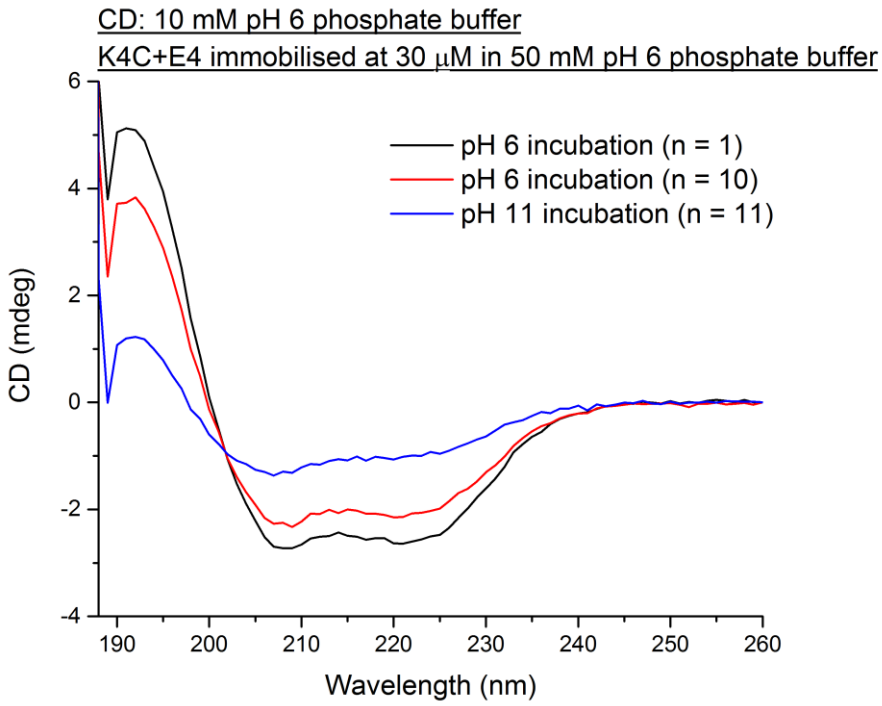

Figure 5.14: Surface CD spectra for K4C+E4 monolayer formed at 30 μM concentration at pH 6, and exposed to repeated pH 6 washes. The black spectrum is the original spectrum whereas the red spectrum is the spectrum after 10 pH 6 washes. The blue spectrum shows the effect of a pH 11 wash, indicating that there was specifically bound E4 in the monolayer that was not removed by repeated pH 6 washes.

the corrected loss of 222 nm signal intensity was around 22 percentage points. After the first pH 11 incubation, the 222 nm signal intensity decreased sharply by around 0.7 mdeg, whereas the corresponding pH 6 incubation on the other set of slides caused no significant change in intensity (the corrected 222 nm signal decrease was 25 percentage points). The 0.7 mdeg decrease for the pH 11 wash was equivalent to ~ 60% of the decrease caused by the previous four pH washes and thus probably indicated the specific, pH triggered, dissociation of the E4 that was bound as coiled coils in the monolayer. Evidence for this conclusion came from the fact that subsequent incubation in 10 μM E4 solution caused a large increase (~ 0.6 mdeg) in 222 nm signal intensity for the surfaces that had previously been incubated in pH 11 buffer, but little increase (~ 0.2 mdeg) in 222 nm signal intensity for the surfaces that were previously only incubated at pH 6 (the corrected increase was 15 percentage points). Therefore it can be concluded that pH 11 incubation caused dissociation of E4 from coiled coils in the monolayer, allowing fresh E4 to bind to the immobilised K4C, whereas repeated pH 6 incubation did not cause E4 dissociation from coiled coils and thus fresh E4 could not bind. A further repetition of the cycle showed the same behaviour for both sets of surfaces. Finally, as shown in Figure 5.14 incubation of the repeated pH 6 surfaces in pH 11 buffer caused a significant loss of helicity (~ 1.1 mdeg), demonstrating that there was indeed bound E4 in the monolayer that had not been removed by repeated pH 6 incubation. For example it might have been the case that, despite being prepared identically to the slides used for the varied pH incubations, the slides used for the repeated pH 6 incubations contained no bound

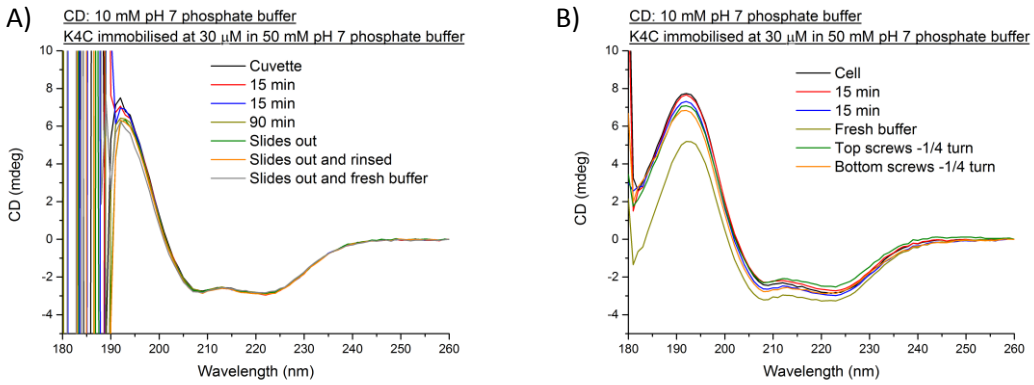

Figure 5.15: Surface CD spectra for K4C+E4 monolayers formed at 30 μM concentration at pH 7.0 for the cuvette used for all other experiments (A) and a custom cell design (B). The cuvette spectra are obscured by noise below 188 nm whereas the cell spectra remain clean down to 183 nm. However, the cuvette spectra remain stable after: a 15 minute wait between measurements, another 15 minute wait, a 90 minute wait, the removal of the cuvette from the machine along with the removal and reinsertion of the slides into the cuvette, the same with a water rinse of the slides, and the same with the complete replacement of the buffer inside the cuvette. In contrast, the cell spectra varied significantly after: a 15 minute wait between measurements, another 15 minute wait, the complete disassembly of the cell to enable a change of buffer, a one quarter turn loosening of the screws holding the cell together at the top, and the same with the screws at the bottom.

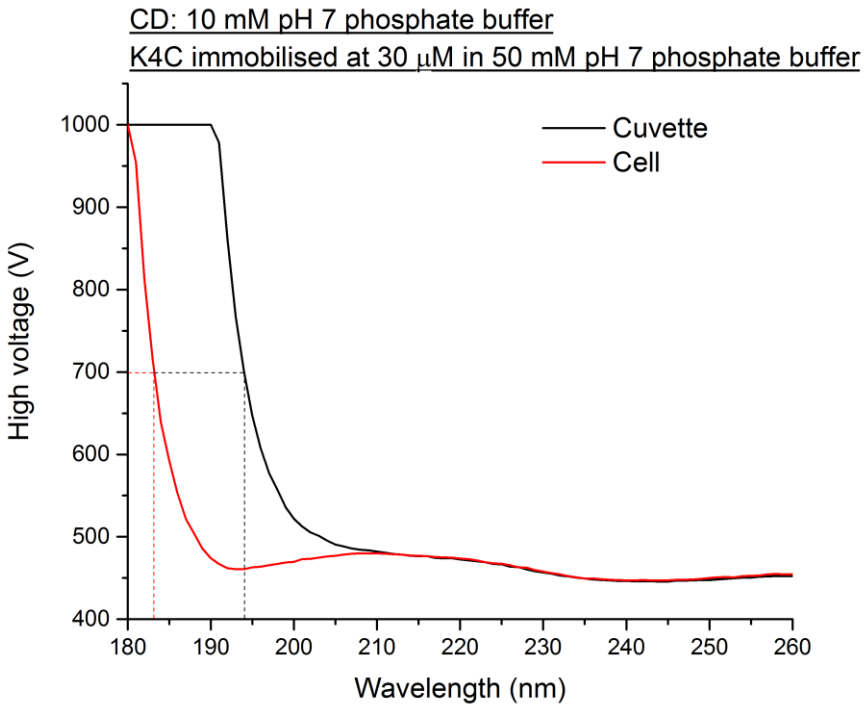

Figure 5.16: Comparison of the high voltage (HV) recorded for CD spectra taken using the cuvette (black curve) and custom cell design (red curve). It is usually recommended that the HV not exceed 700 V. Using the custom cell significantly reduced the wavelength at which 700 V was exceeded.

E4. The fact that they exhibited the same behaviour as the other slides when incubated in pH 11 proved this was not the case.

Note that the variations in helicity associated with removal and addition of E4 lend further support to the theory that the E4 specifically binds into the K4C monolayer as coiled coils.

The use of 5 slides (10 surfaces) with 10 mM buffer allowed the 193 nm peak to be distinguished from the noise caused by interaction of the light with the buffer solution but a significant amount of the peak below ~ 188 nm was still obscured. To remedy this, a 3 slide (6 surface) cell with minimal solution path length (~ 4 mm) was designed and tested. This cell gave a clean spectra down to ~ 183 nm but unfortunately the spectra measured using this cell were not stable, varying slightly over time and varying significantly if, for example, the screws holding the cell together were unscrewed slightly. The spectra for this cell are compared with spectra from the cuvette used for all other measurements in Figure 5.15. High voltage (HV) measurements are shown in Figure 5.16. These indicate the voltage applied to the photomultiplier tubes. To avoid artefacts in the CD spectra it is usually recommended that the HV not exceed ~ 700 V.[3]

Although the spectra obtained using the new cell were not stable and were therefore not useful for measuring E4 binding, they did show that the peptide monolayers formed using the protocols in this work formed fully 'solution-like' alpha helical spectra in the 180-260 nm range typically used for protein CD spectroscopy.

Furthermore, the excellent reproducibility of the spectra using the cuvette, even after slides were taken out of the cuvette and put back in, indicated that any changes in CD signal observed in the binding experiments reflected changes caused by the binding, rather than changes due to orientation of the slides or cuvette. Thus, regardless of whether the binding induced change in signal was caused by changes in circular dichroism signal (e.g. changes in the peptide conformation), changes in linear dichroism signal (e.g. changes in the peptide orientation) or both (e.g. a greater concentration of peptide in the monolayer), the change must have been caused by the binding.

5.4. Conclusions

The purpose of the experiments in this chapter was to establish that the pH dependent peptide interactions studied in solution were also pH dependent when the peptides were immobilised on surfaces, in order to confirm that electronic control of peptide interactions through electrochemical pH change would be possible. These objectives were achieved.

Surface FRET measurements were performed to study the peptide monolayers. K4C-L peptides were immobilised on glass surfaces and E4-L peptides were added and then washed with buffers of varying pH. The results indicated that bound E4-L gradually dissociated over time at a relatively constant rate for washes at pH 9 and below, but that washing with pH 10 buffer caused a rapid and significant loss of bound E4-L, implying that the E4-L was bound to the K4C-L monolayer in a pH dependent manner. E4P-L peptides, which did not form coiled coils with K4 in solution, produced very little FRET emission when introduced to a K4C-L monolayer, providing evidence that E4-L was binding to the K4C-L monolayer by forming coiled coils.

Since pH values greater than pH 11 were required for heterodimer dissociation in solution, it was postulated that dissociation at lower pH 10 was caused by the crowded conditions in the monolayer. SPR measurements were used to test the theory. K4C monolayers were immobilised at pH values from pH 4 to pH 7.5 and E4 peptides were introduced. The monolayers formed at lower pH values appeared to bind greater quantities of E4, which may have been evidence that these monolayers were less dense, providing more room for E4 peptides to bind. The monolayers were then washed with buffers of increasing pH. The monolayers formed at pH 4 and pH 5 showed a significantly increased loss of peptide at pH 11.5, whereas the monolayers formed at higher pH values showed an increased loss at pH 10.5, comparable to the increased loss at pH 10 for the surface FRET experiments, where the K4C-L monolayers were immobilised at pH 7.5. Similar experiments were performed for K4C monolayers formed at various concentration values. A K4C monolayer formed at the relatively low concentration of 65 μM, expected to form a less dense monolayer, showed increased E4 dissociation at pH 11.5, whereas monolayers formed at higher concentrations showed increased E4 dissociation at pH 10.5. By showing that the density of the K4C monolayer affected the E4 dissociation pH, these experiments provided an explanation for the lower heterodimer dissociation pH for surface bound peptides as opposed to the peptides in solution.

Surface CD experiments were then performed to further confirm that the E4 peptides were binding to the K4C monolayers in pH dependent coiled coils. Monolayers formed at lower pH values showed less evidence of alpha helical structure, supporting the theory that increasing the formation pH led to more densely packed K4C monolayers. Preformed K4C+E4 monolayers were then incubated in buffers of increasing pH to find the E4 dissociation pH. Once again, the dissociation was pH dependent, with a significant loss of alpha helical signal only at pH 11 and not at any lower pH values.

In summary, monolayers of K4C and K4C-L were successfully formed and it was shown that E4 and E4-L peptides could bind specifically into these monolayers through coiled coil formation. Dissociation of the E4 and E4-L peptides from the monolayer was shown to be pH dependent, with significant dissociation occurring only at alkaline pH values. The dissociation pH was typically lower than in solution, and could be decreased by increasing the density of the monolayer through increasing the pH and/or concentration of the immobilisation solution.

5.5. References

*1. White, S. J. *et al.* The Influence of Two-Dimensional Organization on Peptide Conformation. *Angew. Chemie Int. Ed.* **54,** 974–978 (2015).

2. Patel, K. & Borchardt, R. T. Chemical pathways of peptide degradation. II. Kinetics of deamidation of an asparaginyl residue in a model hexapeptide. *Pharm. Res.* **07,** 703–711

(1990).

*3. Kelly, S. M., Jess, T. J. & Price, N. C. How to study proteins by circular dichroism. *Biochim. Biophys. Acta* **1751,** 119–139 (2005).

6. Electrochemical pH control

6.1. Introduction

The purpose of the experiments in this section was to measure the spatial and temporal extent of electrochemical pH change, and its dependence on conditions such as the solution properties and the duration and magnitude of the applied current, in order to establish the optimal conditions for electronic control of protein interactions.

This experimental chapter details investigations into electrochemical pH change. For background, see Section 2.4. The materials and methods used in this chapter are described in Section 6.2. The investigations were carried out using CLSM (see Section 3.3.3). The results of the experiments are presented in Section 6.3. The findings are summarised in Section 6.4 and references are detailed in Section 6.5.

6.2. Materials and methods

6.2.1. General materials and methods

Unless otherwise indicated, all chemicals were purchased from Sigma-Aldrich. Where the term 'phosphate buffer' is used, it refers to sodium phosphate buffer in 18.2 MΩ deionised H_2O made by mixing Na_2HPO_4 and NaH_2PO_4 in a ratio calculated to produce the desired pH. The pH was then adjusted to the correct value using NaOH or HCl and the buffer filtered using syringes with 0.22 μM filters. pH measurements were performed using a Mettler Toledo MP225 pH meter.

The pH sensitive fluorescent dye SNARF®-4F 5-(and-6)-carboxylic acid (referred to as SNARF-4F henceforth) was purchased from ThermoFisher Scientific and stored frozen in aliquots of 18.2 MΩ deionised H_2O. The concentration of the dye in solution was 100 μM in all experiments.

6.2.2. ITO electrode fabrication

All experiments used 1 mm diameter ITO electrodes patterned onto No. 2 thickness glass cover slips. The cover slips were cleaned by rinsing and ultrasonication in, successively, acetone, isopropanol, ethanol and water, then dried under a nitrogen stream. Microposit S1813 photoresist was spin-coated onto the slides and baked at 115 ºC for 2 minutes. The slides were then immersed in chlorobenzene for 2.5 minutes, dried under a nitrogen stream, and then exposed to UV light through the mask pattern using a Karl Suss MJB3 mask aligner. Finally, the slides were immersed in Microposit MF-319 developer solution, rinsed in water and dried, before being sent to Evatech AG (Switzerland) for ITO deposition through electron beam evaporation.

Open-ended hollow glass cylinders were glued to the patterned slides to provide a vessel for solutions.

6.2.3. SNARF-4F calibration

An Olympus IX81 Confocal Laser Scanning Microscope with an Olympus UPLSAPO 10x NA:0.40 objective was used to measure the pH dependent fluorescence of SNARF-4F in buffers of known pH. The dye solutions were excited by a 515 nm Ar laser and emission was passed through a 458/515 nm dichroic mirror and measured at 590 nm and 650 nm with a bandwidth of 10 nm. Settings used were: 256x256 pixel scan area, corresponding to 1268x1268 μm, 8 μs/pixel scan speed, 800 μm confocal aperture, 800 V PMT voltage.

For each pH, emission was measured 20 times and averaged. The averaged 590 nm intensity was then divided by the averaged 650 nm intensity to produce a peak intensity ratio.

6.2.4. Electrochemical pH change

All electrochemical experiments were performed using a 1 mm diameter ITO working electrode, Pt wire counter electrode and Ag/AgCl (3.5 M KCl) reference electrode. Current and voltage were controlled and measured using a PalmSens potentiostat. Based on the geometric area of the working electrodes used in all experiments, a current of 1 μA corresponded to a current density of 1.27 A m^{-2}.

All CLSM measurements were performed using the settings in Section 6.2.3. to maintain compatibility with the calibration curve derived using those settings. Images were acquired every 2 seconds during electrochemical pH change experiments. Where areas around the electrode were measured, they were 100 μm wide with the width centred at the indicated distance from the electrode.

6.2.5. SNARF-4F monolayer formation

To form monolayers of SNARF-4F on the patterned slides the following protocol was used. Slides were cleaned by rinsing and ultrasonication in, successively, acetone, isopropanol, ethanol and water then dried under a nitrogen stream. They were then immersed in piranha solution (7:3 ratio of sulphuric acid:hydrogen peroxide) for 5 minutes, then ultrasonicated in water for 10 minutes and dried under a nitrogen stream. An open-ended hollow glass cylinder was then glued to each slide to provide a vessel for solutions.

The cylinder was filled with acetone and left for 2 minutes, then emptied and allowed to dry. It was then filled with 2% (3-aminopropyl)triethoxysilane (APTES) in acetone and left covered for 3 hours.

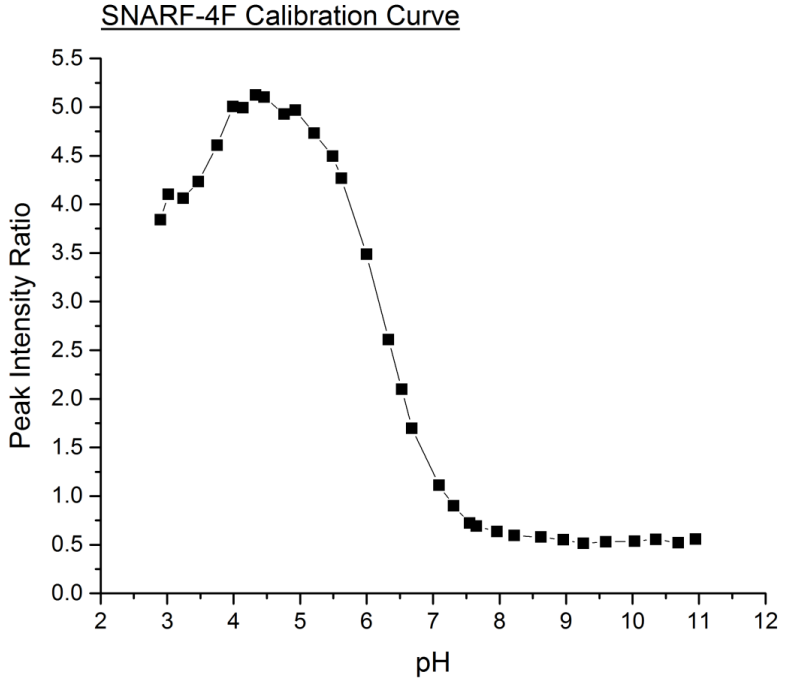

Figure 6.1: SNARF-4F calibration curve showing the relationship between peak intensity ration and pH. The peak intensity ratio was derived by dividing the intensity of the 590 nm emission peak by the intensity of the 650 nm emission peak (the raw data for the 590 nm and 650 nm peaks is shown in Figure 6.2). Note the peak at pH 4.5.

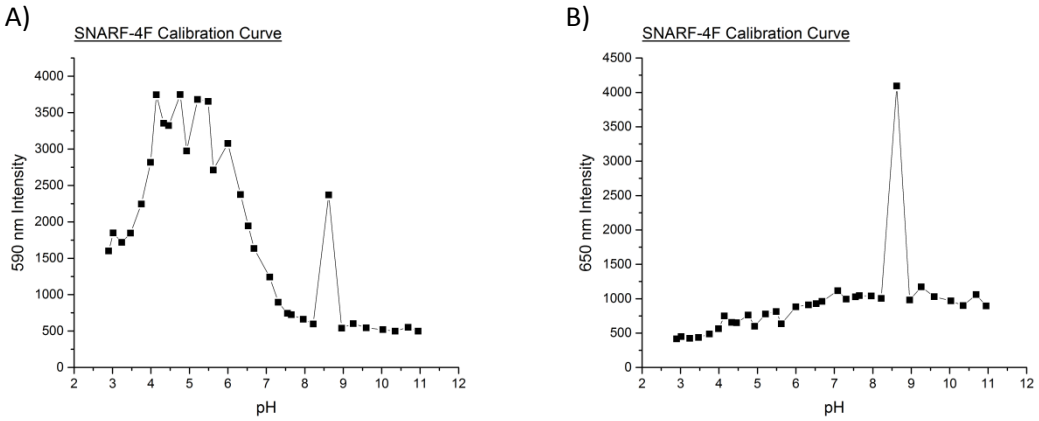

Figure 6.2: Calibration curves showing the pH dependence of the 590 nm (A) and 650 nm (B) peak emission intensities of SNARF-4F used to create the calibration curve in Figure 6.1. Note that the abnormally large intensity at ~ pH 8.5 in both figures is not evident in Figure 6.1, where the ratio of the two intensities is shown. Taking the ratio removes dependence on absolute intensity values and therefore protects against experimental errors such as variance in the dye concentration

A solution of 0.15 mM SNARF-4F with 0.15 mM N-hydroxysuccinimide (NHS) and 0.75 mM 1-ethyl-3-(3-dimethylaminopropyl)carbodiimide (EDC) was prepared in 100 mM pH 5.5 MES buffer and incubated for 15 minutes in the dark. The cylinder was then emptied of APTES, rinsed with water and dried under a nitrogen stream. The cylinder was then filled with the SNARF-NHS-EDC mixture and left covered in the dark for ~ 18 hours. Finally, the cylinder was emptied and rinsed thoroughly with water before measurement.

6.3. Results and discussion

6.3.1. SNARF-4F calibration

To measure electrochemical pH change, the pH sensitive fluorescent dye SNARF-4F was used. SNARF-4F is known to have pH sensitive emission peaks at 590 nm and 650 nm. In order to be able to use SNARF-4F for monitoring electrochemical pH change it was first necessary to create a calibration curve correlating the ratio of the intensities of the dye's two emission peaks to known pH values. To do this, phosphate buffer solutions were made with 32 different pH values in the pH range 3-11. For each pH the two emission peak intensities were measured and the 590 nm peak intensity was divided by the 650 nm peak to obtain a peak intensity ratio. These ratios were then plotted against pH. The results are shown in Figure 6.1. The individual intensities measured are shown in Figure 6.2. The 590 nm peak showed more sensitivity to the solution pH and the 590 nm intensity vs. pH profile was similar in shape to the final ratio vs. pH calibration curve. The 590 nm intensity increased with pH from pH 3, reaching a maximum between pH 4 and pH 5. The intensity then decayed with pH, reaching a minimum at pH 8. In contrast the 650 nm peak intensity simply increased with increasing pH. Note that both intensity curves showed an abnormally intense signal at ~ pH 8.5 caused by an experimental error. Here the advantage of using the peak intensity ratio to measure pH is evident. The ratio calibration curve shown in Figure 6.1 displays no evidence of the error at pH 8.5, and eliminated the large variations in intensity seen between pH 4 and pH 5 on the 590 nm intensity curve. This shows that the ratio calibration curve was insensitive to variation in the overall intensity of the dye emission due to, for example, variations in the dye concentration. Thus it can be seen that the intensity ratio of SNARF-4F was a robust way to measure pH.

6.3.2. Electrochemical pH control with short current application

Figure 6.3 shows the effect of short pulses of positive and negative currents on the pH of water in areas directly above and adjacent to an electrode, measured using SNARF-4F. Based on the pH of the water (measured using a pH meter before the experiment) and the measured changes in peak intensity ratio, it was assumed that the pH during the experiment remained in the range of pH 5 to pH 7 where the ratio calibration curve was approximately linear. For these experiments the peak intensity ratios were therefore converted to pH values via a linear transformation to enable the y-axis to be plotted as pH. As expected (see Section 2.4), negative currents caused an increase in pH and positive currents caused a decrease in pH. As can be seen in Figure 6.3, in the case of the application of -1 nA for 1 s there was an increase of approximately 0.3 pH units at the electrode, 0.1 pH unit 50 μm from the electrode, and no change at further distances. Application of -1 nA current for 5 s caused an increase of approximately 0.7 pH units at the electrode, and larger changes at areas further from

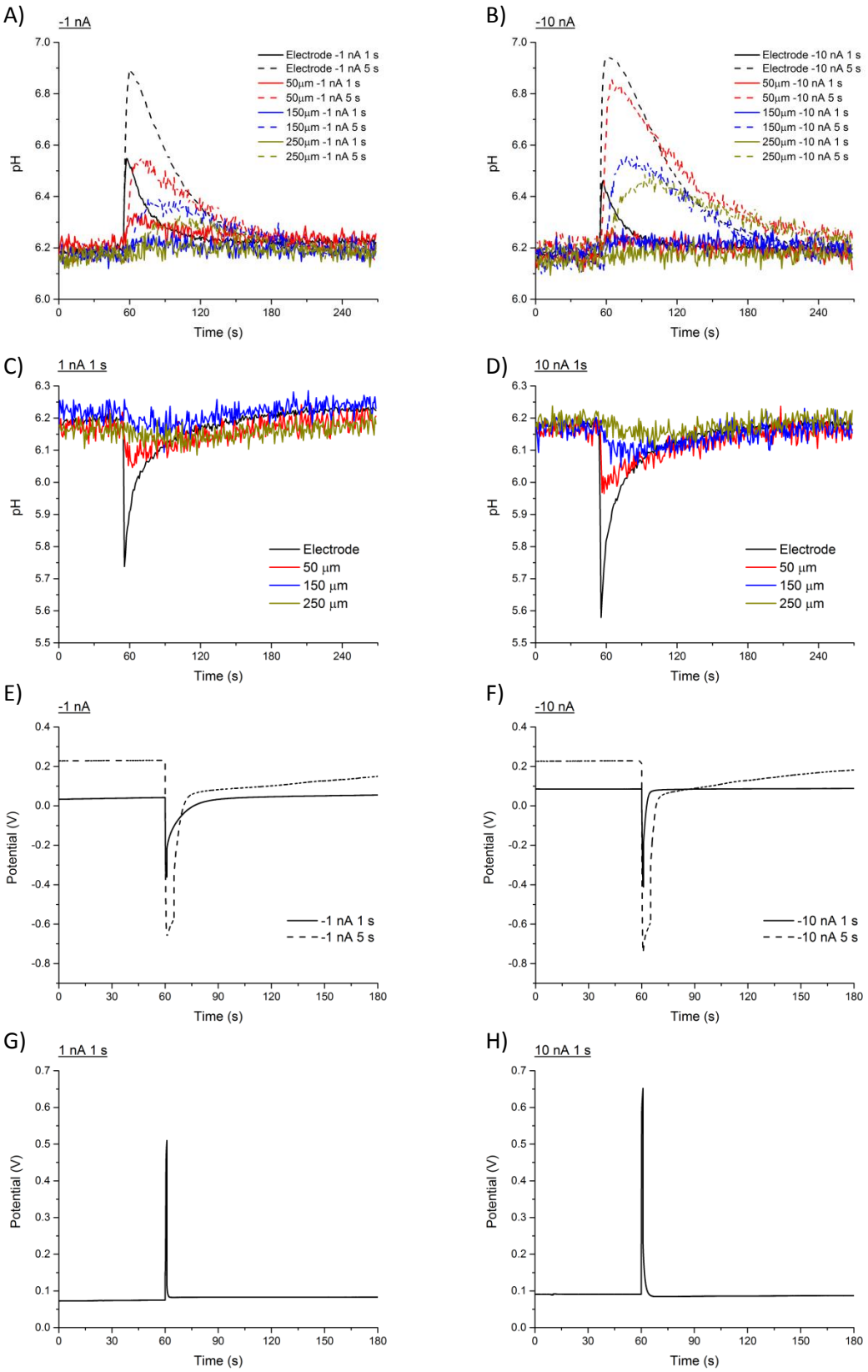

Figure 6.3: Graphs of pH over time showing the effect at the electrode and nearby areas of short pulses of current applied in water. The current application began after 60 s in all cases. A) The effect of -1 nA applied for 1 s (solid lines) and 5 s (dashed lines), and B) the effect of -10 nA, C) the effect of 1 nA applied for 1 s, and D) the effect of 10 nA applied for 1 s. As expected, negative currents increased the pH and positive currents decreased the pH. Increasing the duration or magnitude of the current increased the extent of the pH change. E-H) Voltage graphs for the current applications shown in A-D respectively.

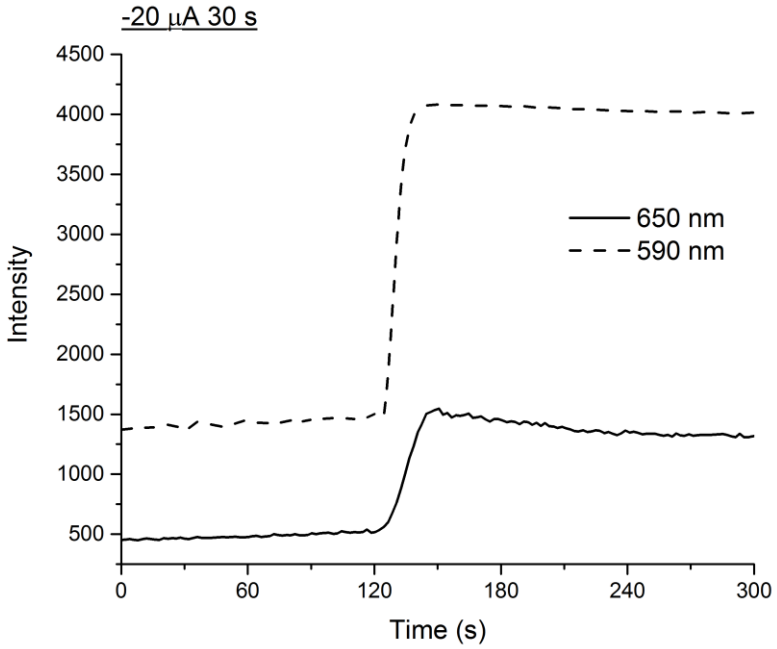

Figure 6.4: Graph of 650 nm and 590 nm intensities showing them effect at the electrode of -20 μA current applied for 30 s in water. The current application began after 120 s. The high current caused the electrode to become opaque and reflective, causing a significant and permanent increase in intensity at both wavelengths.

the electrode, with pH change evident as far as 250 μm from the electrode. Application of -10 nA for 5 s caused a pH change of similar magnitude at the electrode, but significantly increased the pH change in the surrounding areas. Note that each image took 2 s to acquire and the current was only applied for 1 s in some experiments, so it is possible that the change in pH was not fully captured in these cases. This may explain why the pH change at the electrode for -1 nA applied for 1 s appears larger than the change for -10 nA applied for 1 s.

Moving to positive currents, Figure 6.3 shows that application of 1 nA for 1 s caused a pH decrease of approximately 0.45 pH units at the electrode, and a decrease of approximately 0.1 pH unit 50 μm from the electrode, whereas application of 10 nA for 1 s caused a change of 0.6 pH units at the electrode, 0.2 pH units 50 μm from the electrode, and 0.1 pH unit 150 μm from the electrode. The pH changes happened rapidly upon application of the current, and slowly returned to their original values as the pH change diffused away into the bulk solution.

From these experiments it can be seen that SNARF-4F was capable of measuring electrochemical pH change, and that pH change could be increased in magnitude and spatial extent by increasing either the magnitude or duration of the current. This was as expected, since an increase in either magnitude or duration of the current would have increased the number of pH changing reactions, see Section 2.4, and therefore the magnitude of the pH change. An increased pH change would have created a steeper pH gradient, therefore encouraging the diffusion of the pH change further and faster into the bulk solution.

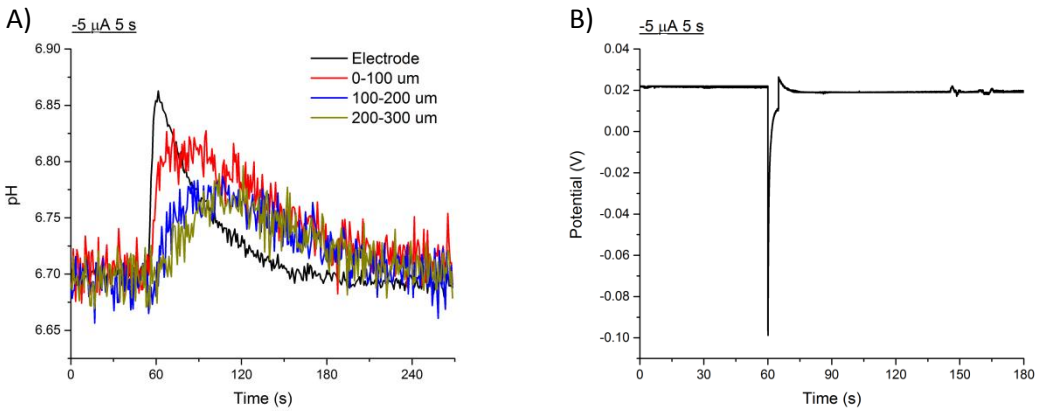

Figure 6.5: A) Graph of pH over time showing the effect at the electrode and nearby areas of -5 µA current applied for 5 s in 5 mM pH 6.7 phosphate buffer. The current application began after 60 s. Because of the buffer, the pH change was smaller than that in the case of the graphs shown in Figure 3, despite a significantly increased current. B) The voltage graph for the same experiment.

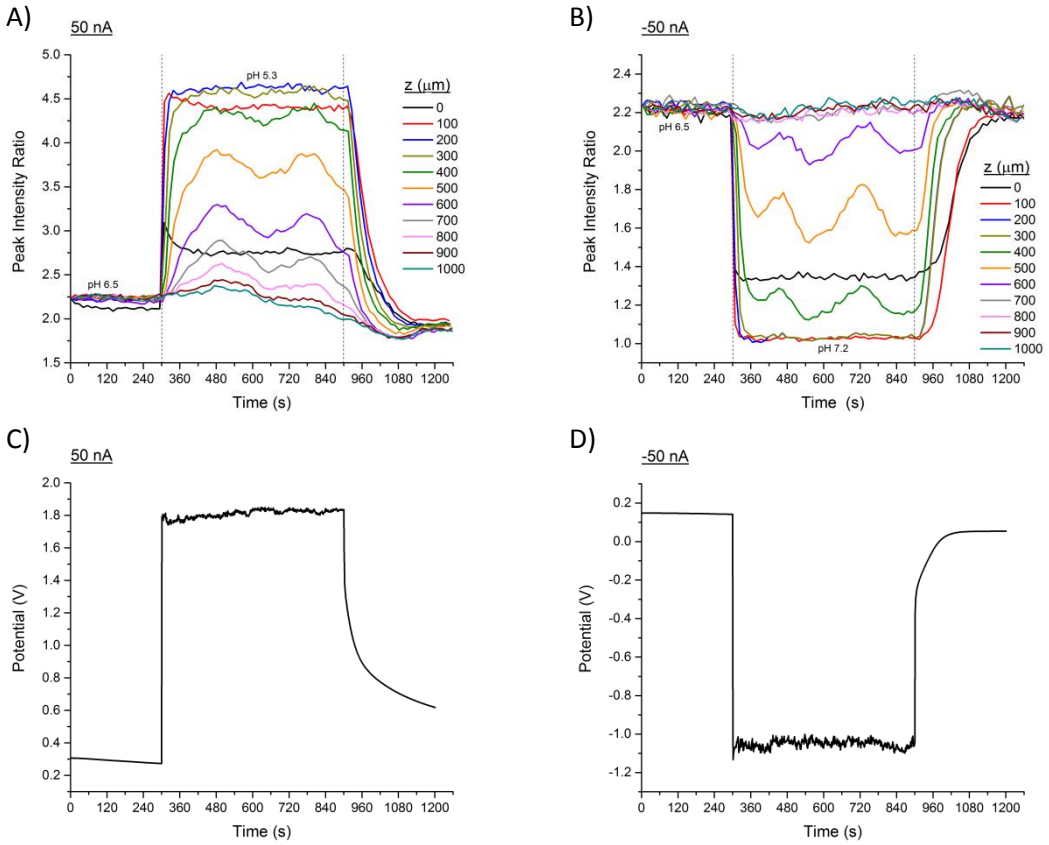

Figure 6.6: Graph of peak intensity ratios over time showing the effect at the electrode and areas above the electrode of A) 50 nA and B) -50 nA current applied for 10 min in water. The current application began after 300 s. The pH change extended to areas 600 µm above the electrode in both cases. C) and D) are the corresponding voltage graphs.

Figure 6.4 shows that the electrode could be damaged by large currents. The application of -20 µA for 30 s caused a significant and permanent increase in the 590 nm and 650 nm intensities. Visual inspection of the electrode after the experiment showed that it had become opaque and reflective. Since the damage to the electrodes was clearly observable from the intensities, it could be assumed that no damage was done when significant permanent increases

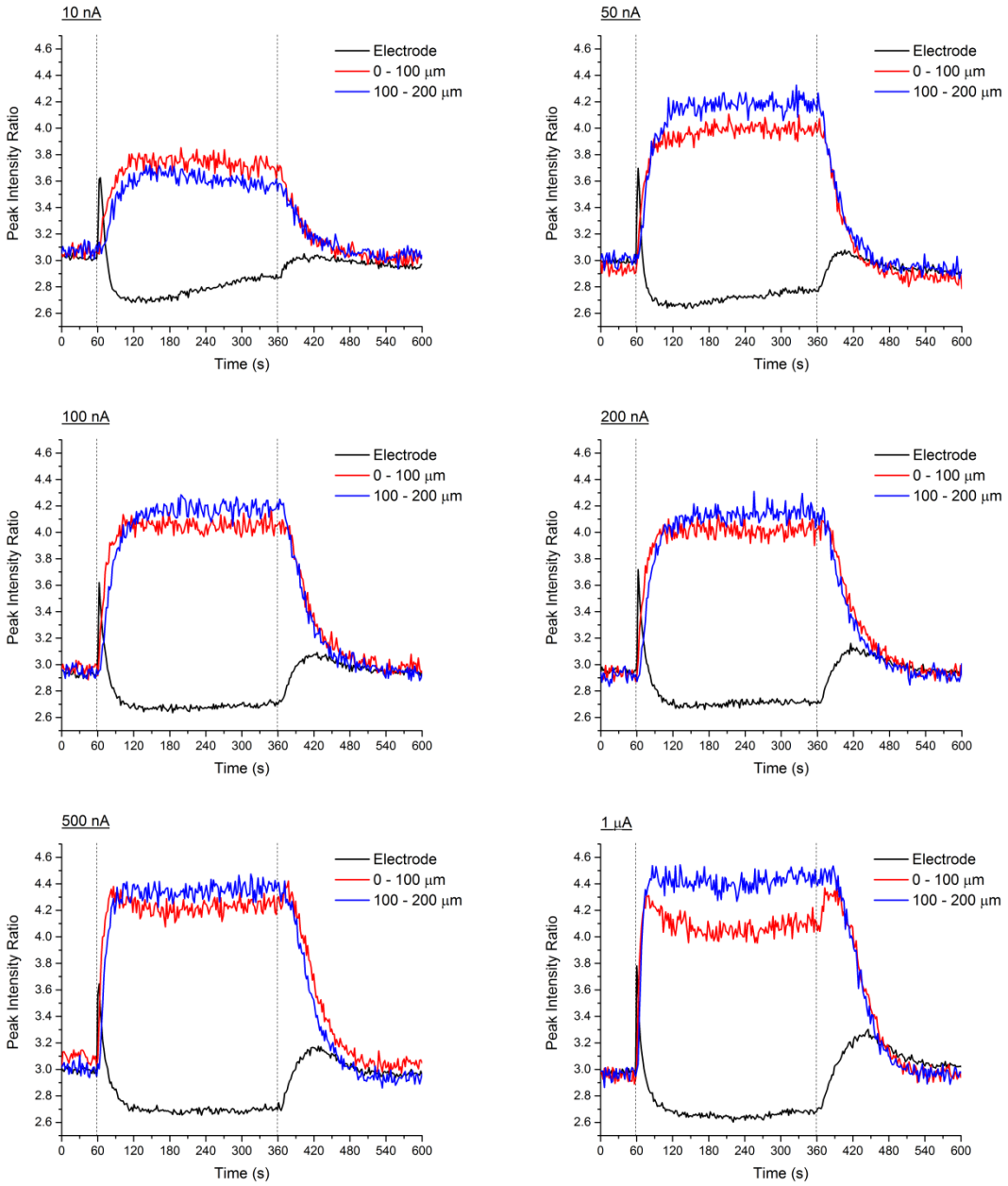

Figure 6.7: Graphs of pH over time showing the effect at the electrode and nearby areas of various positive currents applied for 300 s in water. The current application began after 60 s. In all cases, the current application caused an initial sharp increase in the peak intensity ratio, followed by a decrease to below the original ratio. At 500 nA and 1 µA, this behaviour became evident in the area adjacent to the electrode.

at both wavelengths were not observed. Electrodes were also visually inspected for signs of damage after every experiment.

Figure 6.5 shows the pH change caused by the application of -5 µA for 5 s in 5 mM pH 6.7 phosphate buffer. The pH increase at the electrode was only 0.15 units despite the application of 500x more current than was applied to water for 5 s to achieve a 0.7 pH unit increase, see Figure 6.3. This supported the conclusion that the current was causing a pH change, since a dramatic reduction in pH change was exactly what would have been expected from adding buffer to the solution. The effect of a buffer is to limit pH changes, so the fact that replacing water with

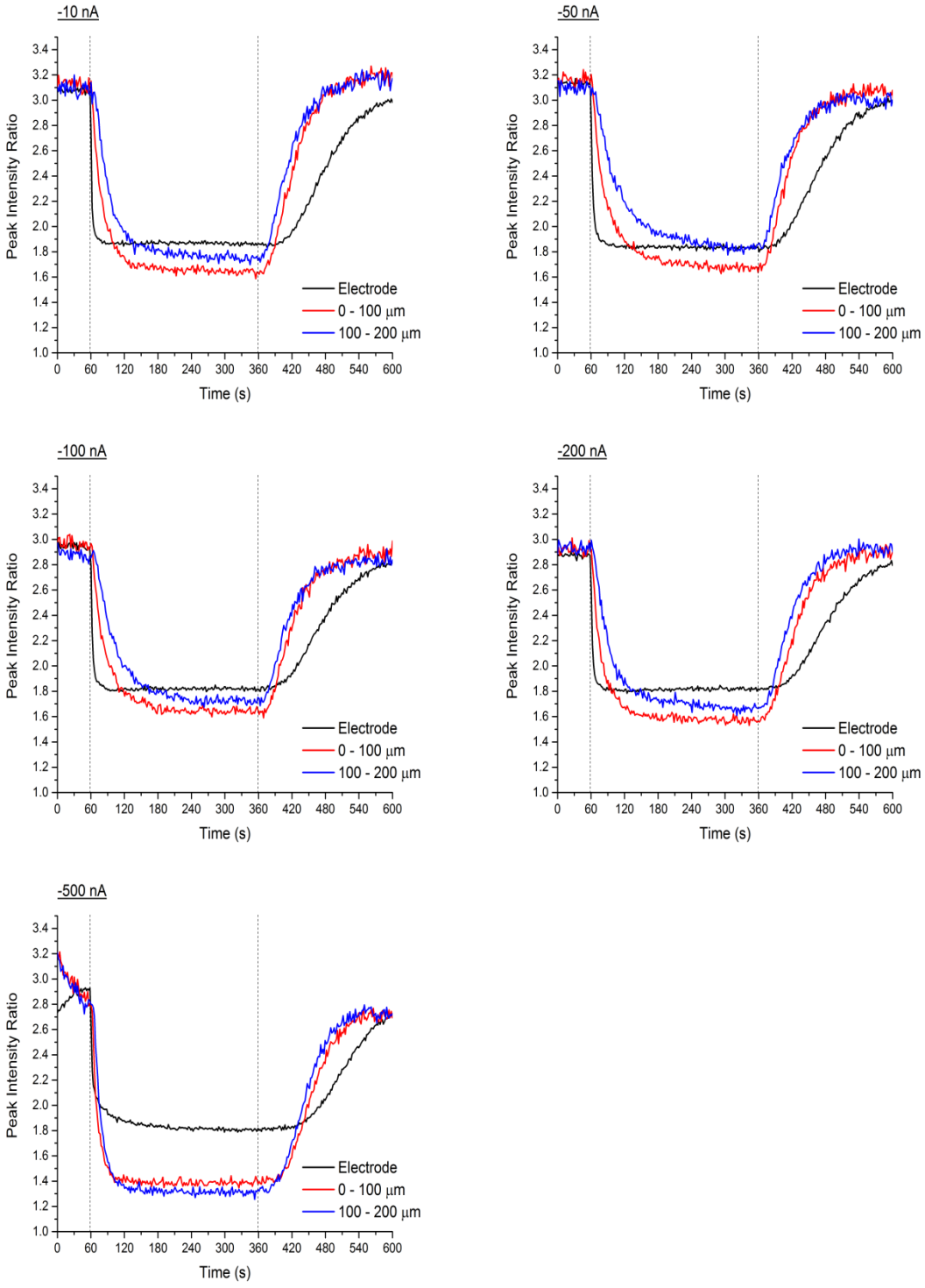

Figure 6.8: Graphs of pH over time showing the effect at the electrode and nearby areas of various negative currents applied for 300 s in water. The current application began after 60 s. In all cases, the current caused a decrease in the peak intensity ratio (corresponding to an increase in pH), as expected.

buffer reduced the change in peak intensity ratio is good evidence that the applied currents were causing pH changes. The voltage trace in Figure 6.5 shows that significantly less potential was needed to drive the current in buffer when compared to the voltage traces in Figure 6.3 for water, as would be expected from the increased ion concentration of the buffer.

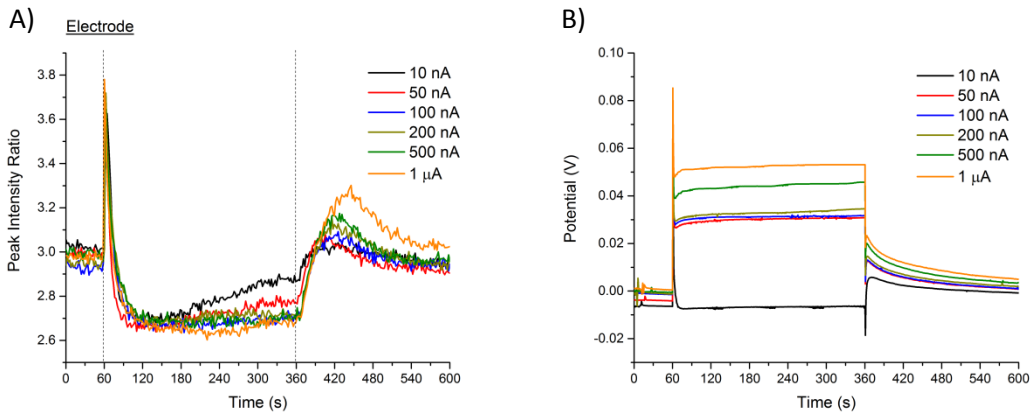

Figure 6.9: Graphs of peak intensity ratio (A) and potential (B) over time showing the effect at the electrode of various positive currents applied for 300 s in water. The data are the same as in Figure 6.8. The current application began after 60 s. In all cases, the current application caused an initial sharp increase in the peak intensity ratio, followed by a decrease to below the original ratio. The reverse behaviour was seen after the current application finished, and the peak size increased with increased current. This implied that the peak was evidence of the pH having decreased below pH 4.

6.3.3. Electrochemical pH control with long current application

Figure 6.6 shows the extent of the pH change in the vertical direction (i.e. perpendicular to the electrode surface) on application of 50 nA and -50 nA currents for 10 minutes in water. In both cases measurable changes in pH reached areas more than 500 µm above the electrode and large changes happened very rapidly in areas closer to the electrodes. Note that in both cases the change in intensity ratio appeared to be smaller at the electrode – this was because the ITO electrodes on this particular slide showed some opacity at 590 nm, leading to distortion of the 590/650 nm peak intensity ratio. This meant that the calibration curve could not be reliably used to determine pH values from the peak intensity ratio, and so the y-axes have been left as peak intensity ratio rather than being converted to pH. For the areas 200 µm above the electrode there was a decrease of 1.2 pH units for 50 nA and an increase of 0.7 pH units for -50 nA. At these distances the change happened rapidly, taking around 35 s to reach a stable value, and then remained stable for the duration of the current. At further distances the pH change contained peaks and troughs. The origin of these is unknown: note that no similar features appeared in the voltage traces, so the peaks and troughs are unlikely to have been caused by fluctuations in the applied current.

Figure 6.7 shows the results of application of current from 10 nA to 1 µA for 300 s in water. Strangely, despite the expected increase in intensity ratio (which corresponds to a decrease in pH) in areas adjacent to the electrode, at the electrode itself the ratio initially increased but then decreased to a value below its pre-current value, i.e. to a value lower than the value before current was applied. At the areas further from the electrode, the pH change behaved as expected, with larger current values reaching a stable value faster: in the region 200 µm from the electrode, a stable pH value was reached after ~ 85 s for 10 nA, decreasing to ~ 30 s for 1 µA. Figure 6.8

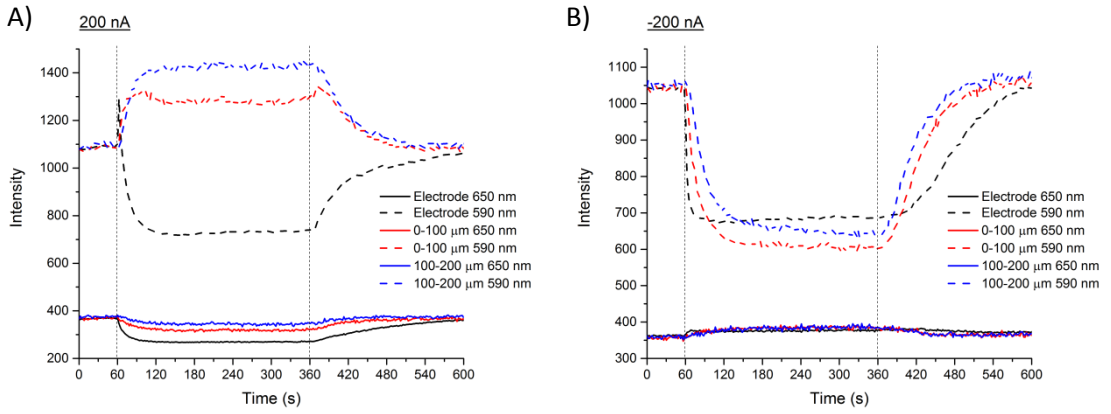

Figure 6.10: Graphs of 590 nm and 650 nm emission intensity over time showing the effect at the electrode and surrounding areas of A) 200 nA and B) -200 nA applied for 300 s in water. The current application began after 60 s. Looking at the calibration curves for the 590 nm and 650 nm emission intensities shown in Figure 6.2, it can be seen that the 200 nA data behaved as expected if the pH decreased below pH 4, i.e. the 590 nm emission initially increased, then decreased, and the 650 nm emission simply decreased. The -200 nA data also behaved as expected: the 590 emission decreased and the 650 nm emission increased.

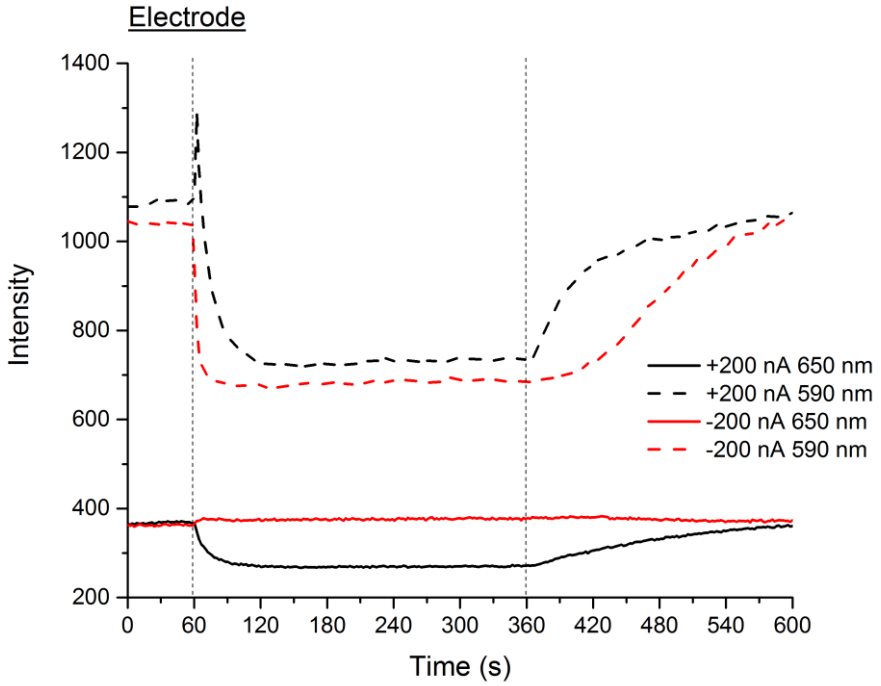

Figure 6.11: Graphs of 590 nm and 650 nm emission intensity over time showing the effect at the electrode of 200 nA and -200 nA applied for 300 s in water. The current application began after 60 s. The data are the same as shown in Figure 6.7. There is a distinct difference in the shape of the 590 nm emission intensity curves after the current application finished, providing evidence that the positive current induced intensity decrease was not caused by an increase in pH.

shows the results of applying the matching negative currents and these behaved as expected in all regions, i.e. a decrease in intensity ratio corresponding to an increase in pH. It was concluded that in the case of positive currents the pH at the electrode must have rapidly increased past pH 4 where the calibration curve reached a maximum and moved into the region at pH < 4 where the intensity ratio began to decrease. This conclusion is supported by a number of observations. First, as the current applied increased to 500 nA and 1 µA, the intensity ratio in the 50 µm region

decreased after the initial increase, implying that these larger currents caused the pH in parts of this area to decrease below pH 4. Second, as can be more clearly seen in Figure 6.8 where the traces for the electrode areas are plotted on the same graph, after the current was switched off, the ratio increased past the original value before returning to it, exactly as expected from the calibration curve if the pH were returning from a value below pH 4. Significantly, the size of the return peak increased with increased currents. The microscope captured light from a volume of solution above the electrode, and as more current was applied, a greater part of that volume would have been at pH < 4. Consequently, a greater part of that volume would have had to return to the original intensity ratio via the peak in the calibration curve and therefore this return would have been seen more clearly for higher current values. Third, by looking at the individual 590 nm and 650 nm emission peaks in Figure 6.10 and comparing their variation with pH to the curves in Figure 6.2, it can be seen that the individual emission intensities behaved exactly as would have been expected for a change to a pH below pH 4. That is, the 590 nm emission intensity initially increased, then decreased, whereas the 650 nm intensity simply decreased. Finally, the different shape of the 590 nm intensity curves after the 200 nA and -200 nA current was stopped, as shown in Figure 6.11, was further evidence that the current-induced intensity decrease for the positive current was not caused by an increase in pH. If it were, one would have expected the shapes of the curves after the current stopped to be similar.

While the above evidence for large decreases in pH at the electrode surface was compelling, it remained clouded by the fact that the measured 'electrode' area actually contained a significant volume of solution above the electrode. To measure the pH change directly at the electrode surface, which is, after all where peptides were to be immobilised for electronic control of peptide interactions, slides with SNARF-4F immobilised directly on the electrode surfaces were created.

6.3.4. Electrode-immobilised SNARF-4F

Figure 6.12 shows the results of electrochemical pH control carried out with SNARF-4F immobilised on the electrode. 1 nA and -1 nA currents were applied for 60 s in water. No SNARF-4F was added to the water, so any changes in fluorescence were necessarily from SNARF-4F immobilised on the electrode surface. z-scans (not shown) were performed before and after current application to ensure the fluorescence was localised at the surface and that no dye had escaped into solution. It can be seen from Figure 6.12 that the application of 1 nA caused an initial increase in intensity ratio, followed by a decrease to below the pre-current intensity ratio, replicating the above behaviour seen with SNARF in solution. The application of -1 nA caused a decrease in intensity ratio corresponding to an increase in pH, as expected, and the individual emission intensities behaved as predicted, i.e. the 590 nm intensity decreased for both positive and negative currents, whereas the 650 nm intensity decreased for positive currents and increased

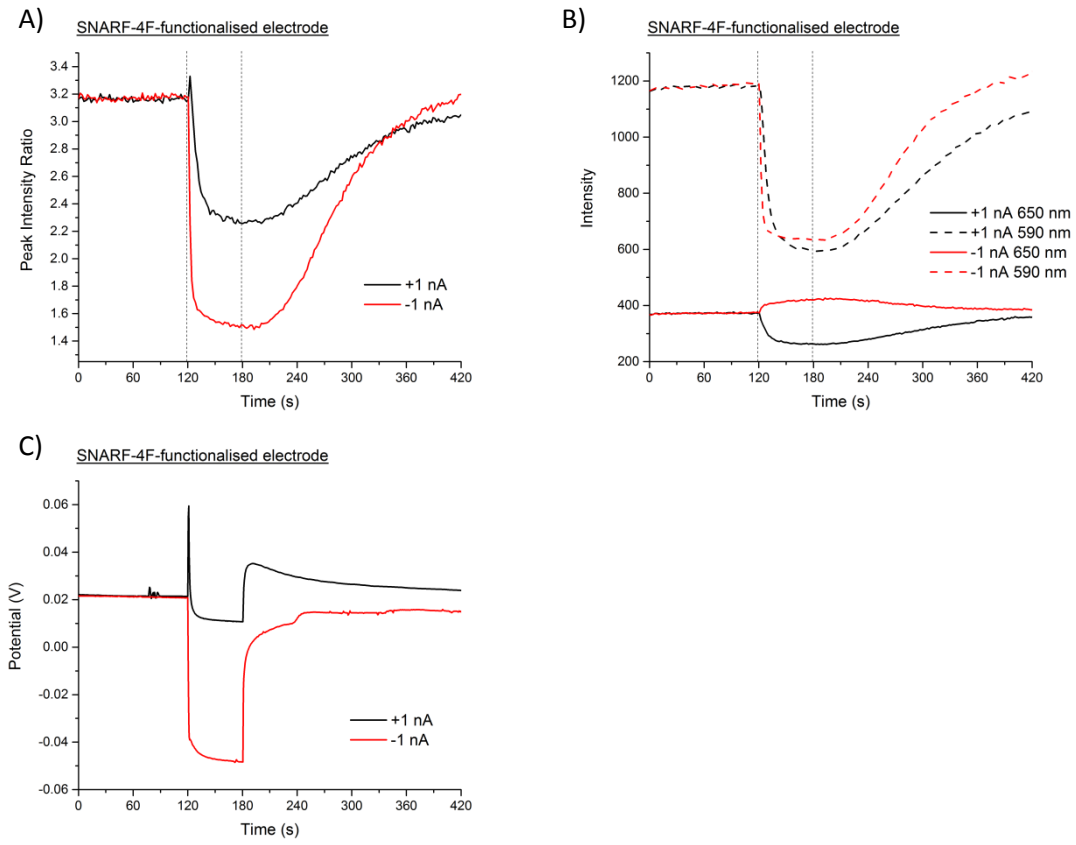

Figure 6.12: Graphs of A) peak intensity ratio, B) 590 nm and 650 nm emission intensities, and C) potential over time showing the effect at the electrode surface of 1 nA and -1 nA applied for 60 s in water. The current application began after 120 s. The SNARF-4F was immobilised on the electrode, so that the measurement was only of changes at the electrode surface. The positive current caused an increase then decrease in the peak intensity ratio, as seen previously.

for negative currents. Therefore, it was concluded that the initial increase and then decrease of the intensity ratio at the electrode was caused by an increase of the pH above pH 4. The fact that the intensities returned to their original values after the current application further confirmed that the SNARF-4F remained immobilised on the electrode, and that the changes in intensity in the solution case were not caused by migration of the dye from the scanned area. Furthermore, the return of the intensities to their original values was evidence that little photobleaching of the monolayer occurred.

As a further test, lower current values were applied. If the intensity increase then decrease behaviour for positive currents had been caused by a decrease in pH to below 4, it should have been possible to show an increase in intensity ratio without the subsequent decrease by applying a small current such that the pH remained above pH 4. Figure 6.13 shows the results of experiments carried out with this aim, which do indeed support the conclusion. Application of 50 pA caused a small increase in intensity ratio, and 100 pA caused a larger increase. An increase in current to 500 pA then caused a decrease in intensity ratio and a further increase to 5 nA caused a larger decrease. Note that the initial sharp increase in intensity ratio was not seen for the larger currents, but this may be because it occurred more rapidly than the 2 s scan time could detect.

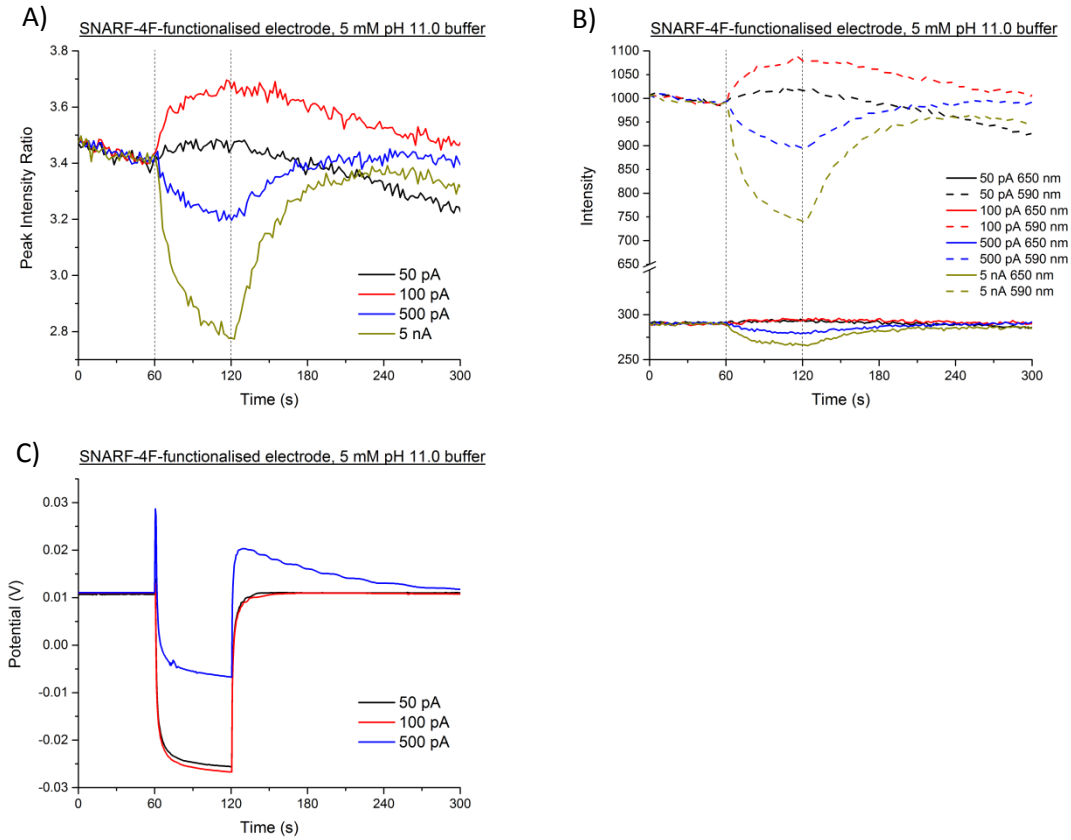

Figure 6.13: Graphs of A) peak intensity ratio, B) 590 nm and 650 nm emission intensities, and C) potential over time showing the effect at the electrode surface of various currents applied for 60 s in water. The current application began after 60 s. The SNARF-4F was immobilised on the electrode, so that the measurement was only of changes at the electrode surface. The positive currents of 500 pA and 5 nA caused a decrease in the peak intensity ratio, signifying a pH decrease below pH 4, whereas the lower currents of 50 pA and 100 pA caused an increase only, signifying a decrease in pH that did not reach below pH 4.

The experiment shown in Figure 6.13 showed that the application of 500 pA caused a decrease of pH below pH 4 at the electrode surface. Note that this experiment was performed in 5 mM pH 11 buffer, meaning that, despite the presence of buffer and the relatively low current used, the pH at the electrode surface must have decreased by over 7 pH units from pH 11 to < pH 4. 500 pA corresponds to a current density of 0.6 mA m^{-2}. A pH change of 7 pH units in weak buffer from a current density of 0.6 mA m^{-2} appears to be significantly larger than has previously been measured in the literature, though it is difficult to find experiments performed in directly comparable situations. Kuhn and Chan's 1983 review of near electrode pH change reports current densities of at least 50 A m^{-2} to achieve pH changes of ~10 pH units, measured using Sb microelectrodes in K_2SO_4.[1] In more recent literature, Rudd *et al*'s finite element modelling of pH change in water appears to predict an increase of at least 5.6 pH units from pH 4.4 in the vicinity of the electrode for a current density of 10 A m^{-2}.[2] However, their results are presented on a mm scale, and not the nm scale measured by the SNARF-4F monolayer technique presented here. The increased size of the pH change measured in this work compared to the literature is likely to

reflect the fact that the SNARF-4F monolayer technique is able to measure pH change closer to the surface of the electrode than any previously reported technique.

Note that a sharp peak is visible in the voltage graphs upon current application in some cases, for example Figure 6.9 and Figure 6.12. However, it was concluded that this voltage peak was not the cause of the initial peak in peak intensity ratio because the shapes of the voltage curves did not mirror the peak intensity ratio curves and intensity curves at other times. For example, there is a sharp change in the voltage traces when the current application is stopped that is not reflected in a sharp change in the peak intensity ratios or intensities. Furthermore, Figure 6.13 shows a sharp initial peak in the voltage trace upon current application that is not evident in the peak intensity ratios or intensities.

6.4. Conclusions

Electrochemical pH control using ITO electrodes was performed, and measured using the pH sensitive fluorescent dye SNARF-4F. First, it was established that SNARF-4F could be used for robust measurement of solution pH by use of a ratiometric calibration curve. It was then shown that applied currents could be used to reversibly alter solution pH, with positive currents causing a decrease in pH and negative currents causing an increase. It was also shown that the size and spatial extent of the pH change depended on the magnitude and duration of the current. Short pulses of current appeared to cause changes of up to 0.7 pH units at the electrode. It was then shown that the use of buffer solution significantly reduced the extent of the pH change, which confirmed that the currents were causing changes in pH. Using longer current application times, relatively stable pH gradients extending up to 1 mm into the solution over long timescales were demonstrated. These appeared to cause changes of up to 1.2 pH units at the electrodes. Finally, it was shown that directly at the surface of the electrode the pH change could be significantly larger than previously detected. This was shown initially by SNARF-4F measurements in solution and then confirmed by measuring the dye when it was immobilised on the electrode surface. A decrease in pH of over 7 pH units for a ~ 1 mA m^{-2} current density appeared to be measured using the surface immobilised SNARF-4F in weak buffer, which was significantly larger than any changes observed in bulk solution, and appears to be larger than any measured pH change for this current density in the literature. Thus it was demonstrated that it would be possible to achieve significant pH changes at electrode surfaces for electronic control of protein interactions.

6.5. References

*1. Kuhn, A. T. & Chan, C. Y. pH changes at near-electrode surfaces. *J. Appl. Electrochem.* **13,** 189–207 (1983).

2. Rudd, N. C. *et al.* Fluorescence Confocal Laser Scanning Microscopy as a Probe of pH

Gradients in Electrode Reactions and Surface Activity microscopy (CLSM) to quantify three-dimensional pH. *Anal. Chem.* **77,** 6205–6217 (2005).

7. Electronic control of peptide interactions

7.1. Introduction

The purpose of the experiments in this chapter was to demonstrate electronic control of peptide interactions using the knowledge obtained from the experiments in previous chapters.

This chapter details the experiments performed to demonstrate electronic control of peptide interactions. The materials and methods used are described in detail in Section 7.2. The effect of applied currents on peptide monolayers was assessed using CLSM and FRET (see Sections 3.3.3 and 3.3.2 respectively). The results of these experiments are presented and discussed in Section 7.3. The findings are summarised in Section 7.4 and references are detailed in Section 7.5.

7.2. Materials and methods

7.2.1. General materials and methods

Unless otherwise indicated, all chemicals were purchased from Sigma-Aldrich. Where the term 'phosphate buffer' is used, it refers to sodium phosphate buffer in 18.2 MΩ deionised H_2O made by mixing Na_2HPO_4 and NaH_2PO_4 in a ratio calculated to produce the desired pH. The pH was then adjusted to the correct value using NaOH or HCl and the buffer filtered using syringes with 0.22 μM filters. pH measurements were performed using a Mettler Toledo MP225 pH meter.

7.2.2. ITO electrode fabrication

All experiments used 1 mm diameter ITO electrodes patterned onto No. 2 thickness glass cover slips. The cover slips were cleaned by rinsing and ultrasonication in, successively, acetone, isopropanol, ethanol and water, then dried under a nitrogen stream. Microposit S1813 photoresist was spin-coated onto the slides and baked at 115 ºC for 2 minutes. The slides were then immersed in chlorobenzene for 2.5 minutes, dried under a nitrogen stream, and then exposed to UV light through the mask pattern using a Karl Suss MJB3 mask aligner. Finally, the slides were immersed in Microposit MF-319 developer solution, rinsed in water and dried, before being sent to Evatech AG (Switzerland) for ITO deposition through electron beam evaporation.

Open-ended hollow glass cylinders were glued to the patterned slides to provide a vessel for solutions.

7.2.3. Peptide immobilisation

ITO surfaces were cleaned by successive rinses and ultrasonication in the following sequence of solvents: acetone, isopropanol, ethanol, water. They were then immersed in piranha

solution (7:3 ratio of sulphuric acid:hydrogen peroxide) for 5 minutes per face then rinsed and ultrasonicated in water, then ethanol, then dried with a nitrogen stream.

The freshly cleaned surfaces were then rinsed and ultrasonicated in isopropanol then incubated in a 2% solution of (3-mercaptopropyl)trimethoxysilane (MPTMS) in isopropanol for at least 18 hours. After silanisation, the surfaces were immersed 10 times in isopropanol then 10 times in ethanol and then incubated in a 1 mM solution of copper (II) perchlorate hexahydrate (CIIPHH) in ethanol for 10 minutes. The surfaces were then immersed 10 times in ethanol then 10 times in 50 mM pH 6 phosphate buffer, then a 30 μM peptide solution in the same phosphate buffer was introduced to the surface and incubated for at least 18 hours.

7.2.4. Surface fluorescence measurements

Fluorescence measurements were performed on an Olympus IX81 Confocal Laser Scanning Microscope with a UPLSAPO 10X NA:0.40 Objective Lens. After initial focusing by eye, z-scans at the donor and acceptor emission wavelengths (508-538 nm and 612-642 nm respectively) were used to find the focal plane to within 0.2 μm. Wavelength scans from 500-700 nm (resolution 2 nm, bandwidth 2 nm) were then performed.

The dyes were excited by a 488 nm Ar laser and emission was passed through a 488 nm dichroic mirror and measured at 523 nm and 627 nm with a bandwidth of 30 nm. Settings used were: 256x256 pixel scan area, corresponding to 1268x1268 μm, 8 μs/pixel scan speed, 50 μm confocal aperture, 800 V photomultiplier tube (PMT) voltage.

7.2.5. Electrochemical pH change

All electrochemical experiments were performed using a 1 mm diameter ITO working electrode, Pt wire counter electrode and Ag/AgCl (3.5 M KCl) reference electrode. Current and voltage were controlled and measured using a PalmSens potentiostat. Based on the geometric area of the working electrodes used in all experiments, a current of 1 μA corresponded to a current density of ~ 1.27 A m^{-2}.

7.2.6. pH dependence of K4C-L emission

To assess the dependence of K4C-L emission on pH, a 30 μM solution of K4C-L in 50 mM phosphate buffer was measured using wavelength scans as described in Section 7.2.4 with the scan speed decreased to 12.5 μs/pixel. 50 scans were then taken and averaged at 523 nm and 627 nm with a bandwidth of 30 nm as described in Section 7.2.4 with the PMT voltage reduced to 440 and 500 V, respectively. After each fluorescence measurement, 1-5 μL concentrated NaOH was added in situ and the pH measured before the next fluorescence measurement.

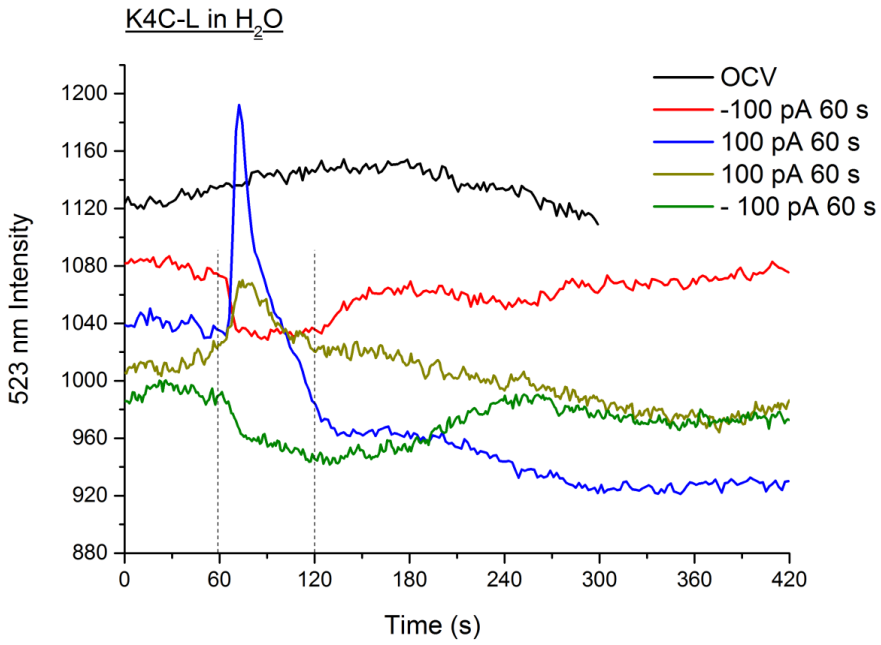

Figure 7.1: Graph showing the effect on the 523 nm emission intensity of a K4C-L monolayer in water of -100 pA and 100 pA currents applied for 60 s to the electrode on which the monolayer was immobilised. Traces labelled OCV are those for which no current was applied. Current application began after 60 s. Unexpectedly, the currents caused changes in the emission intensity. In all but the first 100 pA application the change in emission intensity was reversible, implying that it was caused by the pH change. The apparent large irreversible change seen for the first 100 pA application may be an artefact caused by the instability of the equipment, or may indicate a loss of some peptide from the monolayer. However, the fact that subsequent current applications still showed the change in emission indicated that the monolayer was not removed by current application.

7.3. Results and discussion

A control experiment using a K4C-L monolayer with no E4-L was performed initially to assess the effect of electrochemical pH change on the immobilised K4C-L peptides. The purpose was chiefly to check that the monolayer would not be desorbed by the current application. The results are shown in Figure 7.1. -100pA and 100 pA currents were applied to the electrode for 60 s each and the effect on the K4C-L emission was recorded. Unexpectedly, the emission of the peptides was reversibly affected by the current. Application of negative current caused a decrease in emission intensity for the duration of the current followed by recovery of the emission intensity, whereas application of positive current caused a peak in emission intensity. The first application of positive current appeared to cause an irreversible decrease in emission intensity but this was possibly due to the instability of the apparatus, as evidenced by the significant change in intensity over time in the OCV scan where no current was applied. The fact that subsequent scans retained the pH dependent emission implied that the decrease in intensity seen in the first application of positive current did not correspond to a complete loss of peptide and/or dye from the monolayer. Since the peptide and dye monolayer remained on the surface, the conclusion was that K4C-L emission was pH dependent. To check this, the emission of a 30 μM K4C-L solution was measured across the pH range 7-13. The results are shown in Figure 7.2. The emission of K4C-L was confirmed to be dependent on pH, decreasing rapidly as the pH increased above pH 11. It

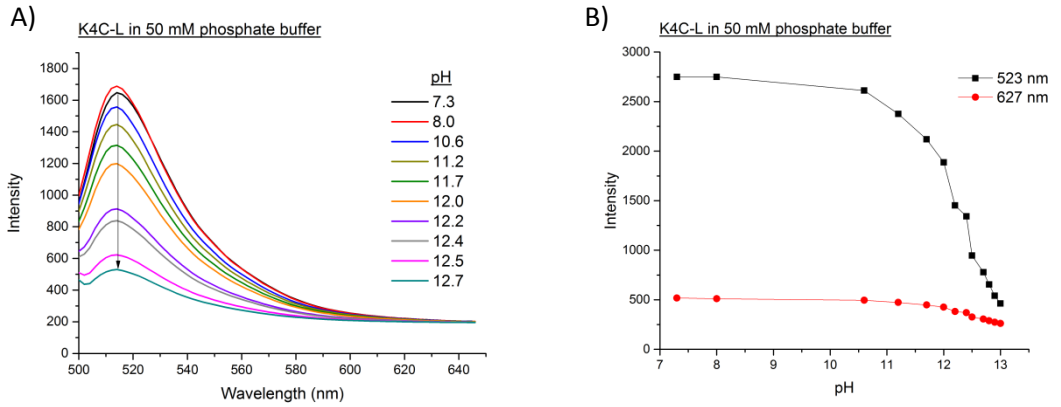

Figure 7.2: Graphs showing effect of increasing pH on K4C-L emission. A) emission spectra. B) plots of 523 nm and 627 nm emission intensity. Above pH 11 the emission of the labelled peptide decreased rapidly.

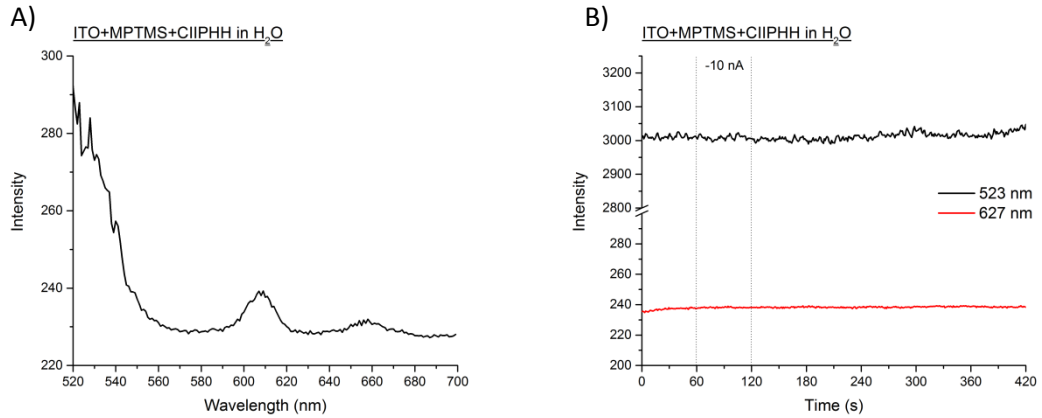

Figure 7.3: Graphs showing the emission spectra of an ITO electrode with a monolayer of MPTMS and CIIPHH in water (A) and effect of -10 nA current applied for 60 s (B) to the same electrode. Current application began after 60 s. The peaks in the emission spectra were caused by reflection of the excitation light. The application of current had no effect on the emission. Any changes in emission caused by application of current to electrodes with immobilised peptides were therefore from the peptides.

was concluded therefore that the changes seen in K4C-L monolayer emission were due to electrochemical pH change, and in particular that the negative currents caused a significant increase in pH. A further control experiment, with results shown in Figure 7.3, confirmed that ITO electrodes with a silane-copper monolayer, but without K4C-L or E4-L, showed no changes in emission on application of current.

Figures 7.4 and 7.5 show the results of applying current to electrodes in water with a monolayer of preformed K4C-L+E4-L heterodimers. Figure 7.4 shows the measured donor and acceptor emission intensities while the current was applied and Figure 7.5 shows wavelength scans taken after each experiment. Open circuit voltage (i.e. no application of current) for 7 min did not lead to any significant change in emission intensity at either wavelength. However, the application of -1 nA for 60 s caused a significant decrease in the 627 nm emission intensity, and the intensity did not recover after the current application stopped, indicating that the bound E4-L had been removed. A small increase in the 523 nm intensity also occurred upon application of

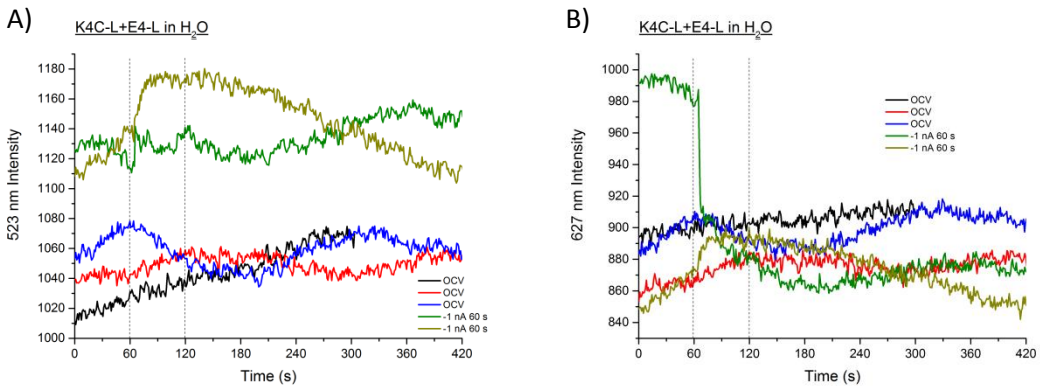

Figure 7.4: Graphs showing the effect on the A) 523 nm and B) 627 nm emission intensities of a K4C-L+E4-L monolayer in water of -1 nA currents applied for 60 s to the electrode on which the monolayer was immobilised. Traces labelled OCV are those for which no current was applied. Current application began after 60 s. The first application of -1 nA caused little change to the 523 nm emission intensity, but a significant, irreversible decrease to the 627 nm emission intensity, implying that the current caused the removal of E4-L peptide from the monolayer. A subsequent application of -1 nA caused a reversible increase in both the 523 nm and 627 nm intensities, indicating that the K4C-L monolayer remained immobilised on the electrode.

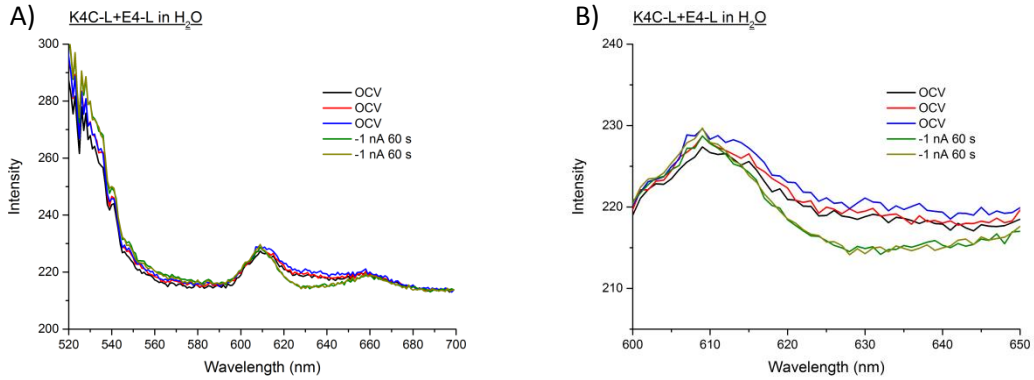

Figure 7.5: A) Graph showing the effect on the emission spectra of a K4C-L+E4-L monolayer in water of -1 nA currents applied for 60 s to the electrode on which the monolayer was immobilised. B) a close-up of the 600-650 nm region. Traces labelled OCV are those before which no current was applied. After the first application of -1 nA current, the 627 nm emission had decreased significantly, and the 523 nm emission had increased, indicating the removal of E4-L peptides from the monolayer. The spectrum after a second -1 nA current application shows no additional change, indicating that all E4-L peptide was removed from the monolayer by the first current application.

current, but was difficult to distinguish from the noise. Close inspection of Figure 7.5 confirms an increase in intensity at 523 nm and a decrease at 627 nm.

The same current was then applied again. In this case, an increase in 523 nm emission intensity was clearly visible, followed by a decrease to the original intensity once the current stopped. Since no fluorescence was observed from the ITO or silane-copper attachment molecules, see Figure 7.3, this pH dependent fluorescence must have been caused by the K4C-L monolayer. From the results shown in Figure 7.1, a decrease in 523 nm emission intensity would have been expected so it is unclear why an increase was seen. Nevertheless, since pH dependent emission was observed, the current application must not have caused removal of the entire peptide monolayer, but instead must have specifically removed the E4-L. Figure 7.5 shows no difference between the spectra taken after the first current application and after the second current application, implying the complete removal of all bound E4-L by the first current application. It

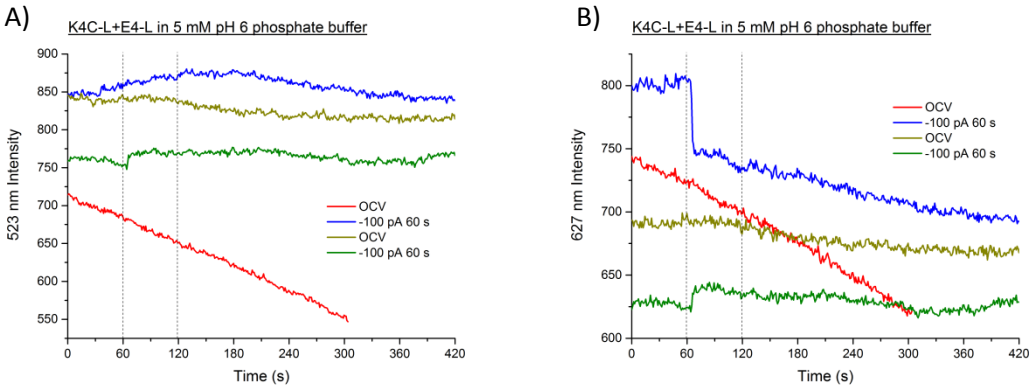

Figure 7.6: Graphs showing the effect on the A) 523 nm and B) 627 nm emission intensities of a K4C-L+E4-L monolayer in 5 mM pH 6 phosphate buffer of -100 pA currents applied for 60 s to the electrode on which the monolayer was immobilised. Traces labelled OCV are those for which no current was applied. Current application began after 60 s. The first application of -100 pA caused little change to the 523 nm emission intensity, but a significant, irreversible decrease to the 627 nm emission intensity, implying that the current caused the removal of E4-L peptide from the monolayer. A subsequent application of -100 pA caused a reversible increase in both the 523 nm and 627 nm intensities, indicating that the K4C-L monolayer remained immobilised on the electrode.

was known from the results shown in Chapter 5 that the binding of E4-L to K4C-L monolayers was pH dependent, and from the results shown in Chapter 6 that applying negative currents caused significant increases in pH at the electrode surface. It was therefore a reasonable conclusion that the results shown in Figures 7.4 and 7.5 indicated that the bound E4-L was removed by an electrochemically generated increase in pH, and that electronic control of peptide interactions had been achieved. However, a number of additional experiments were performed to test the conclusion.

Firstly, the experiment was then repeated in 5 mM pH 6 phosphate buffer, with results shown in Figures 7.6 and 7.7. If the removal of E4-L from the monolayer was caused by a pH change it was to be expected that increasing the buffer strength would prevent E4-L removal by limiting the pH change. However, the first application of -100 pA current caused a significant irreversible decrease in 627 nm emission with barely any change to the 523 nm emission intensity, indicating the removal of bound E4-L. A subsequent application of the same current then caused a noticeable increase in both 523 nm and 627 nm emission intensities, confirming retention of the K4C-L on the electrode.

Note that the current used in the case of buffer was -100 pA rather than the -1 nA used with water. Since -100 pA current was sufficient to remove all bound E4-L from the monolayer in buffer, where pH change should have been reduced, it can be concluded that -1 nA was significantly in excess of the current that would have been required to remove the E4-L from the monolayer in water. Alternatively, it might have been the case that the removal of E4-L was not caused by a pH change. The buffer strength was therefore increased again.

The experiment was repeated in 50 mM pH 6 phosphate buffer. The results are shown in Figure 7.8. Application of a range of currents from -100 pA to -100 nA caused decreases in the 627 nm emission intensity that recovered swiftly once the current stopped. This suggests that the

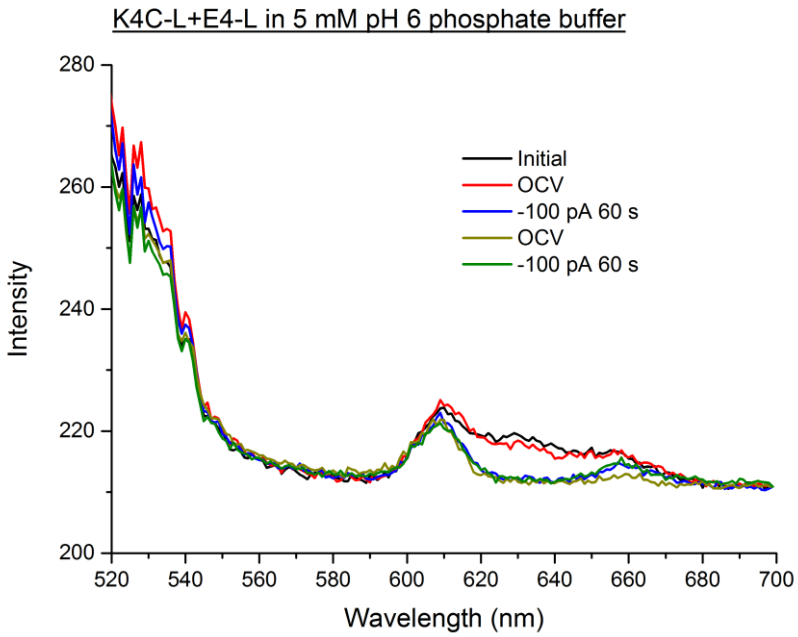

Figure 7.7: Graph showing the effect on the emission spectra of a K4C-L+E4-L monolayer in 5 mM pH 6 phosphate buffer of -100 pA currents applied for 60 s to the electrode on which the monolayer was immobilised. Traces labelled OCV are those before which no current was applied. After the first application of -100 pA current, the 627 nm emission had decreased significantly, indicating the removal of E4-L peptides from the monolayer. The subsequent spectra after OCV and a second -100 nA current application shows no recovery or additional change, indicating that all E4-L peptide was permanently removed from the monolayer by the first current application.

E4-L was not removed from the monolayer. The absence of any significant change in the 523 nm emission intensities (not shown) supports this conclusion. The results shown in Figure 7.1 suggest that negative currents (i.e. an increase in pH) caused a decrease in 523 nm emission intensity. However, if E4-L was present in the monolayer, any changes in the 523 nm emission intensity would have been seen in the 627 nm emission intensity because of FRET, i.e. a reduction in 523 nm emission would have corresponded to a reduction in the energy non-radiatively transferred from the donor to the acceptor and therefore would have resulted in less donor (627 nm) emission. Since increasing the buffer strength prevented the removal of E4-L, it can be concluded that the removal of E4-L in weakly buffered solutions and water was caused by a pH change, as intended.

To further confirm this, the experiment was repeated without current application. Instead, the pH was changed through replacing the buffer solution. The results are shown in Figure 7.9. Some E4-L was removed by pH 9 and pH 10 buffers, with complete removal achieved at pH 11. Therefore, it can be concluded that the application of current in water and 5 mM buffer caused an increase in pH to a value > pH 10 and that this pH change caused the removal of bound E4-L from the K4C-L monolayer.

7.4. Conclusions

The results obtained in this section demonstrate electronic control of peptide-peptide interactions, specifically the removal by application of negative currents of bound E4-L from

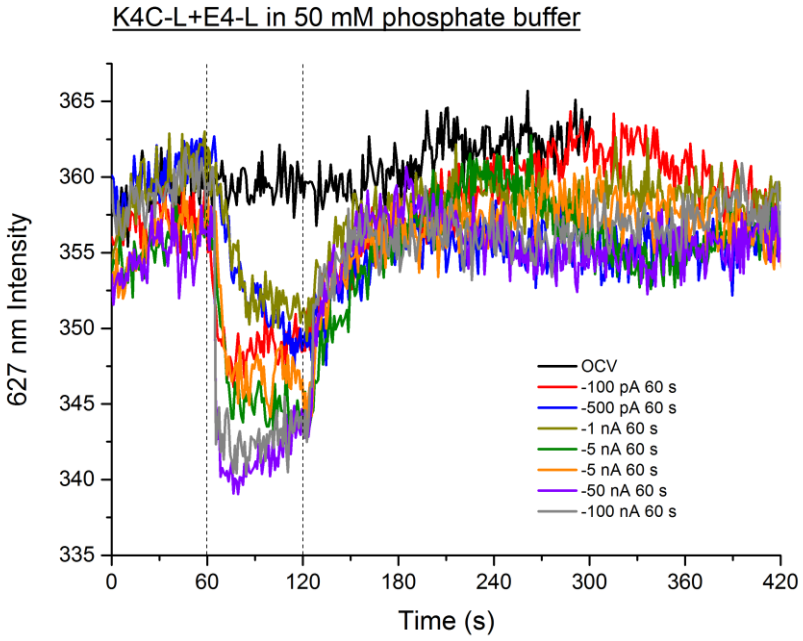

Figure 7.8: Graphs showing the effect on the 627 nm emission intensities of a K4C-L+E4-L monolayer in 50 mM pH 6 phosphate buffer of various negative currents from -100 pA to -100 nA applied for 60 s to the electrode on which the monolayer was immobilised. Traces labelled OCV are those for which no current was applied. Current application began after 60 s. Application of current caused little distinguishable change to the 523 nm emission intensity (not shown), and a reversible decrease to the 627 nm emission intensity. The magnitude of the decrease increased with increasing current. Figure 7.1 shows that negative currents caused a decrease in 523 nm emission. When E4-L peptides were present, 523 nm emission was non-radiatively transferred to excite the E4-L dye and cause 627 nm emission. This explained the decreases seen, and their reversibility indicated that E4-L was not removed from the monolayer. This implied that the increased buffer strength reduced the magnitude of the pH change, as expected.

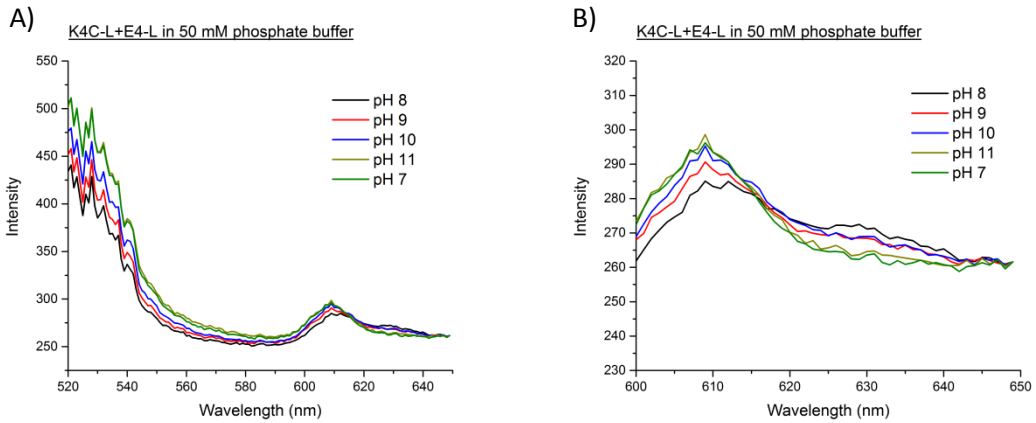

Figure 7.9: A) Graph showing the effect of various pH values on the emission spectra of a K4C-L+E4-L monolayer in 50 mM phosphate buffer. B) a close-up of the 600-650 nm region. Complete removal of E4-L peptide was seen at pH 11, indicated by a significant decrease in 627 nm emission intensity and a significant increase in 523 nm emission intensity. No recovery was seen on changing the buffer to pH 7. This indicated that the applied currents in previous experiments caused an increase in pH to greater than pH 11 when E4-L peptides were removed.

K4C-L monolayers immobilised on electrode surfaces. It was found that the emission of K4C-L was pH sensitive, with significant decreases in emission intensity above pH 11. It was demonstrated that application of current did not cause the K4C-L peptides to be removed from the electrode surface and that the underlying ITO electrode and silane-copper monolayer had no pH sensitive emission. It was then shown that application of -1 nA current for 60 s to an electrode with a monolayer of K4C-L and E4-L in water caused an increase in K4C-L emission and an

irreversible decrease in E4-L emission, indicating the removal of E4-L from the monolayer. Similar results were achieved in 5 mM pH 6 phosphate buffer using -100 pA current, indicating that E4-L was removed under these conditions. The use of 50 mM pH 6 phosphate buffer prevented the removal of E4-L for currents up to -100 nA, providing support to the conclusion that pH change was responsible for the E4-L removal in the previous experiments. An experiment using pH change by manual buffer exchange demonstrated that E4-L was removed at pH 11. This compared well with the results from previous chapters, and indicated that the pH was raised to pH 11 or greater by the current applications that caused E4-L removal.

Thus it was confirmed that, as intended, the mechanism for electronic control of peptide interactions was an electrochemically generated pH change that triggered the pH dependent binding of the peptides. Therefore, the objective of the present work was achieved.

8. Conclusions and further work

8.1. Summary and conclusions

The aim of this work was to demonstrate the feasibility of electronic control of protein interactions by controlling the interaction of a pair of coiled coil peptides through electrochemical pH change. This aim was achieved.

Chapter 1 explained the motivations for the project, detailing the possible academic, industrial and medical applications of techniques for electronic control of protein interactions. Chapter 2 contained background information and the literature review. In particular, it gave details of coiled coil peptides and electrochemical pH control, which formed the basis of this work. Chapter 3 explained the experimental techniques used in the project.

Chapters 4-7 presented the results of the experimental work performed. In Chapter 4 details of the design and synthesis of the E4/K4 coiled coil peptides were given. Four peptides were synthesised, and fluorescently labelled versions of each were produced. E4 and K4 were the standard forms of the acidic and basic coiled coil peptides, respectively. E4P was a version of E4 with a proline residue in place of a hydrophobic core residue. This was designed to act as a control peptide that could not form coiled coils. K4C was a version of K4 with a cysteine residue at the C-terminal to allow immobilisation on surfaces using thiol chemistry. The peptides were synthesised, labelled and purified successfully. It was found that E4 was insoluble at low pH. For this reason, the interactions of E4 and K4 were studied primarily in the neutral to high pH range in this project. Solution-phase characterisation of the peptides was performed by CD and FRET studies. As intended, E4P did not form coiled coils with K4. K4 and K4C peptides were found to form homodimeric coiled coils at neutral pH but had a preference for heterodimeric E4+K4(C) coils in mixed solutions. It was then found that the melting temperatures of E4+K4 and E4+K4C coils were stable over the range pH 5-10 and pH 5-9, respectively, and that they decreased at higher pH values. Conversely, the melting temperatures of K4 and K4C increased as the pH increased. This indicated that K4 and K4C formed increasingly stable homodimers as the pH increased, and that E4+K4 and E4+K4C heterodimers became increasingly unstable as the pH increased. FRET measurements showed that E4+K4C heterodimers had a stable dissociation constant across the range pH 7.5-11, but become destabilised at higher pH values. Overall, the results indicated that K4 and K4C homodimers were preferentially formed over E4+K4 and E4+K4C heterodimers at high pH, but that the heterodimers were preferentially formed at neutral pH. This was a positive result, as it indicated that peptide interactions could be controlled by solution pH. In summary, a pair of peptides E4 and K4 with pH dependent interactions were successfully designed and synthesised along with variants and labelled versions.

Chapter 5 detailed the characterisation of the peptide interactions when K4C peptides were immobilised on surfaces. This was important because the final electronic control of peptide

interaction experiments were to be performed with K4C peptides immobilised on electrodes. The characterisation was performed using FRET, SPR and surface CD. These studies confirmed that the pH dependent interactions of E4 and K4C were retained when K4C was immobilised on surfaces. Specifically, E4 could be removed from monolayers of E4/K4C coils by washing with high pH 10-12 buffer. SPR and CD results indicated that the pH at which E4 dissociated from E4+K4C monolayers was affected by the conditions under which the K4C monolayer was formed. Monolayers formed in conditions expected to lead to high packing densities (such as high pH and high concentration) showed lower dissociation pH values. It was concluded that this was because interactions between E4 and K4C in more dense monolayers were weaker than in less dense monolayers. It was also demonstrated that high-quality CD spectra could be obtained from peptide monolayers. In summary, surface immobilised K4 peptides were shown to have pH dependent interactions with E4 peptides.

Chapter 6 detailed the studies of electrochemical pH control. It was demonstrated that a pH sensitive fluorescent dye could be used to detect and map pH. It was confirmed that the pH of solution in the vicinity of the electrode could be controlled by application of currents, and that the magnitude, duration and direction of the current affected the resultant pH changes. As expected, positive currents led to decreases in pH and negative currents led to increases in pH. Increasing the magnitude or duration of the currents caused the pH changes to increase in magnitude and distance. The use of buffer was shown to significantly reduce the extent of the pH changes. Finally, evidence was obtained that suggested that in the immediate vicinity of the electrode surface, the pH changes could be significantly larger than those observed in the solution above. In summary, it was shown that the pH of a solution near an electrode surface could be controlled electronically.

Chapter 7 combined the lessons learned in the previous chapters to demonstrate electronic control of peptide interactions. It was shown that the application of negative currents to electrodes on which E4+K4C monolayers had been immobilised caused dissociation of the E4 from the monolayer. Control experiments demonstrated that this was caused by the increase in pH caused by the application of the negative current. In summary, the interactions of peptides were controlled electronically. Therefore the objective of the project was achieved.

8.2. Further work

This project was intended to demonstrate that electronic control of protein interactions was possible using electrochemical pH control. Since the work performed did indeed show this, there are now many possibilities for further work.

Initial work might focus on solidifying and expanding the current work with coiled coil systems. It would be useful, as was always intended, to demonstrate that the application of

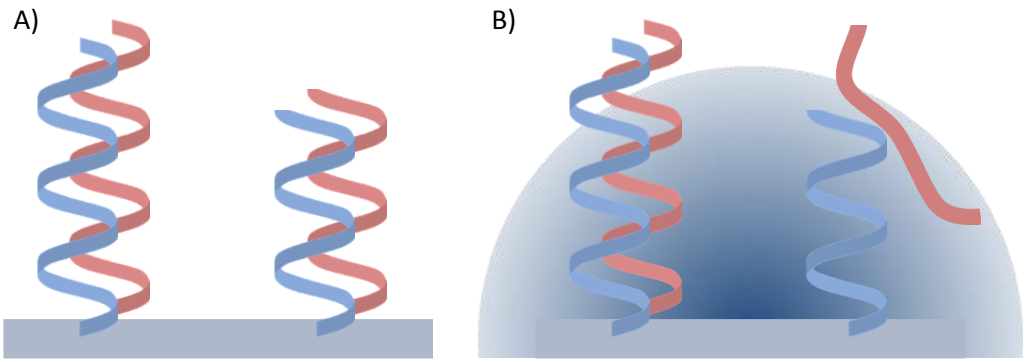

Figure 8.1: Illustration of fine control of pH using coiled coils of different lengths. A) A long coiled coil heterodimer and a short coiled coil heterodimer would be immobilised on an electrode. The longer coil would have a stronger interaction such that there would be a certain range of basic pH values where the shorter coil would dissociate and the longer coil would not. B) By applying a current such that the shorter coil would dissociate and the longer coil would not, it could be demonstrated that fine control of pH is possible.

positive currents to decrease pH could also control peptide interactions. It was hoped that E4 homodimers would preferentially form over E4/K4 heterodimers at acidic pH, but the insolubility of E4 at low pH made this impossible to demonstrate. However, a number of coiled coil systems with soluble acidic homodimers have been reported, for example the ACID/BASE system of O'Shea *et al*,[1] and these could be used to show that electronic control of peptide interactions is possible with both positive and negative currents. This would also provide further evidence for pH control being the mechanism for peptide dissociation from the monolayer. For example, if it could be shown that positive currents (i.e. decreases in pH) caused dissociation of E4 from K4 monolayers but not of E4 from E4 monolayers, and that negative currents (i.e. increases in pH) caused dissociation of E4 from K4 monolayers but not of K4 from K4 monolayers, then this would be very compelling evidence that pH changes were the factor affecting the peptide interactions. To demonstrate the dissociation of homodimers using FRET it would of course be necessary to prepare, for example, K4 peptides labelled with both ATTO 488 and ATTO 594 (i.e. both dyes in a FRET pair).

There are other possible techniques for demonstrating the dissociation of peptides from monolayers. For example, surface CD was used in this work to study the dissociation of E4 from K4 monolayers when the pH was changed manually by buffer exchange. It might also be possible to change pH electrochemically and measure dissociation using CD. This could give valuable information about the changing structure of the monolayer as the peptides dissociate. Though the spectra obtained in this work were not of high enough quality to draw structural conclusions, promising steps were made towards high quality surface CD spectra and further work in this area could be very fruitful. Quartz crystal microbalance with dissipation monitoring (QCM-D) is another technique that could be used to obtain information about dissociation and structural changes in the monolayer.

Other work might focus on demonstrating finer electrochemical control of pH. Appendix 1 details experiments carried out to demonstrate the possibility of controlling pH with multiple

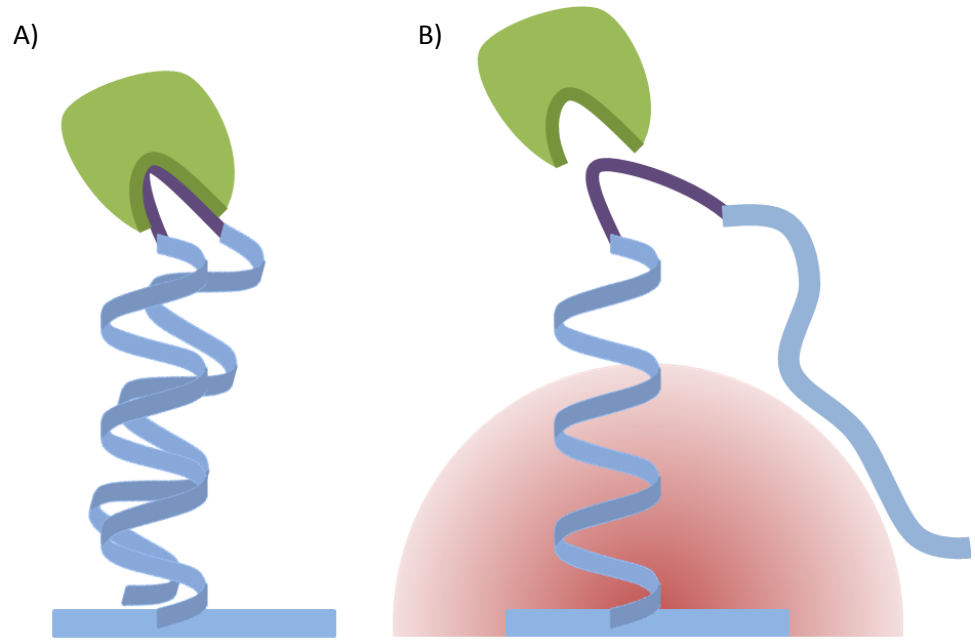

Figure 8.2: Illustration of electronic control of coiled coil peptide interactions for switchable binding of a target molecule. Two basic coiled coil peptides (blue) would be linked by a peptide sequence (purple) with conformational affinity for a target molecule (green). One of the peptides would be immobilised on an electrode. A) in high pH solution the peptides would form a coiled coil, forcing the binding sequence into a tight loop which would bind the target molecule. B) a current would be applied to the electrode to lower the pH to an acidic value. This would cause the coiled coil to dissociate, meaning that the binding sequence would lose its shape and the target molecule would be released.

electrodes, which could be used for more precise pH control. As another example, peptides known to dissociate at one pH might be immobilised on one region of an electrode, and peptides known to dissociate at a higher pH might be immobilised on another. By applying a current that only caused dissociation on one of the regions, it could therefore be demonstrated that pH could be precisely controlled, see Figure 8.1. It has already been demonstrated that reducing the lengths of K4 and/or E4 leads to a range of interaction strengths.[2] These differing interaction strengths might lead to differing dissociation pH values. Alternatively, the dissociation pH might be modified by using different residues in the *e* and *g* positions. Yet another approach might expand on the work performed in Chapter 5 that demonstrated control of the dissociation pH through modification of the monolayer density. For example, one region of an electrode could contain K4C peptide immobilised at low pH/concentration to form a low density monolayer and the other region could contain K4C peptides immobilised at high pH/concentration to form a high density monolayer. It would then be expected that pH values in a certain range would cause dissociation of E4 from the high density monolayer but not the low density monolayer. Successful demonstration of fine pH control using these approaches might require a more robust system for pH measurement at the surface of the electrode than the immobilised SNARF-4F approach used in this work. One option might be electrochemical measurement of pH. Initial experiments using the molecule methylene blue immobilised on electrode surfaces showed that it had pH sensitive redox activity, see Appendix 2, so this might be a useful approach.

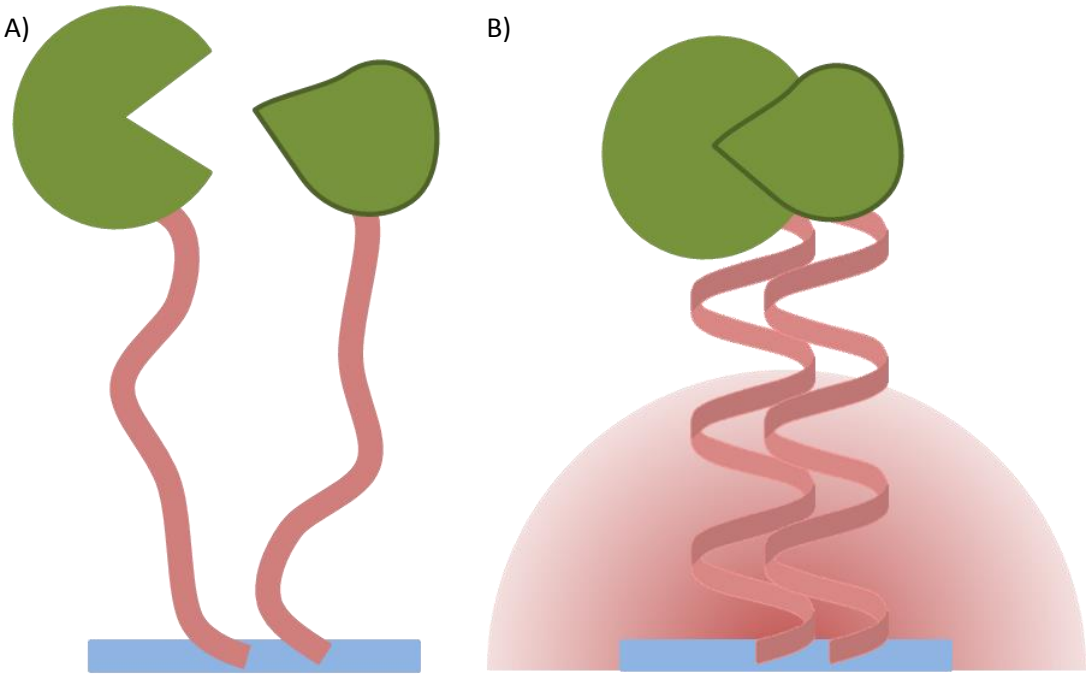

Figure 8.3: Illustration of electronic control of coiled coil peptide interactions for switchable enzyme activity. Two acidic coiled coil peptides (red) would be immobilised on an electrode, with each peptide linked to a portion of a split enzyme (green). A) in neutral pH solution the peptides would not form a coiled coil and the enzyme portions would not come together. B) a current would be applied to the electrode to lower the pH to an acidic value. This would cause the coiled coil to form, bringing the enzyme portions together into a complete assembly. Thus the activity of the enzyme could be enabled by the applied current.

Beyond further confirming the conclusions of this project, future work might focus on applications of electronic control of protein interactions. Initially, this might be achieved using coiled coil peptides as a basis. For example, a pair of coiled coils (e.g. K4C and K4) linked by a short binding loop could be designed. The loop would be a short sequence of residues designed to bind to a target when folded as a loop and to unbind when unfolded. The coil-loop-target complex would be immobilised on an electrode via one of the coils (i.e. K4C). A positive current would be applied to decrease the pH and cause dissociation of the K4 peptide. This in turn would cause the loop to lose its folded structure and release the target, see Figure 8.2. Thus electronic binding and release of a target molecule could be achieved.

Coiled coils have already been used to facilitate and control split enzyme systems, see Chapter 2.[3,4] In another example of further work, a split enzyme system could be used in which two halves of an enzyme are attached to coiled coil peptides immobilised on an electrode. For example, if E4 peptides were used, the coil wouldn't form at neutral pH and the enzyme halves would be separated. Applying a current to the electrode to decrease the pH would allow the coil to form and bring the enzyme halves together to form the complete enzyme, see Figure 8.3. Hence an electronically switchable enzyme chip could be achieved. Of course, it might also be possible to switch a pH sensitive enzyme purely through electrochemical pH control without the need for using coiled coils. Both systems would certainly merit investigation. Looking further ahead, the

academic, industrial, and medical applications suggested in Chapter 1 could be investigated, for example devices to aid proteomics research, or hybrid computing devices.

8.3. References

*****1. O'Shea, E. K., Lumb, K. J. & Kim, P. S. Peptide 'Velcro': design of a heterodimeric coiled coil. *Curr. Biol.* **3,** 658–67 (1993).

*2. Thomas, F., Boyle, A. L., Burton, A. J. & Woolfson, D. N. A Set of de Novo Designed Parallel Heterodimeric Coiled Coils with Quantified Dissociation Constants in the Micromolar to Sub-nanomolar Regime. *J. Am. Chem. Soc.* **135,** 5161–5166 (2013).

3. Shekhawat, S. S., Porter, J. R., Sriprasad, A. & Ghosh, I. An autoinhibited coiled-coil design strategy for split-protein protease sensors. *J. Am. Chem. Soc.* **131,** 15284–90 (2009).

4. O'Hare, H., Juillerat, A., Dianisková, P. & Johnsson, K. A split-protein sensor for studying protein-protein interaction in mycobacteria. *J. Microbiol. Methods* **73,** 79–84 (2008).

A1. Electrochemical pH control with competing electrodes

A1.1. Introduction

This appendix chapter details investigations into electrochemical pH change using competing electrodes. For background, see Section 2.4. The materials and methods used in this chapter are described in Section A1.2. The investigations were carried out using CLSM (see Section 3.2.3). The results of the experiments are presented in Section A1.3. The findings are summarised in Section A1.4.

A1.2. Materials and methods

A1.2.1. General materials and methods

Unless otherwise indicated, all chemicals were purchased from Sigma-Aldrich.

The pH sensitive fluorescent dye SNARF®-4F 5-(and-6)-carboxylic acid (referred to as SNARF-4F henceforth) was purchased from ThermoFisher Scientific and stored frozen in aliquots of 18.2 MΩ deionised H_2O. The concentration of the dye in solution was 100 μM in all experiments.

A1.2.2. ITO electrode fabrication

All experiments used 1 mm diameter ITO electrodes patterned onto No. 2 thickness glass cover slips. The cover slips were cleaned by rinsing and ultrasonication in, successively, acetone, isopropanol, ethanol and water, then dried under a nitrogen stream. Microposit S1813 photoresist was spin-coated onto the slides and baked at 115 ºC for 2 minutes. The slides were then immersed in chlorobenzene for 2.5 minutes, dried under a nitrogen stream, and then exposed to UV light through the mask pattern using a Karl Suss MJB3 mask aligner. Finally, the slides were immersed in Microposit MF-319 developer solution, rinsed in water and dried, before being sent to Evatech AG (Switzerland) for ITO deposition through electron beam evaporation.

Open-ended hollow glass cylinders were glued to the patterned slides to provide a vessel for solutions.

A1.2.3. Electrochemical pH change

All electrochemical experiments were performed using 1 mm diameter ITO working electrodes, Pt wire counter electrodes and Ag/AgCl (3.5 M KCl) reference electrode. Current and voltage were controlled and measured using a PalmSens potentiostat. For the second working electrode, a second identical Pt wire counter electrode was also used, and current was controlled using a Keithley 2400 SourceMeter. Based on the geometric area of the working electrodes used in all experiments, a current of 1 μA corresponded to a current density of 1.27 A m^{-2}.

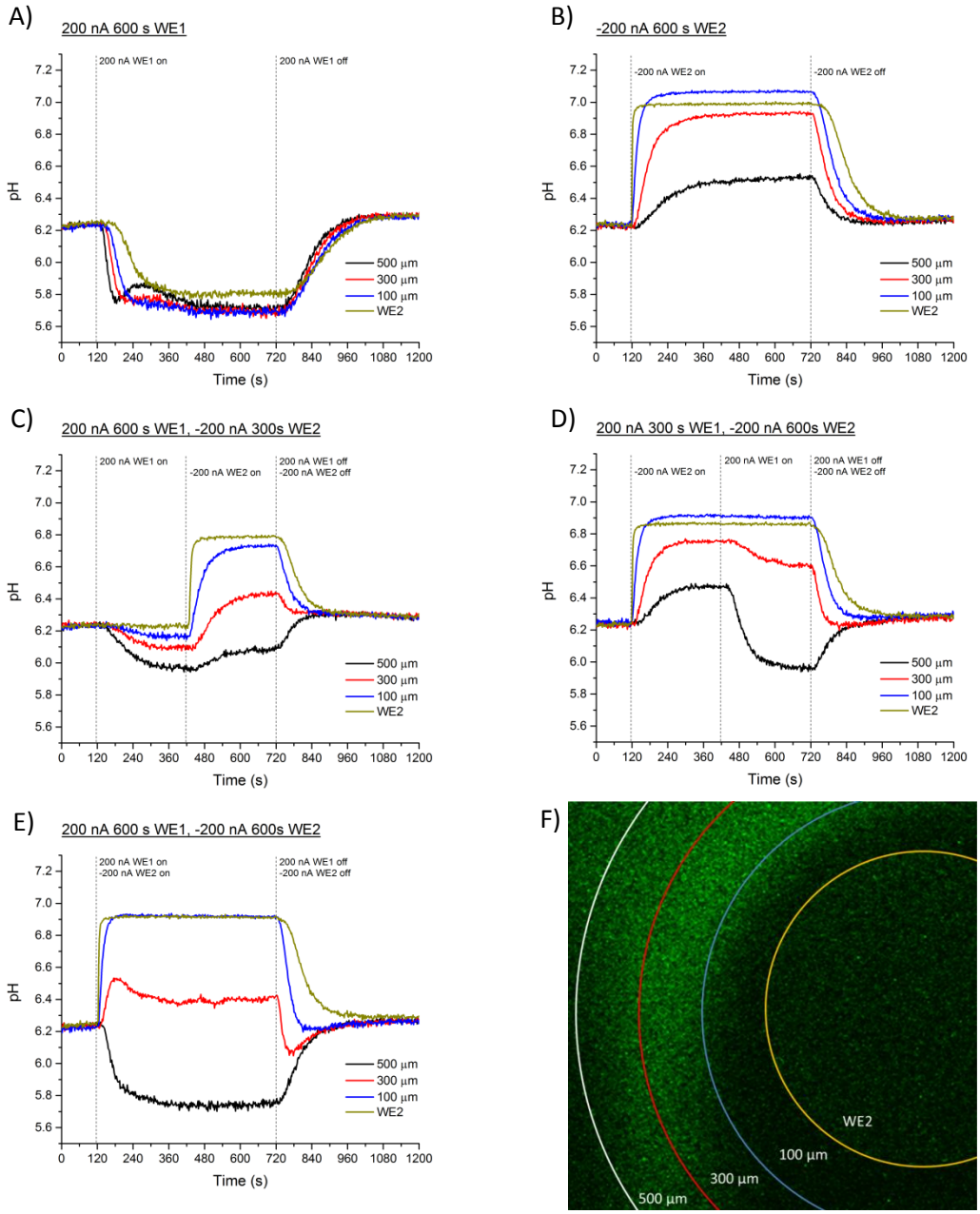

Figure A1.1: Graphs of pH over time showing the effect at the second working electrode (WE2) and nearby areas of currents applied at the first working electrode (WE1) and WE2. The distance between the two electrodes is 1 mm so the area labelled 500 µm (shown in black) is equidistant from both electrodes. A) 200 nA current applied at WE1 for 600 s starting at 120 s. B) -200 nA applied at WE2 starting at 120 s. C) 200 nA applied at WE1 for 600 s starting at 120 s with -200 nA applied at WE2 for 300 s starting at 420 s. D) -200 nA applied at WE2 for 600 s starting at 120 s with 200 nA applied at WE1 for 300 s starting at 420 s. E) 200 nA applied at WE1 and -200 nA applied at WE2, both for 600 s starting at 120 s. F) Image showing the 590 nm emission around WE2 after 600 s of the experiment shown bottom left. As expected, the opposing pH changes caused by the electrodes lead to a stable pH gradient across the space between them.

All CLSM measurements were performed using the settings in Section 6.2.3 to maintain compatibility with the calibration curve derived using those settings. Images were acquired every 2 s during electrochemical pH change experiments. Where areas around the electrode were measured, they were 200 µm wide with the width centred at the indicated distance from the electrode. A 2x objective lens was used to capture a larger image area.

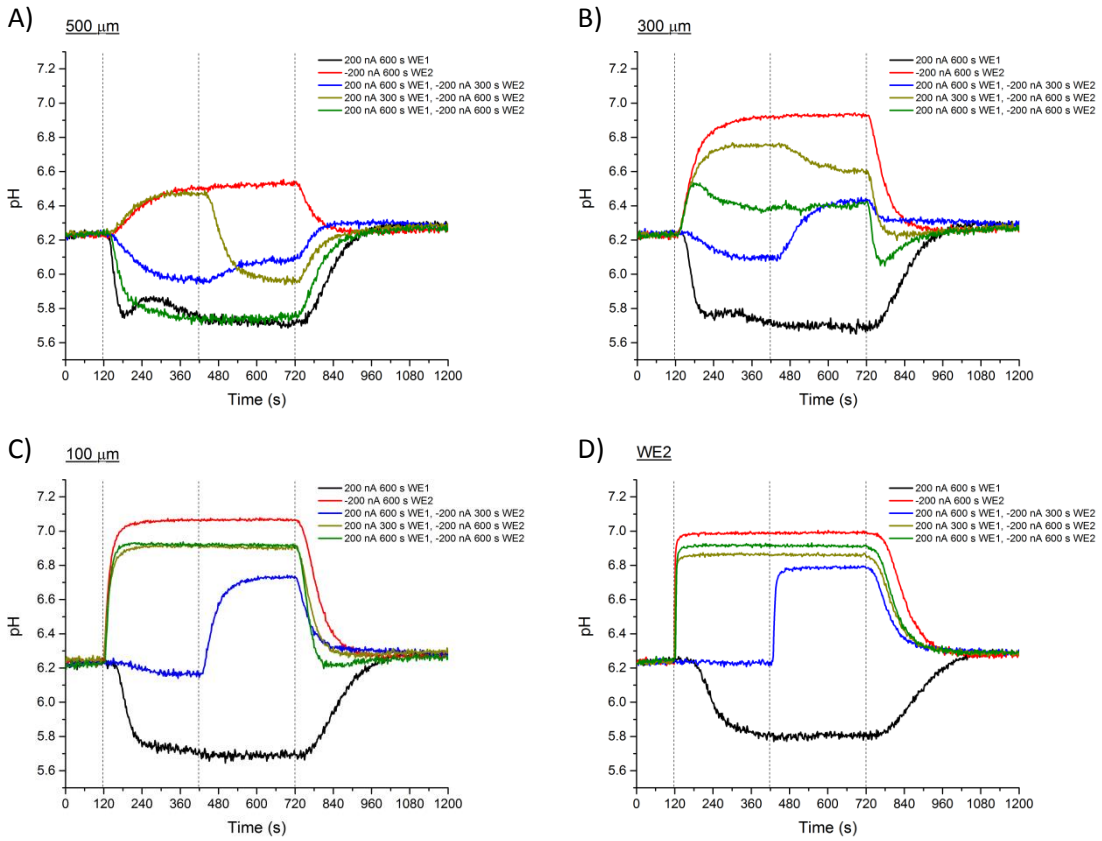

Figure A1.2: Graphs of pH over time from Figure A1.1, replotted so that each graph contains the data from all experiments in a single region. A) the area 500 µm from WE2 (which is equidistant between WE1 and WE2. B) the area 300 µm from WE2. C) the area 100 µm from WE2. D) WE2.

A1.3. Results and discussion

Figure A1.1 shows the effects of generating competing pH changes from two electrodes 1 mm apart. When 200 nA current (Figure A1.1a) was applied at working electrode 1 (WE1), the pH change spread across the solution and saturated at working electrode 2 (WE2) after approximately 5 minutes, causing a decrease of 0.4-0.5 pH units. When -200 nA was applied to WE2 (Figure A1.1b), an increase of 0.8 pH units was seen at the electrode, and the pH change spread across the solution, saturating at an increase of 0.3 pH units in the 500 µm region equidistant between the two electrodes. Next, a 200 nA current was applied to WE1 for 600 s, with a -200 nA current applied at WE2 for the final 300 s (Figure A1.1c). The pH change from WE1 was not as rapid or as large as would have been expected from the results shown in Figure A1.1a, but importantly the application of the opposing current at WE2 caused a competing pH increase which almost entirely counteracted the pH decrease at WE2 and in the 100 µm region, and reduced it in the 300 µm and 500 µm regions. When -200 nA current was instead applied at WE2 for 600 s then challenged with 200 nA current at WE1 after 300 s (Figure A1.1d), the new pH change from WE1 had some effect 500 µm and 300 µm away from WE2, but no noticeable effect in areas closer to WE2. Finally the simultaneous application of opposing currents at the two electrodes (Figure A1.1e) led to a stable pH gradient from pH 5.7 500 µm from WE2 to pH

6.9 at WE2. Figure A1.1f is an image of the 590 nm intensity at the 600 s point of the data shown in Figure A1.1e.

Figure A1.2 shows the data from Figure A1.1 arranged by area rather than by current application, for the convenience of the reader.

A1.4. Conclusions

Electrochemical pH control using competing electrodes was performed, and measured using the pH sensitive fluorescent dye SNARF-4F. It was shown that pH changes at one electrode could compete with changes diffusing from a neighbouring electrode, thereby demonstrating the possibility of using combinations of electrodes for fine control of pH.

A2. Electrochemical pH measurement

A2.1. Introduction

This appendix chapter details investigations into electrochemical pH measurement using methylene blue. For background, see Section 2.4. The materials and methods used in this chapter are described in Section A1.2. The investigations were carried out using CLSM (see Section 3.2.3). The results of the experiments are presented in Section A1.3. The findings are summarised in Section A1.4.

A2.2. Materials and methods

A2.2.1. General materials and methods

Unless otherwise indicated, all chemicals were purchased from Sigma-Aldrich. Methylene blue with carboxylic acid was obtained from Dr. Steven Johnson at the University of York.

Where the term 'phosphate buffer' is used, it refers to sodium phosphate buffer in 18.2 MΩ deionised H_2O made by mixing Na_2HPO_4 and NaH_2PO_4 in a ratio calculated to produce the desired pH. The pH was then adjusted to the correct value using NaOH or HCl and the buffer filtered using syringes with 0.22 μM filters. pH measurements were performed using a Mettler Toledo MP225 pH meter.

A2.2.2. ITO electrode fabrication

All experiments used 1 mm diameter ITO electrodes patterned onto No. 2 thickness glass cover slips. The cover slips were cleaned by rinsing and ultrasonication in, successively, acetone, isopropanol, ethanol and water, then dried under a nitrogen stream. Microposit S1813 photoresist was spin-coated onto the slides and baked at 115 ºC for 2 minutes. The slides were then immersed in chlorobenzene for 2.5 minutes, dried under a nitrogen stream, and then exposed to UV light through the mask pattern using a Karl Suss MJB3 mask aligner. Finally, the slides were immersed in Microposit MF-319 developer solution, rinsed in water and dried, before being sent to Evatech AG (Switzerland) for ITO deposition through electron beam evaporation.

Open-ended hollow glass cylinders were glued to the patterned slides to provide a vessel for solutions.

A.2.2.3. Methylene blue monolayer formation

To form monolayers of methylene blue on the patterned slides the following protocol was used. Slides were cleaned by rinsing and ultrasonication in, successively, acetone, isopropanol, ethanol and water then dried under a nitrogen stream. They were then immersed in piranha solution (7:3 ratio of sulphuric acid:hydrogen peroxide) for 5 minutes, then ultrasonicated in

water for 10 minutes and dried under a nitrogen stream. An open-ended hollow glass cylinder was then glued to each slide to provide a vessel for solutions.

The cylinder was filled with acetone and left for 2 minutes, then emptied and allowed to dry. It was then filled with 2% (3-aminopropyl)triethoxysilane (APTES) in acetone and left covered for 3 hours.

A solution of 0.5 mM methylene blue (MB) with 0.5 mM N-hydroxysuccinimide (NHS) and 1.5 mM 1-ethyl-3-(3-dimethylaminopropyl)carbodiimide (EDC) was prepared in 100 mM pH 5.5 MES buffer and incubated for 15 minutes. The cylinder was then emptied of APTES, rinsed with water and dried under a nitrogen stream. The cylinder was then filled with the MB-NHS-EDC mixture and left covered for either 2 hours or 4 hours. Finally, the cylinder was emptied and rinsed thoroughly with water before measurement.

A2.2.4. Electrochemical pH measurement

All electrochemical experiments were performed using an ITO working electrode, a Pt wire counter electrode and Ag/AgCl (3.5 M KCl) reference electrode. Current and voltage were controlled and measured using a PalmSens potentiostat. Measurement was performed in 100 mM phosphate buffer. Between each pH measurement the cell was emptied of buffer, rinsed 4x with new buffer and then filled with the new buffer. For each pH measurement, three current voltage sweeps were performed between -0.45 V and 0.2 V at a rate of 40 mV s^{-1}.

A2.3. Results and discussion

	Reduction peak voltage (V)		Oxidation peak voltage (V)	
pH	**4 hour**	**2 hour**	**4 hour**	**2 hour**
7.5	-0.24	-0.23	-0.26	-0.25
6.5	-0.20	-0.20	-0.22	-0.21
5.5	-0.16	-0.15	-0.17	-0.16
4.5	-0.10	-0.09	-0.10	-0.10
3.5	-0.02	-0.01	-0.03	-0.02
2.5	0.07	0.07	0.05	0.06
1.5	0.15	0.15	0.14	0.14

Table A2.1: Reduction and oxidation peak voltages for MB monolayers formed in 2 hours and 4 hours, measured in 100 mM phosphate buffer of varying pH.

Figure A2.1 shows the current-voltage profiles for cyclic voltammetry measurements performed using MB functionalized electrodes in 100 mM phosphate buffers of pH values varying from pH 1.5 to pH 7.5. Peaks in the current corresponding to reduction (positive peaks) and oxidation (negative peaks) of the MB molecules are clearly visible, with monolayers formed in 4 hours showing a significant larger peak than those formed in 2 hours. This indicated that significantly more MB was immobilised by the longer incubation period.

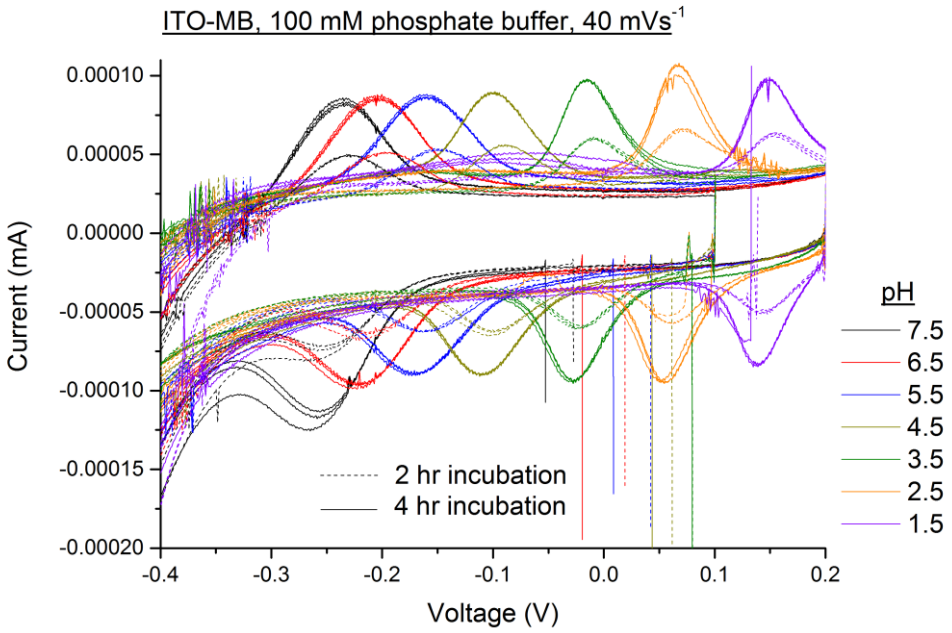

Figure A2.1: Graph showing cyclic voltammetry profiles in 100 mM phosphate buffer for ITO electrodes functionalised with monolayers of methylene blue (MB). The monolayers were formed in either a 2 hour or 4 hour incubation. Peaks indicated reduction and oxidation of the MB molecules, and the peak position depended on pH.

Figure A2.1 also shows that the voltage at which the redox peaks occurred depended strongly on the pH of the solution, and that this behaviour was repeatable, the 2 hour peaks being in the same positions (to within 0.01 V, see Table A2.1) as the 4 hour peaks despite the use of different samples for each measurement. As the pH of the measurement solution was decreased, the voltage at which the redox peaks occurred increased, with a difference of 0.04-0.09 V between each pH unit.

A2.4. Conclusions

Cyclic voltammetry measurements of methylene blue monolayers immobilised on electrode surfaces were shown to be a viable technique for electrochemical measurement of pH at an electrode surface in the neutral to acidic pH range. Such a technique might be a useful alternative to optical pH measurement in situations where optical measurements are impractical.

A3. Additional Material

A3.1. Introduction

This appendix chapter contains additional material omitted from the main chapters for readability.

A3.2. Determination of dissociation constants using FRET

FRET can be used to calculate the dissociation constant (K_d) of a peptide dimer. K_d is defined as:

$$K_d = \frac{[A]_{free}[D]_{free}}{[AD]}$$

Eq. 1

where $[A]_{free}$ is the concentration of unbound acceptor-labelled peptide, $[D]_{free}$ the concentration of the unbound donor-labelled peptide and $[AD]$ the concentration of acceptor-donor heterodimers. If the emission of an acceptor dye attached to one of the peptides is measured as a function of concentration of the acceptor-labelled peptide against a constant concentration of the donor-labelled peptide, a binding curve is produced, from which the K_d may be calculated by fitting the curve with the equation:

$$y = L + (Y - L)\left(1 - \frac{2K_d}{x - [A] + K_d + \sqrt{(K_d + [A] - x)^2 + 4K_d x}}\right)$$

Eq. 2

where y is the measured FRET emission, L the minimum FRET emission, Y the maximum FRET emission, $x = [D]$ the (constant) total concentration of donor-labelled peptide, and $[A]$ the (variable) total concentration of acceptor-labelled peptide.

The FRET signal, y, as a proportion of the maximum, Y, will equal the fraction of bound acceptor-labelled peptides:

$$\frac{y}{Y} = \frac{[A]_{bound}}{[A]_{bound\ max}}$$

Eq. 1

where $[A]_{bound}$ is the concentration of bound acceptor-labelled peptides and $[A]_{bound\ max}$ the maximum concentration of bound acceptor-labelled peptides. $[D]_{bound}$ and $[D]_{bound\ max}$ are similarly defined as the concentration and maximum concentrations of bound donor-labelled peptides, and so in the case of 1:1 binding we have, since the concentration of dimers must necessarily equal the concentration of bound peptide:

$$[A]_{bound} = [D]_{bound} = [AD]$$

Eq. 2

and since the maximum possible concentration of bound peptide must equal the total concentration of acceptor-labelled peptide:

$$[A]_{bound\ max} = [D]_{bound\ max} = [A]$$

Eq. 3

From Eq. 1, 4 and 5, we then have:

$$K_d = \frac{[A]_{free}[D]_{free}}{[AD]} = \frac{([A] - [A]_{bound})[D]_{free}}{[D]_{bound}} = \frac{([D]_{bound\ max} - [D]_{bound})[D]_{free}}{[D]_{bound}}$$

Eq. 4

and so:

$$[D]_{bound} = \frac{[D]_{bound\ max}[D]_{free}}{K_d + [D]_{free}}$$

Eq. 5

Combining Eq. 7 with Eq. 3 and Eq. 5 then gives:

$$\frac{y}{Y}[A]_{bound\ max} = \frac{[D]_{bound\ max}[D]_{free}}{K_d + [D]_{free}} \Rightarrow y = \frac{Y[D]_{free}}{K_d + [D]_{free}}$$

Eq. 6

By definition:

$$[A]_{bound} = [A] - [A]_{free}$$
$$[D]_{bound} = [D] - [D]_{free}$$
$$\Rightarrow [A]_{free} = [A] - [D] + [D]_{free}$$

Eq. 7

From Eq. 1, 4 and 9 we then have:

$$K_d = \frac{[A]_{free}[D]_{free}}{[D]_{bound}} = \frac{[D]_{free}\left([A] - [D] + [D]_{free}\right)}{[D] - [D]_{free}}$$

Eq. 8

and then rearranging:

$$[D]_{free}{}^2 + (K_d + [A] - [D])[D]_{free} - K_d[D] = 0$$

Eq. 9

Solving the quadratic equation then gives:

$$[D]_{free} = \frac{-(K_d + [A] - [D]) \pm \sqrt{(K_d + [A] - [D])^2 + 4K_d[D]}}{2}$$

Eq. 10

And combining with Eq. 8 gives:

$$\begin{aligned} y &= Y\left(\frac{-(K_d + [A] - [D]) \pm \sqrt{(K_d + [A] - [D])^2 + 4K_d[D]}}{2K_d + \left(-(K_d + [A] - [D]) \pm \sqrt{(K_d + [A] - [D])^2 + 4K_d[D]}\right)}\right) \\ &= Y\left(\frac{-K_d - [A] + [D] \pm \sqrt{(K_d + [A] - [D])^2 + 4K_d[D]}}{K_d - [A] + [D] \pm \sqrt{(K_d + [A] - [D])^2 + 4K_d[D]}}\right) \\ &= Y\left(\frac{-K_d + (-K_d + K_d) - [A] + [D] \pm \sqrt{(K_d + [A] - [D])^2 + 4K_d[D]}}{K_d - [A] + [D] \pm \sqrt{(K_d + [A] - [D])^2 + 4K_d[D]}}\right) \\ &= Y\left(\frac{-2K_d + K_d - [A] + [D] \pm \sqrt{(K_d + [A] - [D])^2 + 4K_d[D]}}{K_d - [A] + [D] \pm \sqrt{(K_d + [A] - [D])^2 + 4K_d[D]}}\right) \\ &= Y\left(1 - \frac{2K_d}{K_d - [A] + [D] \pm \sqrt{(K_d + [A] - [D])^2 + 4K_d[D]}}\right) \end{aligned}$$

Eq. 11

Finally, defining $x = [D]$ and adding a correction factor L for the background signal gives Eq. 2:

$$y = L + (Y - L)\left(1 - \frac{2K_d}{x - [A] + K_d + \sqrt{(K_d + [A] - x)^2 + 4K_d x}}\right)$$

A3.3. CD measurement HV data

Figure A3.1 shows the high voltage (HV) data for the CD measurements shown in Figures 4.1 and 4.2 in Section 4.

A3.4. HPLC and mass spectrometry data

Figures A3.2 and A3.3 show the HPLC and mass spectrometry data for all the synthesised peptides, as described in Section 4.

A3.5. Example melting curve data

Figure A3.4 shows the individual measured CD spectra for the example melting curve shown in Figure 4.5 in Section 4.

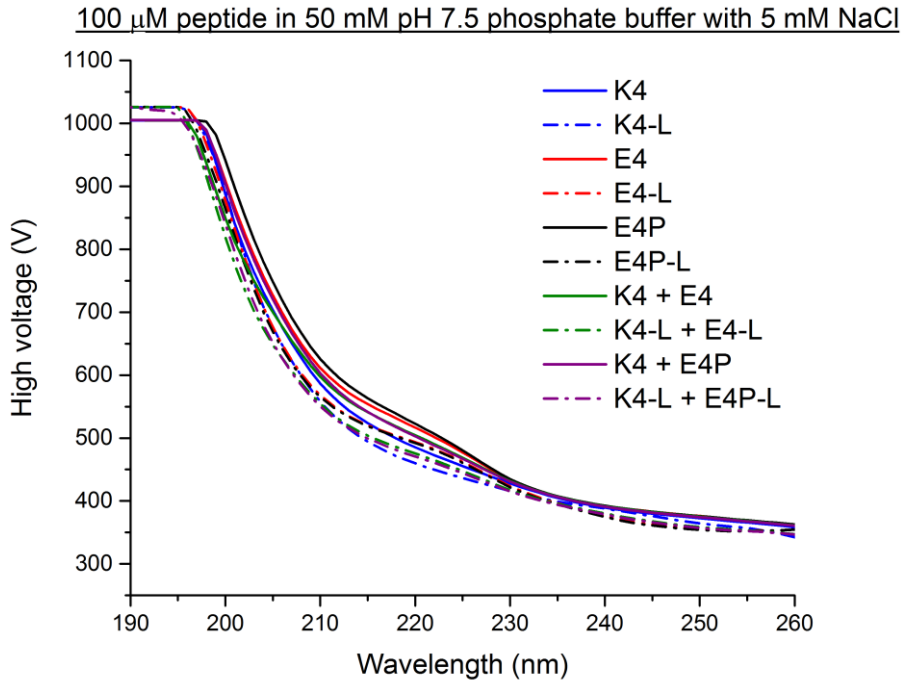

Figure A3.1: High voltage (HV) data recorded for the CD measurements shown in Figures 4.3 and 4.4. It is usually recommended that the HV not exceed 700 V.

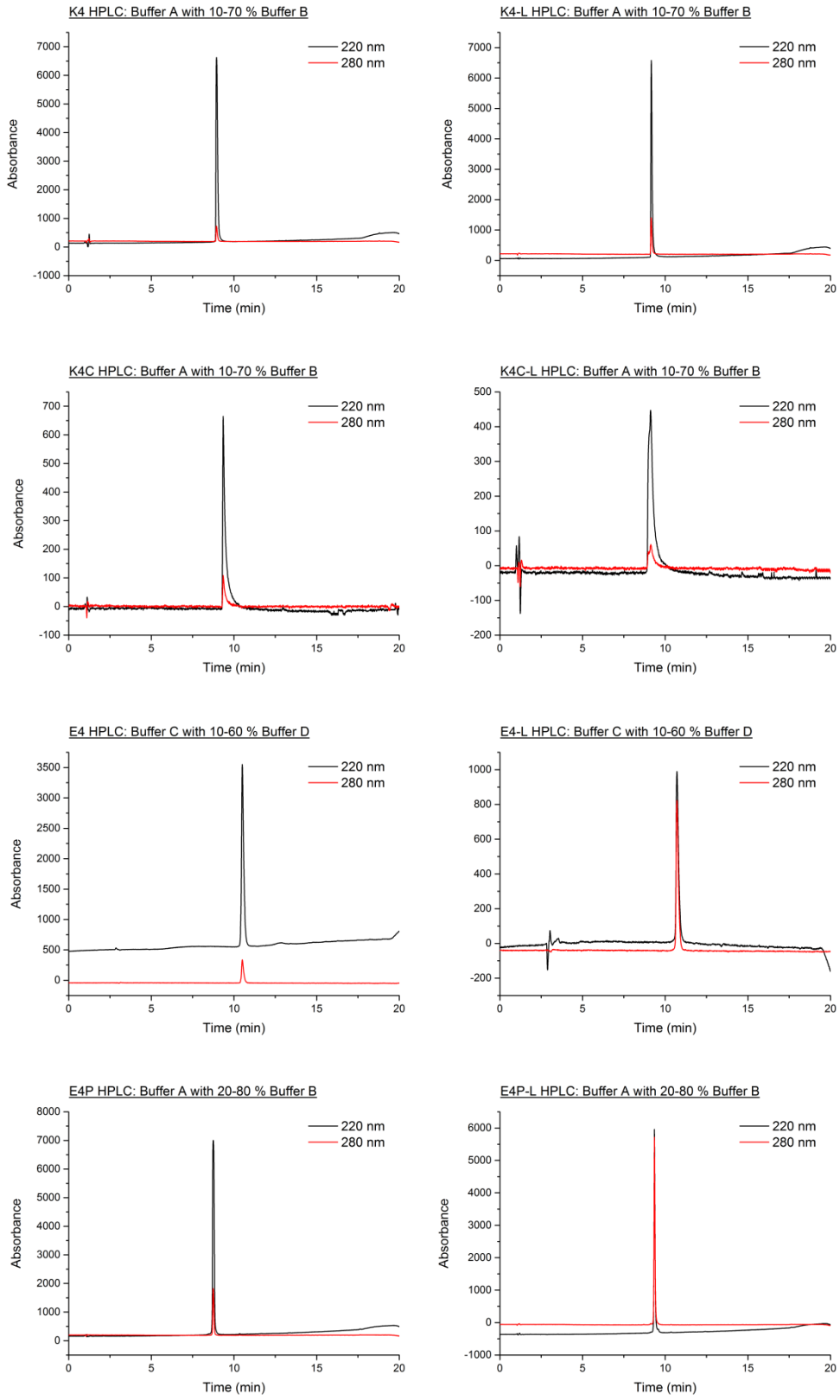

Figure A3.2: Analytical reverse-phase HPLC traces for the synthesised peptides showing absorbance at 220 nm (from the peptide bonds) and 280 nm (from the tryptophan/tyrosine residues). Pure products were obtained for all peptides.

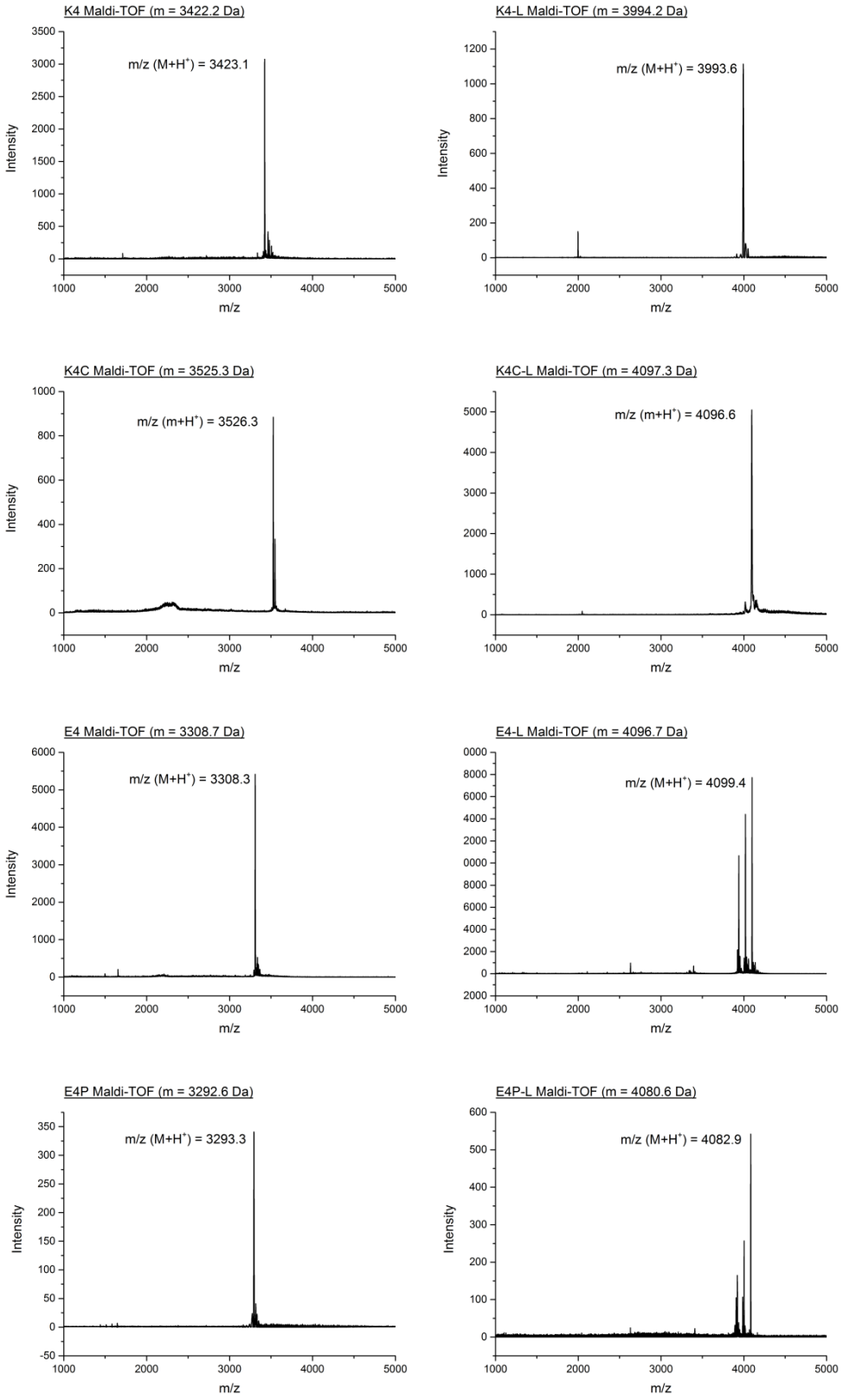

Figure A3.3: MALDI-TOF mass spectra for the synthesised peptides. The title of each graph gives the expected mass for the peptide and the peak is labelled with the mass to charge ratio. In all cases the charge z=1 and so the expected and measured mass may be directly compared. A pure product with the correct mass was found for all peptides, though fragmentation of the ATTO 594 dye was observed for E4-L and E4P-L.

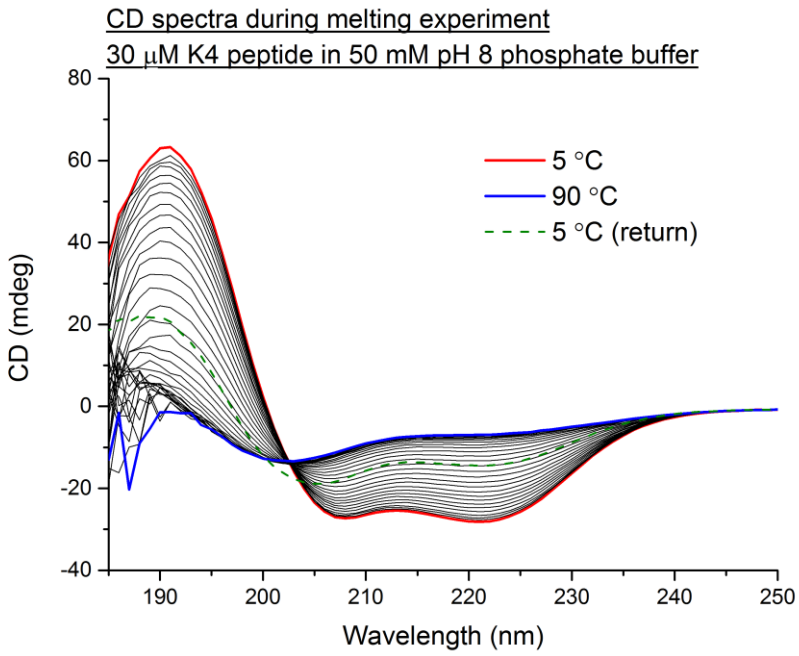

Figure A3.4: Individual CD spectra for the melting curve shown in Figure 4.5 for 30 μM K4 peptide in 50 mM pH 8 phosphate buffer. The initial 5 ºC and final 90 ºC CD spectra are shown in bold in red and blue respectively, with spectra for all intermediate temperatures shown in black. After the 90 ºC measurement, the peptide was returned to 5 ºC and re-measured (bold dashed green spectrum). Since the signal did not return to the initial 5 ºC measurement, it is likely that the peptide was damaged at high temperature.

A4. Figure permissions

I am grateful for kind permission from the rights holders to reuse the following figures in this work:

Figure 1.2 (page 20): Adapted from Molecule of the Month images by David S. Goodsell and the RCSB Protein Data Bank and used under a CC-BY-4.0 license (https://creativecommons.org/licenses/by/4.0/)

Figure 1.4 (page 22): Adapted from Wan, A. M. D. *et al*. Electrical control of protein conformation. *Adv. Mater.* **24**, 2501–2505 (2012) with permission. Copyright © 1999-2017 John Wiley & Sons, Inc.

Figure 2.2 (page 34): Adapted from https://commons.wikimedia.org/wiki/File:Amino_Acids.svg by Dan Cojocari and used under a CC-BY-SA-3.0 licence (https://creativecommons.org/licenses/by-sa/3.0/deed.en)

Figure 2.5 (page 36): Adapted from Kohn, W. D. & Hodges, R. S. De novo design of α-helical coiled coils and bundles: Models for the development of protein-design principles. *Trends Biotechnol.* **16**, 379–389 (1998), with permission from Elsevier.

Figure 2.6 (page 37): Adapted from Crick, F. H. C. The packing of α-helices: simple coiled-coils. *Acta Crystallogr.* **6**, 689–697 (1953), with permission from the International Union of Crystallography (http://journals.iucr.org/).

Figure 2.7 (page 38): Adapted from McLachlan, A. D. & Stewart, M. Tropomyosin coiled-coil interactions: evidence for an unstaggered structure. *J. Mol. Biol.* **98**, 293–304 (1975), with permission from Elsevier.

Figure 2.11 (page 40): Adapted from O'Shea, E., Klemm, J., Kim, P. & Alber, T. X-ray structure of the GCN4 leucine zipper, a two-stranded, parallel coiled coil. *Science* **254**, 539–544 (1991) with permission from AAAS.

Figure 2.12 (page 41): Adapted from O'Shea, E., Klemm, J., Kim, P. & Alber, T. X-ray structure of the GCN4 leucine zipper, a two-stranded, parallel coiled coil. *Science* **254**, 539–544 (1991) with permission from AAAS.

Figure 2.13 (page 41): Adapted from O'Shea, E. K., Rutkowski, R. & Kim, P. S. Mechanism of specificity in the Fos-Jun oncoprotein heterodimer. *Cell* **68**, 699–708 (1992), with permission from Elsevier.

Figure 2.14 (page 43): Adapted from O'Shea, E. K., Lumb, K. J. & Kim, P. S. Peptide 'Velcro': design of a heterodimeric coiled coil. *Curr. Biol.* **3**, 658–67 (1993), with permission from Elsevier.

Figure 2.15 (page 49): Adapted from O'Hare, H., Juillerat, A., Dianisková, P. & Johnsson, K. A split-protein sensor for studying protein-protein interaction in mycobacteria. *J. Microbiol. Methods* **73**, 79–84 (2008), with permission from Elsevier.

Figure 2.16 (page 50): Adapted from Shekhawat, S. S., Porter, J. R., Sriprasad, A. & Ghosh, I. An autoinhibited coiled-coil design strategy for split-protein protease sensors. *J. Am. Chem. Soc.* **131**, 15284–90 (2009), with permission. Copyright (2009) American Chemical Society.

Figure 2.17 (page 52): Adapted from Laromaine, A., Akbulut, O., Stellacci, F. & Stevens, M. M. Supramolecular replication of peptide and DNA patterned arrays. *J. Mater. Chem.* **20**, 68 (2010) with permission of The Royal Society of Chemistry.

Figure 2.18 (page 53): Adapted from Ryadnov, M. G., Ceyhan, B., Niemeyer, C. M. & Woolfson, D. N. 'Belt and braces': a peptide-based linker system of de novo design. *Journal of the American Chemical Society* **125,** 9388–94 (2003) with permission. Copyright (2003) American Chemical Society.

Figure 2.19 (page 54): Adapted from Wu, K., Liu, J., Johnson, R. N., Yang, J. & Kopeček, J. Drug-free macromolecular therapeutics: Induction of apoptosis by coiled-coil-mediated cross-linking of antigens on the cell surface. *Angew. Chemie - Int. Ed.* **49,** 1451–1455 (2010) with permission. Copyright © 1999-2017 John Wiley & Sons, Inc.

Figure 2.20 (page 55): Adapted from Apostolovic, B., Deacon, S. P. E., Duncan, R. & Klok, H. A. Hybrid polymer therapeutics incorporating bioresponsive, coiled coil peptide linkers. *Biomacromolecules* **11,** 1187–1195 (2010) with permission. Copyright (2010) American Chemical Society.

Figure 3.4 (page 75): Adapted from Kelly, S. M., Jess, T. J. & Price, N. C. How to study proteins by circular dichroism. *Biochim. Biophys. Acta* **1751,** 119–139 (2005) with permission from Elsevier.

Figure 3.5 (page 75): Adapted from Rodger, A. & Nordén, B. *Circular Dichroism & Linear Dichroism*. (Oxford University Press, 1997) with permission from Oxford University Press.